

DISCRETE ELEMENT MODELLING OF THE  
DYNAMIC BEHAVIOUR OF NON-SPHERICAL  
PARTICULATE MATERIALS

By

MOHAMMAD HOSSEIN ABBASPOUR-FARD

A thesis submitted for the degree of  
Doctor of Philosophy in Agricultural Engineering  
in the  
Department of Agricultural and Environmental Sciences  
at the  
University of Newcastle upon Tyne

NEWCASTLE UNIVERSITY LIBRARY

200 10096 6

Thesis L 6759.

September 2000

# DEDICATION

This work is dedicated to the soul of my father.  
May his soul rest in perfect peace.

# ABSTRACT

A numerical model based on the discrete element (DE) method, for modelling the flow of irregularly shaped, smooth-surfaced particles in a 3-D system is presented. An existing DE program for modelling the contact between spherical particles in periodic space (without real walls or boundaries) was modified to model non-spherical particles in a system with containing walls. The new model was validated against analytical calculations of single particle movements and also experimentally against data from physical experiments using synthetic non-spherical particles at both a particle and bulk scale. It was then used to study the effect of particle shape on the flow behaviour of assemblies of particles with various aspect ratios discharging from a flat-bottomed hopper.

The particles were modelled using the Multi-Sphere Method (MSM) which is based on the **CSG** (*Constructive Solid Geometry*) technique for construction of complex solids by combining primitive shapes. In this method particle geometry is approximated using overlapping spheres of arbitrary diameter which are fixed in position relative to each other. The contact mechanics and contact detection method are the same as those used for spheres, except that translation and rotation of element spheres are calculated with respect to the motion of the whole particle.

In the analytical validation, the MSM was applied to a number of common dynamic particle-particle and particle-surface situations. The analytical validation of the model confirmed that this method can be used for operations such as sliding, dropping and conveying of non-spherical particles with high aspect ratio. It was found that a smaller time step was needed for simulation of particle collision than for a quasi-static situation. The lobed surface of multi-sphere particles also created a friction-like effect when such particles slid across one another due to the forces opposing the direction of movement. The greater the amount of overlap between the adjacent element spheres, the lower the friction effect. The results of the simulations and theoretical calculations showed that this friction was negligible when the overlap between the adjacent spheres was at least 75% of the element sphere diameters (for cylindrical particles).

The experimental validation of the model was carried out at the particle and the bulk scale. At the micro-scale the method was compared to experiment by replicating as closely as possible the slow controlled flow of a limited number (10) of particles. There was reasonable agreement (82%) between the predictions of the model and the average of experiments in terms of correlation between particle co-ordinate and orientation as a function of time. At the bulk scale there was good agreement between experiment and simulation in terms of bed structure, flow rate and occurrence of arching. In the validation of the model at both scales it was also found that the dynamic coefficient of friction gave a better correlation between experiment and simulation than the static friction coefficient. This suggests that the dynamic coefficient of particles should be used in the DE model for sliding contacts.

Numerical simulations of packing and flow of particles from a flat-bottomed hopper with a range of aspect ratios were performed to investigate the effect of particle shape on packing and flow behaviour of a particulate assembly. It was found that the particle shape influenced both bed structure and flow characteristics such as flow pattern, shear band strength and the occurrence of bridging. The flow of the bed of spherical particles was smoother than the flow of beds of elongated particles in which flow was fluctuating and there was more resistance to shear.

# TABLE OF CONTENTS

<b>DEDICATION.....</b>	<b>I</b>
<b>ABSTRACT.....</b>	<b>II</b>
<b>TABLE OF CONTENTS .....</b>	<b>IV</b>
<b>TABLE OF FIGURES.....</b>	<b>IX</b>
<b>LIST OF TABLES .....</b>	<b>XIX</b>
<b>ACKNOWLEDGMENTS .....</b>	<b>XX</b>
<b>1. INTRODUCTION AND LITERATURE REVIEW .....</b>	<b>1</b>
1.1 INTRODUCTION .....	1
1.1.1. Background .....	1
1.1.2. Objectives .....	4
1.1.3. Organisation of Thesis .....	5
1.2. LITERATURE REVIEW .....	7
1.2.1 Approaches to investigation of particulate behaviour.....	7
1.2.1.1. Experimental approaches .....	7
1.2.1.2. Modelling approaches to particulate material studies .....	10
1.2.1.2.1. Continuum approach.....	11
1.2.1.2.2. Discrete approach .....	14
1.2.2. Development of DEM.....	15
1.2.2.1. Shape representation in the DEM.....	16
1.2.2.2. Parallel programming in DEM.....	21
1.2.2.3. Application of the DEM.....	23
1.2.2.3.1. DEM studies on particulate biomaterials.....	24

1.2.2.4. Role of particle shape on the different behaviours of particulate materials .....	27
1.2.3. Theory of the DEM.....	31
1.2.3.1. Definition of terms describing contact between bodies .....	31
1.2.3.2. Principles of the DEM.....	34
1.2.3.3. Contact representation.....	36
1.2.3.4. Contact models.....	38
1.2.3.4.1. Normal and tangential stiffness coefficients.....	39
1.2.3.4.2. Damping .....	43
1.2.3.5. Time step.....	45
1.2.3.6. Contact search .....	47
1.2.3.7. Contact detection.....	49
1.2.3.8. Calculation cycle .....	51
1.2.3.8.1. Relative velocity at contact point .....	52
1.2.3.8.2. Determination of contact force and moment .....	56
1.2.3.8.3. Calculation of particle motion and updating of particle position ....	58
1.2.3.8.4. Incorporation of damping .....	59
1.3 SUMMARY .....	62
<b>2. MULTI-SPHERE SHAPE REPRESENTATION FOR DEM.....</b>	<b>64</b>
2.1. INTRODUCTION .....	64
2.2. MULTI-SPHERE MODEL PARTICLE CONSTRUCTION .....	66
2.2.1. Determination of the model particle centroid .....	67
2.2.2. Fitting element spheres to the boundary of a real particle .....	68
2.3. CONTACT MECHANICS AND PARTICLE KINEMATICS USING THE MULTI-SPHERE METHOD (MSM) .....	71
2.3.1. Resultant force and moment acting on a particle due to contacts.....	71

2.3.2.	Translational and rotational motion of a particle .....	75
2.3.3.	Velocity and position of element spheres .....	77
2.4.	IMPLEMENTATION OF THE MULTI-SPHERE METHOD IN A DEM CODE .....	81
2.4.1.	Structure of the existing program .....	81
2.4.1.1.	Program development .....	81
2.4.1.2.	Program components.....	82
2.5.	MODIFICATION OF THE ORIGINAL PROGRAM.....	86
2.5.1.	Set up of the simulated system (workspace and particle numbers) .....	87
2.5.2.	Particle generation .....	87
2.5.3.	Generation of workspace (walls) .....	89
2.5.4.	Consolidation (deposition) of model particles.....	91
2.5.5.	Contact search and detection .....	95
2.5.6.	Calculation cycle.....	97
2.6.	POST PROCESSING OF THE SIMULATION RESULTS .....	99
2.6.1.	AutoCAD .....	101
2.6.2.	POV Ray .....	101
2.7.	SUMMARY .....	103
<b>3.</b>	<b>ANALYTICAL VALIDATION AND PARAMETRIC STUDIES ON THE DE MODEL USING THE MUTI-SPHERE METHOD.....</b>	<b>105</b>
3.1.	INTRODUCTION .....	105
3.2	WEIGHT OF A PARTICLE IN A QUASI-STATIC SITUATION .....	105
3.3	COLLISION OF A MULTI-SPHERE PARTICLE WITH A SURFACE .....	111
3.4	SLIDING OF A PARTICLE ON AN INCLINED SURFACE.....	115
3.5	CONVEYING OF A PARTICLE .....	120
3.6	ROTATION AND TRANSLATION OF A PARTICLE DUE TO A COLLISION FORCE ....	122
3.7	PSEUDO-FRICTION IN A MULTI-SPHERE MODEL PARTICLE .....	125

3.2.1	Simulation results.....	126
3.8	ESTIMATION OF ERROR IN CONTACT FORCE FOR A MULTI-SPHERE PARTICLE ..	132
3.9	SIMULATION EXAMPLES.....	137
3.9.1	Conveying a tapered shape particle in a 2-D simulation .....	137
3.9.2	Dropping an irregular shaped particle in a 3-D system .....	138
3.9.3	Conveying an assembly of conical particles.....	141
3.9.4	Discharge (flow) of particles from a bin.....	142
3.9.5	Singulation of an assembly of Spheroidal particles.....	145
3.10	RUN TIME.....	146
3.11	SUMMARY .....	149
<b>4.</b>	<b>EXPERIMENTAL VALIDATION OF THE MULTI-SPHERE METHOD</b>	<b>151</b>
4.1.	INTRODUCTION .....	151
4.2.	MICRO-SCALE EXPERIMENTAL VALIDATION .....	151
4.2.1.	Materials and methods .....	151
4.2.2.	Results and discussion .....	154
4.2.3.	Statistical analysis and discussion .....	159
4.3.	MACRO-SCALE EXPERIMENTAL VALIDATION .....	164
4.3.1.	Materials and method.....	165
4.3.2.	Results and discussion .....	169
4.3.2.1.	Packing structure .....	169
4.3.2.2.	Particle flow .....	173
4.3.2.3.	Flow rate.....	173
4.3.2.4.	Arching phenomenon during particles flow.....	173
4.3.2.5.	Verification of the Beverloo Equation .....	177
4.3.2.6.	Velocity profile during flow.....	181
4.3.2.7.	Stagnant and flow region boundary .....	183

4.3.2.8.	Free surface height and shape .....	184
4.4.	SUMMARY .....	186
<b>5.</b>	<b>AN EXPLORATION OF THE EFFECT OF PARTICLE SHAPE ON BED STRUCTURE AND FLOW CHARACTERISTICS OF PARTICLES DISCHARGED FROM A HOPPER.....</b>	<b>187</b>
5.1.	INTRODUCTION.....	187
5.2	HOPPER CONFIGURATION AND SIMULATION PROCEDURE .....	187
5.3.	RESULTS AND DISCUSSION.....	190
5.3.1.	Packing structure.....	190
5.3.1.1.	Co-ordination number .....	196
5.3.1.2.	Force acting at the bottom of the hopper.....	198
5.3.2.	Effect of particle shape on flow characteristics of particles .....	200
5.3.2.1.	Evolution of solid fraction during flow.....	201
5.3.2.2.	Particle trajectories .....	203
5.3.3.	Particle flow .....	211
5.3.3.1	Development of shear band .....	215
5.4.	CONCLUSION.....	219
<b>6.</b>	<b>CONCLUSION AND RECOMMENDATION FOR FURTHER WORK ...</b>	<b>221</b>
6.1.	CONCLUSION .....	221
6.2.	RECOMMENDATIONS FOR FURTHER STUDIES.....	223
	<b>REFERENCES: .....</b>	<b>225</b>
	<b>APPENDIX A.....</b>	<b>242</b>
	<b>APPENDIX B .....</b>	<b>243</b>
	<b>APPENDIX C .....</b>	<b>245</b>
	<b>APPENDIX D.....</b>	<b>247</b>
	<b>APPENDIX E .....</b>	<b>253</b>
	<b>APPENDIX F .....</b>	<b>254</b>

## TABLE OF FIGURES

<b>Figure 1.1</b>	Contact parameters: a) for smooth non-spherical, convex; b) circular particles as defined in the text.....	33
<b>Figure 1.2</b>	Normal ( $\Delta_n$ ) and tangential ( $\Delta_{st}$ and $\Delta_{sr}$ ) displacements for two particles in contact due to: (a) relative translation and (b) relative rotation of the particles.....	33
<b>Figure 1.3</b>	The DEM procedure for contact force calculations and updating the dynamic situation of particles; a) Recognising the formation of contact points due to relative velocities and position of particles. b) Application of force-displacement law for each contact point to calculate the contact force. c) The moment of contact forces about the particle centroid is calculated and the resultant force and moment on particle centroid is determined. d) Application of Newton's second law of motion to calculate the particle acceleration and velocity.....	35
<b>Figure 1.4</b>	DEM contact models for cohesionless materials: a) the maximum frictional force based on the sum of spring and dashpot; b) the maximum frictional force calculated only from spring (elastic) force (Walton,1983). .....	39
<b>Figure 1.5</b>	Contact detection between particles; a) Circular shape b) Polygonal shape. .....	49
<b>Figure 1.6</b>	Simulation steps in DEM; a) Particle and environment generation, b) Contact search and detection, c) Calculation of contact force, d) update the particle accelerations.....	52
<b>Figure 1.7</b>	Contact definitions between two contacting spheres.....	53
<b>Figure 2.1</b>	Approximating the surface contour of a 2-D particle using (a) non-overlapping and (b) overlapping circles. ....	66
<b>Figure 2.2</b>	Fitting element spheres to the boundary of a real particle: (a) segmentation of the boundary; (b) calculating the position and radius of element spheres. .....	69
<b>Figure 2.3</b>	Spheroidal DEM model particle comprising; (a) 15 spheres and (b) 30 spheres.....	70

<b>Figure 2.4</b>	Schematic of contact between two multi-sphere axi-symmetrical particles, each comprises two element spheres of the same diameter.....	72
<b>Figure 2.5</b>	Method of transfer of forces acting on element spheres to the centroid of a particle. Resultant forces and moments from normal and tangential forces respectively acting on each element (spheres A and B) shown in (a) are transferred to the centre of each sphere as shown in (b). The moments caused by forces whose line of action does not pass through the particle centroid are then transferred, along with moments due to tangential forces, to the particle centroid as shown in (c). .....	74
<b>Figure 2.6</b>	Method of updating the velocity and position of an element sphere from translational and rotational velocities of the particle centroid. ....	77
<b>Figure 2.7</b>	Examples of multi-sphere, axi-symmetrical particle shapes (a) a typical model particle before rendering (3 element spheres), (b) irregular (12 element spheres), (c) tapered (30 element spheres), (d) cylindrical (20 element spheres), (e) 1.3:1 spheroid (18 element spheres) and (f) 2:1 spheroid (28 element spheres). ....	80
<b>Figure 2.8</b>	The main configuration of the original program (CONBAL).....	85
<b>Figure 2.9</b>	Generation of 200 randomly oriented multi-sphere particles each consisting of two element spheres. ....	89
<b>Figure 2.10</b>	Basic wall arrangement for the simulation workspace. The numbers represent the walls.....	90
<b>Figure 2.11</b>	Modified particle, sphere and wall generation algorithm. ....	92
<b>Figure 2.12</b>	Evolution of number of contact points per particle (coordination number, $C_n$ ) during consolidation process for an assembly of 200 particles each comprised of 2 element spheres. ....	93
<b>Figure 2.13</b>	Multi-sphere particle assemblies after random generation and deposition under a gravity field; (a) 200 two-element particles, (b) 200 nine-element cylindrical particles, and (c) 100 twelve-element tapered particles.....	94
<b>Figure 2.14</b>	Contact search and detection between particle-particle and particle-wall in the modified program by recognising spheres of the same particle and discriminating walls from spheres. ....	96

<b>Figure 2.15</b>	calculations cycle in the modified program. ....	100
<b>Figure 2.16</b>	Post-processing steps for DEM results visualisation. ....	102
<b>Figure 3.1</b>	Theoretical relationship between the weight of a particle ( $w$ ) placed on a surface and the contact force ( $F$ ) between the particle and the surface: (a) horizontal and (b) vertical particle orientation.....	106
<b>Figure 3.2</b>	Effect of time step and damping coefficient on: (a) contact velocity, (b) elastic contact force, (c) damping force and (d) resultant contact force for vertical orientation of the particle in the stable situation (resting on the surface) for two damping ratios, 0.21 (left) and 0.5 (right). In these numerical tests the actual weight of the particle was 0.2105 N.....	109
<b>Figure 3.3</b>	Effect of particle orientation (horizontal and vertical) with different number of contact points on simulation results of a particle colliding with a surface; (a) particle movement and (b) evolution of the first collision force. The time step for these simulations was $1 \text{ E } -06 \text{ sec}$ ( $\text{frac}=0.1$ ). ...	112
<b>Figure 3.4</b>	Effect of time step on maximum collision force (damping coefficient=0) for a two element multi-sphere particle dropped on to a flat surface. Initial velocity has been applied to the particle to simulate the collision from an arbitrary height. The particle has been oriented with its major axis normal to the surface. ....	113
<b>Figure 3.5</b>	Comparison between theoretical impulse during particle collision and that of simulated with the DE code for different time steps. In each case the percentage of error is shown on the top of the corresponding column... ..	114
<b>Figure 3.6</b>	Free body diagram of a particle sliding on an inclined surface. ....	115
<b>Figure 3.7</b>	Results of sliding of the particle with different coefficients of friction between the particle and surface in the absence of tangential damping. (T stands for Theory and S for simulation). The inclination angle for these simulations was $30^\circ$ and the model particle comprised five element spheres.....	116
<b>Figure 3.8</b>	Effect of damping on sliding of a particle when applied as an additional dissipation mechanism during sliding on an inclined surface. These results have been obtained for the inclination angle of $30^\circ$ and $\mu=0.3$ .....	117

**Figure 3.9** Prediction of the DE model for particle sliding with different time steps for a cylindrical particle comprised of 9-element spheres.....117

**Figure 3.10** Different model particle configurations for particle sliding simulations on an inclined surface. The particles have the same volume and aspect ratio but different element sphere densities. ....118

**Figure 3.11** (a) Effect of number of element spheres on particle sliding simulations; numbers show the element spheres per particle. The inclination angle and the damping coefficient were 30° and 0.21 respectively. (b) Relationship between the number of contact points and the damping effect. ....119

**Figure 3.12** Effect of time step, damping coefficient and coefficient of friction on the prediction of the DE model with Multi-sphere approach for handling simulation of a particle on a horizontal conveyor. ....121

**Figure 3.13** Model particle configuration for rotational and translational simulations of a particle due to an instantaneous collision force. n is the number of element spheres for the model particle. ....122

**Figure 3.14** Simulation results for particle translation with and without applying damping. The slope of the lines show the predicted velocity of particle before and after particle collision in the absence of contact and global damping. P is the collision point. ....123

**Figure 3.15** Simulation results for the particle rotation: a) evolution of particle orientation before and after particle collision; b) cumulative particle rotation before particle collision. The slope of this line shows the simulated rotational velocity of the model particle. ....124

**Figure 3.16** Simulation set up for measuring particle pseudo friction; (a)  $q=1$ , (b)  $q=2$  and (c)  $q=4$ .....126

**Figure 3.17** Calculation of pseudo friction in DE multi-sphere model particles with different sphere densities from the plot of  $t^2$  against  $X_t-X_0$ .....128

**Figure 3.18** The deviation of contact force from normal direction for the cylindrical model: (a) contact geometry for a model particle of sphere density of 1.  $\gamma$  is the angle between the direction of contact force and the direction of

particle sliding and $\alpha$ is the angle of deviation from normal direction. (b) Evolution of contact force during sliding of one sphere over another....	129
<b>Figure 3.19</b> Component of contact force in the direction of particle sliding during sliding of one element sphere over another. ....	131
<b>Figure 3.20</b> Average trend of the horizontal component of contact force during sliding of one element sphere over another. ....	131
<b>Figure 3.21</b> Particle boundary slope determination between two adjacent element spheres.....	133
<b>Figure 3.22</b> Trigonometric relationship between two adjacent element spheres of a particle when the smallest element sphere belonging to another particle is contacting the particle surface. ....	134
<b>Figure 3.23</b> Trigonometric relationship for the deviation of the direction of the contact force between the smallest element sphere and the adjacent element spheres.....	134
<b>Figure 3.24</b> Detail of the trigonometric representation of the displacement of contact point position on element spheres from the “true” particle surface contour. .....	135
<b>Figure 3.25</b> snapshots of particle handling in a 2-D system. Pov Ray has been used to create the pictures. ....	138
<b>Figure 3.26</b> snapshots of particle handling in a 3-D system. Auto cad has been used to create the pictures. ....	139
<b>Figure 3.27</b> Particle interaction between boundary surfaces and a model particle dropping between two conveyors. a) Normal contact force between model particle and conveyor; b) evolution of collision force between model particle and lower moving surface; c) tangential forces (abrasive) between model particle and conveyors during handling.....	140
<b>Figure 3.28</b> snapshots of particles handling in a 3-D system (Pov Ray pictures).....	141
<b>Figure 3.29</b> Five different model particles used in the flow simulations. In each case the radius of the element spheres and their overlap are such that the	

volume of each particle is equal to the volume of a sphere of unit radius. Numbers in bracket show the aspect ratio of the particles.....	142
<b>Figure 3.30</b> Snapshots of numerical flow experiment for model particles of case 3. (a) At the end of gravitational deposition (consolidation) of particles; (b) during particle flow and (c) at the end of flow (Pov Ray pictures). .....	143
<b>Figure 3.31</b> Examples of flow simulation results for model particles of different shapes (aspect ratio) from a flat bottom hopper. ....	144
<b>Figure 3.32</b> Spheroidal particle singulation simulated by DE model using multi-sphere method.....	145
<b>Figure 3.33</b> Simulations of gravity deposition of multi-sphere particles: (a) 2-element spheres, (b) 3-element spheres and (c) 5-element spheres particles respectively. The simulation have been performed for the same particle mass, same time step and same time elapsed (same number of time steps). .....	147
<b>Figure 4.1</b> Section of experimental apparatus showing three images from (a) the start, (b) during, and (c) the end of an experimental run. ....	152
<b>Figure 4.2</b> Arrangement of particles in the model assembly to simulate the experimental assembly shown in Fig. 4.1a prior to movement of the piston. Each particle was numbered as shown.....	154
<b>Figure 4.3</b> Tracks of the centroids of particles in two experiments, using an identical arrangement of particles (i.e. the same particle with the same position in both replicates).....	155
<b>Figure 4.4</b> Tracks of particle centroids from simulations using different coefficients of inter-particle friction. The time step for these simulations was equal to the critical time step.....	156
<b>Figure 4.5</b> Effect of time step on the prediction of the DE model: a) at critical time step, b) 0.10 of critical time step ( $\text{frac}=0.1$ ). For both replicates the coefficient of inter-particle friction was 0.1. ....	158
<b>Figure 4.6</b> Examples of change in particle orientation in the experiments and simulation. Comparisons were made between the simulation results and	

	the minimum and maximum limits of particle orientation for five experimental replications. ....	160
<b>Figure 4.7</b>	Evolution of particle trajectories in experiments and simulation. ....	161
<b>Figure 4.8</b>	Experimental particle assembly for particle flow. (a) The experiment bed consists of 200 elliptical particles, which were machined plastic buttons. The solid fraction of the bed is 0.86. (b) Section through orifice release mechanism. ....	164
<b>Figure 4.9</b>	Comparison the profile boundary of the buttons and an equivalent theoretical ellipse of the same size and aspect ratio. The red line is the profile of a theoretical ellipse with the same aspect ratio as the average for the buttons. ....	167
<b>Figure 4.10</b>	DE model particle with seven element spheres. This particle was created to approximate the boundary of the theoretical ellipse obtained from the real particle boundary. ....	167
<b>Figure 4.11</b>	Model particle assembly after generation using a) friction based assembly generation (solidfraction=0.79) and b) frictionless particle generation (solid fraction=0.84). ....	171
<b>Figure 4.12</b>	Solid fraction of particle assemblies in the experiment and simulation: a) changing during particle flow in the experiment and simulation (frictionless based assembly generation), the dark curves show the experimental results; b) average during steady flow. The brighter curves show the simulation results for friction and frictionless based assembly generation. The average solid fraction for frictionless-based assembly with 5cm orifice has not been shown due to observation of an arch. ....	172
<b>Figure 4.13</b>	Discharged mass of particles from hopper with different orifice size in the experiments and simulations (error bars show the 95% confidence interval). ....	174
<b>Figure 4.14</b>	Calculations of flow rate in experiments and simulations for different orifice dimensions. These data were taken from the linear segments of cumulative curves in Fig.4.13. ....	175

<b>Figure 4.15</b> Comparison between the flow rate in experiments and that of model predictions for different orifice sizes. ....	176
<b>Figure 4.16</b> The occurrence of temporary arching in: (a) simulation and (b) experiment for an orifice width of 5 cm (equivalent to approximately 5 particle mean diameters).....	176
<b>Figure 4.17</b> Plot of $q^{\frac{2}{3}}$ against orifice width (D) and fitted lines to calculate the term $kd$ in the modified Beverloo equation (4.5). ....	178
<b>Figure 4.18</b> Comparison of velocity profile in experiment and simulation at 9 cm above orifice for: a) 10 cm orifice size; b) 7.5 cm orifice size. The negative values indicate that the velocities are in the opposite direction of the Z-axis. In both cases the curves show the fit of kinematic model with the corresponding B from experiment and simulation.....	182
<b>Figure 4.19</b> Hopper stagnant / flowing regions: a) Photograph of experiment with 10 cm orifice with low shutter speed at 0.08 sec after flow; b) simulation result at the same time, green (high velocity particles), blue (particles with medium velocity), red (particles with very low velocity or stationary)..	184
<b>Figure 4.20</b> Comparison between the results of simulations and experiments for the formation of free surface during flow in term of height and shape: a) orifice size 7.5 cm and b) 10cm. The (s) means simulation. ....	185
<b>Figure 5.1</b> Simulation set up and hopper configuration; $H_G$ is the height of the upper section which could be changed to accommodate assemblies of different particle shape during particle generation. ....	188
<b>Figure 5.2</b> Bed height and structure at the end of consolidation for particles of aspect ratio: (a) 1, (b) 2, (c) 3 and (d) 4. ....	191
<b>Figure 5.3</b> Distribution of solid fraction in the hopper for the consolidated assemblies of aspect ratio (a) one, (b) two, (c) three and (d) four. ....	193
<b>Figure 5.4</b> Frequency distribution of solid fraction in different particle assemblies.	194
<b>Figure 5.5</b> Relationship between the average solid fraction of the particle bed and aspect ratio of particles at the end of consolidation. ....	196

<b>Figure 5.6</b>	Types of line contact between two multi-sphere particles comprising mono-sized, non-overlapping spheres which have been considered as a single contact for calculation of co-ordination number: (a) particles of aspect ratio two, (b) particles of aspect ratio three and (d) particles of aspect ratio four.....	197
<b>Figure 5.7</b>	(a) Change in co-ordination number ( $C_n$ ) during consolidation of beds of different aspect ratio, and (b) co-ordination number for the consolidated particle assemblies. ....	197
<b>Figure 5.8</b>	Total force acting on the bottom of the hopper for particle assemblies of different aspect ratio in frictionless contact condition. The dashed line shows the actual weight of assemblies.....	199
<b>Figure 5.9</b>	Evolution of solid fraction during flow of spherical particles (top row) and elongated particles with aspect ratio three (bottom).....	202
<b>Figure 5.10</b>	The initial approximate position of the nine selected particles in the consolidated particle assembly. H is initial bed height and D is orifice size. ....	203
<b>Figure 5.11</b>	(a) Comparison of the trajectories of nine selected particles in the hopper for different particle aspect ratio, (b) comparison of trajectories of particles in the right side of the hopper for three particle beds of different aspect ratios.....	204
<b>Figure 5.12</b>	Comparison of the evolution of particle orientation during flow for particle bed of spherical particles (Top) and particle bed of aspect ratio three (Bottom) at left, centre and right side of the hopper. In each graph the black line correspond to the highest particle, the green line to the particle at the middle and the red line to the lower particle.....	206
<b>Figure 5.13</b>	Comparison of the lateral velocities of particles discharge of the bed of particles of aspect ratio three and of the bed of spherical particles at left side, middle and right side of the hopper.....	207
<b>Figure 5.14</b>	Effect of particle shape on the energy ratio of the particulate assemblies during flow. The top row shows the average energy ratio in the left, centre and right side of the hopper for three particulate assemblies and the bottom	

shows the average energy ratio in the whole of the hopper for these assemblies. ....	210
<b>Figure 5.15</b> (a) Change in particle discharged from hopper against time for beds comprising particles of different aspect ratio; (b) zoom up of the curves in section (a) for the beginning of flow.....	211
<b>Figure 5.16</b> Example of the occurrence of temporary arching during flow for elongated particles (AR=4).....	212
<b>Figure 5.17</b> Snapshot of positions at time $t = 1.4$ s for the assemblies of different aspect ratio. ....	214
<b>Figure 5.18</b> The interface of shear band for the assemblies of particles with different aspect ratio. The particles have been coloured according to the velocity of a particle with maximum velocity i.e. green for particles of velocity more than 70 %, Blue for particles of velocity between 30 – 70 % and the red for particles of velocity less than 30 % of the maximum velocity.....	216
<b>Figure 5.19</b> Normal contact force between particles and a sidewall from the beginning of flow in different particle assemblies. The curves show the total normal contact force acting on different parts of the wall. The sidewall has been partitioned into ten vertical sections each equal to 0.1 of the initial height of the bed (H). ....	217
<b>Figure 5.20</b> Wall pressure distribution for beds of spherical particles (AR=1) and elongated particles (AR=2 and 3). ....	218

## LIST OF TABLES

<b>Table 1.1</b> Summary of literature survey of DEM simulations using different model particle shapes. ....	21
<b>Table 3.1</b> Simulation results for vertically positioned particle at three different time steps with damping coefficient of 0.5. ....	107
<b>Table 3.2</b> Simulation results for vertically positioned particle at three different time steps with damping coefficient of 0.21. ....	107
<b>Table 3.3</b> Simulation results for horizontally positioned particle at three different time steps with damping coefficient of 0.5. ....	108
<b>Table 3.4</b> Pseudo friction coefficient for model particles of different sphere density. ....	128
<b>Table 3.5</b> Average run time per time step of simulations for model particles of different number of element spheres. ....	149
<b>Table 3.6</b> Average run time per time step for the simulation of the gravity depositions of particulate assemblies of spherical particles. ....	149
<b>Table 4.1</b> Physical properties of experimental particles.....	153
<b>Table 4.2</b> Results of statistical analysis for quantification of agreement between experiments and simulation.....	162
<b>Table 4.3</b> Physical and mechanical properties of experimental particles (buttons). The particle mass and the coefficient of restitution is the average of 10 replications. Poisson's ratio and Elastic modulus were taken from measurement group web site. ....	165
<b>Table 4.4</b> Estimate for C factor in experiments.....	179
<b>Table 4.5</b> Estimate for C factor in simulations.....	180
<b>Table 4.6</b> Statistical t test between the average of C in experiment and simulation. .	180
<b>Table 4.7</b> Statistical t test between the velocity profiles in experiment and simulation. .	183
<b>Table 5.1</b> Model parameter values. ....	189
<b>Table 5.2</b> Some descriptive statistics of the frequency distribution of solid fraction for different particle assemblies.....	195

## ACKNOWLEDGMENTS

I would like to express my deep appreciation to my supervisor Dr. John Favier for his tireless and timely guidance throughout the course of this research. His comments on all the manuscripts and the encouragement that I received throughout the study have resulted in additional gratitude.

I wish to acknowledge the financial support of the Ministry of Culture and Higher Education of IRAN and the University of Mashhad for providing me the financial support and the opportunity to carry out this work

My warm appreciation goes to my fellow students in the Biological Systems Engineering Group especially Dr. A.O. Raji for their useful discussions and suggestions. Many thanks also go to Mr. Duncan McCullum from the workshop of the Dept. of AES for technical support in certain phases of this work.

To all members of Iranian Society who made me feel at home with their participation on my happiness and sadness. A lot more deserves my thanks but could not be mentioned, I do not forget you.

My greatest thanks are extended to my beloved family, my wife, my son, Mohammad and my daughter, Hedyeh (who joined us during this study). They all highly participated in the research in their own ways, which must not be left unacknowledged. I am also indebted to all other members of my family in particular my mother, brother and sister for their moral support during my stay abroad.

# 1. Introduction and Literature Review

## 1.1 Introduction

### 1.1.1. Background

Handling and storage are standard post-processing operations for agricultural particulate materials such as grains, fruits and vegetables. Depending on the properties of these materials and the types of operation, different kinds of damage may occur to the materials (e.g. bruising of fruits, breakage of grains) or the system parts (e.g. failure of silo walls). Improvements in the design and performance of machinery and structures used in these operations require knowledge of the physical properties and the dynamic behaviour of the particulate materials for a safe and efficient operation. These materials are usually processed and handled in bulk, thus the properties and mechanical behaviour of these materials are required at bulk as well as at individual object scales, since the behaviour of bulk particulate material is usually different from that of a single particle. Traditionally these data have been obtained from experimental studies and by trial and error methods. Experimental investigations of the behaviour of particulate systems can provide useful information, but are constrained by the limitations of measuring methods. Experimental data on the internal dynamics of three-dimensional assemblies of particles are very difficult if not impossible to obtain.

Most engineering designs of particulate handling systems are based on assumptions of material continuity and homogeneity of physical properties. Such assumptions enable analytical solutions to design problems and application of continuum modelling methods such as the finite element method. However these methods usually require simplification of the problem definition or modification of the continuity assumptions to account for the unique dual nature (solid and fluid-like) of particulate systems. Moreover, continuum models have constitutive equations for bulk materials which contain some macroscopic parameters. The lack of information about these parameters may limit the application of the continuum method for the study of particulate materials. Even when numerical modelling is avoided by use of empirical

methods, problems may arise in extrapolation of results from laboratory experiments to full scale.

Discrete numerical methods have been used for over two decades as an alternative for research into particulate behaviour. These methods take into account the discrete nature of particulate material and model the movement of individual particles in a system comprising a large number of particles. Apart from the common issues of model formulation and validation, the major constraint on this approach is number of particles which can be modelled if computing times are to be kept within feasible limits. The Discrete Element (DE) method is a widely used method which solves the equations of motion explicitly for each particle with computing times that scale to the order  $O(N)$ .<sup>1</sup> However, most applications of the DE method are still limited to thousands rather than millions of particles. Scaling constraints with the DE models are being overcome with faster computers and use of parallel computing methods. The inherent parallelism in discrete particle models, i.e. a similar set of calculations has to be carried out for every particle in the model, suggests use of a parallel approach by sharing the particles and their calculations between several processors. Using of parallel programming in implementations of the Discrete Element Method can speed up the simulation and enables modelling of particulate systems comprising a few million particles which is closer to a realistic system.

The DEM originally has been applied in the areas of soil and rock mechanics to study the load behaviour of these materials. However, the discrete characteristic of the DEM has attracted the attention of the researchers dealing with particulate materials in other areas such as powder technology, process engineering and more recently agricultural particulate materials. Although the mechanical properties of biomaterial particulates may differ from that of other engineering materials DEM has the potential capability of modelling the behaviour of agricultural particulate systems.

In DEM a particulate medium is represented by an assembly of discrete model particles. The shape of these particles is arbitrary, but ideally should match the shape of actual particles under consideration. Contact forces, velocities and position of particles

---

<sup>1</sup> In early DE models each particle was tested for contact with every other particle in the assembly which resulted in computation times which scaled  $O(N^2)$ . Current models employ associative techniques which reduce computation times to the order  $O(N)$  (see Vemuri *et al.*, 1998 for more detail).

are determined and updated through a series of calculations for all contacts based on the relative velocities and position of adjacent particles. The dynamics of the particulate system evolves over time in small time steps during which the velocity and acceleration of particles are assumed to be constant. The calculations are carried out by the application of a force-displacement law and Newton's second law of motion. The out-of balance force for each particle is calculated from the contact with adjacent particles and the new accelerations of particles are updated from out-of-balance force and moment, using the law of motion.

The choice of particle shape representation in discrete element modelling of the mechanical behaviour of particulate systems is critical to the accuracy of the simulation of real particle behaviour, the method of contact detection and the method of contact forces calculations. The application of the DE method to particular applications has resulted in various methods of particle shape representation. While the earliest DE models were two-dimensional and employed circular elements with a linear contact models, more recently models have been developed with complex shape representation such as polygon, ellipse, superquadrics and a combination of primitives (mainly circle). A disadvantage associated with the two-dimensional models is the loss of the effect of particle moment in the third dimension. As most two-dimensional particulate systems can not be found in reality, some aspects of particulate assemblage like porosity may not be properly represented. Consequently, two-dimensional DE models have been extended to three-dimensions to overcome this limitation. However, three-dimensional systems require larger number of particles to make the results meaningful and the analysis of the results is more difficult.

The simplest algorithm for contact detection is that for circular and spherical particles, because there is always a unique form of contact between these particles. In spite of this advantage for circular particles, the normal contact forces do not contribute to the moment acting on a particle as these forces always act through their centre. Moreover, particle rotation is constrained only by frictional forces due to contact with adjacent particles. This feature of circular model particles is the major source of overestimation of the rotation of non-spherical particles whose rotation in reality is arrested by interlocking as well as friction. Using elliptical model particles provides a means of representing non-spherical particles. Rolling of elliptical particles, which is a

characteristic of circular model particles, is more limited. Two-dimensional elliptical model particles have been recently extended to three-dimensions but they involve a significant computational overhead. Polygonal model particles are suitable for modelling of particulate materials of high angularity such as rock and ice, however due to different types of contacts (e.g. face-face and face corner) for these particles, some ambiguities may arise when a set of these contacts has to be changed due to further motion of particles, resulted in a high computational demand.

Although spherical (circular) model particles are the simplest models, these model particles do not match the actual shape of agricultural particulates which are usually non-spherical but with smooth surfaces (low angularity) and a good degree of symmetry. Polygonal model particles, on the other hand, are not also suitable for representing the shape of agricultural material since for particles of smooth surface the number of polygons required to present the actual shape of particles will increase. A computationally efficient method of modelling non-spherical particles is needed in order to simulate the agricultural particulate handling systems. While the number of grains involved in handling and storage systems is typically in the millions, the numbers of fruits and vegetables will usually number between hundreds and thousands. If a suitable method can be found to model these types of particles then simulation of full-scale systems should be possible.

### **1.1.2. Objectives**

The general objective of this research was to develop a procedure for shape representation of non-spherical DE model particles with smooth surfaces. The specific objectives were:

- Review the existing methods of shape representation and contact detection in DEM and highlight the advantages and disadvantages of their applications.
- Develop a new method for model particle representation which will overcome the disadvantages of the existing methods for modelling agricultural particulate materials.

- Select and modify an existing DEM code according to the proposed model particle representation scheme.
- Validate the modified DEM program analytically and experimentally.
- Finally, numerically investigate the effect of particle aspect ratio on flow from a hopper.

### 1.1.3. Organisation of Thesis

This thesis describes the development of a new technique for modelling the dynamic behaviour of non-spherical particles with high aspect ratio. The technique is called the multi-sphere method (MSM) and is based on well established principles for modelling the dynamic behaviour of rigid spheres using the Discrete Element Method (DEM).

Chapter One outlines the role of numerical modelling of the mechanical behaviour of particulate materials and the background on which this research is based. The principles underlying the continuum and discrete element (DE) approaches are presented and their application to particle mechanics are reviewed. The limitations of the continuum approach for studying the mechanical behaviour of particulate materials are highlighted. The development of the DEM and some of its applications are discussed including theoretical and computational advantages and limitations. The importance of particle shape in modelling the behaviour of particulate systems is assessed.

The methodology of the multi-sphere method (MSM) is derived in Chapter Two. A method of generating irregular composite particles consisting of several overlapping spheres and the theoretical basis for using them in a DE model is presented. The proposed calculation cycle takes into account the rotation of particles and incorporates contact damping as well as global damping as an alternative energy dissipation mechanism. A brief review of the structure of the parent DEM program (CONBAL) in which the MSM was incorporated and details of the implementation of the multi-sphere approach is then presented.

Chapter Three deals with the analytical validation of the multi-sphere approach as well as parametric studies on the performance of the model. Analytical validation entailed comparison of computational with analytical calculation of weight, sliding and rotation of a multi-sphere particle in different scenarios. The effect of parameters such as time step and contact damping on the prediction of the DE model was also investigated.

The experimental validation of the DE model at both micro- and macro-scales is presented in Chapter Four. In the micro-scale validation, comparisons were made between the results of a physical model and a simulation with respect to particle rotation and translation by tracking the movement of each particle. The experiments were conducted on 1:1 scale between the physical model and simulation in a controlled flow system with a small number of particles. The model was also validated at a macro-scale by comparing the results of the numerical model for the flow of a bed of ellipsoid particles with a 1:1 scale physical model. The comparison was made in terms of flow rate, velocity profile, solid fraction and the free surface profile during flow. The Beverloo equation for flow of particles was verified experimentally and numerically. The effects of time step and damping coefficient on the simulation results are also presented in this Chapter.

In Chapter Five the DE model using the multi-sphere method was employed to simulate the flow of particles from a hopper. In these simulations the effect of particle shape on the structure of the particulate assembly was investigated by creating model particles of different aspect ratio. The relation between the mass flow rate, orifice size and particle shape was analysed. Finally, conclusions based on the results obtained in this study and recommendations for further research are presented in Chapter Six.

## 1.2. Literature review

### 1.2.1 Approaches to investigation of particulate behaviour

#### 1.2.1.1. Experimental approaches

The experimental studies on particulate systems can provide some useful quantitative information about what actually happens inside these systems. These studies are still common since they use real material and system with reliable results especially for those which are carried out in full scale. Such information is required for the improvement of particulate processing. The handling and processing of particulate agricultural and food processing starts at planting and ends at the hands of consumers. Depending on the type of product, most of these operations can potentially cause damage. Such damage includes bruising in softer materials or breakage in harder materials. Losses due to such damage can be as high as 30% on a global scale (Peleg, 1986).

Information on the physical properties and mechanical behaviour of agricultural materials is needed to reduce damage and for design of processing equipment for safe and efficient operation. In the past agricultural engineering design has often relied on empirical data and experiments (e.g. Morrow and Mohsenin, 1968; Diener *et al.*, 1977). More recently however, the advantages of using analytical (e.g. Pitt and Chen, 1982) and numerical (e.g. Schembri and Harris, 1996) models showed that these methods of investigation can also be considered as alternative approaches for providing the required information to improve the performance of processing machinery.

Although most agricultural materials are handled and processed in bulk, the properties and mechanical behaviour of these materials are required at both the individual object and bulk scales. The bulk mechanical behaviour of the particle assembly depends on the contact forces at the particle scale. Bulk systems of particulate material often consist of particles of varying shape and size, exhibiting different mechanical behaviour (Rothenburg and Bathurst, 1992). The behaviour of bulk particulates is usually considerably different than that of a single particle (Foutz and Thompson,

1993). This difference will be even greater if the bulk consists of particles of varying size and shape.

Extensive experimental studies on the mechanical behaviour of agricultural materials for the purpose of improving machine design can be traced back to 1945 (Sitkei, 1986). Out of these studies has developed gradually the material laws and the characteristic physical properties related to mechanical loading. Experimental investigations have largely focused on bruising of fruits and vegetables (e.g. Holt, *et al.*, 1981), breakage and load response of grain (e.g. Paulsen, 1978) and particulate flow behaviour (e.g. Ooms, and Roberts, 1985; Thompson, *et al.*, 1985; Wilcke, *et al.*, 1992) to improve design and reduce handling problems.

Bruising can occur during transport and handling of fruits and vegetables in processing operations due to collisions between the fruits and with the machinery. Studies on the bruising of fruits have usually entailed experimental measurements of the relationship between contact force and deformation and physical properties of the materials. Initial studies focused on individual objects (Diener *et al.*, 1983) which provided information for some processing operations.

Recognition of the difference between the mechanical behaviour of materials at particle and bulk scale has led to the extension of experimental studies on bruising of fruits and vegetables to bulk systems. The requirement of understanding the factors affecting bruising caused by impacts in handling and transporting systems has led investigators to develop instrumentation for measuring these parameters and relating them to bruising. Efforts have been made to develop an instrumented synthetic fruit (*Instrumented Sphere*) in order to record the impact history of a fruit during handling (Brown *et al.*, 1990; Chen and Yazdani, 1991; Marshal and Burgess, 1991). Such a device can provide information to investigate the relationship between collision force and bruising. It can monitor and record impacts on a typical fruit in terms of peak acceleration and velocity while handled with like-sized fruits such as apples and oranges within a system comprising many objects (Zapp *et al.*, 1990).

Although an IS can provide some information to improve sorting and handling systems for biological products (Hyde, *et al.*, 1992 and Pang *et al.*, 1994), it has some

significant limitations; (i) an IS records an impact as the resultant acceleration on itself, therefore, in the case of several simultaneous contacts the contact force at each contact point can not be separated and analysed; (ii) The magnitude and distribution of mass of an IS may differ from that of the fruits resulting in an error in estimation of collision forces; (iii) use of an IS in a system comprising objects of non-spherical shape, may lead to an extra error in estimation of impacts, as shape is an important factor in the mechanical behaviour of particulate materials (Ting *et al.*, 1995).

Information on the load-deformation characteristics of particulate agricultural materials can enhance handling and storage design problems. A wide range of studies have been reported, such as load response of packed and individual grains (Manbeck and Nelson, 1972), the relationship between moisture content and mechanical properties of grain (Paulsen, 1978) and grain damage during handling operations.

Most agricultural products, especially grains, have to be handled and stored for further processing operations. The majority of these operations involve particle flow. During the last few decades, several problems related to this subject have been studied experimentally. For example, flow from silos (Vibrascrew, 1977; Tuzun and Nedderman 1979; Muhlhaus and Vardoulakis, 1988; Wilcke *et al.*, 1992; Ooi *et al.*, 1998); flow pressure in silos (Ooms and Roberts, 1985; Schmidt and Wu, 1989; and Bucklin *et al.*, 1990;) and measurement of flow rates through orifices (Beverloo *et al.*, 1961; Maysay, 1987; Bucklin *et al.*, 1991). The following can be concluded from the results of these studies.

It is widely accepted that the loads on the walls in grain bins are much higher during discharge than filling. Knowledge of the flow state and the dilatancy of grains during discharge may help in estimation of the stress which is exerted on the hopper walls during grain discharge (Thompson *et al.*, 1985). The friction angle of particulate materials can be affected by factors such as bulk density and particle size and shape. Moysay and Lambert (1987) reported that for some oil seeds, these factors can change the friction angle between 13 and 35 degrees.

Bucklin *et al.* (1990) stated that lack of full understanding of the pressure generated in eccentric discharge from the bin is the reason for the failure of many grain bins. They

suggested that, until the establishment of a theory that can describe the eccentric unloading behaviour of grain bins, this discharge method should not be used. Bucklin *et al.* (1991) investigated grain discharge from a hopper for different grain depths and outlet locations. The flow pattern varied with grain depth and outlet position and could not be predicted adequately by theoretical methods in the literature.

The experiments show that although the current empirical methods can provide some data and observations at a macro scale (e.g. Ooi *et al.*, 1998), they are inadequate for full understanding of the mechanical behaviour of particulate materials during flow. Therefore, an alternative method is required which can provide some data about what is happening inside a particulate assembly (at the particle scale) as well as bulk scale observations.

#### **1.2.1.2. Modelling approaches to particulate material studies**

Generally, most experimental studies on the behaviour of particulate materials are carried out at less than full scale and are restricted to very simple cases to save time and cost. The data and observations from these experimental laboratory models have to be extrapolated to full scale. Extrapolations of the results obtained from experimental laboratory models to full scale industrial systems are most uncertain so that several experiments have been misinterpreted in the past (Ooi *et al.*, 1998).

Having recognised these limitations, a suitable model is required to predict the behaviour of material through the particulate system at full scale. The model predictions can be reliable for the design of particulate systems if the model is able to reproduce the results and observations obtained from the experiments.

The wider availability of computers has led to the increasing use of numerical models in many different disciplines including modelling particulate systems. In comparison to numerical simulations, experimental investigations are not only more expensive, but their observations are limited to the macroscopic behaviour of particulate assemblies (Thornton 1989). Computational models are more flexible in their application than experimental laboratory models and can predict micro-scale dynamic variables at any

time during the test (Ng and Dobry, 1994). They can also provide useful information about the inside of the particulate system which can not be obtained experimentally. Numerical studies on particulate systems behaviour are based on two different principles: (i) continuum mechanics, and (ii) particle or discrete mechanics. In the following section the fundamentals of the continuum approach and the discrete approach are presented.

#### **1.2.1.2.1. Continuum approach**

Generally, problems in mechanics can be addressed by deriving differential equations which describe the behaviour of the system. However, problems can arise with complex systems in solving the resulting equations. To overcome this difficulty, in numerical analysis the mechanical system is divided into a number of small simple geometrical regions (referred to as Finite Elements). Using the derived constitutive equation a separate approximating function is established for each region and then they are linked together to solve the problem for the whole system. As these regions are now a series of simple geometrical shapes, the approximating functions are algebraic relations and not differential equations. Once this is done, a matrix of size equal to the number of unknowns for the element can be created. The whole system can thus be represented as a larger algebraic equation by assembling the matrices of each element in a computer program according to the continuity between the regions.

The Finite Element Method (FEM) and the Boundary Element Method (BEM) are two popular continuum methods which have been used to model particulate material problems. The BEM application has the advantage that it needs only to be discretised at the boundary of the system, instead of within its volume as needed in FEM. Therefore there is a significant reduction of time and cost for the analysis (Carini and Gioda, 1986).

The continuum approach has shown that it can provide useful quantitative information on the macroscopic behaviour of particulate materials. The continuum approach can be successful in the simulation of particulate systems when the size of the particles is

much smaller than the entire system (Cundall and Hart, 1992). These systems of closely packed particles are treated as continua such as granular-solid systems in silos and other grain storage systems and are analysed by FEM (Xu *et al.*, 1996; Ooi *et al.*, 1996; Lu *et al.*, 1997; Ooi and She, 1997). In the continuum method the constitutive modelling of a particulate system is one of the most important steps in the predicting behaviour of the system. A constitutive model describes the responses of the particulate material to deformation or loads. For example, the concept of fluctuation velocity was introduced by Goodman and Cowin (1971) and has been used by many researchers to develop constitutive relationships for granular solids flow (Haff, 1983; Hui and Haff, 1984; Campbell, 1990). Fluctuation velocity creates pressures and governs the internal transport rate of mass, momentum and energy (Lu *et al.*, 1997).

Xu *et al.* (1996) developed a stress-based constitutive model to relate strains to stresses in grain en masse and compared the predictions of the model with previous triaxial test data and also with the results of a strain-based model in terms of deviatoric stresses and volumetric strains. Although the predictions of the proposed model closely followed the experimental data, the average of the prediction of the two models was in closer agreement with the experimental data than with either theory alone.

Hutter and Schelwiter (1983) used a continuum model to study the flow of granular material down a chute. The analysis was performed for a chute with different inclination angles and a layer of the granular material of 0.5 m thickness. The effect of the coefficient of restitution, the ratio of the particle diameter to the thickness of the shear layer, and the inclination angle on velocity profiles and density profiles were investigated. Velocity profiles agreed with the qualitative features observed by previous experimental researches, but density profiles were different from those reported by others.

Stuart and Savage (1983) used a continuum model to study the flow of granular material down rough inclines. They compared their theoretical results with previous experimental observations of the flow of glass beads down an inclined chute with a roughened bed. They observed that theoretical velocities were approximately similar in magnitude to those measured.

In a collaborative study conducted by Rotter *et al.* (1998) to investigate the power of two numerical methods (FEM and DEM) in predicting the behaviour of particulate materials in silos, it was concluded that although the FEM models could provide convincing quantitative predictions of silo pressures with smoother curves for wall pressures than the DEM models, they were unable to model the filling operation of the hopper. Most FEM models do not appropriately cope with the dynamic discharge process. Despite the advantages of continuum models as a promising tool for prediction of silo pressures, the assumption of continuity is not always true for granular solids (Rong *et al.*, 1995).

Although continuum methods enable approximating of the behaviour of discontinuous material, their formulation is usually restricted in one or more of the following ways: (i) the logic may break down when many intersecting interfaces are used; (ii) there may not be an automatic scheme for recognising new contacts and (iii) the formulations may be limited to small displacements and rotations (Cundall and Hart, 1992). Dobry and Ng (1992) noted that using FEM for numerical simulation of granular material requires a major computational effort in rearranging and reformulating the stiffness matrix for the inter-particle contacts whenever a contact is formed or disappears.

The continuum approach also has some difficulties in expressing the characteristic of particulate materials, which has a dual nature, both discrete and continuous. For example, discontinuities have frequently reported during flow of material especially near the outlet and the area changing from parallel to convergent flow where the particles start to rotate (Rong *et al.*, 1995a). The FEM is not satisfactory for analysing these regions of hoppers because large shear deformation occurs in these areas. For this reason Lu *et al.* (1997) proposed a hybrid FEM/DEM to simulate the flow of granular solids (soybeans) from silos where FEM was used to model the particulate system in the regions which were a continuum and the discrete approach was used in the regions near the outlet. Continuum models need constitutive equations for bulk materials, these equations usually contain some macroscopic parameters, which can not be easily measured experimentally, but must be known before any prediction is possible (Ooi *et al.*, 1996). The lack of information about these parameters may limit the application of the continuum approach for the study of particulate materials.

### 1.2.1.2.2. Discrete approach

Increases in computer speed have made possible the calculation of the position of individual particles in particulate assemblies comprising a large number of particles. As a result, the method which takes into account the discrete nature of particulate material and traces the movement of material particle by particle is an alternative approach rather than the continuum method which can be implemented in a computer program numerically. This method is known as Discrete Element Method (DEM). Cundall and Hart (1992) proposed this name but it is also referred to as the *Distinct Element Method* (Sakaguchi *et al.*, 1994; Ning *et al.*, 1997a) and *Discrete particle Method* (Xu and Yu, 1997). Cundall and Hart (1992) suggested that a particle dynamics model can be defined as being of the discrete element type if: (a) finite displacements and rotations of particle are allowed and (b) new contacts are automatically identified during calculations.

The foundation of DEM can be found in the late 1960's when modelling of the mechanical behaviour of jointed rocks was carried out by introducing discontinuities into the existing continuum models (Munjiza *et al.*, 1995). Cundall originally developed this method in the early 1970's to investigate rock mechanics problems (Cundall, 1971) and later the method was extended to particulate materials in general (Cundall and Strack, 1979). The method is explicit in time (see Appendix A) which keeps track of the motion of each particle and updates the contacts with the neighbouring particles in the particulate model. Nowadays, this approach is employed as an effective method for modelling of particulate assemblies (Ng, 1994). Since agricultural materials are mostly particulate assemblies, interest has developed in the application of DEM to the area of agricultural processing (e.g. Rong *et al.*, 1993).

There are three main steps in a DEM simulation:

- (i) Contact detection between pairs of discrete particles.
- (ii) Calculation of contact forces.
- (iii) Update of particle motion due to out of balance contact forces including gravitational force.

The first step depends on the geometry of the particles in simulation and is achieved using a suitable geometrical relationship between two neighbouring particles. The simplest contact detection is between two circular particles (spheres in 3-D) and depends only on the position of their centres and their radii (Cundall and Struck, 1979).

The second step is carried out by applying a force-displacement law to all contact points (Cundall and Struck, 1979; Walton and Braun, 1986; Ng, 1989).

Newton's second law of motion is applied to update the acceleration of the particles. In DEM, acceleration and velocity of particles are assumed to be constant (Cundall and Struck, 1979) during each time step. Consequently, the velocity and new position of particles can be updated at the end of each time step.

### 1.2.2. Development of DEM

The original application of the DEM can be found in research by Cundall and Strack (1979). They used a DE model to study the mechanical behaviour of granular media such as sands. Their model had 197 two-dimensional discs of different sizes to simulate the load behaviour of cohesionless sands. Some important aspects of their development of the DEM can be summarised as:

- (i) Incorporation of particle rotation during simulation.
- (ii) Using a linear force-displacement law with arbitrary normal ( $k_n$ ) and tangential ( $k_t$ ) stiffness.
- (iii) Incorporation of global and contact damping to dissipate energy as well as friction. Their parametric studies show that although damping does not effect the equilibrium value of the contact force, it will reduce the number of cycles which are needed to reach equilibrium. To validate the model they compared the simulation results with photo-elastic test results.

The DEM was later developed further in the representation of the shape of model particles, contact representation and areas of application.

### 1.2.2.1. Shape representation in the DEM

The choice of particle shape representation in discrete element modelling of the dynamic behaviour of particulate assemblies is critical to the accuracy of the simulation of real particle behaviour, the method used for contact detection and the method of computation of contact forces (Hogue, 1998). Although contact detection and computation time are very important, the critical objective in DE modelling is accurate simulation of the behaviour of an assembly of real particles. The influence of particle shape on the predicted behaviour is less well documented than the relationship between shape and the efficiency of contact detection (Favier *et al.*, 1999). Exceptions are DE models using polyhedra which can be designed to closely represent the shape of flat surfaced, angular particles (Hart *et al.*, 1988; Gaboussi and Barbosa, 1990).

Earlier DE models were two-dimensional and employed circular elements (Cundall and Strack, 1979). This DE model has been used frequently by many researchers in different disciplines (Walton, 1983; Thornton, 1989; Ng, 1989; Bathurst and Rothenburg, 1988) and is still the most common element type employed (Ghanem and Elmcstkamy, 1996; Kafui and Thornton, 1997; Kuhn, 1999).

Since the late 1980's three-dimensional DE models using spheres instead of discs, have been reported (e.g. Cundall 1988a; Ng 1989). However, 3-D systems require larger numbers of spheres to make the results meaningful, and the analysis of results is more difficult. In spite of this, DEM with spherical elements has the advantage of simplicity in contact detection and contact force calculation, thus the current trend is toward using 3-D models in various engineering problems (Ghadiri and Ning, 1997; Thornton and Kafui, 1997 and Liu *et al.*, 1999; Kafui and Thornton, 2000).

While spherical elements have the great advantage of computational simplicity, particle rotation is constrained only by frictional forces due to contact with neighbouring particles. This feature has been thought to be one of major sources of deviation in the simulation of non-spherical particles whose rotation is arrested by interlocking (Lin and Ng, 1995). In addition, normal contact forces do not contribute to the moment acting on a spherical element as each normal contact force always acts through the centre of the element. This has the effect of weighting the rotational effect of the

contact force vector towards the tangential component (Ting *et al.*, 1993). These two inherent attributes of circular or spherical particles will contribute to degradation in the accuracy of simulations of the behaviour of particles which deviate to any significant degree from purely spherical (Favier, *et al.*, 1999).

For this reason, another type of DEM model with polygonal shaped elements was developed (Walton, 1983). The polygonal elements are best suited to the engineering problems like rock mechanics and ice fragmentation (Selvadurai and Sepehr, 1999). Similar to spherical models, the polygonal models was also extended to 3-D systems (Cundall, 1988; Hart *et al.*, 1988; Hocking, 1989).

In polygonal models several different types of contact can be found such as face-face, face-corner and corner-corner. However, some difficulties can arise when a set of these types of contacts has to be changed due to further motion of particles. Krishnasamy and Jakiela (1995) reported some of these ambiguities and proposed an algorithm to overcome some of them.

As particle roundness increases (less angularity), the number of polygons needed to present the actual shape of particles, will increase (Ting *et al.*, 1993). On the other hand circular models as mentioned before have an inherent tendency to roll and normal contact forces can not contribute to the moment acting on particles. Because of this, elliptical elements have been used to simulate such materials with non-circular shape and less angularity.

Ting *et al.* (1995) and Ting and Meachum (1995) used elliptical elements as an improvement on circular elements to represent real curved surface particles with an aspect ratio greater than one. Significant improvements were reported in the accuracy of simulations using elliptical particles instead of circular elements to represent sand under quasi-static compression (Ting *et al.*, 1995; Zhu *et al.*, 1996). However due to the complexity of current methods of contact detection for elliptical elements, the computation time is much greater than for circular elements for which a simple test of distance between element centres is required (Lin and Ng, 1995; Oudfel and Rothenburg, 1999).

Using elliptical elements instead of circular elements provides a possibility of simulating particulate materials with different shapes by changing the aspect ratio of the ellipses. Furthermore rolling of particles which is a characteristic of circular elements, and which has been thought to be one of the important factors in the lack of correlation between simulation using circular particles and experimental real non-spherical particles, decreased by using ellipses (Ting *et al.*, 1993). Most elliptical models have been used to model soil mechanics problems such as the behaviour of granular soil under monotonic and cyclic loads (Ng, 1994; Ting *et al.*, 1995; Zhu *et al.*, 1996).

An additional disadvantage associated with elliptical elements, and any other non-circular two-dimensional element, is the loss of the effect of particle rotation in the third dimension. As most of 2-D particulate material models can not be found in reality, some aspects of particulate assemblage like porosity and co-ordination number may not be represented truly by these types of models. Two-dimensional elliptical models were recently extended to three-dimensions to overcome this limitation (Ng and Fang, 1995; Ouadfel and Rothenburg, 1999; Wang, *et al.*, 1999) but they incurred a significant computational overhead and error related to contact detection.

Smooth (non-circular) irregular shaped particles have been represented by using one or more continuous functions to describe the surface of a particle. These may be arbitrary functions or super-quadrics which are the generalised form of an ellipse. Different particle shapes can be created using one or more super-quadrics (Barr, 1981; Williams and Pentland, 1989; Cleary, 1999). Contact resolution and detection between two super-quadrics may be carried out through the intersection of their functions which is computationally expensive and almost impossible (Hogue, 1998).

To enable the use of super-quadric derived shapes, Williams and O'Conner (1995) proposed (for two-dimensional shapes) a Discrete Function Representation (DFR) method. The DFR is also applicable to arbitrary shapes defined by one or more continuous functions. The boundary of the body with arbitrary shape is discretised using a certain density of nodes. The particle thus has both a continuous and discrete representation. Contact detection techniques similar to those employed for polygonal

shapes are then used for detecting contacts between particles. Detection is straightforward for a super-quadric using DFR as the ingress of a contacting node into the inside of the particle is easily determined from the value returned by using the node co-ordinates in a function derived from the super-quadric (termed the inside-out function).

An alternative type of discrete representation is that described by Munjiza *et al.* (1995) who represented arbitrary two-dimensional shapes by a set of boundary nodes with associated information on their mode of connectivity. Contact detection is achieved by first narrowing the search space and then discretising the space with a grid of points and determining which grid points lie inside both contacting bodies. This method allows the generation of intricate geometries but requires a fairly complex contact detection algorithm and is limited to two-dimensional shapes.

Hogue (1998) extended the application of the DFR to three-dimensional particles using a 3-D polar descriptor to generate surface nodes. Contact detection is similar to that used in the 2-D case; a bounding sphere is used to narrow the search range and then the contacting nodes are tested using either the inside-out function or, for other arbitrary shapes, by testing whether a contacting node lies inside a plane defined by the three closest surface nodes. A common feature of both DFR schemes is the dependence of the accuracy of contact detection on the number and distribution of nodes on the surface of the particle. Hogue (1998) noted that the efficiency also depends on the particle shape with efficiency decreasing with increase in aspect ratio.

In addition to basic element shapes, some researchers have used the combination of simple primitives (mostly circular) to represent non-circular particles. The pair element model particle is the simplest case which first proposed by Taylor and Preece (1992). This model particle comprises a pair of circular elements of equal diameter fixed rigidly together with their centres one diameter apart giving a particle aspect ratio two. The element circles can not rotate independently of each other so rotational as well as translational acceleration will be applied to the whole particle. Therefore, this model particle can provide the contribution of the moment of normal contact forces in the rotation of particles which does not occur in the case of circular elements but still can

be used with circle-circle contact detection algorithm which is a straightforward procedure. Taylor and Preece (1992) used this method of shape representation for rock motion simulation due to blasting and Sakaguchi *et al.* (1994) used it for flow simulation of rice. Although pair-element particles were defined in two dimensions the same principles could be applied to paired spheres.

The idea of pair element was extended to a group of non-overlapping circles to create an arbitrary irregular shape model particle (Jensen *et al.*, 1999). In this method which is termed *particle clustering*, a 2-D model particle can also be created as a cluster of a number of joined circles of equal diameter, thus changing the number and arrangement of circles within the cluster could create model particles of different shapes.

The idea of the combination of primitives was presented by Potapov and Campbell (1998) in a different way, but still restricted to 2-D. They proposed a method to represent two-dimensional, non-round particles using circular segments of different radii. The boundary of a model particle is constructed by joining some circular segments in such away that the connections between the segments are continuous. The standard contact detection for two circles was used to calculate the contact between the circular segments of two neighbouring particles.

Ning (1995) joined many spheres together (3-D system) and Higashitani and Iimura (1998) joined some circles (2-D system) by applying adhesion between spheres (circles) to create an agglomerate. Such agglomerates could be considered as irregular shaped particles with a surface contour following the exposed surface of the spheres positioned on the exterior of the agglomerate. In their study they tracked the position of, and contacts between spheres during impact of agglomerate against a planar surface but this model was not really a particle shape method representation because all internal particle contacts were modelled.

A survey was carried out to evaluate the degree of popularity of different particle shapes in the DE models. This survey is basically based on the review of 306 articles in a large number of different research disciplines in which a DE model has been used.

**Table 1.1** Summary of literature survey of DEM simulations using different model particle shapes.

Particle shape	% of popularity
Sphere (circle)	66
Polygon	23
Ellipsoid (ellipse)	6.5
Super-quadric	2
Combined primitives	2.5

The summary of this literature survey is shown in Table 1.1. As it is shown, the vast majority of DEM researches used spherical (circular) particles within a wide range of subject areas. The second largest percentage of the researches use polygonal shapes but most of these researches only concentrated on rock mechanics problems. Due to the complexity of superquadrics and their inefficient contact detection only a few researches have been done with this particle shape generator. This survey also showed that the method of combination of primitives is recently becoming more popular.

#### 1.2.2.2. Parallel programming in DEM

Although the complex shape representation methods (e.g. ellipse and superquadric) can provide more realistic results, DEM models with these model particles suffers from the limitation that the running time is high for simulating a system comprising a large number of particles. This disadvantage is due to its huge computational requirement. At present, usually, the maximum number of particles that can be handled in a DEM model is around tens of thousands. One possible solution to ease this problem is “*parallel programming*”.(Zacharia and Simunovic, 1995; Washington and Meegoda, 1996). Because of the inherent parallelism in discrete particle models, i.e. a similar set

of calculations has to be performed for every particle in the model, a parallel approach can be used to share the particles and their calculations between several processors. Dividing the physical space in the DE model into small cells, parallelization can be achieved by allocating all cells within a certain physical domain to a given processor. In this regard the homogeneity of particle density in the numerical particulate system can affect the parallel model performance. Fluctuations in the particle density lead to uneven distribution of computing load on processors with static allocation of the domain. Therefore in general, dynamic allocation of the domain can be applied to overcome this problem (Dury *et al.*, 1998).

Another critical issue in creating an effective interactive simulation for large scale engineering problems with DE models is the visualisation of results. At present, the interactive rendering of particles for systems in the range of a million would be beyond the graphical capabilities of most existing workstations. Parallelisation techniques have also been utilised to divide the visualisation of DE model as well as its numerical simulation between several processors, allowing a proper distribution of the total load (Carrillo *et al.*, 1999).

DEM with parallel programming showed that it can speed up the simulation about nine times than conventional (scalar) programming (Bjedov and Perry, 1996). Recent researches (Horner *et al.*, 1998 and Carrillo *et al.*, 1999) also indicated that realistic DEM simulations with parallel programming comprising a few million particles are feasible employing large parallel computers. For instance, Dowding *et al.* (1999) employed a parallel 3-dimensional DEM code to simulate the dynamic response of jointed rock masses with up to 2,000,000 blocks.

As discussed, one promising technique in representing non-spherical model particles in DEM is the combination of simple primitives. Generally, by increasing the number of elements per model particle the performance of the model is decreased (Potapov and Campbell, 1998). Parallelisation can be used to share the calculations of the elements of the model particles between several processors to enhance the performance of the model.

### 1.2.2.3. Application of the DEM

The Discrete Element method is a discontinuous approach which considers the discrete nature of the particulate material. It is therefore generally agreed that, this approach is the most appropriate in modelling discontinuous mechanical systems (Ng and Dobry, 1994; Munjiza *et al.*, 1995; Thornton and Antony, 2000 ). Examples of such systems include geomechanics problems (soil and rock), granular flow, powder technology problems, ice fracture and particulate processing operations (e.g. Ball mills). In addition, materials which are usually treated as continuous at a macroscopic level but are composed of individual grains at a microscopic level (Asphalt, and Biomaterials tissue); can also be modelled successfully using DEM.

The first application of DEM was to rock mechanics problems (Cundall, 1971). The common approach in this field is use of polygonal particles in 2-D. However, the exception is the research of Taylor and Preece (1992) which used circular particles and pair element to model the motion of rocks caused by blasting. Problems such as stress distribution and failure in tunnels due to external loading (Cundall and Hart, 1992) and rock cutting (Huang *et al.*, 1999) are other examples of the application of DEM in rock mechanics. Due to a similarity between ice and rock, the same approach (using polygonal particles) has been used by Hocking (1989) and Selvadurai and Sepehr (1999) to simulate the fragmentation of floating sea ice caused by offshore platform contact.

The second successful application of DEM is in soil mechanics and geotechnics problems. Most of these researches have been performed to simulate the loading behaviour (monotonic and cyclic) of soils. Although earlier research on this area was carried out, using circular particles (Ng, 1989), later research has replaced this type of model particle with elliptical particles, to study the effect of particle shape on simulation results (Ting *et al.*, 1993). Apart from 2-D models, 3-D models using both circular and elliptical particles have been employed in the area of soil mechanics. For instance Ng (1996) used arrays of spheres with several different sizes for the simulation of loading behaviour of granular soil; while Ng and Fong (1995) used array of ellipsoids with different aspect ratios for the same purpose.

Among DEM applications, a large number of these researches have been done in the field of material flow simulation to study different aspects of particulate flow. Examples include; flow of granular material from bins (Thornton, 1989; Rong *et al.*, 1995); fluidisation (Tsuji *et al.*, 1993), flow of particles down an incline (Drake and Walton, 1995 and Zhang and Vu-Quoc, 2000). These studies have been performed in 2-D (e.g. Kuhn, 1999, Cheng *et al.* 2000) or 3-Dimensionally (e.g Liu *et al.*, 1999) with mono or polydisperse particles (e.g. Kafui and Thornton, 1997). In most of these investigations circular particles were used in simulation. However, Walton (1983) used both circular and polygonal particles in his simulation models.

Process engineering is another area to which DEM has been applied. Circular (spherical) models have been employed for simulation of operations in the pharmaceutical and allied industries where particulate materials are in the form of powder and pallet. For instance impact breakage of chemical agglomerates (Ning *et al.*, 1997a and b; Thornton *et al.*, 1999 Kafui and Thornton, 2000) and attrition of particulate solids (Ghadiri and Ning, 1997). Other applications of DEM include, ball mill operations simulation (Mishra and Rajamani, 1993; Watanabe *et al.*, 1995; Yokohama, 1996; Cleary, 1998; Watanabe, 1999) and asphalt and concrete behaviour studies (Meegoda and Chang, 1993; Ng, 1993).

#### **1.2.2.3.1. DEM studies on particulate biomaterials**

DEM has the potential capability of modelling the mechanical behaviour of agricultural particulate systems due to similarity between these systems and other engineering particulate systems such as soil, rock and agglomerate. However, the mechanical properties of biomaterial particulates may differ from that of engineering materials since these materials have generally rough surfaces and low moduli of elasticity. Although the mechanical and rheological properties of biomaterials are different from most of engineering materials, use of visco-elastic contact models incorporating viscous damping such as those of Tsuji *et al.* (1992 and 1993) have facilitated the application of DEM to agricultural particulates.

The earliest research in the field of agricultural processing operations employed a simple DE model using a limited number of circular model particles with a linear contact model to study the dynamic behaviour of jumble packed apples on a truck base which was subjected to load from road ramp and bumps during truck motion (Rong *et al.*, 1993). They used two different truck motion models to prepare the load data for the DEM model. Two different packing arrangements of apples (non-random filling) both having a vertical column of five apples with 11 and 12 apple in total were performed in DEM models and the simulation results compared. By incorporating the damping force in normal and tangential directions the apples were considered as viscoelastic materials. The damping coefficients were calculated from the coefficient of restitution of apples. Considering the calculated velocities and contact forces on apples from the DE model, they recommended 11-element type packaging for fruit transporting purposes. However, using circular elements for their DEM model limits the application of these results to spherical shape fruits.

Primitive shapes such as circles have the advantage of computational simplicity. However the difficulty arises when using this simple geometric shape for modelling real agricultural particulate materials whose shape is not usually circular so that the predicted behaviour may differ from that of real materials. DEM models with larger number (several hundreds) of non-circular (elliptical and pair element) model particles as well as circular model particles were introduced to the field of biomaterials by Sakaguchi *et al.* (1994) to examine the influence of model particle shape on the prediction of DEM for flow of elongated particles (rice). In this study the flow simulation results were compared with experimental measurements of the actual flow of white rice and glass beads. A linear contact law with constant stiffness coefficients in normal and tangential directions in conjunction with an arbitrary damping coefficient was used to calculate the contact forces between particles. They observed different simulation results with different selected particle shape. The effects of these shapes on simulation results are presented in the next section.

Flow simulations have also been carried out for the flow of particulate materials using a 2-D circular model particle with mechanical properties within the range of agricultural particulate (Rong *et al.*, 1995a and b). The model was validated by

comparing with the experimental flow of hollow cylindrical particles 25 mm in diameter. The comparisons between the results of simulation and experiment in terms of particle positions during flow showed a general agreement between them. They used this model to study the flow pattern and formation of shear bands during the particle discharge from hoppers.

More recently polygonal model particles with a new contact model incorporating both compressive and tensile forces between the model particles has been introduced to the field of agricultural materials to simulate the impact on the biomaterial tissue (Schembri and Harris, 1996). In this study the impact of shredder hammer on sugar cane stalk was modelled using two-dimensional polygonal elements to represent the cells in the stem section. The model was composed of two different types of elements, hexagonal elements representing storage cells and 18-sided elements representing fibrovascular cells. The cells were connected via an elastic bond; these bonds could break if the tensile or compressive forces exceeded a maximum predetermined value. The contact model comprises a dashpot as well as spring for each contact point to take into account the rheological behaviour of the plant tissue. Comparing simulation results with experiments, they showed that the model provided a good approximation of the failure pattern of sugar cane stalks due to impact forces.

The amalgamation of deformation kinematics with the discrete element structure has also led naturally to a combined finite and discrete element approach. This solution is mainly suited to problems in which progressive breakage is taking place (Munjiza *et al.*, 1995). Alternatively, DEM was linked to FEM by Lu *et al.* (1997) to study the flow of soybean from silos by proposing a hybrid model based on the FEM and DEM to calculate the stress and velocity field. The DEM was utilised when the bulk solids no longer behaved as a continuum (e.g. lower part of the silo near the outlet and the junction between the vertical bin walls and inclined hopper walls) where there are large shear deformations. A good agreement has been found between the experimental results and the predictions of this model (Negi *et al.*, 1997) for wall pressures. The statistical analyses showed that the predicted wall pressure was within the 95% confidence interval calculated from the observed data.

Most researches on DEM are based on the assumption that the deformation of the geometrically shaped particles is a virtual deformation. In other words, model particles are allowed to overlap rather than deform due to contact force so that changes to particle shape is not possible. This assumption may not be extended to soft materials under comparison such as fruits and vegetables. Raji (1999) developed a new approach in DEM, which incorporates a non-linear deformation dependent contact damping relationship and a shape change while particles (agricultural produces) are subjected to external loads. In this method instead of particle overlap (virtually) the deformation between contacting bodies is calculated. Consequently the deformed shape of particles could be determined.

The effect of particle shape on the prediction of DE model was considered by Zhang and Vu-Quoc (2000) to model the flow of soybeans down an inclined chute using DEM with non-spherical particles. In this study the model particles were represented as a cluster of four spheres to create non-spherical particles close to the general shape of soybean. The simulation results such as velocity profile and average velocity of granular flow were compared with experiment. A better agreement obtained between simulation and experiment when, instead of a linear model, they used an improved tangential force-displacement model in which, tangential contact stiffness was dependent on the history of tangential force. The method for calculating the change in position and orientation of the model particles was not presented.

These researches have demonstrated the possibility of the application of DEM in biomaterials studies. Because of the wide range of problems in this field, it seems that DEM has a great potential in this area.

#### **1.2.2.4. Role of particle shape on the different behaviours of particulate materials**

Shape and size of particles are two inseparable parameters, which are needed for satisfactory description of particles in the field of particulate mechanics. These two parameters can become more important for some areas. For example in powder technology most particles are within the size of a millimetre, while in agricultural

products the shape and size of particles ranges from seeds which may be less than a millimetre in diameter to fruits whose dimensions can exceed tens of centimetres. Agricultural products have many shapes from round (approaching spheroid) to quite irregular in some seeds and fruits with high aspect ratio.

Several attempts have been made to describe and compare the shape of those particles deviating from a sphere. Beverloo *et al.* (1961) expressed the shape of some non-spherical seeds as a shape factor to study the influences of particle shape on the flow of different granular materials. Assuming that the particles were spherical, their *spherical diameter*,  $d_s$  was calculated from the specific surface and the void fraction. They defined the shape factor  $\lambda$  as the ratio of the of the average screen size of the particles to their spherical diameter.

Particle shape can also be described using measures such as *charted standards*, *roundness* and *sphericity* (Mohsenin, 1970). In the standard chart, the shape of a particle is defined either by a number or by descriptive terms on the charts. Roundness is used to measure the sharpness of the corner of the solid as  $A_p/A_c$ , where  $A_p$  is the largest projection area of the particle in a natural rest position and  $A_c$  is the area of smallest circumscribing circle. A practical 3-D expression can be stated for estimating the sphericity of a particle as the ratio of the diameter of a sphere of the same volume as the particle to the diameter of the smallest circumscribing sphere ( $d_e/d_c$ ). The effect of particle shape on the mechanical behaviour of particulate materials has been investigated experimentally and numerically which are reviewed in the following section.

An experimental study on the mechanical behaviour of particulate materials (loading response of packed grain and individual kernel, Foutz *et al.*, 1993) revealed that this behaviour might be different in particle and bulk scale. The difference between the mechanical behaviour of particulate materials in particle and bulk scale was related to void space, grain shape and size and the orientation of kernel. It should be noted that void ratio and orientation in turn may be affected by particle shape.

Apart from the shape of particles the particle size itself also can affect the physical properties and mechanical behaviour of particulate materials in both particle scale and

bulk. In a study on the fracture resistance of soybeans to compressive loading, Paulsen (1978) found that the average toughness was greater for smaller than the larger seeds which show the smaller soybeans had greater resistance to seed coat cracking. At a bulk scale, Moysay and Lambert (1987) observed that a combination of seed size and shape can change the friction angle of grains and oilseeds by up to 20 degrees.

One of the earliest experimental studies related to the effect of particle shape on the flow characteristics of particulate materials has been carried out by Beverloo *et al.* (1961). In this research the flow of granular solids of different shapes including some seeds through orifices was investigated. Their empirical equation for prediction of flow rate, derived from experiment, was correlated with particle size. Further study suggested that the correlation factors in the Beverloo equation might be related to the shape of particles (Nedderman 1985).

In experimental studies of particulate flow, Behringer and Baxter (1994) also observed that particle shape can play an important role in granular flow. Immediately after the opening of a hopper filled with long grain grass seeds, they observed an unusual forked shape pulse due to initial orientation of the seeds in the lowest part of the hopper; a phenomenon which seems to be unique to long grained materials.

In addition to experiment, numerical studies on particulate materials have shown that the particle shape and size can strongly affect the mechanical behaviour of particulate material. Generally the DE models with mono-disperse circular (spherical) particles do not properly predict the behaviour of a real granular system. Random arrays of disks or spheres tend to crystallisation in regular patterns. Increasing the number of particles in the model to a true scale (Ng 1989) or polydispersity can make the numerical model closer to a real granular system (Langston *et al.*, 1995). Some numerical studies on the strength of chemical agglomerate also showed that polydispersity can change the strength of the agglomerate when the distribution of particle sizes within agglomerate was changed (Ning *et al.*, 1997a).

Although the mechanical behaviour of the DE models with poly-disperse circular elements may reproduce general characteristics of granular materials, the magnitude of parameters such as peak friction angle and peak dilation rate are much lower than those

of real materials. This is either due to the shape of the particles or to the planar nature of systems simulated two-dimensionally (Rothenburg and Bathurst, 1992).

Particle inter-locking is a phenomenon which is frequently reported for assemblies of non-spherical particles which can affect flow and bulk properties such as shear strength. In contrast, circular or spherical particles tend to rotate individually and consequently, exhibit a lower shear strength and dilation. Ng and Dobry (1994) noted that when the rotation of spherical particles in the DE model was prohibited, higher shear strength, higher stiffness and stronger dilation were found compared to the case in which particle rotation was allowed. They concluded that, the excessive rotation was due to the use of uniform spherical shape for particles in simulation and also high degree of uniformity of particle sizes. This deviation in simulation results can be due to this fact that granular particles have a higher frictional angle than completely spherical particles.

In a numerical study on the flow of oil shale on an incline in a 2-D system using both circular and polygonal particles, Walton (1983) observed a significant difference between simulation results of circular and polygonal models. While in circular particles the difference between the velocity of particles in the upper layer was significantly higher than in the bottom layer; in polygonal particles only after travelling a few hundreds particle diameters there was very little difference between the velocity of the top and bottom particles. This behaviour was related to interlocking between polygonal particles.

One possible solution to incorporate particle shape on the behaviour of granular system is the use of elliptical particles of different aspect ratio in the numerical model. Comparisons between the prediction of numerical models with circular and elliptical particles showed that shape of particles can affect some mechanical behaviours of particulate material such as flow behaviour (Sakaguchi *et al.*, 1994), load transfer and transmission of stress wave through particulate assembly (Shukla *et al.*, 1993), strength of particulate assembly (Ting *et al.*, 1995) and packing porosity (Hwang *et al.*, 1996). From the literature it is concluded that in general, for less rounded particles more interlocking occurred which reduced the tendency for the particles to rotate resulted in

more dilation and any deviation from spherical particles increased the observed macroscopic strength.

The study on the effect of particle shape on the shear strength of particulate assemblies was also carried out numerically with the use of *clustering method* to create non-spherical particles (Jensen *et al.*, 1999). The numerical results demonstrated that particle rotations were reduced when cluster model particles were used comparing with non-cluster particles (circular shape). Consequently, the shear strength of the cluster particle assembly was higher than the circular particle assembly.

The effect of particle shape and angularity of particles on flow characteristics of particulate material was investigated using continuous functions (Cleary, 1999). In this study the 2-D model particles of different aspect ratios and angularity (blockiness) were generated using super quadric functions. It was reported that although both angularity and particle shape influenced the flow rate, the latter had more effect on flow behaviour of particles. It was observed that the flow rate reduced by 29% when the aspect ratio of particles changed from 1 (circular particles) to 5 (elongated particles).

### **1.2.3. Theory of the DEM**

The DEM is based on the application of particle contact mechanics. In this section the terms used to describe contact are first defined and then the theory of the DEM such as contact models, contact detection and the calculation cycle for particle motion are presented.

#### **1.2.3.1. Definition of terms describing contact between bodies**

Hertz (1882) pioneered the study of contact between two particles and developed a theory for the behaviour of frictionless convex elastic objects. Hertzian objects are homogeneous, perfectly smooth and elastic (i.e. no energy can be dissipated during loading and unloading). Mindlin (1949) extended the solution to contact between

frictionless elastic bodies in the absence of slip for spheres of different size. Further studies have investigated the effect of friction and tangential loading at the contact point (Mindlin and Deresiewicz, 1953) and contact deformation for rough surfaces (Rogers and Reeds, 1984).

In contact mechanics of convex particles a number of parameters can be considered to characterise the contact problems:

*Contact point:* Particles within a particulate assembly can make contact with one or more neighbours at their boundary. At a microscopic scale there is contact over a finite surface area on the contacting bodies. The contact force is therefore distributed over the contact area. In the DEM it is assumed that the radius of the contact area is small in comparison with the particle radius (Cundall and Hart, 1992) hence, it is acceptable to presume that the contact occurs at a point and the contact forces are concentrated at the centre of the contact surface. This point is referred to as the *contact point*. The average number of contact points per particle is called the *coordination number* of the particle assembly.

*Contact Normal:* A *contact normal*  $n$  is the outward normal to the tangential plane at the contact point between contacting particles (Fig. 1.1).

*Contact vector:* For a particle of arbitrary irregular shape, this term is used to identify the contact point with reference to the centroid of the particle (Bathurst, and Rothenburg, 1988). For each contact point a contact vector  $l$  is defined from the centroid of the particle to that contact point. In the simplest case, for spherical particles, the direction of contact vector is coincident with that of the contact normal and its length is always constant and equal to the particle radius (Fig. 1.1b).

*Contact displacement and deformation:* If a contact point exists between two particles, the relative displacement between the particles will result in a change of the degree of deformation at that contact point. In DEM it is assumed that inter-particle penetration (overlap) occurs between two contacting bodies instead of deformation at the contact point. The magnitude of the contact force is proportional to this deformation (overlap).

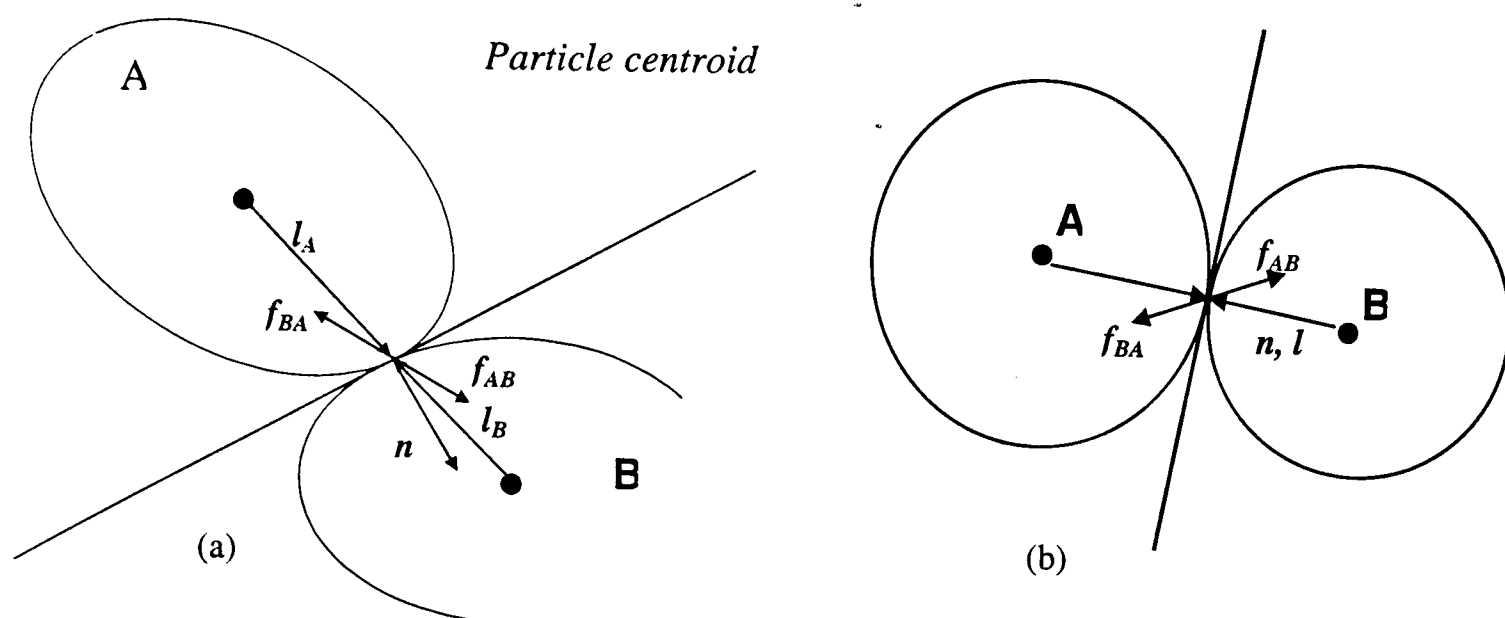


**Figure 1.1** Contact parameters: a) for smooth non-spherical, convex; b) circular particles as defined in the text.

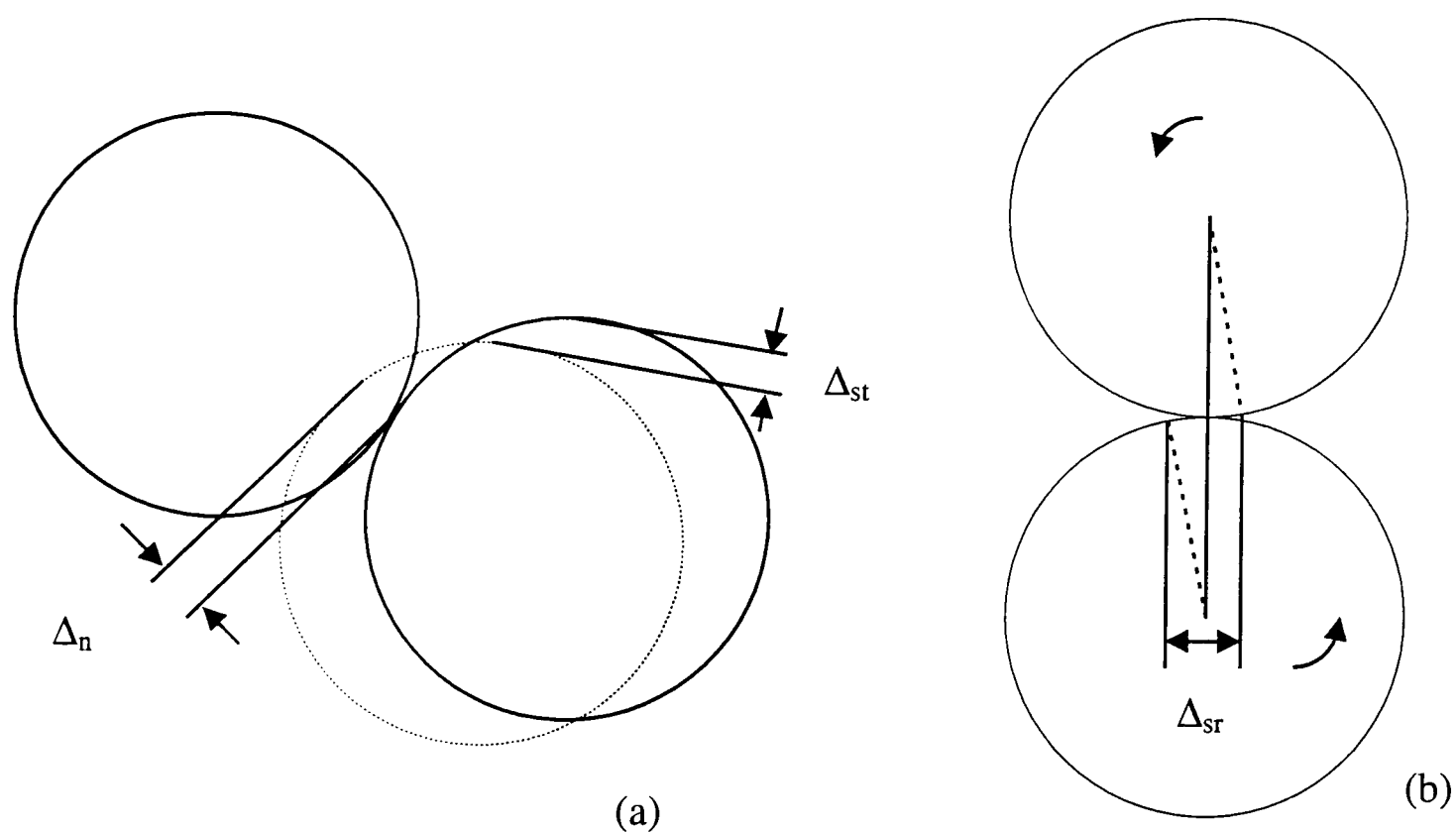


**Figure 1.2** Normal ( $\Delta_n$ ) and tangential ( $\Delta_{st}$  and  $\Delta_{sr}$ ) displacements for two particles in contact due to: (a) relative translation and (b) relative rotation of the particles.

In practice, in order to use the existing mathematical relationships between deformation and contact force to calculate the contact force ( $f_{AB}$  or  $f_{BA}$ ), this deformation is resolved into its components in the normal ( $\Delta_n$  in Fig. 1.2) and tangential ( $\Delta_{st}$  due to particle translation and  $\Delta_{sr}$  due to particle rotation) directions of the tangent plane of contact.

tangential ( $\Delta_{st}$  due to particle translation and  $\Delta_{sr}$  due to particle rotation) directions of the tangent plane of contact.

The maximum tangential component of the contact force is limited by the amount of friction between the particles. If the tangential contact force calculated from relative tangential displacement reaches the maximum frictional force ( $\mu N$ ) then sliding occurs and the magnitude of tangential force remains constant at this level. Thus, for the case of frictionless particles the tangential force does not exist. Figure 1.2 shows the normal and tangential deformation which is created by relative translational and rotational displacement of two particles in contact.

### 1.2.3.2. Principles of the DEM

A particulate medium is represented in the DEM by an assembly of discrete model particles. The shape of these particles is arbitrary but, ideally, should match the shape of actual particles under consideration. Contact forces, velocities and displacements of particles are determined and updated through a series of calculations for all contacts from the relative velocities and position of neighbouring particles.

The dynamic behaviour of the system evolves over time in small time steps during which the velocity and acceleration of particles are assumed to be constant. The size of the time step is constrained not only to satisfy this assumption but also to ensure computational stability. The latter constraint usually results in a time step which is small enough to make reasonable the assumption of constant velocity and acceleration. In DEM the calculations are carried out by the application of two laws; force-displacement and Newton's second law of motion. These features of DEM are illustrated in figure 1.3. Body forces and moments acting on a particle due to contact with other particles and with the environment<sup>2</sup> are calculated at each time step.

---

<sup>2</sup> "Environment" means the surfaces of the structure containing the particle assembly.

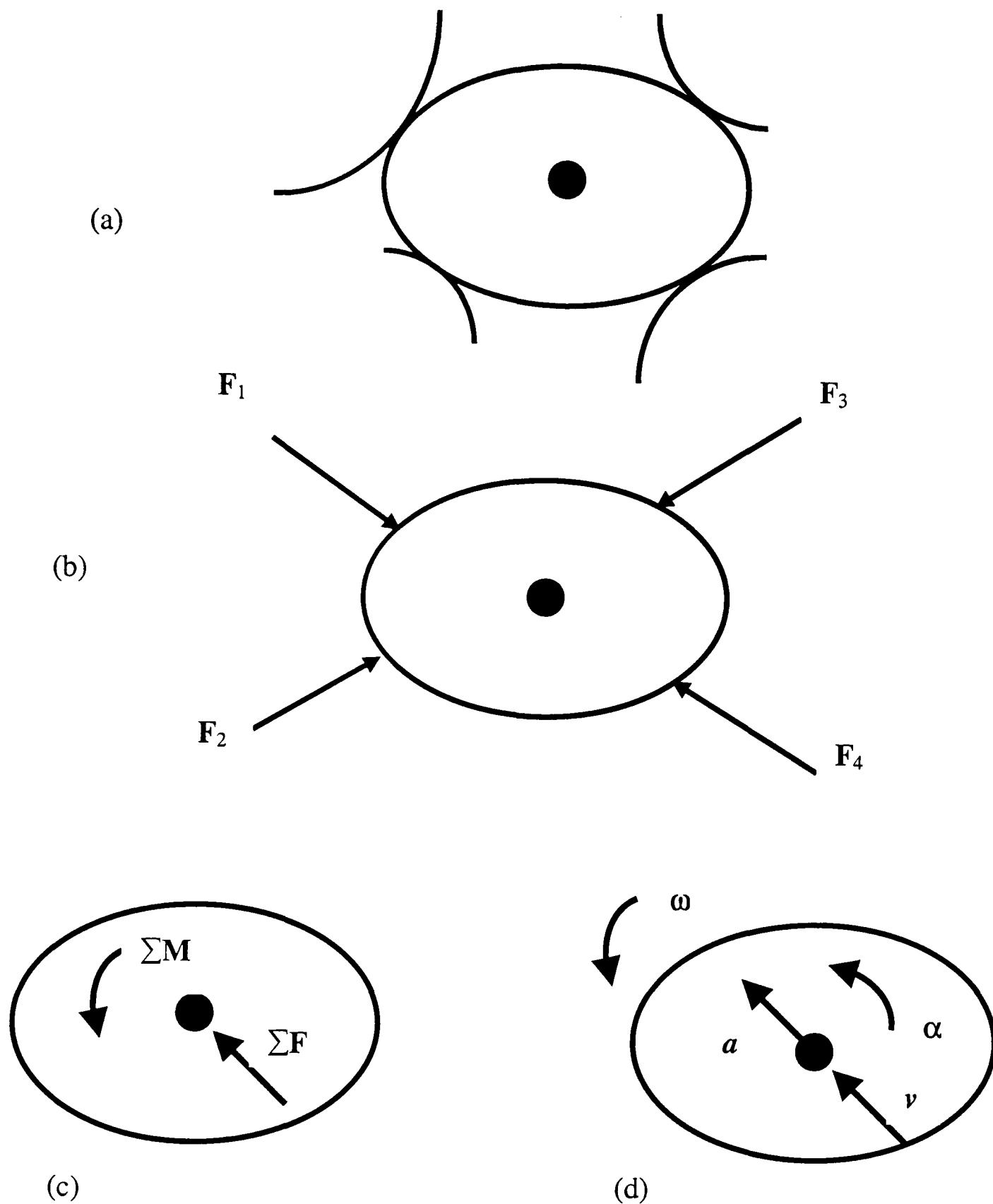


**Figure 1.3** The DEM procedure for contact force calculations and updating the dynamic situation of particles; a) Recognising the formation of contact points due to relative velocities and position of particles. b) Application of force-displacement law for each contact point to calculate the contact force. c) The moment of contact forces about the particle centroid is calculated and the resultant force and moment on particle centroid is determined. d) Application of Newton's second law of motion to calculate the particle acceleration and velocity.

The out-of-balance contact force and moment for each particle is then calculated. The new accelerations of particles within the system are determined from their out-of-balance force and moment, using Newton's second law of motion for a rigid body. The translational acceleration is calculated from the out-of-balance force and the angular acceleration (spin) is calculated from the moment. The translational and rotational velocity of each particle is determined by integration of its respective accelerations over the time step. Particle velocities are then integrated over the time step to give the particle displacement. The positions of particles are then updated at the end of each time step. From the relative velocity and position of two contacting particles the deformation (overlap) at contact point is calculated. A suitable force-displacement law is then applied at each contact point to determine the net force on the particle. The corresponding moment acting on each particle is determined from the position of particle's centroid and the magnitude and direction of the contact force. The calculation cycle is then repeated using the calculated contact force and moment in the law of motion to determine the new state for particles.

### 1.2.3.3. Contact representation

There are two approaches in the DEM for representation of contact and consequently calculation of contact force. The first approach assumes that particles can deform at the contact point as a result of friction and stress; this is known as the *soft contact* approach. The normal stiffness is taken to represent the relationship between the deformation and the magnitude of contact force. An example of this approach is the Hertz theory which is used to calculate the normal stiffness for two deformable elastic spheres in contact. Alternatively an arbitrary normal stiffness can be used to represent the contact model for two contacting particles. In the soft contact model, it is assumed that the amount of penetration is very small compared to the particle dimensions (Cundall and Hart, 1992). However, in a physical particle there is no real penetration between particles; instead the particles deform at the contact area and a flat surface is formed between the particles rather than penetration. This procedure is most suitable for handling of particulate materials such as grain and other biomaterial particles.

The second approach uses a *hard (rigid) contact* model which assumes that instead of deformation between contacting bodies an instantaneous inter-particle collision occurs (Walton, 1983). The velocity and position of particles after collision are determined according to their initial condition and the rules governing two-body collision such as instantaneous momentum exchange. Energy may or may not be conserved by the system. The hard contact assumption is appropriate in simulation of gas and molecular dynamics (Cundall and Hart, 1992).

The choice of contact representation depends on physical properties of material. For instance when particles are frictionless and the contacting forces are very small the rigid contact assumption is better, while in the presence of friction and larger contact forces, taking into account the contact stiffness is essential and therefore the soft contact model is more appropriate.

In soft-contact models two different assumptions can be made for representation of the solid material that constitutes the particles. The shape of particles may be assumed to be either constant or variable, while in hard contact models it is always assumed that the material of the particles can not deform (no further change in particle shape). The fixed particle shape assumption is acceptable when deformation is concentrated at particle boundary and the stress is low. On the other hand, if the applied stress on the particles is relatively high, the deformation of particles can not be neglected. An example of this condition may occur when soft materials are compressed. If the shape change due to deformation of particles can not be ignored, it must be included in the model. Cundall and Hart (1992) reported an approach which can be used to incorporate the flexibility of particles. In this method the body of particle is divided into several internal elements to increase the number of degrees of freedom for the whole of particle.

Munjiza *et al.* (1995) proposed a combined Finite-Discrete Element method for 2D simulation of some large-scale problems involving deformable bodies. Each discrete element was assumed to be a deformable body and were discretised into finite elements. The stress and strain field of each body was calculated each time step so that the contour of each body could therefore change over each time step.

Raji (1999) developed a DEM model for spherical deformable particles with shape change under compression loading. A number of simplifying assumptions were made such as uniform stress distribution, homogeneous material properties and uniform distribution of the deformed volume at contact over the remaining non-contacting surface using the principle of conservation of volume. The model was applied to spherical material under compression. It was observed that with this approach a better approximation of bed voidage (which standard DEM underestimated) was obtained in comparison with physical material. The model was also used for prediction of mechanical oil expression in oilseed beds and similar patterns in the variation of the related parameters were achieved as observed in experiment.

#### **1.2.3.4. Contact models**

In particulate systems energy is dissipated to allow the system to reach a quasi-static equilibrium. During particle collision energy is dissipated through friction between particles and / or deformation of particles. In the case of pure elastic behaviour without any energy dissipation mechanism the system will oscillate and can not reach equilibrium. In viscoelastic materials, the energy is absorbed due to the plastic deformation at the contact point. Since most materials exhibit viscoelastic behaviour, the rheological contact model should consider these energy dissipation effects.

In order to calculate the contact forces the mathematical model should consider the relationship between the contacting particles including contact stiffness coefficients and energy dissipation mechanisms. The use of a suitable contact law is crucial for proper prediction of the DE model. Rotter *et al.* (1998) conducted an international collaborative study to investigate the prediction of various computational models (based on both DEM and FEM) on granular solids flow problems. They found a wide variation in the results of simulations of simple (standardised) hopper filling and discharge problems by both FE and DE models. They noted that the particle packing structure and the wall pressure distributions predicted by DE models was sensitive to the contact algorithm even for circular model particles.

The contact model usually consists of a spring (for elastic properties) and a dashpot (for viscous properties) in parallel in both normal and tangential directions and is known as the Kelvin-Voigt model. Fig. 1.4 shows two different contact models used in the soft contact approach. The difference between them is the way in which the maximum tangential force is calculated. Model (a) limits the maximum frictional force according to both spring and dashpot forces and has been found to give more realistic results when modelling impacts (Rong *et al.*, 1993; Ting *et al.*, 1993).

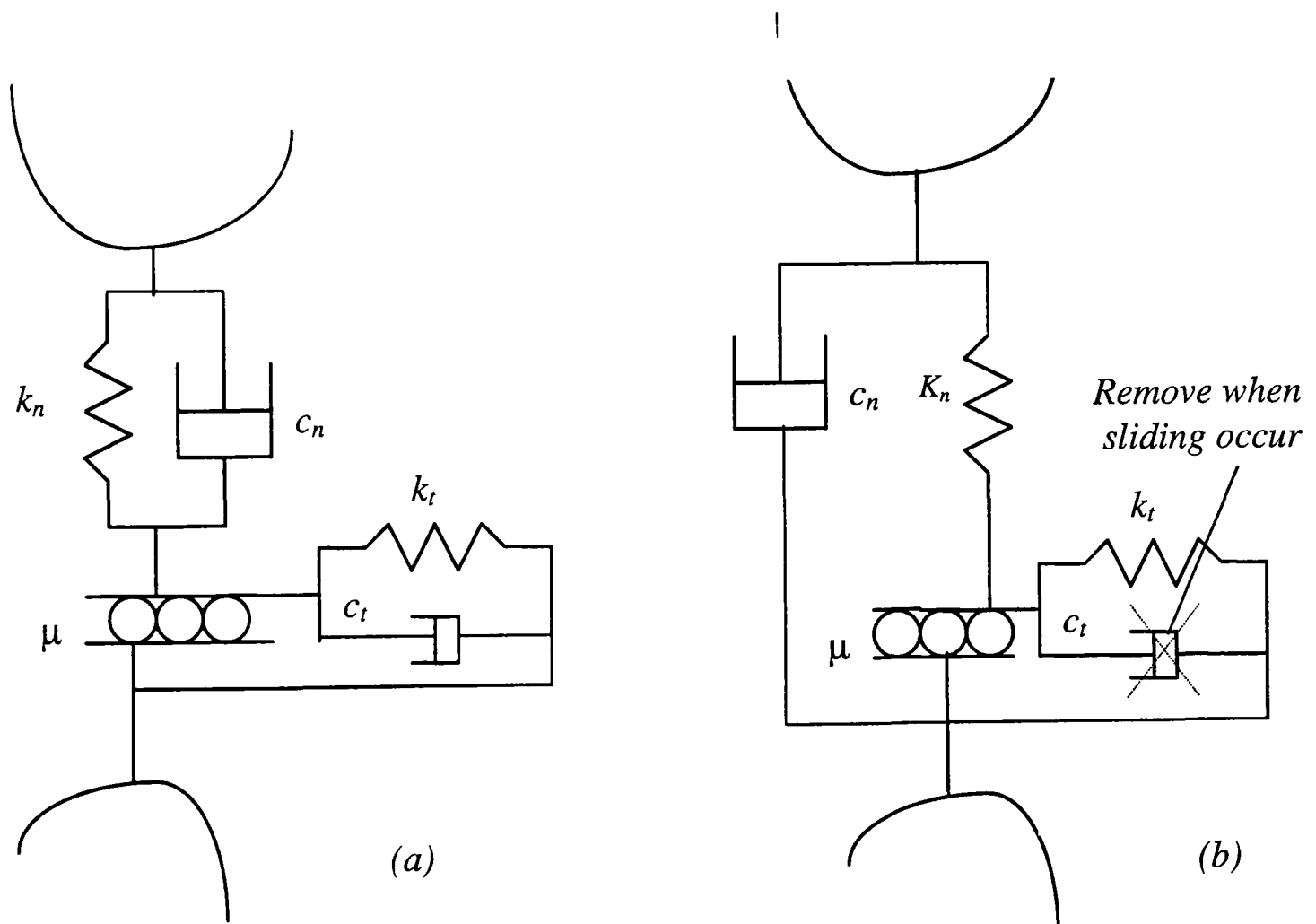


**Figure 1.4** DEM contact models for cohesionless materials: a) the maximum frictional force based on the sum of spring and dashpot; b) the maximum frictional force calculated only from spring (elastic) force (Walton, 1983).

#### 1.2.3.4.1. Normal and tangential stiffness coefficients

In the early DEM models a simple procedure was employed to take into account the stiffness of materials. In this approach, a linear constant coefficient was used to calculate the contact force. The criterion for selection of normal stiffness ( $k_n$ ) is that,

the chosen stiffness should create a deformation small in comparison with the dimension of particles in the range of applied contact forces. The value of tangential stiffness ( $k_t$ ) is selected according to Mindlin's theory for elastic rough materials such that the ratio  $\frac{k_t}{k_n}$  lies between 2/3 and 1 (Cundall and Strack, 1979).

This method is applicable for flow and monotonic loading and is still widely used in DEM simulation. However, using this model for simulation of materials with varying loads (cyclic) may create some deviation in simulation results because the stiffness of materials can be different in loading and unloading (Mindlin and Dercsiewicz, 1953; Dobry and Ng, 1992).

Alternatively, many researchers have recommended a non-linear approach for calculation of contact stiffness. In this method, the normal stiffness can be inferred from the Hertzian contact theory for elastic spheres in contact as

$$F_n = K \delta^{\frac{3}{2}} \quad (1.1)$$

where  $\delta$  is the normal deformation and  $K$  is dependent on the material properties and can be calculated as

$$K = \frac{4}{3} R^{\frac{1}{2}} E \quad (1.2)$$

where  $R$  and  $E$  are defined as

$$\frac{1}{R} = \frac{1}{R_1} + \frac{1}{R_2} \quad (1.3)$$

$$\frac{1}{E} = \frac{1-\nu_1^2}{E_1} + \frac{1-\nu_2^2}{E_2} \quad (1.4)$$

Substituting (1.3) and (1.4) in (1.2),  $K$  becomes

$$K = \frac{4}{3} \left[ \frac{E_1 E_2}{(1-\nu_1^2)E_2 + (1-\nu_2^2)E_1} \right] \left[ \frac{R_1 R_2}{R_1 + R_2} \right]^{\frac{1}{2}} \quad (1.5)$$

If the spheres have the same material properties then (1.5) becomes

$$K = \frac{4}{3} \left[ \frac{E}{(1-\nu^2)} \right] \left[ \frac{R_1 R_2}{R_1 + R_2} \right]^{\frac{1}{2}} \quad (1.6)$$

For the case of contact between a sphere and a rigid planar surface  $R_2$  and  $E_2$  approach infinity and for this case  $K$  is

$$K = \frac{4ER^{\frac{1}{2}}}{3(1-\nu^2)} \quad (1.7)$$

Another approach based on the Hertz theory for the case of identical spheres gives the normal stiffness  $k_n$  in terms of contact area as

$$k_n = \frac{2G_s a}{1-\nu} \quad (1.8)$$

where  $G_s$  and  $a$  are the shear modulus and radius of the contact area respectively. The contact radius can be approximated for two contacting spheres with different radius as

$$a = \sqrt[3]{\frac{3(1-\nu)F_n R_e}{8G_s}} \quad (1.9)$$

where  $R_e$  is the equivalent radius and is defined as

$$R_e = \frac{2R_1 R_2}{R_1 + R_2} \quad (1.10)$$

As it can be seen in this solution  $k_n$  is dependent on the normal force and therefore can change during simulation (Ng, 1989).

Taylor and Preece (1992) used  $K$  in (1.2) with a constant factor to define the normal constant stiffness independent of normal contact force based on the Hertz theory as

$$k_n = fK \quad (1.11)$$

where  $f$  was constant and set to  $10^{-4}$ .

Ting *et al* (1993) reported another equation for normal stiffness based on the Hertz theory as

$$k_n = \frac{2\pi G_s}{(1-\nu) \left[ 2 \ln\left(\frac{2R_e}{A}\right) - 1 \right]} \quad (1.12)$$

where

$$A = \left[ \frac{2R_e(1-\nu)F_n}{\pi G_s} \right]^{\frac{1}{2}} \quad (1.13)$$

It can be seen that the normal stiffness also depends on normal force.

In non-linear methods different solutions were recommended to calculate the tangential stiffness all of which can be inferred from the theory of Mindlin and Deresiewicz (1953). Some researchers such as Walton and Braun (1986) modified Mindlin's solution to reduce its complexity. In this method, which is termed "*linear pressure dependent*" (Dobry and Ng, 1992), tangential stiffness was defined as a function of normal force as

$$k_t = \frac{2 \left[ 3G_s^2 (1-\nu)R_e \right]^{\frac{1}{3}}}{2-\nu} F_n^{\frac{1}{3}} \quad (1.14)$$

The most complicated solution used to calculate the tangential stiffness was reported by Ng (1989). This is based on the complete Mindlin's solution and  $k_t$  not only depends on the normal contact force, but also depends on the history of tangential forces. For example, for the case of constant normal force it can be calculated as

$$k_t = k_{to} \left( 1 - \frac{F_s}{\mu F_n} \right)^{\frac{1}{3}} \quad (1.15)$$

where  $k_{to}$  is obtained from (1.14),  $F_s$  is the tangential force and  $\mu$  is the inter-particle friction coefficient. However, further research of this group (Ng and Dobry, 1994) on this concept indicated that the *pressure dependent* model in which the tangential stiffness is calculated as a function only of normal contact force can provide acceptable results for simulation in most engineering problems.

All of these contact models only calculate compressive contact forces and do not take into account tensile forces between two contacting particles. They can therefore only simulate the behaviour of cohesionless particulate material. However, cohesion should be considered in the case of materials such as concrete, agglomerates and vegetative tissue. Although they consist of discrete grains and units at a microscopic level, they are usually treated as continuous at the macroscopic scale due to the bonding between their particles. As a result the former contact models are not sufficient to simulate the load and impact behaviour of such materials. A bond model is needed to calculate the adhesion forces between joined particles as well as compressive forces between discrete particles. Ning *et al.* (1997a and 1997b) incorporated surface adhesion into a 3-D model to investigate the breakage of an agglomerate due to impact, where van der Waals adhesion forces determined the bond strength between individual particles in the agglomerate. Other examples of this approach are research of Trent and Margolin (1994) on cemented granular material and impact modelling of sugar cane by Schembri and Harris (1996). In the present research it is assumed that the particles are cohesionless and a Hertzian based relationship (Eq. 1.8) is used for normal stiffness ( $K_n$ ) while the linear pressure dependent method (Eq. 1.14) is used for tangential stiffness (see section 2.5 for the implementation of the model).

#### 1.2.3.4.2. Damping

Apart from friction, two additional energy dissipation mechanisms, viscous contact damping and global damping can be used to dissipate the energy during simulation for viscous materials.

*Contact damping* operates on the relative velocities of contacting bodies at the contact point i.e. the damping force is proportional to the normal and tangential relative velocities. The damping force in a linear system is

$$F_d = -D\dot{x} \quad (1.16)$$

where  $D$  is the contact damping coefficient and  $\dot{x}$  is the relative velocity between contacting bodies. Contact damping force can be resolved into normal and tangential directions as

$$F_{dn} = c_n \dot{n} \quad \text{and} \quad F_{ds} = c_t \dot{s} \quad (1.17)$$

where  $\dot{n}$  and  $\dot{s}$  are relative velocities in normal and tangential direction respectively. Usually, in linear systems the contact damping coefficients  $c_n$  and  $c_s$  are taken to be proportional to the stiffness coefficient as

$$c_n = \gamma k_n \quad \text{and} \quad c_t = \gamma k_t \quad (1.18)$$

where  $\gamma$  is a proportionality constant.

Alternatively, damping may be directly related to the coefficient of restitution for the individual particles (Tsuji *et al.*, 1992; Ting *et al.*, 1993). In this approach which is based on the Hertz theory the damping force in the normal and tangential direction is calculated as a function of a damping ratio and material stiffness coefficient. In this approach the equivalent mass of the contacting bodies  $m^*$  is obtained in a similar way to  $R$  (1.3) i.e.

$$\frac{1}{m^*} = \frac{1}{m_1} + \frac{1}{m_2} \quad (1.19)$$

where  $m_1$  and  $m_2$  are the masses of each contacting particle. The damping ratio  $\beta$  can be related to the coefficient of restitution as

$$\beta = -\frac{\ln e}{\sqrt{(\ln e)^2 + \pi^2}} \quad (1.20)$$

where  $e$  is the coefficient of restitution of contacting bodies. The normal damping coefficient can be derived using (1.19) and (1.20) as

$$C_n = 2\beta\sqrt{k_n m^*} \quad (1.21)$$

The same relationship was reported by Ning and Ghadiri, (1995) which is very similar to the Ting procedure as

$$c_n = \frac{-2\ln e\sqrt{k_n m^*}}{\sqrt{(\ln e)^2 + \pi^2}} \left(\sqrt{\frac{5}{6}}\right) \quad (1.22)$$

The difference between 1.21 and 1.22 is the term  $\sqrt{\frac{5}{6}}$ , which is approximately equal to one.

*Global damping:* Global damping may be envisioned as a series of dashpots connecting the particles to the ground (global axis). Unlike contact damping, global damping operates on the absolute velocities and rotations of the particles as resistance acting in the opposite direction of velocities. It can be useful for simulation of particles with high velocities in a viscous medium. In the present study the global damping can be applied as well as contact damping whenever applicable (see section 2.5 for model implementation).

### 1.2.3.5. Time step

In DEM the time step is the time during which force is transmitted from one contact point to another along the particle boundary. The time step should be as large as possible to increase the efficiency of simulation and still be smaller than the critical time step to justify the assumption of constant acceleration within each time step and to ensure stability of the calculations (Cundall and Strack, 1979; Taylor and Preece, 1992). The idea is based on the assumption that the selected time step is small enough so that no new contacts take place in the current time step except those that have already been recognised at the beginning of the time step. Thus, the out-of-balance

force for a particle at the end of each time step is the resultant of the contact forces arising solely from the contacts the particles shared in the current time step.

The calculation of critical time step is based on the frequency determined from a single degree of freedom in the system of particles with the mass element connected to the ground. The critical time step for a linear contact model is based on the natural frequency in a linear spring system which is

$$(f = \sqrt{\frac{k}{m}}) \quad (1.23)$$

Therefore, the critical time step in this method is based on the mass of the smallest particle in the model and a constant contact stiffness which is calculated as

$$\Delta t_{cr} = 2\pi \sqrt{\frac{m}{k}} \quad (1.24)$$

where  $m$  and  $k$  are the mass of the smallest particle in the model and contact stiffness respectively (Cundall, 1979; Negi *et al.*, 1992 and Ting *et al.*, 1995).

To take into account the visco-elastic properties of materials, the damping ratio (1.20) is introduced to the critical time step (1.24) as

$$\Delta t_{cr} = \frac{\pi}{\sqrt{\frac{k}{m} \left(1 - \frac{\ln^2 e}{\pi^2 + \ln^2 e}\right)}} \quad (1.25)$$

Since in a non-linear system the contact stiffness ( $k$ ) changes with contact force, the time step will be changed during simulation if the above method is used. Ning and Ghadiri (1995) proposed a method for a non-linear system which uses the frequency of propagation of Rayleigh surface waves on one of the objects on application of force. The frequency of wave propagation is calculated as

$$f_R = \psi \sqrt{\frac{G}{\rho}} \quad (1.26)$$

where  $G$  is the shear modulus and  $\rho$  is the particle density.  $\Psi$  is a parameter dependant on the Poisson ratio ( $\nu$ ) which can be estimated as

$$\psi = 0.1631\nu + 0.8766 \quad (1.27)$$

The critical time step is related to three physical properties of the particulate material as

$$\Delta t_{cr} = \frac{\pi R_{\min}}{f_R} = \frac{\pi R_{\min}}{\psi} \sqrt{\frac{\rho}{G_{\max}}} \quad (1.28)$$

where  $R_{\min}$  is the radius of the smallest particle in the system and  $G_{\max}$  is the maximum shear modulus in the particulate assembly.

As an alternative approach to calculate the critical time step in a non-linear system, Ng (1989) replaced contact stiffness ( $k$ ) with shear modulus of elasticity ( $G$ ) in equation (1.24). In this procedure the critical time step will always be less than that calculated from equation (1.24), because in Mindlin's solution the stiffness ( $k$ ) is obtained as

$$k = \frac{4G_s a}{2 - \nu_s} \quad (1.29)$$

where  $G_s$  is the shear modulus of elasticity and  $a$  is the radius of the contact area which is very small and  $\nu_s$  is the Poisson's ratio which is always less than one. The term  $(2 - \nu_s)$  is greater than unity, so that  $k$  will always be less than  $G_s$ . For this reason by replacing  $k$  with  $G_s$  in equation (1.24) the critical time step becomes smaller than when using  $k$ . In the present research the Ning and Ghadiri procedure (1.28) is used for the calculation of time step (see section 2.5 for model implementation).

### 1.2.3.6. Contact search

In DE simulations, the most important step prior to any mechanical calculation is determination of which surfaces are in contact and the type of contact. It is estimated that more than 80% of the computational time can be spent on this task (Williams and Pentland, 1989). In a very simple approach each particle is checked against every other

particle to determine any probable contact. The computational time for this simple procedure with  $n$  particles will be proportional to  $n^2$ , which is too long if there are hundreds of particles in the simulation (Cundall and Hart, 1992).

Various strategies have been employed to decrease the search time to an acceptable level. For 2-dimensional models a “link list” algorithm has been used (Ting *et al.*, 1993; Rong *et al.*, 1995a) which is suitable for densely packed systems. In this method, the simulation space is divided into relatively large cells. A separate list of particles for each cell is provided, including the particles in the home cell and surrounding cells. The particles within a cell and its neighbouring cells are considered as potential contacting bodies. Therefore, contact detection for such list would be an efficient process regarding time consumption.

Rong *et al.* (1995a) used another algorithm termed “*grid search*” which, was claimed to be more suitable for loosely packed material and small numbers of particles. In this method the cells were sized such that no more than one particle occupies a cell. Subsequently, the link list is used which simply cycles over all cells and only conducts contact test over the cells which are within a certain distance of the cell of interest.

For 3-dimensional models Cundall proposed a link list scheme in which the simulation space was divided into 3-D sub-boxes. Firstly, all sub-boxes occupied by a particle are determined, then the search is followed for any neighbouring particles in the sub-box list. Finally the search procedure is completed by contact detection through this neighbouring list. The contacting list is updated when new contacts are made and contacts which are broken are deleted from the list. This algorithm has been used in several DEM programs; such as “BALL” and “TRUBAL” and then adopted for “3DEC” to model a system of blocks (Cundall, 1988). This method also has been employed by those researchers who modified “BALL” or “TRUBAL” (Ng, 1989; Ghadiri and Ning, 1997).

### 1.2.3.7. Contact detection

Contact search algorithms are used to reduce the search time for contact detection by spatial sorting but the particles in the neighbours list may or may not be in contact. A contact detection algorithm is needed to resolve contacts within the list (Williams and O'Connor, 1995).

The simplest algorithm is that for circular and spherical particles, because there is always a unique form of contact between particles. A contact will be registered if the distance ( $L$ ) between the centre of two neighbouring particles with radius  $R_1$  and  $R_2$  is less than the sum of their radii

$$L \leq R_1 + R_2 \quad (1.30)$$

as shown in Figure 1.5.

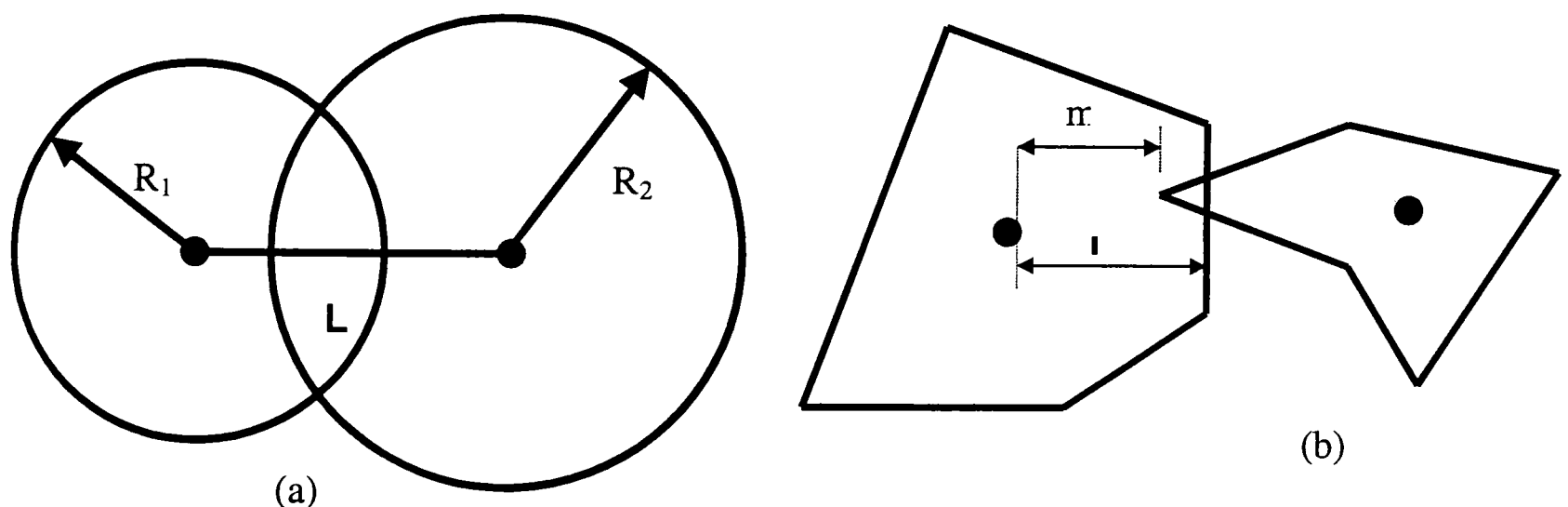


**Figure 1.5** Contact detection between particles; a) Circular shape b) Polygonal shape.

For elliptical and polygonal particles the contact detection algorithm is more complex, because of the greater complexity in geometry of an ellipse or polygon than a circle. In the context of elliptical particles, Ting *et al.* (1993) proposed a contact detection algorithm in which the contact point of two elliptical particles was calculated based on the intersection of two ellipses in 2-D. The contact point in this model was found as the mid-point of the line connecting the intersection points of the two ellipses. In this procedure the equation of each ellipsoid particle is first defined with respect to their local co-ordinate systems. Then for two neighbouring particles the equation of one particle is transformed to the local co-ordinate system of the other particle. This

particle is transformed to the local co-ordinate system of the other particle. This process gives a quartic equation for the intersection of these two particles. Since in DEM simulation, particles are usually marginally in contact, use of the above procedure (using only one quartic equation from intersection of two contacting ellipses) may result in considerable error. This is particularly true where both particles are fairly flat near the contact location and also in situations where both particles have major axis aligned with each other. To overcome above problems, Ting *et al.* (1993) proposed an alternative solution for contact location. In this solution they defined a new function which is the locus of all points where two ellipses share the same slope. This procedure can provide two quartic equations from the intersection of the new function with one of two intersecting ellipses. Furthermore, this algorithm can be extended to 3-D more easily than the first solution.

Lin and Ng (1995) discussed the above algorithm and proposed another contact detection algorithm based on the common normal concept. In this method the equations of two neighbouring ellipses in global co-ordinates are defined. Then according to the co-ordinates of two points on the ellipses which define the contact normal, and the equation of ellipses, the contact can be recognised. The details of the mathematical procedure can be found in the literature (e.g. Ting *et al.*, 1993). They implemented these two algorithms in two different 3-D simulation programs and their performance in terms of accuracy and efficiency were compared.

Ouadfel and Rothenburg (1999) proposed an alternative algorithm for contact detection between two ellipsoid particles. In this method of contact detection, in addition to the information about the amount of overlap, contact normal direction and contact point co-ordinates, some other geometric information such as contact area and its shape is also calculated.

Contact detection for polygonal particles is more complex than for spherical and ellipsoid particles, because in this case, in addition to the position of the contact point, the type of contact (face-face, face-corner or corner-corner) also should be determined (Figure 1.5). Several attempts have been made to implement a feasible algorithm for DEM to detect contact between polygonal particles.

Cundall (1988) proposed a scheme for contact detection in a multi-block system using “common plane” concept. In this procedure a common plane was defined as a plate that is held between two neighbouring blocks and bisects the gap between these two blocks. If two neighbouring blocks touch the common plane then they must touch each other, as the common plane is defined as bisecting the space between blocks. If contact occurs, the unit contact normal will be the same as the unit normal of the common plane.

Ikegava and Hudson (1989) presented another contact detection algorithm for 3-D polygonal models based on *directed body* idea for detect of contact in convex and concave blocks. In this method a directed body is defined as a block formed by a number of directed faces and each directed face has an external and internal face vector perpendicular to the face. The magnitude of a face vector is proportional to the area of the face area and the sum of all external or internal face vectors of a directed body is a zero vector. Therefore, each block can be shown via a number of vectors. The volume of a block is calculated based on the triple scalar product by using the external face vector. A face between two blocks, a common face, (which can be consider as one face, in the directed block concept) it is considered as two directed faces because the direction of their external face vectors are opposite to each other. This idea was used to detect contact between particles.

### 1.2.3.8. Calculation cycle

In Discrete Element Method each simulation entails several steps which are shown in Fig.1.6. Following particle generation, each cycle starts with contact detection between neighbouring model particles.

The procedure starts with determination of the relative position and velocities and terminates by updating the velocity and position of particles. Since, this research is based on spherical particles in three dimensions the calculation cycle will be followed for the case of two spheres in contact.

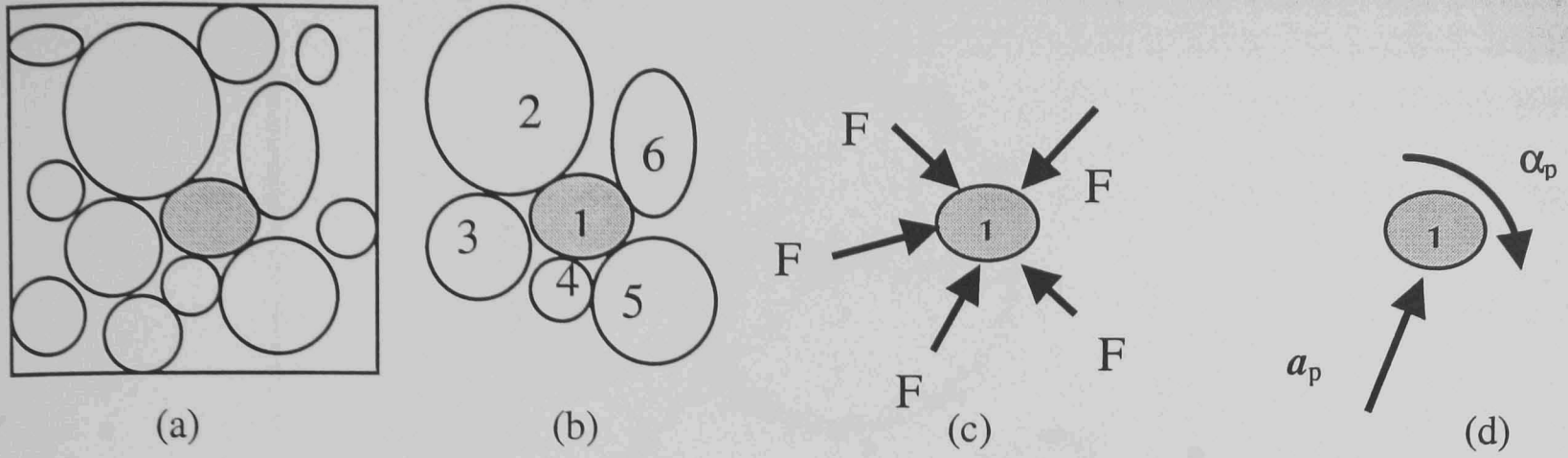


**Figure 1.6** Simulation steps in DEM; a) Particle and environment generation, b) Contact search and detection, c) Calculation of contact force, d) update the particle accelerations.

### 1.2.3.8.1. Relative velocity at contact point

If the condition for contact between two particles is met, the relative displacement at contact point can be calculated by integration of the relative velocity between these particles over time step  $\Delta t$ . The orientation of the normal contact is defined by a normal unit vector, which is perpendicular to the tangential plane of contact (pointing from the centre of particle 1 toward the centre of particle 2 in Fig. 1.7) as

$$\mathbf{n} = \cos\theta_x \mathbf{i} + \cos\theta_y \mathbf{j} + \cos\theta_z \mathbf{k} \quad (1.31)$$

where  $\mathbf{i}$ ,  $\mathbf{j}$  and  $\mathbf{k}$  are the unit vectors in the direction of global axes,  $X$ ,  $Y$  and  $Z$ , respectively and  $\cos\theta_x$ ,  $\cos\theta_y$  and  $\cos\theta_z$  are the direction cosines of the normal unit vector.

The direction cosines of the normal unit vector for two contacting spherical particles are defined

$$\cos\theta_x = \frac{x_2 - x_1}{L}, \quad \cos\theta_y = \frac{y_2 - y_1}{L} \quad \text{and} \quad \cos\theta_z = \frac{z_2 - z_1}{L} \quad (1.32)$$

where  $x$ ,  $y$  and  $z$  are the global co-ordinates of particle's centre and  $L$  is the magnitude of the relative position vector " $\mathbf{d}$ " (Fig. 1.7) pointing from centre of particle "1" to particle "2" which can be calculated as

$$L = \sqrt{(x_2 - x_1)^2 + (y_2 - y_1)^2 + (z_2 - z_1)^2} \quad (1.33)$$

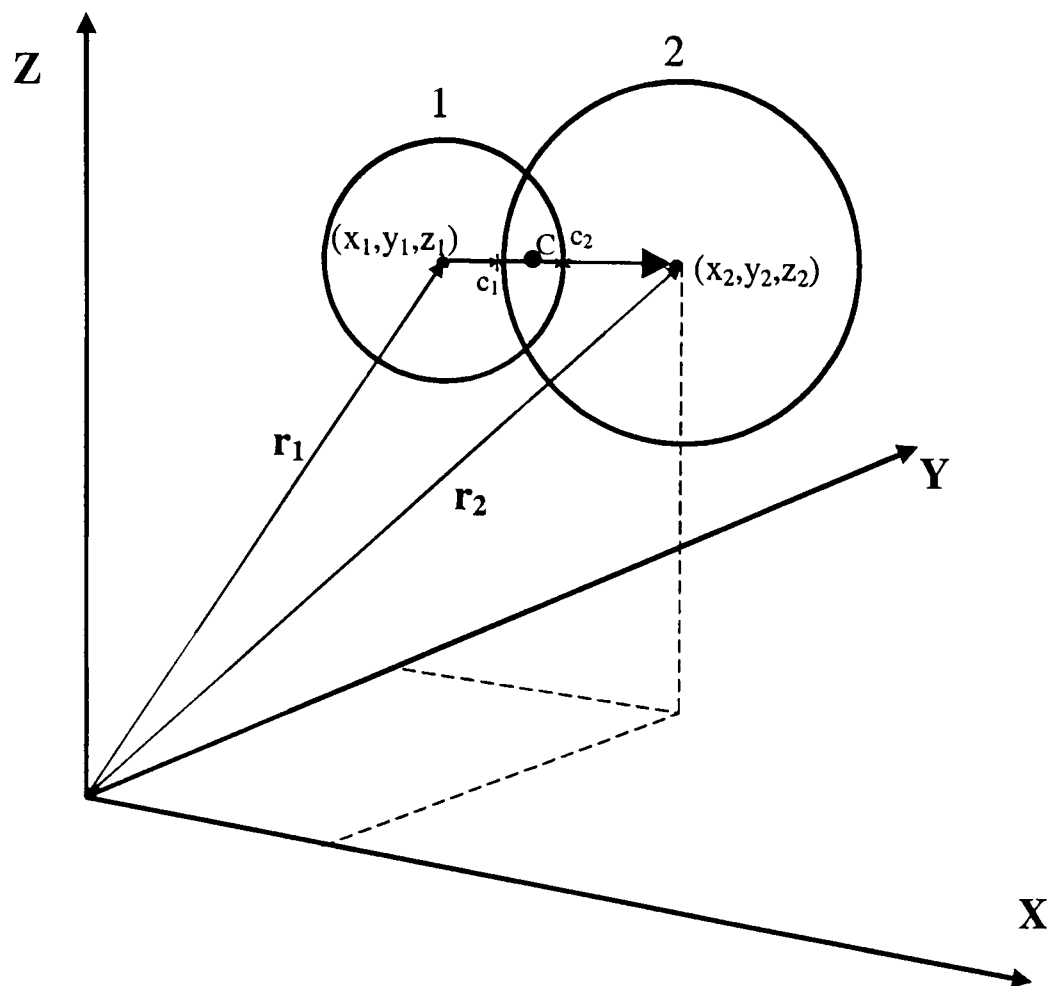


**Figure 1.7** Contact definitions between two contacting spheres.

Consequently, the relative position vector of contacting particles is

$$\mathbf{d} = \mathbf{r}_1 - \mathbf{r}_2 \quad (1.34)$$

$$\mathbf{d} = (x_2 - x_1)\mathbf{i} + (y_2 - y_1)\mathbf{j} + (z_2 - z_1)\mathbf{k} \quad (1.35)$$

The relative velocity at contact is calculated as the difference between the velocity of point  $C_1$  on the boundary of particle 1 and point  $C_2$  on the boundary of particle 2.

$$d\mathbf{v}_c = \mathbf{v}_{c2} - \mathbf{v}_{c1} \quad (1.36)$$

where  $\mathbf{v}_{c2}$  and  $\mathbf{v}_{c1}$  are the velocity of contact point on the boundary of sphere “1” and “2” respectively. These velocities are due to both translation and rotation of the contacting particles (Fig. 1.2) as

$$\mathbf{v}_c = \mathbf{v}_{ct} + \mathbf{v}_{cr} \quad (1.37)$$

where  $\mathbf{v}_{ct}$  and  $\mathbf{v}_{cr}$  are the velocity of contact point  $c$  due to translation and rotation of a particle respectively. The velocity of contact point  $c$  due to translation of the particle can be defined

$$\mathbf{v}_{ct} = v_x \mathbf{i} + v_y \mathbf{j} + v_z \mathbf{k} \quad (1.38)$$

where  $v_x$ ,  $v_y$  and  $v_z$  are the global components of the translational velocity of the particle

The velocity of contact point  $c$  due to rotation of the particle is calculated

$$\mathbf{v}_{cr} = \boldsymbol{\omega} \times \mathbf{R} \quad (1.39)$$

where  $\boldsymbol{\omega}$  is the rotational velocity vector of the contacting particle and  $\mathbf{R}$  is a vector which connects the centre of the particle to the contact point. This vector has a magnitude equal to the radius of the sphere and its direction is either in the direction or opposite of unit normal vector  $\mathbf{n}$ . For sphere  $I$  it can be written as

$$\mathbf{R}_1 = |R_1| \mathbf{n} \quad (1.40)$$

$$\mathbf{R}_1 = |R_1| (\cos\theta_x \mathbf{i} + \cos\theta_y \mathbf{j} + \cos\theta_z \mathbf{k}) \quad (1.41)$$

The rotational velocity of the contacting sphere can also be written in term of its global components as

$$\boldsymbol{\omega} = \omega_x \mathbf{i} + \omega_y \mathbf{j} + \omega_z \mathbf{k} \quad (1.42)$$

Combining (1.39), (1.41) and (1.42), the contact velocity due to particle rotation becomes

$$\mathbf{v}_{cr} = \begin{vmatrix} \mathbf{i} & \mathbf{j} & \mathbf{k} \\ \omega_x & \omega_y & \omega_z \\ \cos\theta_x & \cos\theta_y & \cos\theta_z \end{vmatrix} |R| \quad (1.43)$$

Combining (1.37) and (1.43) the contact velocity at the boundary of a contacting particle is

$$\mathbf{v}_c = v_x \mathbf{i} + v_y \mathbf{j} + v_z \mathbf{k} + \begin{vmatrix} \mathbf{i} & \mathbf{j} & \mathbf{k} \\ \omega_x & \omega_y & \omega_z \\ \cos\theta_x & \cos\theta_y & \cos\theta_z \end{vmatrix} |R| \quad (1.44)$$

The relative contact velocity (1.36) is then resolved in the direction parallel and perpendicular to the contact unit normal to yield the incremental normal and tangential contact velocities

$$d\mathbf{v}_{cn} = (d\mathbf{v}_c \cdot \mathbf{n})\mathbf{n} \quad (1.45)$$

The tangential relative velocity now can be calculated as

$$d\mathbf{v}_{cs} = d\mathbf{v}_c - d\mathbf{v}_{cn} \quad (1.46)$$

The normal and tangential contact velocity is also resolved in the direction of global axis as

$$d\mathbf{v}_{cn} = dv_{(cn)x}\mathbf{i} + dv_{(cn)y}\mathbf{j} + dv_{(cn)z}\mathbf{k} \quad (1.47)$$

$$d\mathbf{v}_{cs} = dv_{(cs)x}\mathbf{i} + dv_{(cs)y}\mathbf{j} + dv_{(cs)z}\mathbf{k} \quad (1.48)$$

The magnitude of normal and tangential contact velocities now are

$$\dot{n} = \sqrt{(dv_{(cn)x})^2 + (dv_{(cn)y})^2 + (dv_{(cn)z})^2} \quad (1.49)$$

$$\dot{s} = \sqrt{(dv_{(cs)x})^2 + (dv_{(cs)y})^2 + (dv_{(cs)z})^2} \quad (1.50)$$

Integration of the relative velocities with respect to time gives the components of the relative displacement increment as

$$\Delta n = \dot{n}\Delta t \quad \text{and} \quad \Delta s = \dot{s}\Delta t \quad (1.51)$$

Consequently, the unit tangential vector can be calculated via its direction cosines which can be used to resolve the tangential force in the direction of global axis as

$$\mathbf{t} = \cos\beta_x\mathbf{i} + \cos\beta_y\mathbf{j} + \cos\beta_z\mathbf{k} \quad (1.52)$$

where

$$\cos\beta_x = \frac{dv_{(cs)x}}{\dot{s}}, \quad \cos\beta_y = \frac{dv_{(cs)y}}{\dot{s}} \quad \text{and} \quad \cos\beta_z = \frac{dv_{(cs)z}}{\dot{s}} \quad (1.53)$$

### 1.2.3.8.2. Determination of contact force and moment

The relative displacement increments (1.51) are used with a force-displacement law to calculate increments of the normal and shear forces

$$\Delta F_n = k_n \dot{n} \Delta t \quad \text{and} \quad \Delta F_s = k_t \dot{s} \Delta t \quad (1.54)$$

where  $k_n$  and  $k_t$  are the spring (elastic) stiffness coefficients in the normal and tangential directions respectively. Having determined the incremental force over the time step, the normal and tangential contact forces at time  $t$  for this contact point is

$$(F_n)_N = (F_n)_{N-1} + \Delta F_n \quad \text{and} \quad (F_s)_N = (F_s)_{N-1} + \Delta F_s \quad (1.55)$$

where the indices  $N$  and  $N-1$  refer to time  $t_N$  and  $t_{N-1}$  respectively, thus the time step  $\Delta t$  is equal to  $t_N - t_{N-1}$ . Ting *et al.* (1993) stated that adding incremental normal forces at each time step could lead to a cumulative error. Thus they suggested calculating the total normal force from the total normal overlap at each instant.

The normal and tangential forces for each contact point of a contacting particle is then written as their unit vectors using (1.31) and (1.52)

$$\mathbf{F}_n = |F_n| (\cos\theta_x \mathbf{i} + \cos\theta_y \mathbf{j} + \cos\theta_z \mathbf{k}) \quad (1.56)$$

$$\mathbf{F}_s = |F_s| (\cos\beta_x \mathbf{i} + \cos\beta_y \mathbf{j} + \cos\beta_z \mathbf{k}) \quad (1.57)$$

Therefore, both normal and tangential contact forces can be resolved in the direction of global axis as

$$\mathbf{F}_n = F_{nx} \mathbf{i} + F_{ny} \mathbf{j} + F_{nz} \mathbf{k} \quad (1.58)$$

$$\mathbf{F}_s = F_{sx} \mathbf{i} + F_{sy} \mathbf{j} + F_{sz} \mathbf{k} \quad (1.59)$$

The vectorial summation of these contact force components over all of contact points for each sphere gives the resultant contact force in term of its global components

$$\begin{aligned}
 F_x &= \sum_{i=1}^k (F_{nx} + F_{sx})_i \\
 F_y &= \sum_{i=1}^k (F_{ny} + F_{sy})_i \\
 F_z &= \sum_{i=1}^k (F_{nz} + F_{sz})_i
 \end{aligned} \tag{1.60}$$

where  $i$  refers to a contact point and  $k$  is the total number of contact points for the contacting sphere at the current time step.

In the case of spherical particles  $\mathbf{F}_n$  always passes through the centre of the sphere, thus, these forces can not contribute to the resultant moment acting on spheres, but tangential forces can. The corresponding moment due to tangential force at a contact point  $i$  is

$$\mathbf{M}_i = \mathbf{F}_{si} \times \mathbf{R} \tag{1.61}$$

where  $\mathbf{M}_i$  is the moment of tangential force at contact point  $i$  about the centre of the contacting sphere. This moment is then resolved into its components in the direction of global axis as

$$\mathbf{M}_i = M_{ix}\mathbf{i} + M_{iy}\mathbf{j} + M_{iz}\mathbf{k} \tag{1.62}$$

The resultant moment acting on the contacting sphere is the vectorial summation over all of its contact point as

$$M_x = \sum_{i=1}^{i=k} M_{ix}, \quad M_y = \sum_{i=1}^{i=k} M_{iy} \quad \text{and} \quad M_z = \sum_{i=1}^{i=k} M_{iz} \tag{1.63}$$

At the end of each time step the resultant force and moment acting on the sphere can be written in term of their global axis components

$$\mathbf{F}_p = F_x\mathbf{i} + F_y\mathbf{j} + F_z\mathbf{k} \tag{1.64}$$

$$\mathbf{M}_p = M_x\mathbf{i} + M_y\mathbf{j} + M_z\mathbf{k} \tag{1.65}$$

Having determined the resultant force and moment on a particle, Newton's second law of motion is used to calculate the translational and rotational acceleration of the particle.

### 1.2.3.8.3. Calculation of particle motion and updating of particle position

The acceleration of a particle has to be determined at each cycle, in order to update the position of the particle at the end of current cycle. Assuming the sphere is a rigid body, these accelerations can be calculated from resultant force and moment as

$$\mathbf{a}_p = \frac{\mathbf{F}_p}{m} + \mathbf{g} \quad \text{and} \quad \boldsymbol{\alpha}_p = \frac{\mathbf{M}_p}{I_p} \quad (1.66)$$

where  $m$  and  $I$  are the mass and the mass moment of inertia of the particle,  $\mathbf{a}$  and  $\boldsymbol{\alpha}$  are the translational and rotational acceleration vectors and  $\mathbf{g}$  is the gravitational acceleration vector.

Using a central-difference scheme (Cundall and Strack, 1979) and explicit numerical integration and assuming acceleration and velocities remain constant during time step  $\Delta t$ , the translational and rotational velocities of a particle can be calculated as

$$\mathbf{v}_p^{(N+\frac{1}{2})} = \mathbf{v}_p^{(N-\frac{1}{2})} + \left[ \frac{\mathbf{F}_p}{m_p} + \mathbf{g} \right] \Delta t \quad (1.67)$$

$$\boldsymbol{\omega}_p^{(N+\frac{1}{2})} = \boldsymbol{\omega}_p^{(N-\frac{1}{2})} + \left[ \frac{\mathbf{M}_p}{I_p} \right] \Delta t \quad (1.68)$$

The above equations are applied to all of the particles in turn. The new velocities now can be used in the force-displacement law and the cycle will be repeated for the next time step.

Using another integration over time gives the position and the orientation of the particles as

$$\mathbf{r}_p^{(N+1)} = \mathbf{r}_p^{(N)} + \mathbf{v}_p^{(N+\frac{1}{2})} \Delta t \quad (1.69)$$

$$\boldsymbol{\theta}_p^{(N+1)} = \boldsymbol{\theta}_p^{(N)} + \boldsymbol{\omega}_p^{(N+\frac{1}{2})} \Delta t \quad (1.70)$$

The global co-ordinates of particles (1.69) at the end of each calculation cycle can be used for the next contact detection and updating the contact list.

#### 1.2.3.8.4. Incorporation of damping

The previous equations (1.56 and 1.57) calculate only the spring normal and tangential forces. To dissipate energy the friction and damping can be included in these equations.

The shear force  $F_s$  can not exceed a maximum possible value which can be calculated from Coulomb law

$$F_{s(Max)} = \mu F_n + C \quad (1.71)$$

where  $\mu$  is the coefficient of inter-particle friction of the two contacting spheres and  $C$  is the cohesion which is zero in the case of cohesionless materials. Based on the contact model (Fig. 1.4), the normal force ( $F_n$ ) in (1.56) can be calculated using two different approaches (Walton, 1983). The difference between these methods is the way in which the frictional force limitation is calculated. In the first method the normal force used for the friction limit is the sum of the spring force and damping force

$$F_n = k_n \Delta n + c_n \dot{n} \quad (1.72)$$

In the second method the normal force used for the friction limit is based only on the spring force (damping force is excluded)

$$F_n = k_n \Delta n \quad (1.73)$$

At every time step the absolute value of shear force is checked against maximum shear force and if it is larger than maximum, then it is set to  $F_{s(\max)}$ .

If contact damping is taken into account in the force summation (1.64) the damping force must be included, giving

$$\mathbf{v}_p^{(N+\frac{1}{2})} = \mathbf{v}_p^{(N-\frac{1}{2})} + \left[ \frac{\sum_{i=1}^k [\mathbf{F}_{c_i} + \mathbf{F}_{d_i}]_p}{m_p} + \mathbf{g} \right] \Delta t \quad (1.74)$$

$$\boldsymbol{\omega}_p^{(N+\frac{1}{2})} = \boldsymbol{\omega}_p^{(N-\frac{1}{2})} + \left[ \frac{\sum_{i=1}^k M_{p_i}^{(N)}}{I_p} \right] \Delta t \quad (1.75)$$

where  $i$  refers to a contact point and  $k$  is the total number of contact point for particle  $p$ . The difference between (1.68) and (1.75) is in the magnitude of moment. In the latter, the moment includes the contribution of the contact damping force to the moment sum.

If global damping is included in addition to contact damping, the equation of motion (1.66) becomes

$$\mathbf{a}_p = \frac{\left[ \sum_{i=1}^{i=k} (\mathbf{F}_{c_i} + \mathbf{F}_{d_i})_p - C' \mathbf{v}_p \right]}{m_p} + \mathbf{g} \quad (1.76)$$

$$\boldsymbol{\alpha}_p = \frac{\sum_{i=1}^{i=k} \mathbf{M}_{p_i} - C'' \boldsymbol{\omega}_p}{I_p} \quad (1.77)$$

where  $C'$  and  $C''$  are the coefficients of global damping for mass and moment of inertia.

Since

$$\mathbf{a}_p = \frac{(\mathbf{v}_p^{(N+\frac{1}{2})} - \mathbf{v}_p^{(N-\frac{1}{2})})}{\Delta t} \quad \text{and} \quad \boldsymbol{\alpha}_p = \frac{(\boldsymbol{\omega}_p^{(N+\frac{1}{2})} - \boldsymbol{\omega}_p^{(N-\frac{1}{2})})}{\Delta t} \quad (1.78)$$

Substituting  $\mathbf{a}$  and  $\boldsymbol{\alpha}$  in (1.75) and (1.76) gives

$$\mathbf{v}_p^{(N+\frac{1}{2})} = \frac{\left\{ \mathbf{v}_p^{(N-\frac{1}{2})} \left( 1 - \frac{C'\Delta t}{2m_p} \right) + \frac{\sum (\mathbf{F}_c + \mathbf{F}_d)_p^N \Delta t}{m_p} \right\}}{\left( 1 + \frac{C'\Delta t}{2m_p} \right)} \quad (1.79)$$

$$\boldsymbol{\omega}_p^{(N+\frac{1}{2})} = \frac{\left\{ \boldsymbol{\omega}_p^{(N-\frac{1}{2})} \left( 1 - \frac{C''\Delta t}{2I_p} \right) + \frac{\sum (\mathbf{M})_p^N \Delta t}{m_p} \right\}}{\left( 1 + \frac{C''\Delta t}{2I_p} \right)} \quad (1.80)$$

The global damping coefficients are taken to be proportional to mass and mass moment of inertia

$$C' = fm_p \quad \text{and} \quad C'' = fI_p \quad (1.81)$$

where  $f$  is the mass and moment of inertia proportionality constant for global damping.

Using (1.80) in (1.78 and 1.79) the particle's velocities can be updated if both global and contact damping are applied as

$$\mathbf{v}_p^{(N+\frac{1}{2})} = \frac{\left\{ \mathbf{v}_p^{(N-\frac{1}{2})} \left( 1 - \frac{f\Delta t}{2} \right) + \frac{\sum (\mathbf{F}_c + \mathbf{F}_d)_p^N \Delta t}{m_p} \right\}}{\left( 1 + \frac{f\Delta t}{2} \right)} \quad (1.82)$$

$$\boldsymbol{\omega}_p^{(n+\frac{1}{2})} = \frac{\left\{ \boldsymbol{\omega}_p^{(N-\frac{1}{2})} \left( 1 - \frac{f\Delta t}{2} \right) + \frac{\sum (\mathbf{M})_p^N \Delta t}{m_p} \right\}}{\left( 1 + \frac{f\Delta t}{2} \right)} \quad (1.83)$$

These velocities can now be used to update the position of each individual sphere by substituting (1.84) in (1.71) having considered all the necessary conditions on the particles. The cycle is repeated for time step  $(N + 1)$  and beyond.

### 1.3 Summary

The main points of this review can be summarised as:

- 1) Application of the continuum approach to discontinuous media undergoing large deformations such as flow of particulates is restricted due to the lack of suitable constitutive laws and parameters used in the constitutive models and lack of information about what happens inside granular systems. Therefore, more investigations are needed especially from a microscopic point of view, to identify the appropriate physically sound continuum model which might then be incorporated into continuum analyses of true scale problems.
- 2) The Discrete Element Method can be an effective research tool for the investigation of the micro-mechanics of granular materials in order to identify the appropriate physical parameters which are needed in continuum models to facilitate the analysis of engineering scale problems. In this regard, DEM simulations can provide information about what happens inside particulate systems. Such information, in conjunction with the facility to change the properties of particles in the DE models, enhances understanding of particulate behaviour. In DEM simulations a particulate system can be recreated exactly with different particle properties to enable their effect. This is impossible in experimental studies.
- 3) Factors such as particle shape and size and contact model can affect the results of DEM simulations. A number of improvements on the original DE models have been carried out in relation to particle shape representation, contact model and contact detection algorithm to facilitate the application of this method to a wider area.
- 4) Three different model particle shapes have been commonly used: spherical, polygonal and ellipsoid (more generally super-quadric functions). Combined primitives

---

such as pair element and clustering which are based on circular elements have been used in a limited number of models. Most researches which considered the effects of particle shape and size on simulation results, confirmed that these effects are important for most applications. This implies that, in DEM the chosen particle shape has to approximate as closely as possible the actual material particle shape.

5) At present the application of DEM to 3-D systems is limited to models with simple element shapes. In the case of biomaterial particles with a high degree of irregularity, these simple shapes (sphere and ellipse) do not match the actual particle shapes. Furthermore, DE models with non-spherical particles such as super-quadratics can not easily be extended to 3-D due to computational complexity.

---

## 2. Multi-sphere shape representation for DEM

### 2.1. Introduction

As discussed in Chapter One (table 1.1), the majority of DE codes are based on circles (or spheres). In summary, these primitive model particle shapes have the great advantage of computational simplicity and the contact theory for such primitives is well established. However, this simple geometry can be inadequate for modelling real granular particles whose shape deviates from circular. Polygonal model particles and continuous functions (e.g. ellipsoid) can be used to represent irregularly shaped particles. Nevertheless, as the equations are non-linear, the contact detection process is computationally demanding and in case of superquadric functions almost impractical for 3-D systems (Hogue, 1998).

In this chapter, a method of particle shape representation using overlapping spheres to create composite non-spherical particles is proposed. Although the model particles are non-spherical, contact search and detection is based on a single sphere approach. Walton and Braun (1993) used a similar method to create rigid non-spherical particles as a cluster of some spheres to compare the frictional behaviour of spherical and non-spherical particles. However the idea was limited to generation of a model particle comprised of four planar element spheres and the details of the algorithm have only recently been published (Vu-Quoc *et al.*, 2000). Vemuri *et al.* (1998) proposed a contact detection algorithm which could be applied to any non-spherical particle including Walton and Braun type model particles. This model particle has been employed in a DE code to represent the general shape of soybean (Zhang *et al.*, 1995) and has been later utilised for chute flow of soybean (LoCurto *et al.*, 1997; Zhang *et al.*, 2000).

The proposed method in this study is termed the Multi-Sphere Method (MSM) which can be used to generate and simulate contacts between three-dimensional axis-symmetrical particles constructed of overlapping spheres. Since the majority of fruits and vegetables are symmetrical along their longitudinal axis, the method can be used for modelling of such particulates with better match between the shape of real and model particles. The idea is based on the **CSG** (*Constructive Solid Geometry*) technique for construction of complex solids by combining primitive shapes.

---

Constructive Solid Geometry technique has been used in computer graphics to model complex objects as a combination of simpler objects (Sanna *et al.*, 1997; Mazzetti and Ciminiera, 1994; Anand and Knott, 1991) in application such as CAD/CAM software (Li *et al.*, 1998; Ji and Marefat, 1997). In this technique, different kinds of primitive shapes (such as sphere, box, cone, dome, pyramid, etc.) can be combined to create any arbitrary shaped 3-D object. Any number of element shapes with or without overlap can be used to alter the overall shape of the composite object. In addition to particle generation in DE models, contact between particles has also to be detected and resolved. If the model particles consisted of different element shapes, a suitable contact detection would have to be implemented for each element shape, which would in turn lead to a highly complex DEM model. Since contact detection between two spheres is straightforward and is well established, in this research, the construction of model particles is limited to the combination of spheres. The use of spheres in the multi-sphere particles greatly simplifies contact detection by retaining the principles normally employed for systems of single spheres. Theoretically any arbitrary shape can be generated using the MSM but in this research attention is restricted to axis-symmetrical particles with curved surfaces.

The method of generating irregular particle shapes using clusters of spheres presented by Jensen *et al.* (1999) appears similar to the MSM in use of groups of spheres to represent the contour of a particle. However, there are significant differences between the two methods. The main difference is the freedom of movement of the spheres making up a particle. Element spheres in the MSM are fixed with respect to the particle centroid (this is discussed with more detail in the following sections), whereas in the clustering method each sphere can translate and rotate with respect to other spheres in the cluster. A cluster particle is therefore more like an agglomerate (e.g. Ning, 1995; Ning *et al.*, 1997a and b; Ghadiri and Ning, 1997) than a particle; i.e. the cluster can break up and each element sphere can move independently.

In this Chapter the MSM algorithm is derived and the mechanical calculations for updating the dynamics of particles and their element spheres are proposed. Examples of possible particle shapes which can be created and simulations of particle deposition under a gravity field for assemblies of multi-sphere particles with high aspect ratio are presented. The implementation of the MSM algorithm in an existing DE code, which utilised spherical model particles, is then presented.

## 2.2. Multi-sphere model particle construction

Model particles are comprised of spheres whose centres are located on the particle axis of symmetry. Spheres may overlap and vary in diameter along the length of the axis. The surface of a particle is approximated by inscribing spheres such that the surface of each sphere is tangent to the surface of the particle at the point of contact. The position of each element sphere is fixed relative to the other spheres within a particle.

The degree of surface fitting depends on the number of element spheres used to create the particle. Increasing the number of element spheres per particle proportionally reduces the overall number of particles that can be handled within a particular simulation using a given level of computing power. The choice of number of element spheres therefore depends on the application and the desired approximation to actual particle shape. The degree of approximation to the particle surface governs the magnitude of the error in calculation of the contact force vectors. The term “*sphere density*” is used to define the number of element spheres in a model particle. In this regard, for a cylindrical model particle made of equal sized spheres, the sphere density is defined as the number of element sphere centres within the diameter of an element sphere. Using overlapping spheres of different sizes in the MSM rather than identical non-overlapping circles as used in the clustering method leads to a better fitting of the model particle to the shape of real particle. This limitation of the clustering method creates the outer boundary of the model particle (the cluster) with circular segments that cause an additional frictional effect (which could be called pseudo-friction). Pseudo-friction in the model particle can be reduced if the element circles are allowed to have overlap (Fig. 2.1).

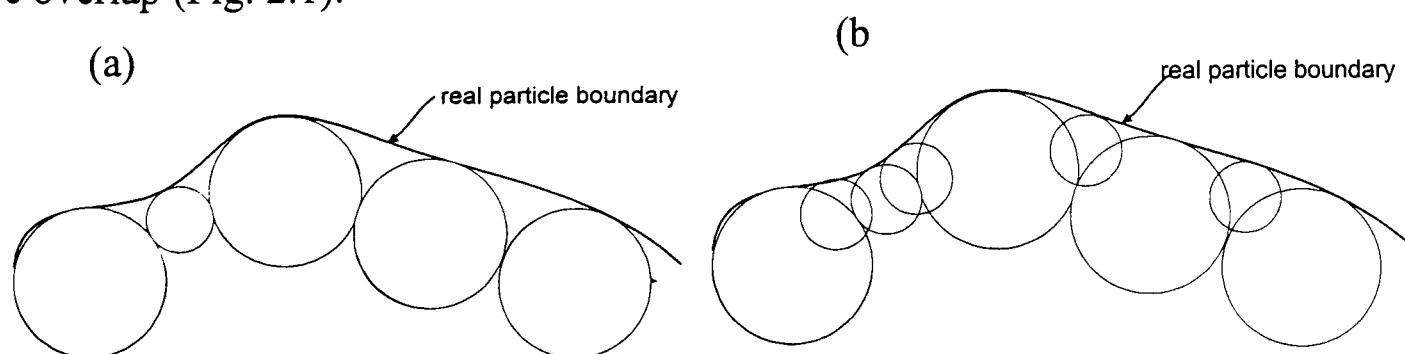


**Figure 2.1** Approximating the surface contour of a 2-D particle using (a) non-overlapping and (b) overlapping circles.

Detailed analysis of the magnitude of maximum deviation of contact normals from theoretical values for the true particle surface, the pseudo friction due to the lobed surface of a multi-sphere model particle and a method for fitting spheres are presented in sections 3.7 and 3.8 respectively.

### 2.2.1. Determination of the model particle centroid

According to the DEM procedure (Section 1.4), the position of the particle centroid is required to update the accelerations, velocities and displacements of particles. For a geometrically simple shape such as sphere and ellipse, the position of the centroid is always known. However, for an axi-symmetrical irregular shaped particle which is created by a number of spherical segments, the particle centroid and sequentially the relative position between particle centroid and centres of the element spheres needs to be determined. As the body of a multi-sphere particle consists of some spherical segments, the principle of Varignon (principle of moments) can be used to calculate the position of the centroid as follows:

$$\bar{X} = \frac{\sum_{i=1}^n V_i \bar{x}_i}{\sum_{i=1}^n V_i}, \quad \bar{Y} = \frac{\sum_{i=1}^n V_i \bar{y}_i}{\sum_{i=1}^n V_i} \quad \text{and} \quad \bar{Z} = \frac{\sum_{i=1}^n V_i \bar{z}_i}{\sum_{i=1}^n V_i} \quad (2.1)$$

where  $\bar{X}, \bar{Y}$  and  $\bar{Z}$  are the co-ordinates of the model particle centroid with respect to a reference axis.  $\bar{x}, \bar{y}$  and  $\bar{z}$  are the co-ordinates of the individual spherical segments of the particle,  $V$  is the volume of each segment and  $n$  is the number of segments in the particle. Since the model particles are axi-symmetrical only  $\bar{X}$  needs to be calculated. The relative distance between particle centroid and the centre of element spheres can then be determined from the co-ordinate of particle centroid and the centre of element spheres.

### 2.2.2. Fitting element spheres to the boundary of a real particle

Although theoretically the MSM can create asymmetrical particle shapes, in this research attention is confined to the more simple problem of generation of axi-symmetrical particles. An algorithm has been implemented to determine the position and radius of the element spheres required to approximate the actual shape of a real axi-symmetrical particle. In this algorithm, the profile of the real particle boundary along its longitudinal axis is first defined (either mathematically or graphically) and then divided into a number of line segments of equal length  $\ell$ . Fig 2.2a shows the method of segmentation of the real particle boundary. The segmentation starts with drawing a circle of radius equal to the segment length ( $\ell$ ), positioned at the beginning of the profile. The first segment point is the intersection of the circle and the profile of particle boundary. The following is carried out by iteration to define the  $X$  and  $Y$  coordinates of a segment point “ $n$ ”:

- (i)  $Y_{n+1}$  is defined by rotating a point anticlockwise starting from point  $(x_n, y_n - \ell)$ ; point  $p$  in Fig. 2.2a) about the centre of the circle positioned in  $(x_n, y_n)$  in increments of  $\Delta\lambda$ . Having determined the segment point  $n+1$ , the angle  $\beta$  which is the angle between  $X$  axis and the segment line  $n$  can be calculated.
- (ii) For any point on the circumference of the locating circle ( $\Delta x^2 + \Delta y^2 = \ell^2$ ) the following is held

$$x_n = x_{n-1} + \Delta x \quad \text{and} \quad y_n = y_{n-1} + \Delta y \quad (2.2)$$

where  $\Delta x = \ell \cos\beta$  and  $\Delta y = \ell \sin\beta$ .

- (iii) Starting with  $\Delta\lambda = \pi/3$ , a test is carried out for the sign of  $(y_n - f(x_n))$  changes.
- (iv) If the above sign was changed  $\Delta\lambda$  is then halved and the new point is defined with the same procedure but reverse direction of rotation.
- (v) The procedure is repeated until  $|y_n - f(x_n)| \leq \xi$ , where  $\xi$  is a chosen tolerance.

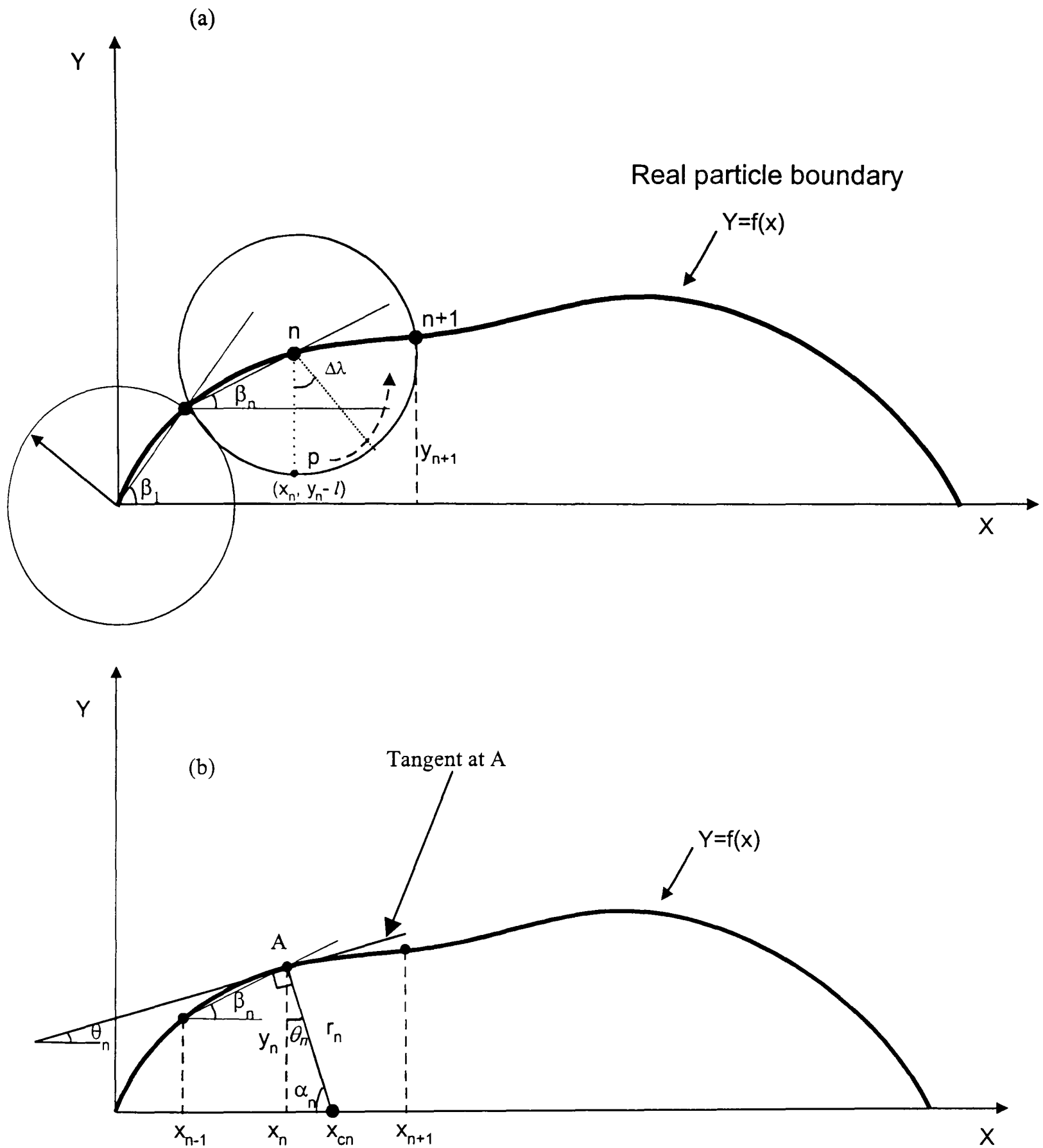


**Figure 2.2** Fitting element spheres to the boundary of a real particle: (a) segmentation of the boundary; (b) calculating the position and radius of element spheres.

Having determined  $\beta_n$ ,  $x_n$  and  $y_n$  for a segment point  $n$ , the slope of the boundary at this point ( $\theta_n$ ) is defined from  $f'(x_n)$ .

According to Fig.2.2b, a sphere can be found with a specific radius ( $r_n$ ) and position in such a way that it is tangent to the real particle boundary at point  $n$ . The radius of the fitting sphere ( $r_n$ ) and its position ( $x_{cn}$ ) is then determined as

$$r_n = \frac{y_n}{\cos \theta_n} \quad \text{and} \quad x_{cn} = x_n + y_n \tan \theta_n \quad (2.3)$$

where  $\theta_n$  is the slope of the boundary profile at segment point  $n$ ;  $x_n$  and  $y_n$  are the coordinates of segment point  $n$ .

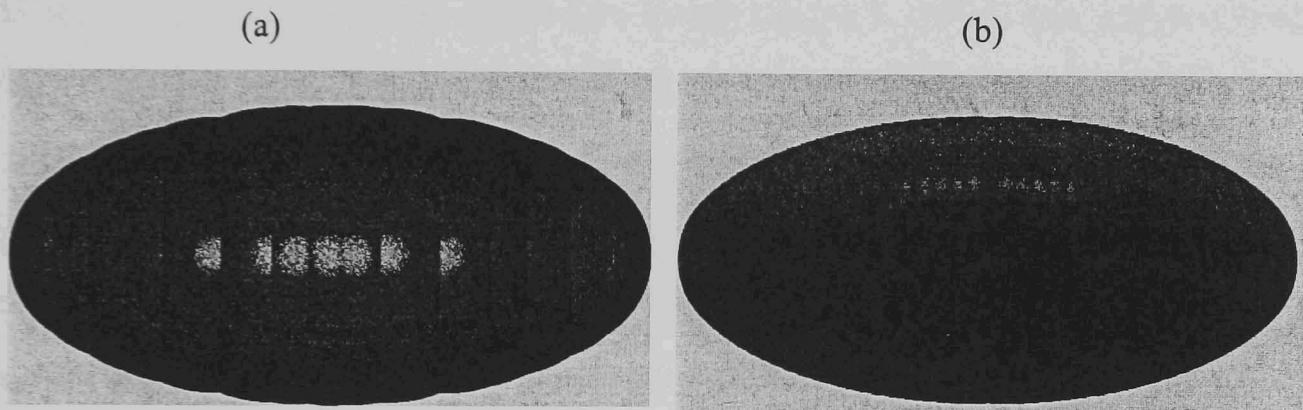


**Figure 2.3** Spheroidal DEM model particle comprising; (a) 15 spheres and (b) 30 spheres.

Fig. 2.3 shows a spheroid with aspect ratio of 2 created with different number of overlapping spheres using the above procedure. This method is, however, not suitable for particles with profile boundary of great irregularity, where the slope of the boundary changes sharply. In this case the element sphere at the turning point intersects the boundary of the real particle so that some part of the element sphere is placed outside the real particle boundary. A fitting sphere would be placed outside the boundary of the real particle boundary if the sphere intersects the profile of the particle boundary at more than one point. This can be tested by the intersection of the function of the fitting sphere with the function of real particle profile ( $f(x)$ ). This may be acceptable in order to obtain a reasonable approximation to the overall shape. The

surfaces of inscribed spheres are by definition inside the surface of the real particle everywhere except at the point of contact unless the fit is perfect (i.e. the real surface is spherical in the region of the fitted sphere). Depending on the application it may be desired to approximate the real particle by fitting spheres such that volume rather than surface contour differences are minimised.

### 2.3. Contact mechanics and particle kinematics using the Multi-Sphere Method (MSM)

Although the model particles in MSM are made up from element spheres, these spheres are not independent objects in the system. They are part of the body of a model particle and only the exposed segment of each element sphere can make contact with neighbouring particles. This is the default condition since non-exposed sphere segments are positioned inside other element spheres and can not make contact with a sphere from a neighbouring particle. The contact forces acting on element spheres are transferred to the centroid of the particle to which they belong for calculation of the particle dynamics from which their positions are updated. In the following sections the mechanical calculations which are needed to update the dynamics of a model particle and its element spheres are presented.

#### 2.3.1. Resultant force and moment acting on a particle due to contacts

Consider two particles, each comprised of two spherical elements of the same diameter, in contact at point  $c$  as shown in Fig 2.4 (only two dimensions are shown but the theory is developed for three dimensions). The global position of each particle is determined at its centroid by its global position vector  $\mathbf{r}_{p(G)}$ . The relative position vector between the particle centroid and the centre of an element sphere  $\mathbf{d}_{ps}$  is known *a priori* because the position of each sphere within a particle is determined in advance. The position of contact point,  $c$ , on each element sphere relative to the particle centroid is:

$$\mathbf{l}_{pc} = \mathbf{d}_{ps} + \mathbf{r}_{psc} \quad (2.4)$$



where  $\mathbf{f}_c$ ,  $\mathbf{f}_n$  and  $\mathbf{f}_t$  are the total, normal and tangential contact forces respectively. The total moment about the centre of an element sphere due to tangential forces is

$$\mathbf{M}_{t_{ps}} = \sum_{c=1}^C \left( \mathbf{r}_{psc} \times \mathbf{f}_{t_{psc}} \right) \quad (2.6)$$

where  $\mathbf{f}_{t_{psc}}$  is the tangential component of the contact force at contact point  $c$  and  $C$  is the total number of contact points on each sphere at the current time-step (Fig 2.5a). The resultant contact force acting on each element sphere is

$$\mathbf{f}_{ps} = \sum_{c=1}^C \mathbf{f}_{psc} \quad (2.7)$$

This force is transferred to the centre of each element sphere (Meriam, 1975a) as shown in (Fig 2.5b). The moments generated by forces acting on the centre of each element sphere which do not pass through the centroid of the particle are then added to the moment of the tangential forces, giving the total moment acting on the particle as

$$\mathbf{M}_p = \sum_{s=1}^S \left[ (\mathbf{d}_{ps} \times \mathbf{f}_{ps}) + \mathbf{M}_{t_{ps}} \right] \quad (2.8)$$

$$\mathbf{M}_p = \sum_{s=1}^S \left[ (\mathbf{d}_{ps} \times \mathbf{f}_{ps}) + \sum_{c=1}^C (\mathbf{r}_{psc} \times \mathbf{f}_{t_{psc}}) \right] \quad (2.9)$$

where  $S$  is the total number of element spheres within the particle (Fig 2.5c). The total out-of-balance force acting on the particle is the vectorial sum of resultant contact forces acting on its element spheres

$$\mathbf{f}_p = \sum_{s=1}^S \mathbf{f}_{ps} \quad (2.10)$$

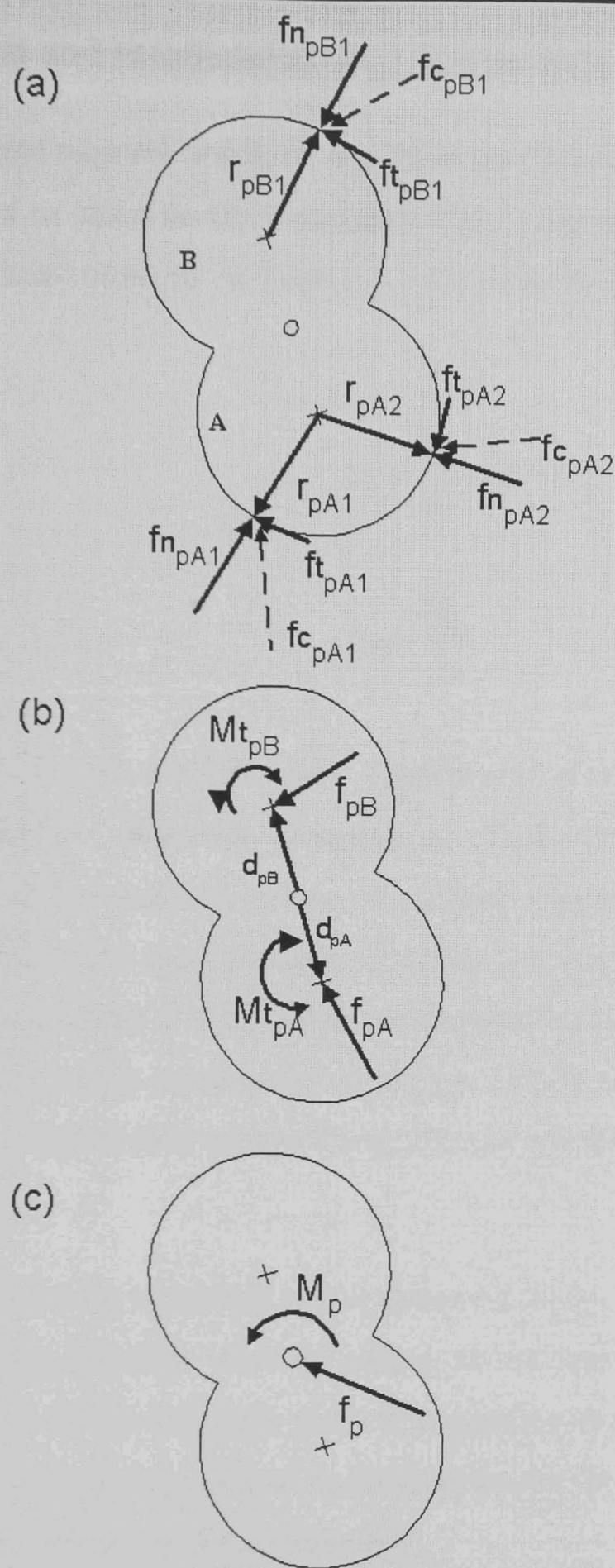


**Figure 2.5** Method of transfer of forces acting on element spheres to the centroid of a particle. Resultant forces and moments from normal and tangential forces respectively acting on each element (spheres A and B) shown in (a) are transferred to the centre of each sphere as shown in (b). The moments caused by forces whose line of action does not pass through the particle centroid are then transferred, along with moments due to tangential forces, to the particle centroid as shown in (c).

### 2.3.2. Translational and rotational motion of a particle

Once the total force and moment acting on a particle are determined, Newton's second law of motion is used to calculate the translational and rotational accelerations of the particle. Using the mass moment of inertia  $I_p$ , the undamped accelerations can be expressed as

$$\mathbf{a}_p = \frac{\mathbf{f}_p}{m_p} + \mathbf{g} \quad (2.11)$$

$$\alpha_p = \frac{\mathbf{M}_p}{I_p} \quad (2.12)$$

where  $m_p$ ,  $\mathbf{a}_p$  and  $\alpha_p$  are the particle mass, translational acceleration and rotational acceleration respectively. However, equation (2.12) is valid only for spheres. Accurate calculation of the rotational motion of particles with aspect ratio greater than one requires calculation of the mass moment of inertia with respect to the global axes. This factor cannot be neglected in DE models of non-spherical particles because it will have a significant effect on the rotational acceleration. This is of particular importance for particles with large aspect ratio such as those that can be generated using the multi-sphere method.

The rigid body motion can be expressed by the Euler equations of motion of a body in space in relation to the principle axes of inertia of the body (Hart *et al.*, 1988). Knowledge is required of the principle axes of a particle, the three principle mass moments of inertia and the exact position and orientation of the particle at each time-step with respect to the spatially fixed global axes.

Favier *et al.* (1999a)<sup>1</sup> proposed an accurate solution for updating the rotational acceleration of a multi-sphere particle. In this method, first the total applied moment on a particle from global co-ordinates  $\mathbf{M}_G = \mathbf{M}_p$  (2.9) is transferred to the local co-ordinate system during each time step, using a transformation matrix  $\mathbf{R}$ . This matrix is determined by comparing the rotation of three arbitrary particle reference points  $A_1, A_2$

<sup>1</sup> The contribution of the third author (M. Kremmer) for the calculation of particle rotation is acknowledged.

and  $A_3$  in the local co-ordinate frame of a particle. The position vectors of these points have to be linearly independent, so that their determinant is not equal to zero. The matrix  $\mathbf{R}$  in each time step is determined by comparing the rotated reference points with their origins using

$$[\mathbf{R}] = [\mathbf{A}] \left[ \mathbf{B} - \mathbf{r}_{P(G)} \right] \quad (2.13)$$

where  $\left[ \mathbf{B} - \mathbf{r}_{P(G)} \right]$  is the matrix of the rotated reference frame. The local applied moment is then

$$[\mathbf{M}_L] = [\mathbf{R}] [\mathbf{M}_G] \quad (2.14)$$

The local rotational acceleration  $\alpha_{p(L)}$  can be calculated using the Euler equations as follows

$$\begin{aligned} M_{X(L)} &= I_{XX} \alpha_{pX(L)} + (I_{ZZ} - I_{YY}) \alpha_{pY(L)} \alpha_{pZ(L)} (\Delta t)^2 \\ M_{Y(L)} &= I_{YY} \alpha_{pY(L)} + (I_{XX} - I_{ZZ}) \alpha_{pX(L)} \alpha_{pZ(L)} (\Delta t)^2 \\ M_{Z(L)} &= I_{ZZ} \alpha_{pZ(L)} + (I_{YY} - I_{XX}) \alpha_{pX(L)} \alpha_{pY(L)} (\Delta t)^2 \end{aligned} \quad (2.15)$$

where  $M_{X(L)}$ ,  $M_{Y(L)}$  and  $M_{Z(L)}$  are the applied moments on the particle in the direction of local co-ordinate system.  $I_{XX}$ ,  $I_{YY}$  and  $I_{ZZ}$  are the principle moments of inertia of the particle and  $\Delta t$  is time step. The acceleration according to global co-ordinates,  $\alpha_{p(G)}$  is then determined by a transformation with the inverted matrix  $\mathbf{R}^{-1}$  i.e.  $\alpha_{p(G)} = \alpha_L \mathbf{R}^{-1}$  (for more details see Favier *et al.*, 1999a). Alternative approaches to calculation of particle acceleration for non-spherical particles with an assessment of the relative computational overhead associated with each method when implemented in a DE algorithm are given in Kremmer and Favier (2000).

Having determined the global translational and rotational accelerations of the particles and assuming accelerations and velocities during a certain time-step remain constant, the translational and rotational velocity of the particles are then computed

$$\mathbf{v}_p^{(N+\frac{1}{2})} = \mathbf{v}_p^{(N-\frac{1}{2})} + \mathbf{a}_p^N \Delta t \quad (2.16)$$

$$\omega_p^{(N+\frac{1}{2})} = \omega_p^{(N-\frac{1}{2})} + \alpha_{p(G)}^N \Delta t \quad (2.17)$$

Using equation (2.16) and integrating over the time-step the new position of the particle is

$$\mathbf{r}_{p(G)}^{(N+1)} = \mathbf{r}_{p(G)}^N + \mathbf{v}_p^{(N+\frac{1}{2})} \Delta t \quad (2.18)$$

### 2.3.3. Velocity and position of element spheres

The absolute velocity of the centre of an element sphere with respect to the global axes is calculated according to Fig. 2.6 as

$$\mathbf{v}_{ps} = \mathbf{v}_p + (\omega_p \times \mathbf{d}_{ps}) + \mathbf{v}_{rel} \quad (2.19)$$

where  $\mathbf{v}_{rel}$  is the relative translational velocity of the element sphere with respect to the particle centroid (observed from local co-ordinate system).

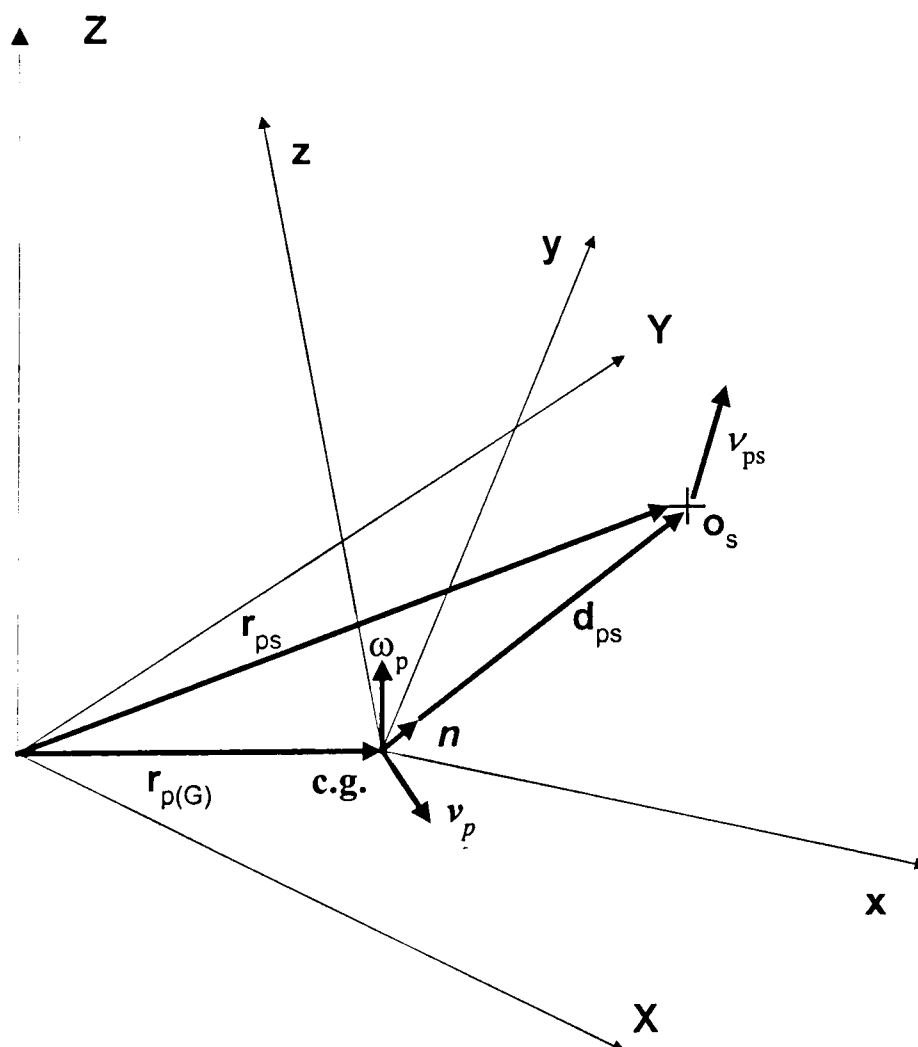


**Figure 2.6** Method of updating the velocity and position of an element sphere from translational and rotational velocities of the particle centroid.

However, the distance between the centroid of the particle and the centre of an element sphere is always fixed. Therefore (2.19) becomes

$$\mathbf{v}_{ps} = \mathbf{v}_p + (\boldsymbol{\omega}_p \times \mathbf{d}_{ps}) \quad (2.20)$$

The magnitude of the vector  $\mathbf{d}_{ps}$  which locates the centre of sphere  $s$  with respect to the particle centroid, is fixed, however, its direction can be changed due to particle rotation. The vector can be written in terms of its unit vector  $\mathbf{n}$  as

$$\mathbf{d}_{ps} = |\mathbf{d}_{ps}| \mathbf{n} \quad (2.21)$$

The unit vector expressed in terms of its direction cosines with respect to the global axis is

$$\mathbf{n} = \cos\theta_x \mathbf{i} + \cos\theta_y \mathbf{j} + \cos\theta_z \mathbf{k} \quad (2.22)$$

where  $\theta_x, \theta_y$  and  $\theta_z$  are the directional angles of the vector with respect to the global axes. The magnitude remains constant (unity) if

$$\cos^2\theta_x + \cos^2\theta_y + \cos^2\theta_z = 1 \quad (2.23)$$

The change in a unit vector due to particle rotation is expressed as (Meriam, 1975b)

$$\dot{\mathbf{n}} = \boldsymbol{\omega}_p \times \mathbf{n} \quad (2.24)$$

However, (2.24) is true only for infinitesimal rotations, i.e. when the time-step,  $\Delta t$ , approaches zero. Since the actual time-step is greater than zero, there will be an error in calculation of the new unit vector. This error can be reduced by keeping the time-step as short as possible and by normalising the error difference using the following procedure. Over a given time-step the increment of  $\mathbf{n}$  is

$$\Delta \mathbf{n} = \dot{\mathbf{n}} \Delta t \quad (2.25)$$

The new unit vector of the vector  $\mathbf{d}_{ps}$  is

$$\mathbf{n}_{new} = \mathbf{n} + \Delta \mathbf{n} \quad (2.26)$$

As  $\mathbf{n}_{new}$  needs to remain a unit vector, it is normalised to fix its magnitude to unity as follows

$$\mathbf{n}_{new} = \text{Cos}\theta_{x_{new}} \mathbf{i} + \text{Cos}\theta_{y_{new}} \mathbf{j} + \text{Cos}\theta_{z_{new}} \mathbf{k} \quad (2.27)$$

$$|\mathbf{n}_{new}| = \left[ \text{Cos}\theta_{x_{new}}^2 + \text{Cos}\theta_{y_{new}}^2 + \text{Cos}\theta_{z_{new}}^2 \right]^{\frac{1}{2}} \quad (2.28)$$

giving normalised direction cosines

$$\cos\theta_{x_N} = \frac{\cos\theta_{x_{new}}}{|\mathbf{n}_{new}|}, \quad \cos\theta_{y_N} = \frac{\cos\theta_{y_{new}}}{|\mathbf{n}_{new}|} \quad \text{and} \quad \cos\theta_{z_N} = \frac{\cos\theta_{z_{new}}}{|\mathbf{n}_{new}|} \quad (2.29)$$

The new unit vector at the end of each time-step is now

$$\mathbf{n}_{new} = \text{Cos}\theta_{x_N} \mathbf{i} + \text{Cos}\theta_{y_N} \mathbf{j} + \text{Cos}\theta_{z_N} \mathbf{k} \quad (2.30)$$

and the new relative position vector for an element sphere  $s$  is given by

$$\mathbf{d}_{ps_{new}} = |\mathbf{d}_{ps}| \mathbf{n}_{new} \quad (2.31)$$

The global position vector of sphere  $s$  is then updated using (2.31)

$$\mathbf{r}_{ps_{new}} = \mathbf{r}_{p(G)} + \mathbf{d}_{ps_{new}} \quad (2.32)$$

The algorithm applies to each element sphere in a particle that may contain any number of spheres. The calculation cycle for a particle over the current time-step is completed through updating the position and velocity of all element spheres. As the magnitude of the relative position vectors between the centre of element spheres and the particle centroid are fixed (i.e.  $|\mathbf{d}_{ps}|$  is constant) and the direction of these vectors are updated from the direction of the unit vector  $\mathbf{n}_{new}$  the geometry of the particles remains fixed when the orientation of the particle is changed.

Although the MSM algorithm has been developed for a typical model particle comprised of two identical overlapping spheres, since there is no theoretical limitation, the method can be used to generate a model particle of any number of element spheres of different sizes with or without overlap. A wide range of shape representations is

possible including ellipsoid, cylindrical, and irregular axi-symmetric examples of which are given in Fig.2.7.

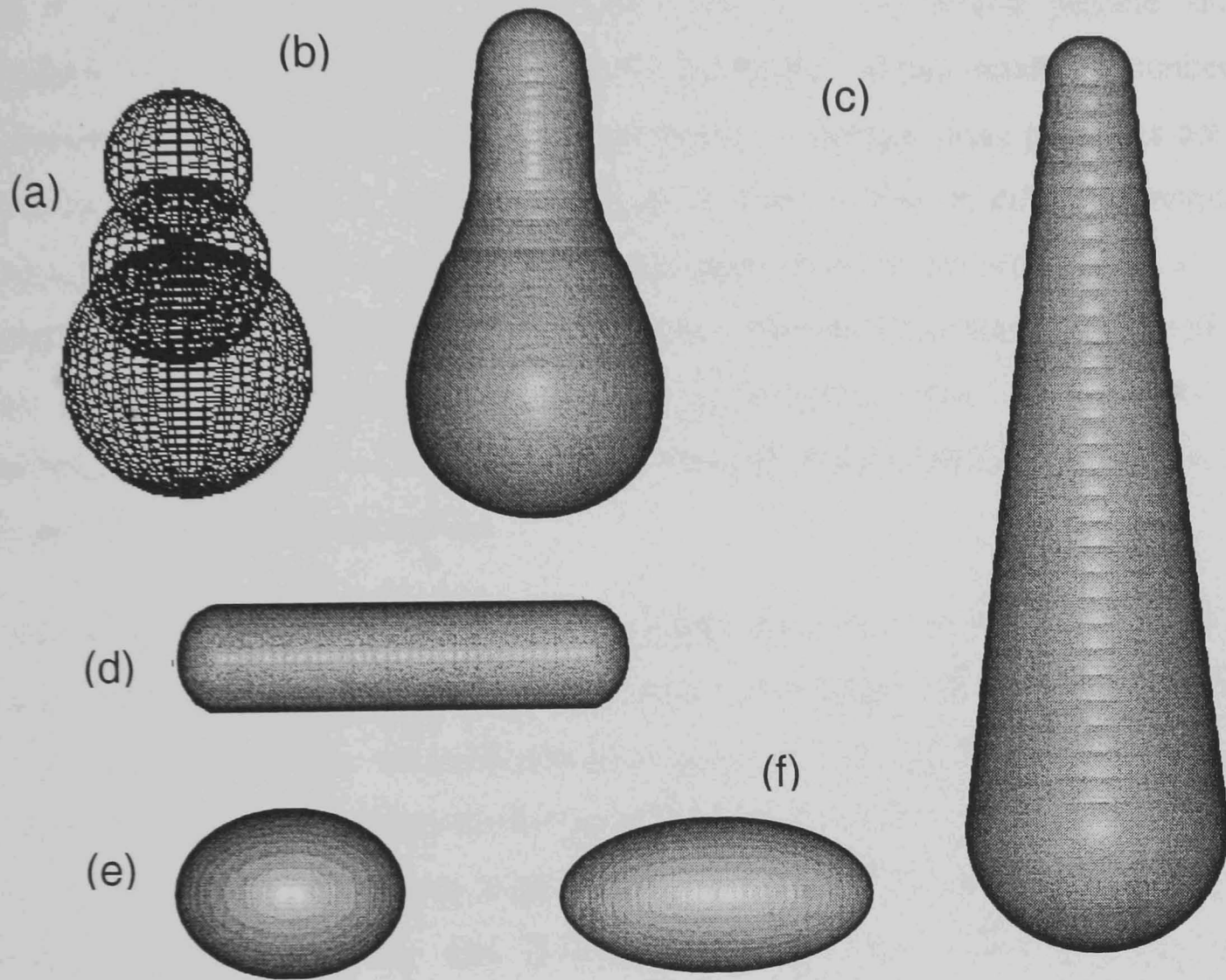


**Figure 2.7** Examples of multi-sphere, axi-symmetrical particle shapes (a) a typical model particle before rendering (3 element spheres), (b) irregular (12 element spheres), (c) tapered (30 element spheres), (d) cylindrical (20 element spheres), (e) 1.3:1 spheroid (18 element spheres) and (f) 2:1 spheroid (28 element spheres).

---

## 2.4. Implementation of the Multi-Sphere Method in a DEM code

Many factors can affect the overall configuration of a DEM computer program such as type of problem, number of dimensions (2-D or 3-D), model particle shape representation, etc. As reviewed in Chapter 1, during the last two decades a number of implementations of the DEM have been developed. Although these programs are all based on the principles of the DEM, they have been written in different computer languages and are usually appropriate for application to particular problem areas. For instance, CONBAL (developed by Ng and Dobry, 1990) used circular particles and has been designed for simulation of soil mechanics problems, while 3DEC (created by Cundall, 1988 and Hart *et al.*, 1988) used 3-D polyhedral particles to simulate the dynamic behaviour of rock and ice.

In this study, to avoid the replication of previous researches, as its starting point, an existing program based on a DEM code which was originally developed by Cundall (1971), has been chosen. The selected program known as CONBAL was developed for modelling granular systems of circular and spherical particles (2 and 3 dimensions) enclosed by virtual walls known as periodic space. It has also been modified by other researchers (Ng, 1989; Ng and Dobry, 1990, and Raji, 1999) for their own applications.

In this section, a short view of the selected program is first given with an emphasis on the main structure of the program and its subroutines. Modification of the program based on the theory proposed in the previous sections is then discussed. Finally, a number of simulation examples are presented employing the program based upon the multi-sphere approach.

### 2.4.1. Structure of the existing program

#### 2.4.1.1. Program development

Program CONBAL is a combination of two programs, TRUBAL first developed by Cundall and Struck (1979) which was a revised version of BALL (1971) and

---

CONTACT written by Ng and Dobry (1990). TRUBAL uses some standard techniques such as grid masking to determine the neighbouring particles, link-list data to store the information about neighbours and also DEM calculation cycles. In TRUBAL an arbitrary linear contact stiffness is specified to determine the contact forces due to particle overlap at contact points. Ng and Dobry (1990) attached the program CONTACT to TRUBAL as a subroutine and renamed the new combined program, CONBAL. This improvement gave the non-linear force-deformation at the inter-particle contacts using the complete Mindlin's solution. Although, this program has been originally employed to simulate the behaviour of granular soil in 2-D, it has been later extended to 3-D and renamed CONBAL-3. The concept of periodic space has been used to eliminate the effect of walls on the model of soil sample. This could provide the simulation of soil system made up of a very large number of particles by choosing a sub domain of this continuous system with a virtual boundary. The Program CONBAL uses a global damping mechanism to dissipate energy through the simulation. An additional characteristic of the program is prohibition of particle rotation despite the spherical particle shape.

#### **2.4.1.2. Program components**

The code consists of the main program and more than 30 subroutines and functions written in FORTRAN 77. The subprograms can be categorised according to their tasks as follows:

*1) Subprograms that manage and organise the overall program configuration.* This group of subprograms is used to perform the DE program configuration. They are SET UP, NEXT, MATCH, TIDY, SAVE, GETFN, RECIO, VAR, IVAR, and RVAR. This group of subroutines has various functions including initialising variables, constants, specifying material properties, interpreting input command lines from input file, and declaration of any probable error during execution. Since this group carries out basic functions regardless of the application, they have been retained in the modified program. However, some improvements have been needed such as deleting unused variables and adding some new variables and arrays.

---

2) *Data input-output routines.* This group of subprograms: a) facilitate data entry such as strain rate and applied stress and b) print out the output data and results from program during the program execution. In a flow application no external load or strain is applied to the particulate assembly so, the subroutines which are used for this purpose were no longer needed and have been removed from the original program. The deleted subroutines include RUNSRV and SETSERV. The subprograms used for displaying the results have been retained may need modification according to a specific application. This group includes; PRINT, PUT, OUT, APOLT and CONDAT.

3) *Main subprograms:* These are utilised for basic DEM tasks during simulations such as:

a) Random generation of particles within periodic space.

b) Reboxing of particles and search for neighbouring particles along with contact detection between them.

c) Calculation cycles such as computation of contact forces at contact points and updating the acceleration, velocity and displacement of particles. This group of subprograms includes: GEN, TURBRAN, REBOX, BBTEST, UPDATE, CYCLE, FORD and COMP.

In subroutine COMP (CONTACT) the tangential stiffness ( $k_t$ ) is calculated according to the complete Mindlin's solution, where the non-linear response depends on the load history of the normal and tangential forces for elasto-plastic materials ( Mindlin and Deresiewicz, 1953 and Dobry *et al.*, 1991). However, further study by the authors of the CONBAL program (Ng and Dobry 1992) showed that there was no significant difference between the simulation results using this approach and the simplified linear approximation of Mindlins' solution. Accordingly, they recommended that the simplified solution is suitable for most engineering problems. As a result, subroutine COMP that spends much more time in comparison with a linear solution has been replaced with the linear pressure dependence approach, which is still based on the Mindlin's solution.

The subroutines GEN and TURBRAN have been used for particle generation. In these routines, the particles are created randomly, initially without any contact in the

---

periodic space, then by applying a suitable strain rate, the particles are consolidated to achieve a desired porosity for the assembly. This method of particle generation was suitable only for spherical particles and could not be used for multi-sphere particles which are non-spherical. These subprograms are not appropriate for the application of multi-sphere approach and have been replaced with a new particle generation algorithm, which also creates actual walls for the workspace. Fig. 2.8 shows the main configuration of the original program.

Along with these three main groups of subprograms, the main program contains an input file and two INCLUDE files. In INCLUDE files (MATCOM and BALCOM, Appendix C) all the arrays are defined and their dimensions specified. The input file contains the particles' material parameters and some operative commands for a certain simulation. For instance, the dimension of the workspace, physical properties of material such as density, coefficient of inter-particle friction and global damping coefficient, and the number of calculation cycles which are needed can be defined through this file (Appendix D). Each line of the input file is a command, which starts with a keyword followed by a list of parameters. The program can only recognise the first three letters of the keyword. A space or comma separates the parameters of each command line from others. This kind of operative command presentation provides an efficient and flexible method for handling different problems without revising the main program.

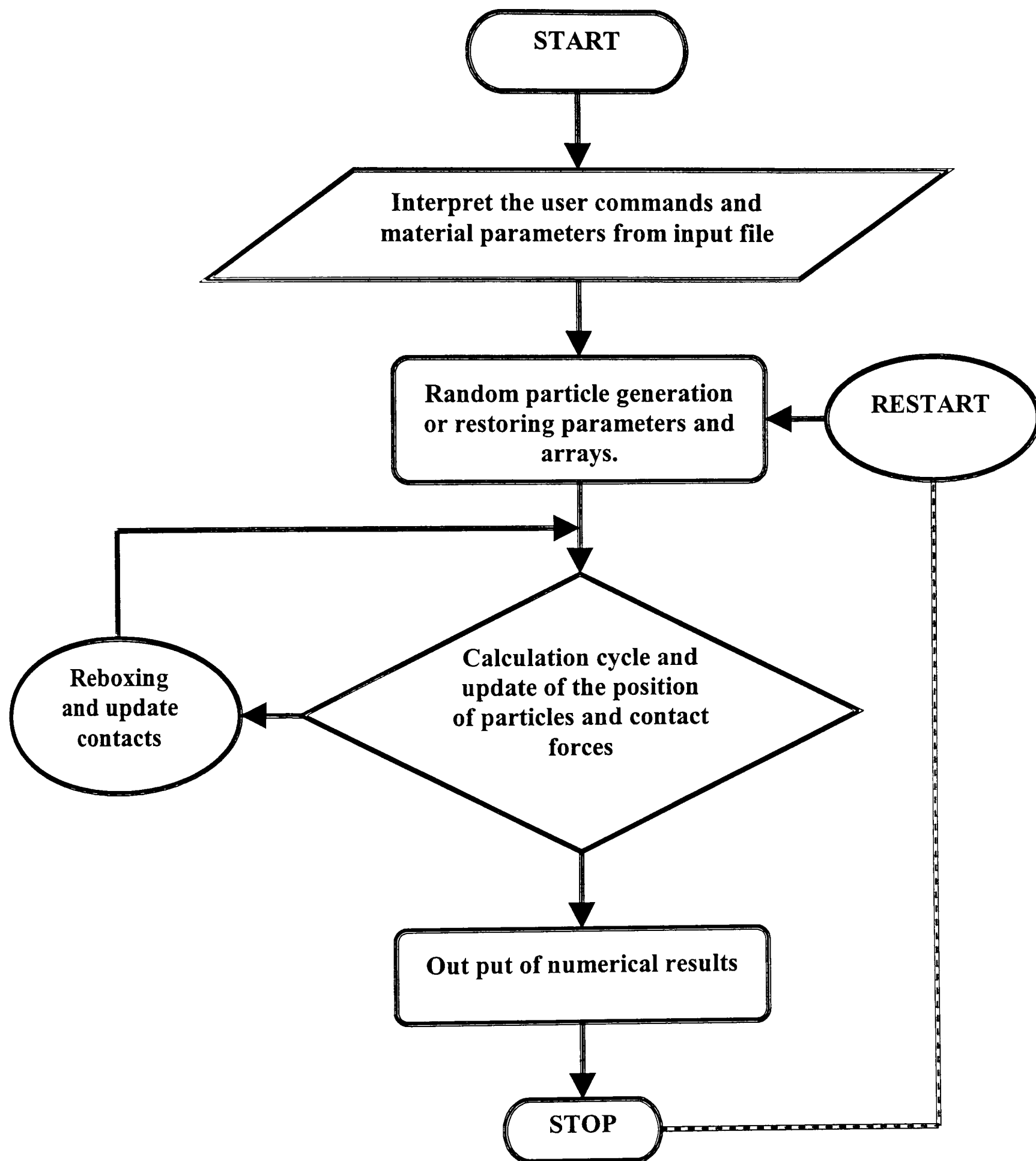


**Figure 2.8** The main configuration of the original program (CONBAL)

---

## 2.5. Modification of the original program

Although the multi-sphere method is mainly based on the principles of sphere-to-sphere contact (which was used in the original program), the element spheres in the system are not independent objects. Only the exposed section of each element sphere is used for contact detection between two neighbouring model particles. The contact forces acting on element spheres is transferred to the centroid of the model particles to update their dynamic situation. These characteristics of the multi-sphere method require the addition of some new arrays and calculations to the existing code including particle generation, contact search and calculation cycle for force transformation to the particle centroid. These modifications included:

- i)* Changing the particle creation procedure; axi-symmetrical model particles (composed of several spheres) have been generated with an original random orientation rather than simple spherical particles.
- ii)* Changing program set-up from simulation of compression loading of particulate assemblies to gravity movement of particles. This has been carried out by means of some actual planar walls for the workspace rather than the virtual walls (periodic space) of the original program, including particle-wall as well as particle-particle contact detection algorithms.
- iii)* A new calculation cycle for irregular shape particles including taking into account the particle rotation by calculating the moment of contact forces and transformation of contact forces from the surface of element spheres to the centroid of particle.
- iv)* Incorporation of contact damping as well as global damping as an alternative energy dissipation mechanism (most appropriate for modelling visco-elastic materials).

The language of the program has been changed from FORTRAN 77 to FORTRAN 90 to make use of more features available in this version.

The functions performed by each of the subroutines in the modified programme are presented in Appendix B.

### 2.5.1. Set up of the simulated system (workspace and particle numbers)

In the modified code a simulated system can be set up through a single command at the beginning of the input file. The command starts with keyword **STArt** (Appendix D) followed by a number of parameters including: *xdim*, *ydim*, *zdim*, *nballm*, *nbox*, *npar*, *ntype* and *nwall*. The first three parameters are the maximum length of numerical workspace in x, y and z directions. The fourth parameter is the maximum number of elements which include spheres and walls to be generated. The last four parameters are the number of virtual sub-boxes in the workspace for contact search purposes; maximum number of model particles (multi-sphere); number of element spheres per model particle and maximum number of walls in the system respectively. Since, altering the number of particles and the number of element spheres per particle requires the new arrangement for the dimension of arrays; it was necessary to modify the *INCLUDE* file *BALCOM* accordingly. The dimension of arrays is updated automatically if the new information is entered in this file correctly.

### 2.5.2. Particle generation

In the original program the subroutine *GEN* creates spherical particles in a periodic space. Particle generation is through a command line in the input file which starts with the keyword **GEN**. The first particle created is positioned at the centre of periodic space and the rest of particles are placed randomly. This method is only suitable for spherical particles.

In the modified program the generation algorithm has been changed such that the non-spherical particles can be created instead of simple spherical particles. In this procedure particle generation is performed through a set of command lines (equal to the number of element sphere per particle) **RADius**, *radius*, *ntype* specifying the radius of an element sphere and its type number (Appendix D). Having determined the radius of element spheres comprising a model particle, another command line is used to determine the distances between the centroid of the model particle and the centres of its element spheres. This command contains the keyword **PROduce**, followed by some parameters, *fix1*, *fix2*, ..., *fixn*, each specifying the distance between the centre of

an element sphere and particle centroid, where  $n$  is the number of element spheres per model particle.

Specifying the global co-ordinates of the first-particle centroid starts the particle generation. Conventionally, the first particle is placed at the bottom left hand corner of the workspace; however the user can specify any initial position for the first particle for a particular purpose. The next particle position is determined according to the maximum diameter of the particle i.e. the distance between two neighbouring particles equals to the biggest dimension of the model particles plus a tolerance specified by the user. This means at this stage particles are generated without any contact side by side in the X-Y plane (each model particle occupies a spherical volume of workspace equals to the maximum model particle length). The next layer of particles in the X-Y plane is determined by moving upwards in the Z direction by an amount equal to the largest diameter of the model particles. Model particles can be created uniformly in the whole of workspace or deposited in a particular spatial domain to set up a specific particle bed. This can be carried out by altering the position of the first particle and the number of rows of particles in x, y and z direction of the workspace. Having determined the position of a model particle, its original orientation (the orientation of the longitudinal axis of an axi-symmetrical particle) is selected in a random manner. FORTRAN random number generator is used to create the particles with random orientations. The direction of the longitudinal axis of an axi-symmetrical particle can be specified randomly by random selection of the direction cosines of its unit vector ( $\text{COS}(\theta_x)$ ,  $\text{COS}(\theta_y)$ ,  $\text{COS}(\theta_z)$ ). Two random numbers between  $-1$  and  $1$  are selected as  $\text{COS}(\theta_x)$  and  $\text{COS}(\theta_y)$ .

The third direction cosine of the unit vector is then calculated as

$$\text{COS}(\theta_z) = (1 - [\text{COS}^2(\theta_x) + \text{COS}^2(\theta_y)])^{0.5} \quad (2.33)$$

Once the direction of the longitudinal axis of the current model particle is determined the positions of its element spheres are specified and then mapped into the boxes they occupy (Figure 2.9). All element spheres of a certain particle are given an address number according to the particle's number which is created i.e. all element sphere of a particle have an identical address number called NADELM. The address number can

be used in the process of contact search to ignore the contact between two neighbouring spheres of the same particle.

If the predetermined workspace is not sufficient for generating all particles, an error message occurs and the program is terminated. The dimension of the workspace needs to be increased or the number of particles must be decreased.

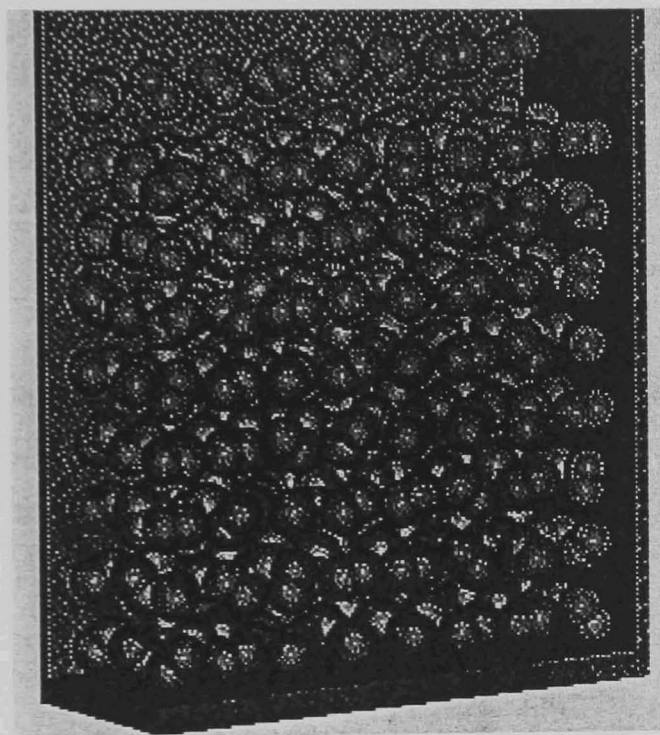


**Figure 2.9** Generation of 200 randomly oriented multi-sphere particles each consisting of two element spheres.

### 2.5.3. Generation of workspace (walls)

As the original program used periodic space, there was no algorithm for wall generation. However, for most processing operation systems such as handling, filling and flowing from a container the system is confined within actual walls and the interaction between the particles and the walls can affect the overall behaviour of the particles within the system. Therefore, an algorithm has been developed in the modified program to create and recognise walls to simulate the interaction between the particles and walls.

In the new code the creation of walls is started when all of particles have been generated. The number of walls in the simulation is selected through the command `STArt` with parameter `nwall`. This can be either 5 or 10 walls. The 5-walls option is used if simulation of particle packing is of interest. In this option five planar walls are generated which are coincident with the dimensions of workspace; including four vertical side walls and a horizontal wall for the bottom of the workspace.

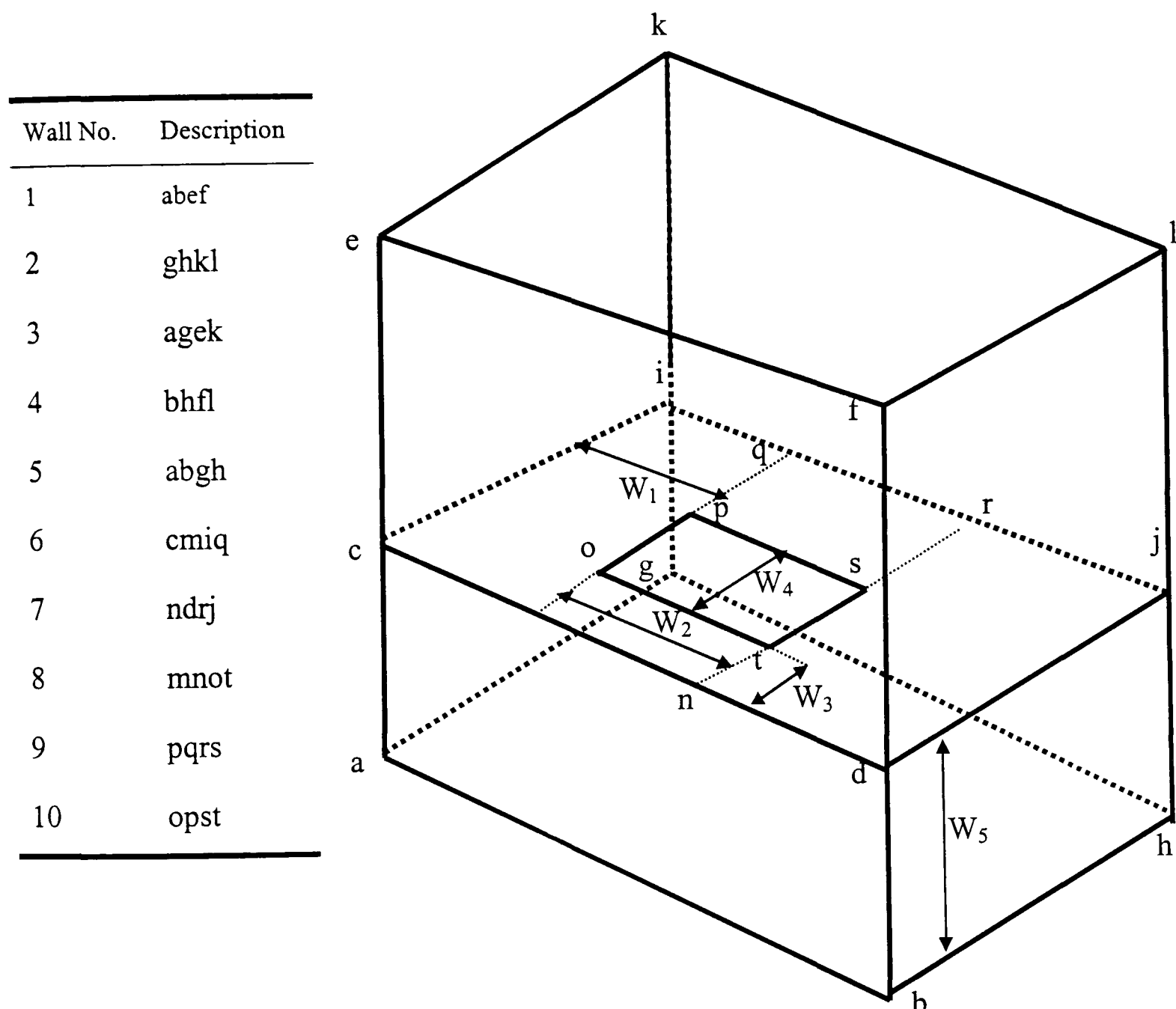


Figure 2.10 Basic wall arrangement for the simulation workspace. The numbers represent the walls.

If in addition to packing of particles, flow and handling of particles is desired, the user can select the 10-walls option. In this option, instead of five walls, ten walls are generated. The additional five walls are used for creation of the bottom of the upper box (middle wall) and an orifice through which particles can flow from the upper box

---

to the bottom of workspace box. In this case the upper box is created at an optional height from the bottom of the workspace. This is specified by command **BOTtom**,  $w_1$   $w_2$   $w_3$   $w_4$   $w_5$ , where  $w_1$ ,  $w_2$ ,  $w_3$ ,  $w_4$  and  $w_5$  are a series of dimensions which define the dimensions of the middle wall partitions and the size of orifice. In this option particle generation is started from the bottom of the upper box.

The arrangement for creation of the upper box and the orifice is show in Figure 2.10. The middle wall is partitioned into five walls such that the wall at the middle can act as the orifice. Fig 2.11 shows the flow chart of the modified sphere, particle and wall generation procedure.

Bulk particle dynamic phenomena such as flowing, conveying, dropping and singulating can be numerically simulated by altering the parameters in the command **BOTtom**. Some of these examples are shown in figures 2.17 to 2.22.

A conveyor can be constructed by specifying a linear velocity or acceleration in any direction through the command line **MOVE**, *velwall*. Where *velwall* is the selected velocity of a chosen wall in any desired direction. An inclined wall also can be generated for side walls using **CONfig** Command. In this command the position and the orientation of the side-walls are specified

#### 2.5.4. Consolidation (deposition) of model particles

In the particle generation procedure described in the previous section, particles are generated in the workspace with no inter-particle contact which results in a very loosely packed particle assembly. To consolidate the particles and represent a real particulate assembly in which the particles are in contact with each other, a packing procedure is carried out to reduce the porosity of the generated assembly. In the original program because the particles were massless, this process has been carried out by applying a suitable strain rate to compact the particles. In the modified program, as the weight of particles is significant and actual walls confine the particles, the particle's body force (gravitational force) is used to consolidate the particles.

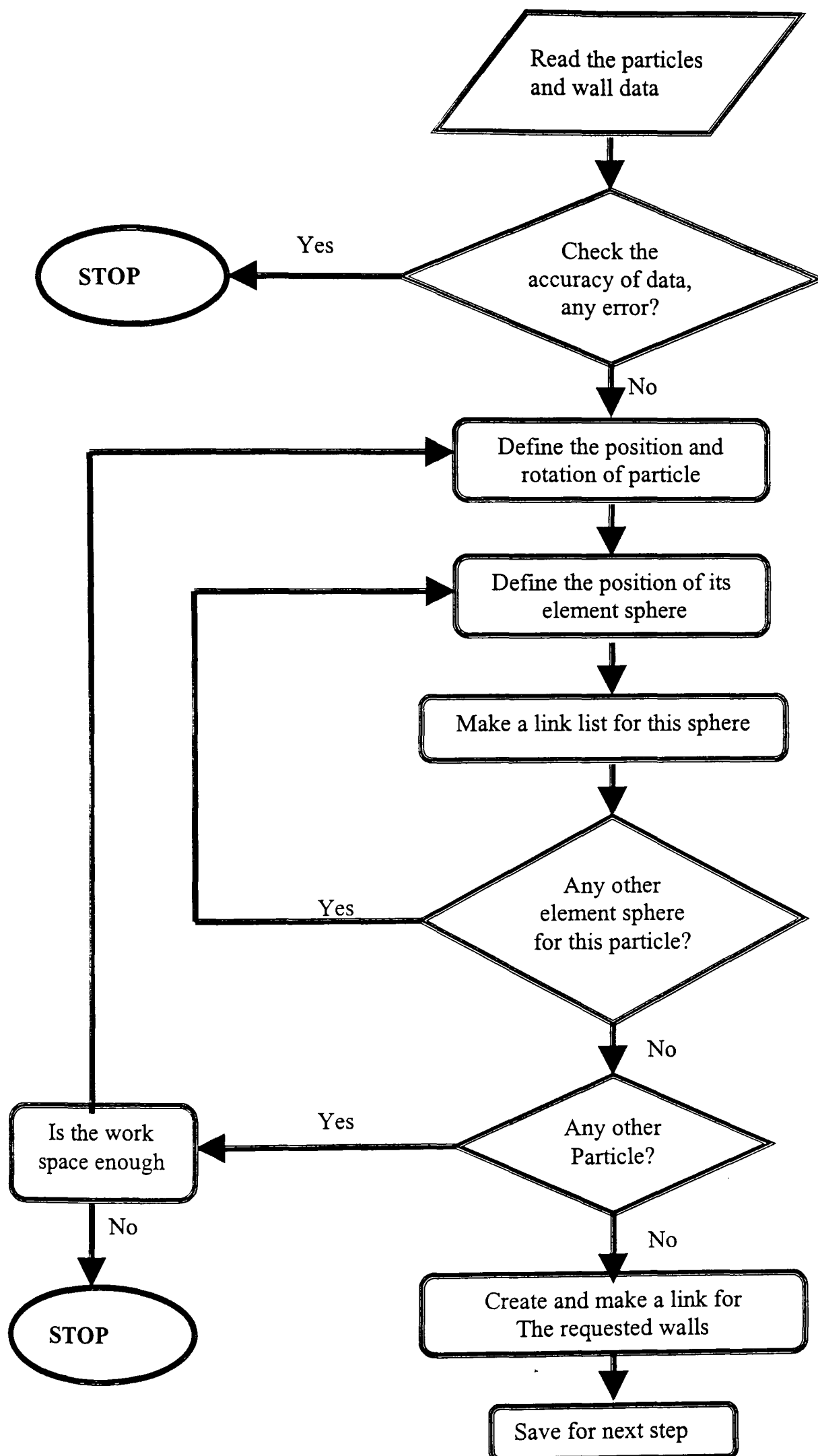
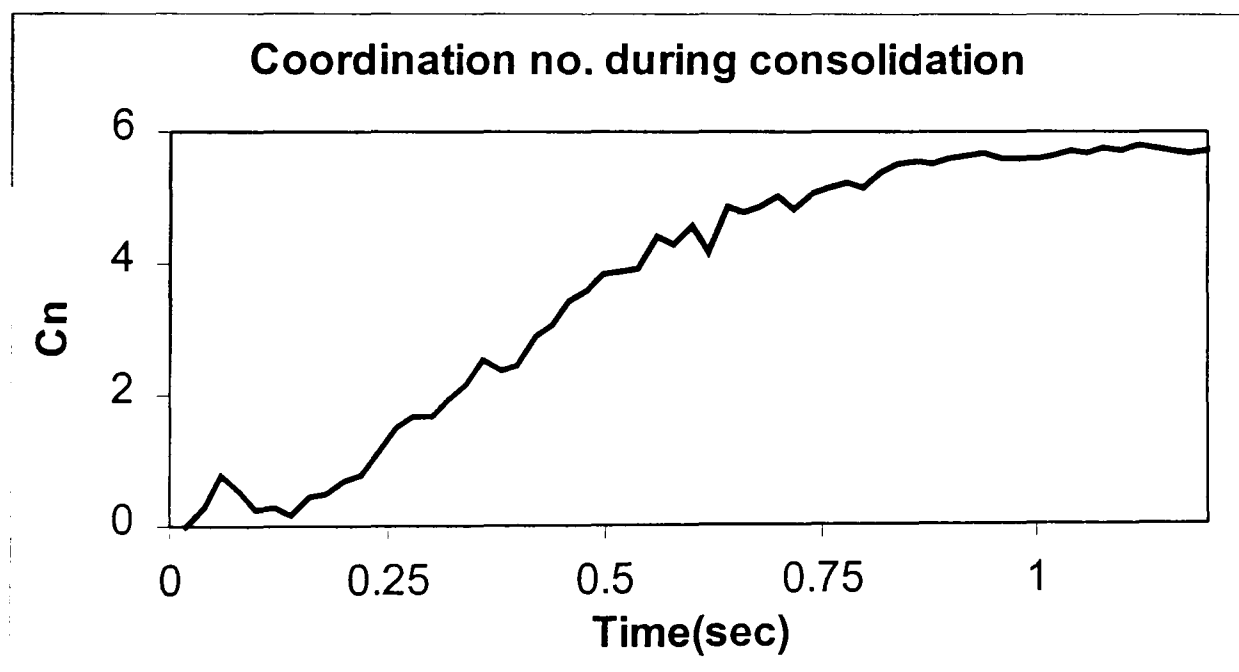


Figure 2.11 Modified particle, sphere and wall generation algorithm.

In this method, particles are simultaneously subjected to gravitational force, acting in the negative direction of Z-axis which pulls them towards the bottom of the upper box or workspace. It should be mentioned that although the particles are put in the box sequentially, the consolidation step is a non-sequential process, because the movement of particles affects the trajectories of other particles. Therefore, the particles at the end of consolidation process will be placed in a random manner with wide variety of void shape and size. This process can be speeded up if the contact damping is selected relatively high and the inter-particle friction very low.

The simulation is continued until a relatively stable condition for the assembly is obtained. The consolidation can be terminated if the porosity and/or co-ordination number ( $C_n$ ) remain almost constant (Fig. 2.12). Three examples of deposition of multi-sphere particles of different shapes in a box under a gravity field are shown in Fig 2.13.



**Figure 2.12** Evolution of number of contact points per particle (coordination number,  $C_n$ ) during consolidation process for an assembly of 200 particles each comprised of 2 element spheres.

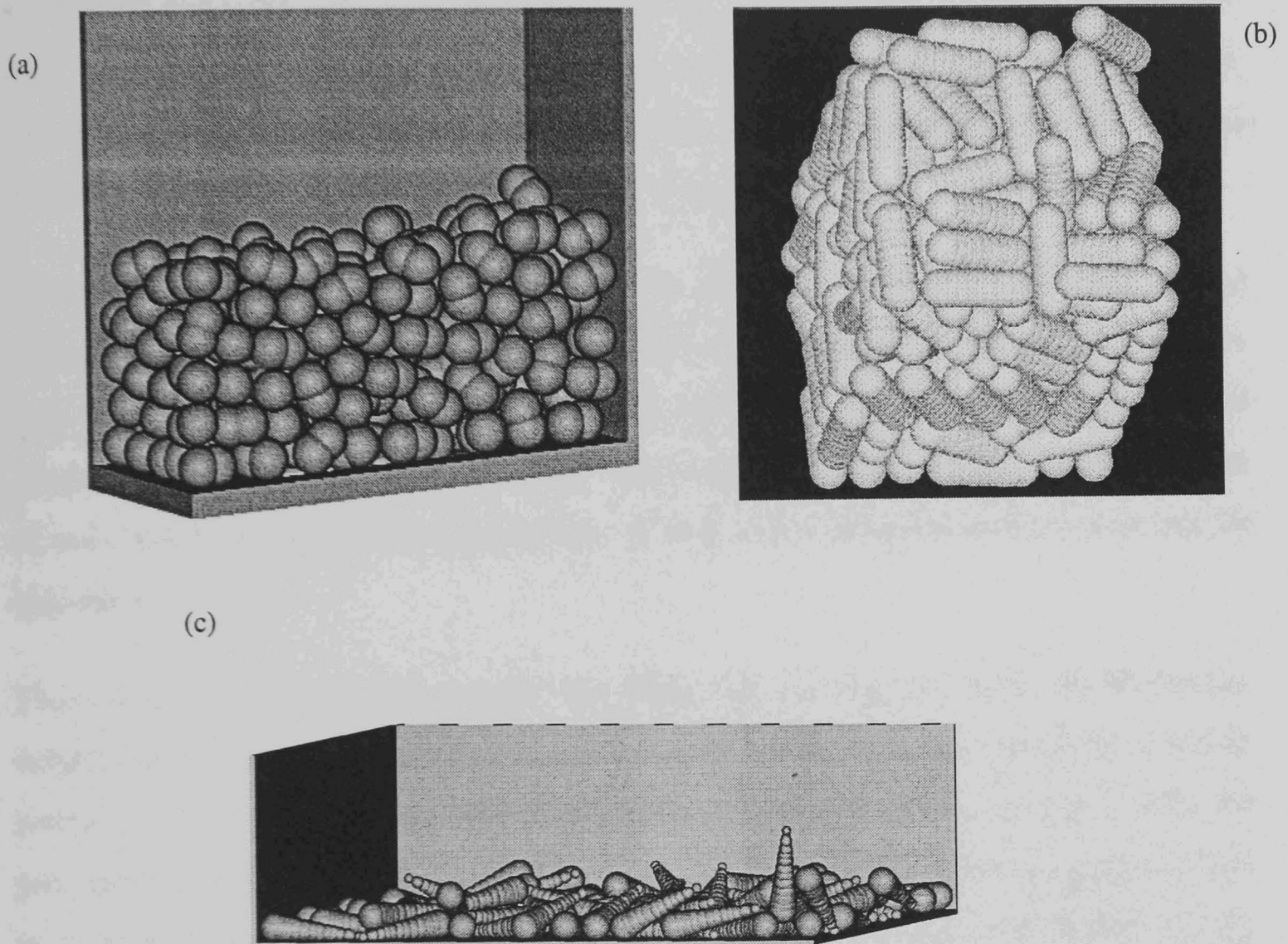


**Figure 2.13** Multi-sphere particle assemblies after random generation and deposition under a gravity field; (a) 200 two-element particles, (b) 200 nine-element cylindrical particles, and (c) 100 twelve-element tapered particles.

### 2.5.5. Contact search and detection

One of the most important features of a DEM program is the contact search and detection function. The contact search algorithm in the original program is carried out through four subroutines: REBOX, SEARCH, BBTEST, and UPDATE. The cubic workspace is divided up into a series of cubic cells in such a way that the dimension of each cell should be greater than or equal to the diameter of the largest sphere. However, in the modified program the workspace may not necessarily be cubic and the workspace can have any size in the direction of global axes.

After positioning a sphere or a wall in the generation process (and also during calculation cycle to update the dynamic situation of particles), it is mapped into the cells which it occupies. The mapping step is carried out according to its position and diameter in the direction of global axes. Having done this, the origin, and the number of cells which are occupied by the sphere or wall in the direction of three axes can be calculated.

Those spheres or walls that occupy the same cell (virtual sub box) are immediate neighbours and possibly can form a contact therefore, they are registered for checking contact (linked list method). In the modified program during contact search the program can recognise the spheres of the same particle, so the contact is ignored if this is a contact between two spheres of the same particle. As mentioned earlier, during particle generation each sphere is allocated with a *sphere address number* (NADELM). At the beginning of contact detection between two immediate neighbouring spheres in the link list, their NADELM are compared with each other, if they are the same it means they are from the same particle, thus, this contact is ignored. The walls are treated as sphere with infinite radius but are recognised as wall by allocating the *sphere address number* equal to zero (NADELM=0). Therefore, the program can discriminate spheres from walls and conducts sphere-sphere or wall-sphere contact detection route or ignore a contact between two walls or two spheres of the same particle. Figure 2.14 shows the flowchart of modified program to recognise the sphere of the same particle and discriminates the spheres from walls.

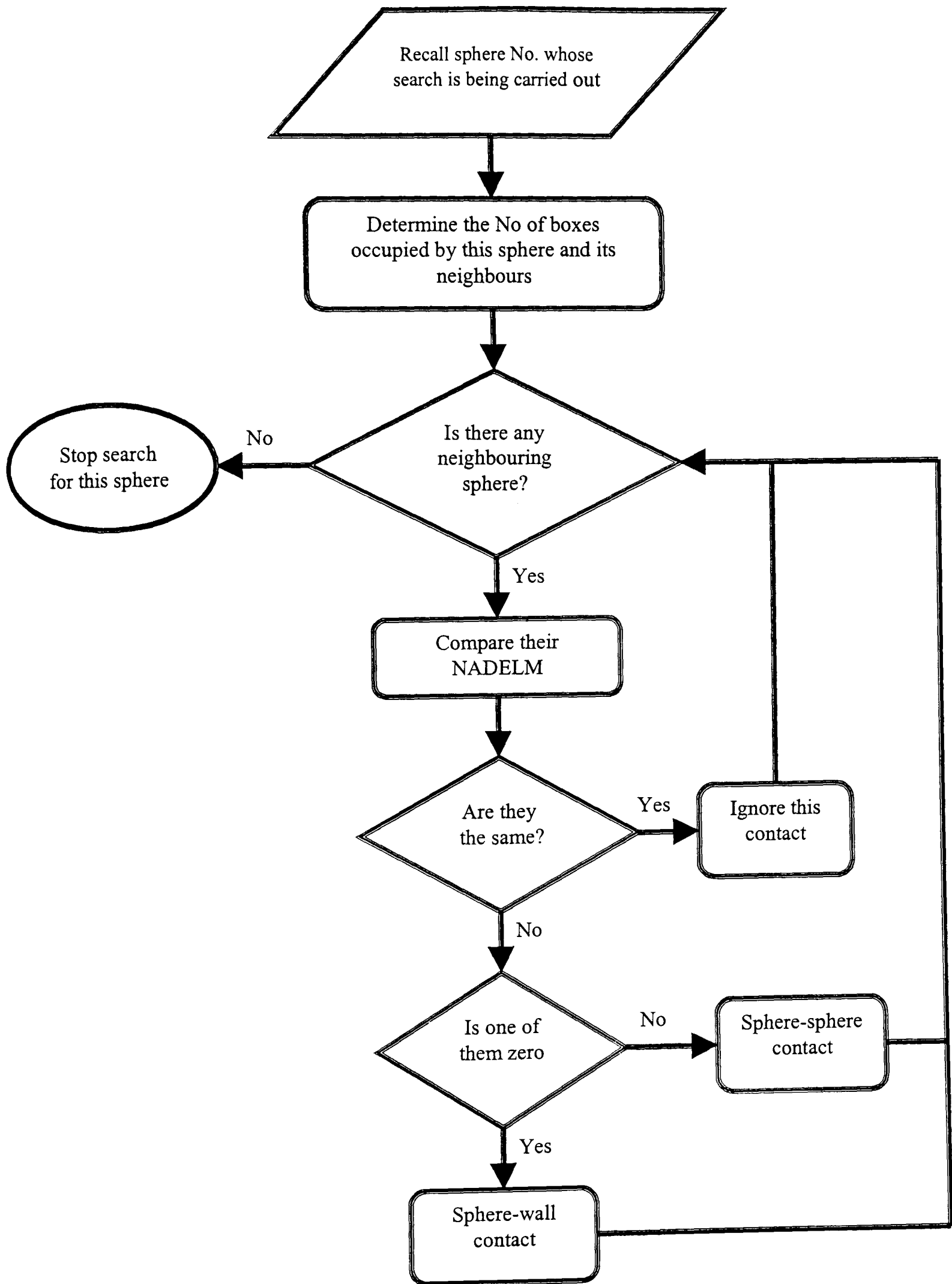


**Figure 2.14** Contact search and detection between particle-particle and particle-wall in the modified program by recognising spheres of the same particle and discriminating walls from spheres.

---

In each time step prior to the contact search process, the stability of the program is checked for the sphere whose search is being carried out. According to the current time step ( $\Delta t$ ) and the sphere velocity, the maximum displacement of the sphere is calculated. If the sphere can move more than a tolerance (usually equal to the diameter of its immediate neighbour) the program is unstable and will be terminated. The magnitude of the time step may also affect the calculated behaviour of a particle due to effects which are explored in sections 3.2 and 3.3. In addition as noted by Raji (1999), the criterion for choosing the time step in a DE simulation may require consideration of dynamic conditions within a particulate assembly. For example, if compressive stresses are very high then a particle may escape from an assembly with a very high velocity which may cause excessive inter-penetration in the next time step. This problem is also relevant to non-spherical particles subjected to a large instantaneous rotational acceleration. Given that the linear acceleration of any point on the particle is a positive function of its distance from the particle centroid, then it may be the case that parts of very elongated particles will accelerate excessively over a time step which could result in extreme overlap. This problem is not usually addressed in DE model formulation but must be taken into consideration depending on the application.

Once a contact is detected the required information about that contact such as the name of contacting spheres and the direction of contact force is stored in the memory block. Whenever a contact is broken its memory space no longer needed and will be added to the available memory block to be used for a new contact; this saves the computer space and time.

### **2.5.6. Calculation cycle**

The calculations for updating the dynamic situation of particles such as acceleration and velocity are carried out in three subroutines, INITP, CYCLE and FORD. As in the original program the individual spheres are considered in the calculation therefore, these calculations needed to be modified to accommodate the multi-sphere approach. This included, linking between particles and their element spheres, transfer of forces and moments from element spheres to the particle centroid. Having made these modifications, it was necessary to add some new arrays for particle acceleration,

---

velocity and displacement in addition to arrays for spheres in the original program. The following statements summarises the modifications carried out in calculation cycle:

- (i) Prior to the calculation loop, depending on the model particle configuration (number of element sphere, their relative positions within the particle and amount of overlap between them) and the particle material density, the mass of particle is calculated in subroutine INITP.
- (ii) The time step ( $\Delta t$ ) is calculated according to Ning's procedure (Ning and Ghadiri, 1994) using equation (1.31) in which the time step is calculated based on the Rayleigh wave propagation velocity. As mentioned in Chapter 1 in this solution the critical time step is based on the minimum size of sphere in the assembly and mechanical properties of the material (Compressive Modulus of Elasticity). In this solution the modulus of elasticity of particle material plays a key role, as material become stiffer (higher  $E$ ) the calculated time step becomes smaller and independent of coefficient of stiffness ( $k$ ). Therefore, in spite of changing the stiffness coefficient ( $k$ ) during simulation the time step remains constant.
- iii) The calculation cycle starts with updating the velocity and displacement of particles according to their out-of-balance force and moment. The original program did not take into account the rotation of particle. Therefore, in the modified program the procedure presented in section 2.3 has been coded to calculate the rotation of the particles. The position of their spheres is updated according to both linear and rotational velocity of particles.
- vi) According to the new position and velocity of spheres the normal and tangential forces between contacting spheres are calculated. Based on the Hertz theory the normal spring contact force between two spheres (or sphere and wall) is calculated using equations 1.8-1.10. The tangential stiffness ( $k_t$ ) is calculated using equation (1.14) based on simplified Mindlin solution which is termed *Linear pressure dependent* (Ng and Dobry, 1994). In the original program contact damping forces have not been included; this type of energy dissipation has also been added to the program which is most appropriate for

---

modelling visco-elastic materials such as agricultural produce. The damping ratio ( $\beta$ ) is calculated from the coefficient of restitution of the material using equation (1.22). This can be read from the input file command **DAMPing**. Knowing the damping ratio and the normal and tangential stiffness, the normal and tangential damping coefficients ( $C_n, C_t$ ) are determined using equations (1.23) and (1.24). The normal and tangential damping forces are calculated using these coefficients and added to the contact force. This procedure has been implemented in the modified program to calculate the contact force incorporating contact damping. The modified calculation cycle is shown schematically in Figure 2.15.

## 2.6. Post processing of the simulation results

The results of simulation can be extracted from DEM code at any stage of simulation. These results can be different from one application to another and most can not be obtained easily in a physical experiment. Examples of these are the velocity and position of any particle or sphere of interest; the evolution of contact force (magnitude and direction) between two spheres or particles and a wall etc. These data can be graphically presented using an appropriate package.

In 3-D simulation visualisation of the results is also important as it can be used for further quantitative analysis. Still or video animation of the particle assembly (or a particular particle) during the simulations have been produced using a suitable graphical package such as *Paint Shop Pro* and *GIF animator*. Attempts have been made to find a suitable computer package for creation of still pictures of particles in a 3-D system and video clips.

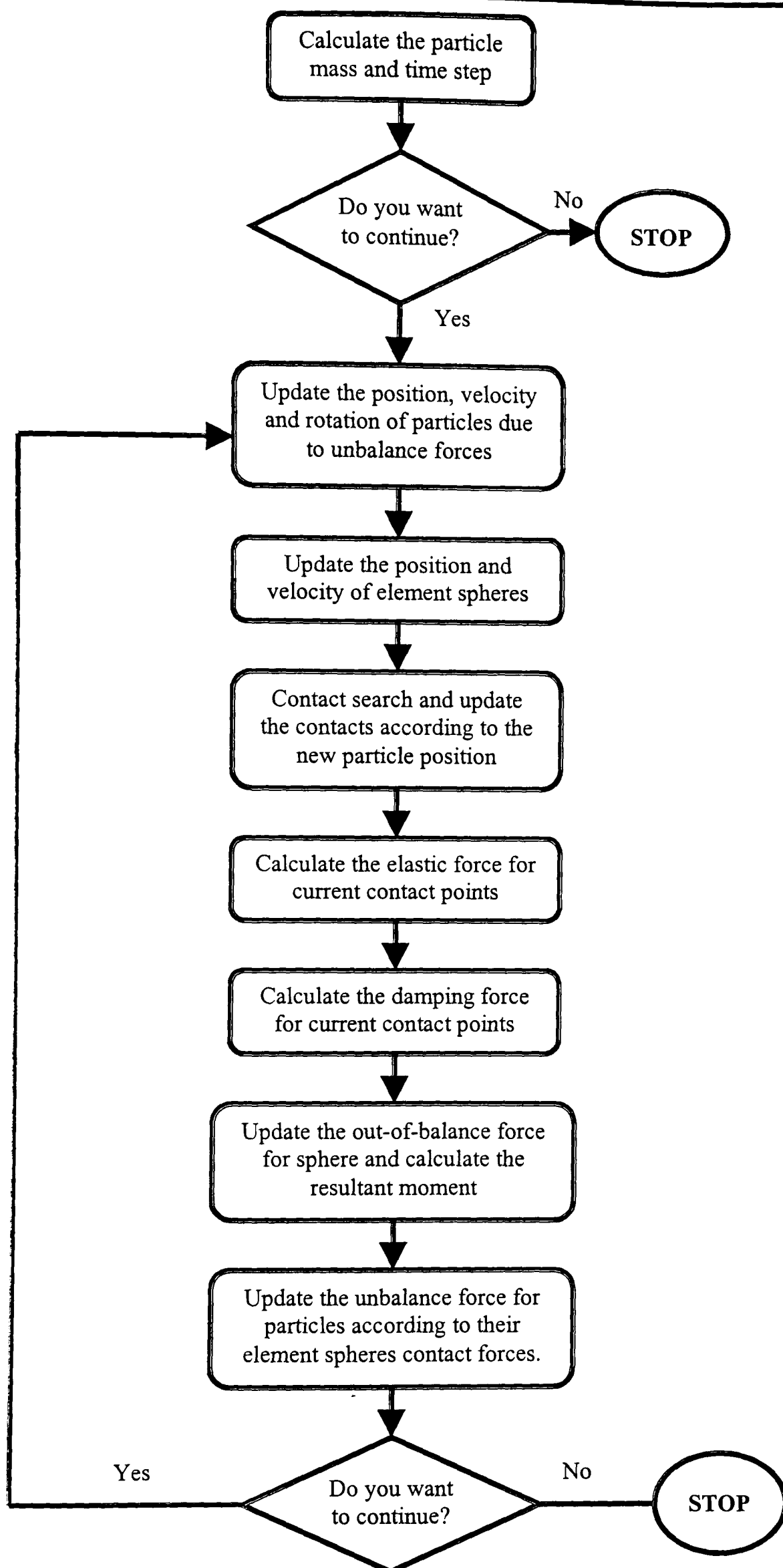


Figure 2.15 calculations cycle in the modified program.

---

### 2.6.1. AutoCAD

AutoCAD constructs three-dimensional polygonal mesh objects (such as sphere) that look like wire-frame objects but which have surfaces. The 3D objects can then be shaded or rendered to appear as solid objects. Since the model particles are comprised of some overlapping spheres, drawing their element spheres can visualise the whole of particle as unit objects (Figure 2.7a). The mesh objects are then rendered to look like solid particles (Figure 2.7 and 2.13a and c). The rendered objects can be saved as an image file in GIF or TIFF format to create the still pictures. Animations are created from stills which, have already provided from simulation results in a time sequence, using an appropriate animator package (Appendix F).

Script files have been provided to read the DEM output into AutoCAD automatically. However, it has been observed that when the number of spheres in the simulation was high (more than 200), it took a long time to draw a complete picture of particles assembly. In addition, the memory requirement for rendering such a drawing picture was higher than the RAM of available ordinary PCs. Due to this limitation of AutoCAD a more efficient package has been required for visualisation of a particle assembly comprised of thousands of particles.

### 2.6.2. POV Ray

A good replacement for AutoCAD in dealing with the visualisation of DE results has been found to be The *Persistence of Vision*<sup>™</sup> *Ray-Tracer (POV RAY)* package. This package creates three-dimensional, photo-realistic images using a rendering technique called *ray tracing*. The data for an image is read from a text file with a special language called *scene description language*. This file contains information describing the objects to be draw, light and camera position and viewpoint. The package produces high quality images with realistic reflections, shading, perspective and other effects very fast and efficient compare with AutoCAD. An image containing thousands of particles can be created much more quickly than with AutoCAD.

The text files are created directly in the DE code during simulation and then read in the POV RAY. The images created by the package are saved automatically as image files

in **BMP** format (Figures 2.22 and 2.24). Video clips are then created using an appropriate animator package. Figure 2.16 shows the post processing steps of simulation results.

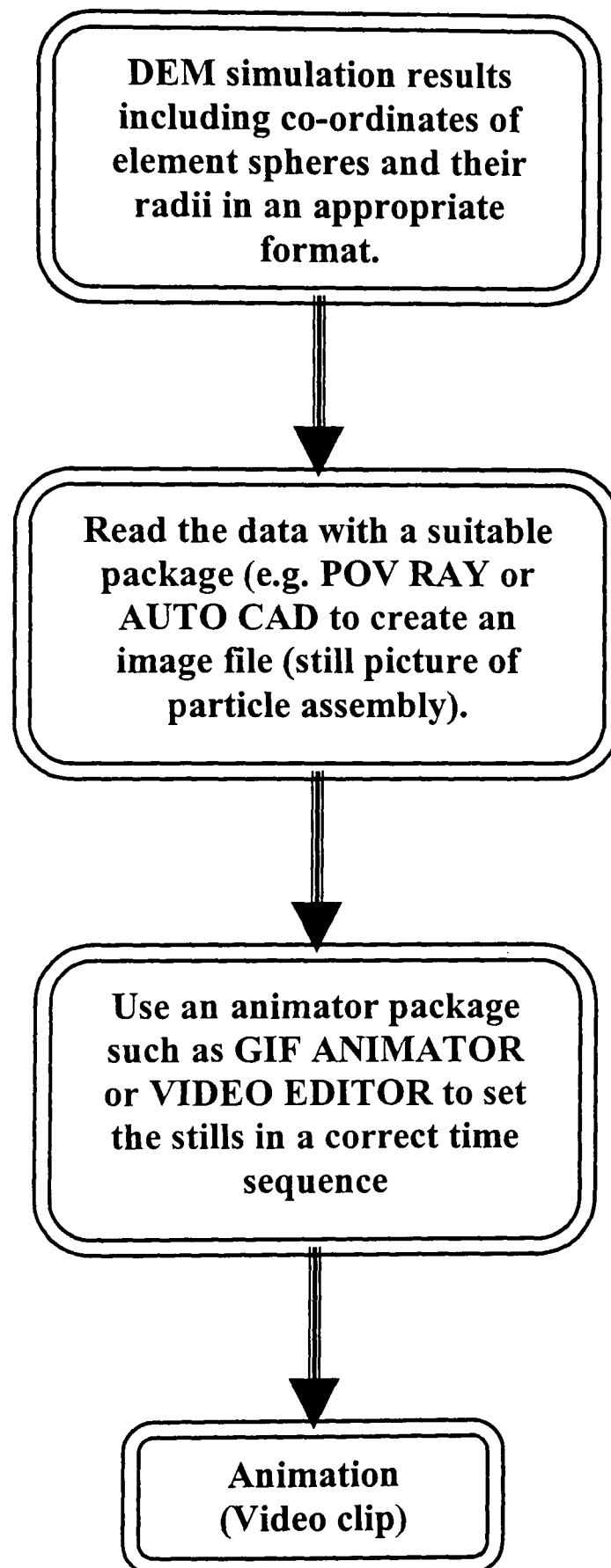


**Figure 2.16** Post-processing steps for DEM results visualisation.

## 2.7. Summary

A method of shape representation (MSM) for non-spherical axi-symmetrical particles (typical of most agricultural particulate materials) has been proposed. The algorithms required for calculation of the dynamics of particles based on the multi-sphere method have been developed. These calculations included contact forces and moment, transformation of forces and moments to the centroid of particles and updating of particle rotation.

Although the MSM appears similar to the clustering method presented by Jensen *et al.*, (1999), there are considerable differences between the two methods. A cluster is more like an agglomerate than a particle i.e. a cluster can break up and each element sphere can move independently. An apparent advantage of the clustering approach to the MSM is the capacity of a clustered particle to fragment (similar to the agglomerates presented by Ning, 1995). However, the assumptions made in applying cohesion forces between particles and the validity of the correlation between spheres (grain) size and real particle fracture is questionable unless proved experimentally. The advantage of a deformable, fracturing particle is offset by the computational overhead associated with contact detection between spheres in a cluster. The MSM does not require detection of contacts between element spheres. The degree of approximation to the surface topology is much higher using the MSM. The clustering method cannot represent an edge (only 2-D shapes have been represented to date) with a better approximation than, at a minimum, a semi-circular arc. This is the most primitive form of shape representation possible in the MSM.

The original program (CONBAL) used for simple spherical particles has been adapted to implement the multi-sphere approach. These modifications included

- \* A new method of particle creation has been proposed. In the modified program, axi-symmetrical particles comprised of some element sphere are constructed instead of simple spherical particles.
- \* Virtual walls of the periodic space in the original program have been replaced with actual walls in the form of a hopper with a bottom chamber. Actual walls

---

are required for flow simulations. The wall positions can be altered to enable simulation of conveyors by application of a velocity to the walls.

- \* Particle consolidation has been changed from a strain based to a self-weight method. After particle generation a gravitational field system is applied which is closer to the real process of assembly generation.
- \* Contact search has been changed such that in the new program, walls can be discriminated from spheres and also the contacts between the element spheres of the same particle are recognised from others and are ignored.
- \* Viscous contact damping has been incorporated as an alternative energy dissipation to global damping which is most appropriate for visco-elastic material such as agricultural materials.
- \* Visualization of the DEM results (stills and video clip) have also been presented using some graphical packages such as AutoCAD and POV RAY.

---

### **3. Analytical Validation and Parametric Studies on the DE Model using the Multi-Sphere Method**

#### **3.1. Introduction**

The accuracy of a method such as the DEM for prediction of the dynamic behaviour of a real material depends on two main factors concerning the accuracy of the physical model and the validity of the numerical assumption at two scales; (i) the inter-particle mechanics (Macro-scale), and (ii) the particle kinematics (Micro-scale). The effect of the former on the simulation results must be evaluated by comparison with the results of experiments on an assembly of real particles but the latter can be investigated analytically. In this chapter the logic of the kinematic model for multi-sphere particles is examined by comparing the predictions of the DE model using the Multi-Sphere Method (MSM) with the results of analytical calculations of the movement of particles in different situations.

The accuracy of the contact model and the method of force transformation for a multi-sphere model particle have been investigated using various scenarios. The scenarios included the weight of a static particle, collision of a particle with a surface, sliding of a particle along a surface, behaviour of a particle on a moving surface and particle rotation due to application of an external force. The effect of time step, damping coefficient and number of contact points between contacting bodies on the dynamic behaviour of the particles have been also investigated. All particles in these tests were axi-symmetrical and comprised of two to nine element spheres of the same diameter. The length of a model particle and the number of element spheres per particle were varied according to the purpose of the simulation.

#### **3.2 Weight of a particle in a quasi-static situation**

In the DEM a particle can not reach static equilibrium if it is subjected to gravitational acceleration. However, if the relevant parameters are set correctly, the contact force

between the particle and a surface calculated from relative velocity and position (after relative stability) should be close to the weight of the particle. In the following simulations the effect of time step and number of contact points per particle on the accuracy of calculated contact force between a particle and a flat surface has been investigated by comparison with the actual weight of the particle. In these simulations, a model particle comprised of two identical overlapping spheres has been generated. The particle has been then placed on a flat rigid surface in two different orientations, horizontally and vertically (Fig. 3.1). The difference between the two orientations is the number of contact points (one for vertical and two for horizontal orientation of the major axis).

Regardless of the physical properties of the particle and surface, the shape of the particle, and the orientation of the particle, according to Newtonian mechanics, the contact force between the particle and the surface should be equal to the weight of the particle when the particle is at rest (Fig. 3.1).

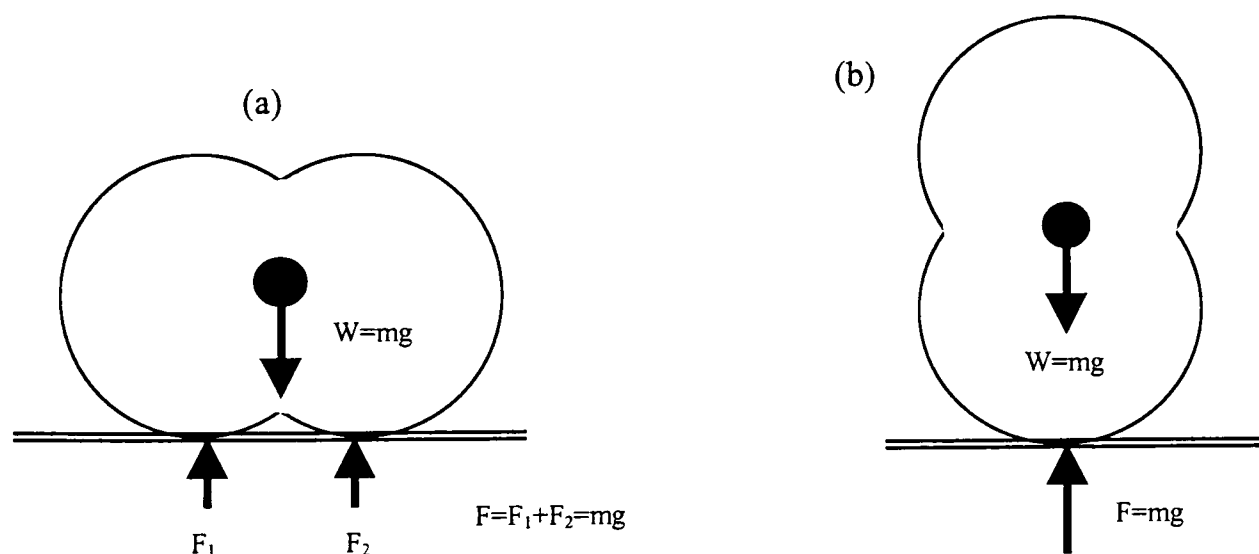


**Figure 3.1** Theoretical relationship between the weight of a particle ( $w$ ) placed on a surface and the contact force ( $F$ ) between the particle and the surface: (a) horizontal and (b) vertical particle orientation.

Tables 3.1 to 3.3 show the calculated contact force and the corresponding deformation (overlap) between the particle and a rigid surface for vertical and horizontal placements of the particle after 0.005 sec, when the amplitude of the oscillation of contact force had reduced to a negligible value (Fig. 3.2d). In these tables the percentage error has been calculated as

$$\text{Error (\%)} = \frac{|F_s - W_a|}{W_a} \times 100 \quad (3.1)$$

where  $F_s$  and  $W_a$  are the simulated contact force and the actual weight of the particle respectively. The critical time step (1.044E-5 sec) has been calculated from the radius and properties of the particle material (Eq. 1.31) and could be altered by multiplying with a desired factor to investigate the effect of time step on the DE model predictions.

**Table 3.1** Simulation results for *vertically* positioned particle at three different time steps with damping coefficient of 0.5.

Time step (sec)	Deformation (m)	Difference between calculated contact force and the weight of particle (N)	Error (%)
1.044E -5	3.5 E -7	2.E -7	9.60E-05
1.044 E -6	1.84E -6	1.38E -5	6.63E-03
1.044 E -7	7.62E -6	2.19E -3	1.1

**Table 3.2** Simulation results for *vertically* positioned particle at three different time steps with damping coefficient of 0.21.

Time step (sec)	Deformation (m)	Difference between calculated contact force and the weight of particle (N)	Error (%)
1.044 E -5	1.2E -7	1.E -8	4.80E-06
1.044 E -6	8.1E -7	2.4E -5	1.15E-02
1.044 E -7	1.1E -6	2.4E -5	1.15E-02

**Table 3.3** Simulation results for *horizontally* positioned particle at three different time steps with damping coefficient of 0.5.

Time step (sec)	Deformation (m)	Difference between calculated contact force and the weight of particle (N)	Error (%)
1.044 E -5	1.7E -7	1.E -7	4.80E-05
1.044 E -6	5.E -8	6E -8	2.40E-05
1.044 E -7	6.96E -6	2.2E -3	1.0

A required time step has been calculated as

$$\Delta t_r = \text{frac} \times \Delta t_c \quad (3.2)$$

where  $\Delta t_c$  is the critical time step (Eq. 1.31) and *frac* is a factor which can be greater or less than 1 but should not be much greater than 1 or the simulation becomes unstable.

As shown in Tables 3.1 to 3.3 these simple simulations demonstrate that regardless of particle orientation (number of contact points per particle) the contact force between the particle and surface calculated in the model was very close to the weight of the particle for most simulations. However, when the time step and damping coefficient have been altered some differences have been observed between the weight of particle and the predicted contact force at quasi-equilibrium of the particle in the DE model. The main reason for these differences is the fact that in the DEM the particle can not reach complete static equilibrium. The particle oscillates because the gravitational force works in opposition to the elastic component of the contact force. As the time step is increased the amplitude of this oscillation increases (Fig. 3.2d). The effect of the time step and damping coefficient on this error can be considerable and is discussed in the following section.

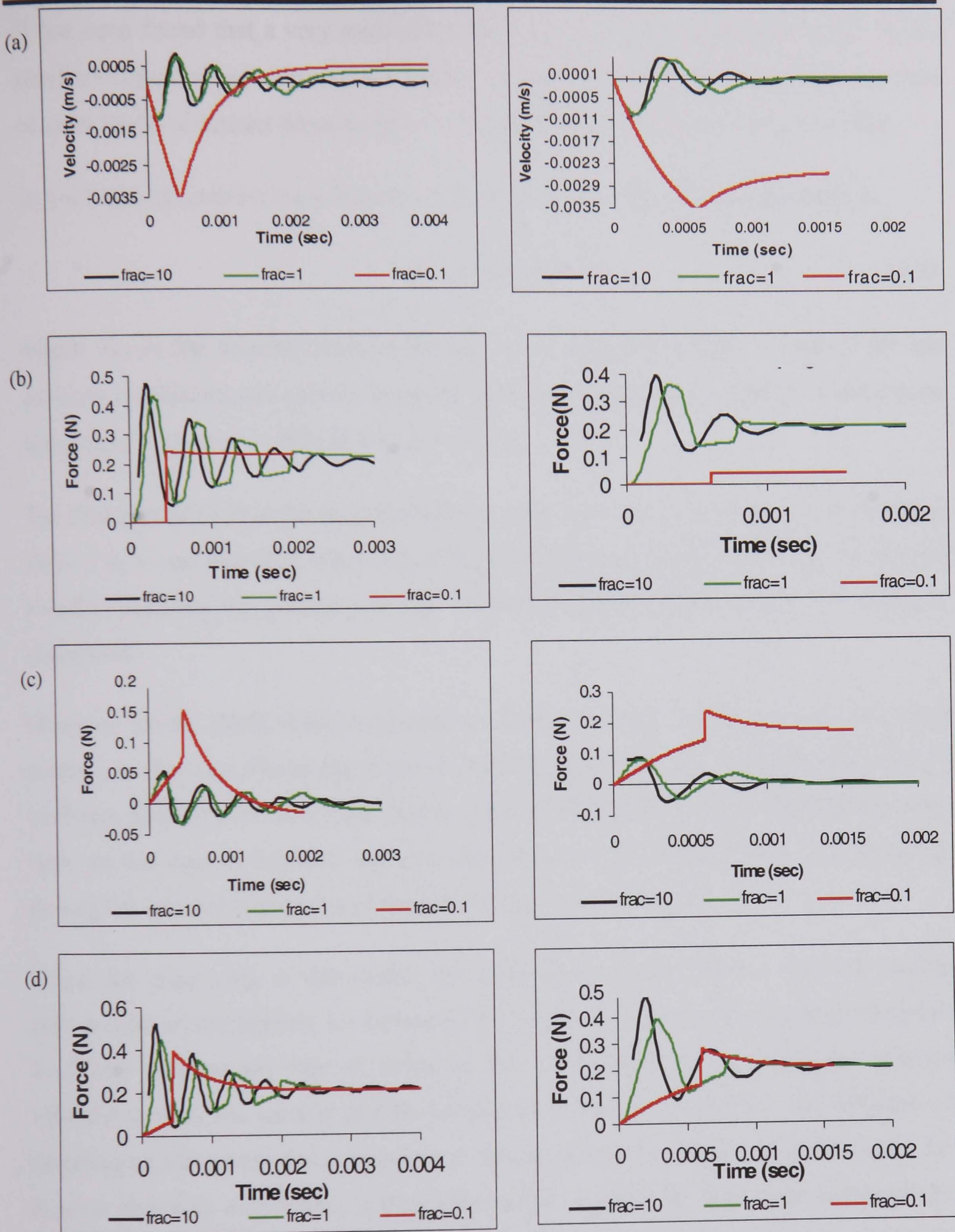


**Figure 3.2** Effect of time step and damping coefficient on: (a) contact velocity, (b) elastic contact force, (c) damping force and (d) resultant contact force for vertical orientation of the particle in the stable situation (resting on the surface) for two damping ratios, 0.21 (left) and 0.5 (right). In these numerical tests the actual weight of the particle was 0.2105 N.

It has been found that a very small time step increased the error in calculation of the resultant contact force. There are a number of reasons for this effect due to the method of calculation of contact force based on relative velocity which is used in the DEM.

In the DEM the contact force between a visco-elastic particle and another body is

$$F = K V_{rel} \Delta t + C V_{rel} \quad (3.3)$$

where  $V_{rel}$  is the relative velocity between the contacting bodies,  $K$  and  $C$  are the stiffness coefficient and contact damping coefficient respectively, and  $\Delta t$  is the chosen time step (Tsuji *et al.*, 1992; Zhang and Whitten, 1996).

The first part of (3.3) is the spring (elastic) contact force and the second is the damping force. In a real situation when a particle is placed on a surface there is no relative velocity between the particle and the surface (static equilibrium) and no energy is dissipated.

However in the DEM there is always a relative velocity between the particle and surface, in this case due to gravitational acceleration. Thus, the damping term of (3.3) is always applied even in a quasi-static condition. The effect of time step and damping ratio on the contact velocity and components of contact force (elastic and damping forces) for vertical orientation of the particle is shown in Fig. 3.2.

When the time step is decreased, the magnitude of the relative velocity during stabilisation of the particle is increased (Fig. 3.2a). In each oscillation decreasing the time step reduced the rate of damping (Eq. 3.3) therefore the maximum relative velocity between the particle and the surface increased. Consequently, the influence of damping on the contact force increases at shorter time steps. Figure 3.2c shows that for a given damping coefficient, a time step below the critical time step increased the magnitude of the damping force. In Table 3.1 it can be seen that the amount of error in the calculation of contact force was higher when a shorter time step has been used. This error is therefore related to the effect of damping force on the resultant of contact force. Furthermore, when the time step is very small ( $10^{-7}$ s) the round off error in the calculations can be the reason for a considerable high error in Tables 3.1 and 3.3. From Fig. 3.2d the final value of the contact force (resultant) is almost the same as the weight of particles with an error equal to or less than 1.1% (Table 3.1).

---

The influence of the number of contact points acting simultaneously between the particle and the surface on the accuracy of the calculation of particle weight has been investigated by placing the particle in a horizontal orientation (two simultaneous contact points). Table 3.3 shows the results of the DE code with horizontal orientation. Comparing Table 3.1 (for vertical orientation) and Table 3.3 (for horizontal orientation), similar results have been obtained. Apart from an exception in the table 3.3, in both orientations the amount of error increased as the time step decreased. However the error in horizontal orientation was less than vertical orientation for all time steps which indicates that less damping occurred at each contact point for the particle in a horizontal orientation.

From the above it can be concluded that for a quasi-static condition in which particles are stable with low relative velocities, a very small time step is not required and as there is no energy dissipation, the damping coefficient should be set to a minimum value.

### **3.3 Collision of a multi-sphere particle with a surface**

Collision of a particle with the surface of machine parts is common in agricultural processing operations. When visco-elastic particles are dropped on to a flat surface they bounce a number of times, losing energy at each impact before coming to rest. The following simulations have been performed to investigate the accuracy of the contact model in prediction of contact force during particle collision with a surface and the effect of the number of contact points on this prediction. A particle comprising two overlapping spheres has been dropped on to a flat, rigid surface in vertical orientation (one contact point during collision) and horizontal orientation (two contact points). The contact-damping coefficient for these simulations was 0.1.

Fig. 3.3 shows the change in the position of the particle centroid with time (Fig. 3.3a) and the contact force during the first collision for horizontal and vertical orientations of the particle (Fig.3.3b). The total contact force for the particle with horizontal orientation is the sum of the contact force at each contact points. The maximum contact force of the first collision for horizontal orientation at each contact point (half of the

maximum force) is less than that for the particle in a vertical orientation. Since the resultant contact force is the sum of the elastic and damping force and the damping force is calculated from the relative velocity of the contact points then the rate of damping on the particle velocity in horizontal orientation is twice that for a vertically oriented particle. The rate of particle deceleration is therefore less for a vertically oriented particle resulting in higher maximum relative contact velocity and deformation which results in higher maximum contact force at the first collision of particle for vertical orientation than horizontal (per contact point).

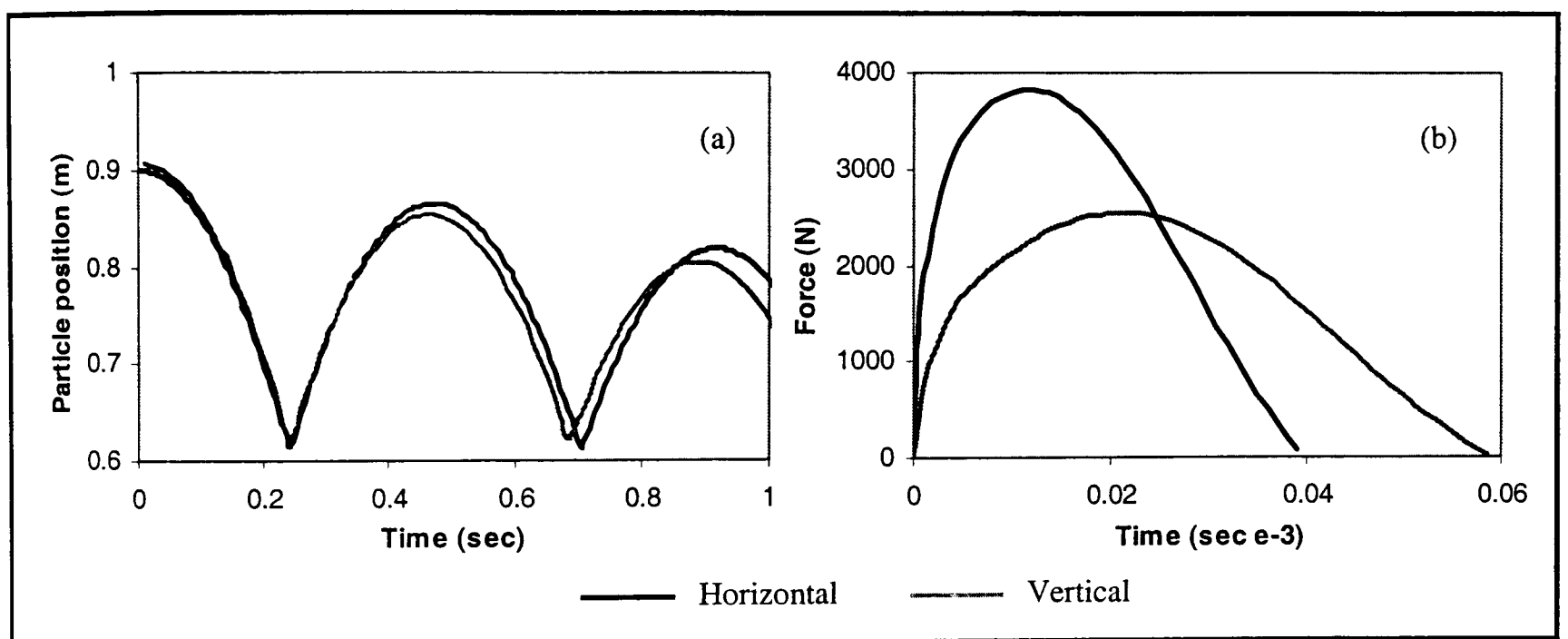


**Figure 3.3** Effect of particle orientation (horizontal and vertical) with different number of contact points on simulation results of a particle colliding with a surface; (a) particle movement and (b) evolution of the first collision force. The time step for these simulations was  $1 \text{ E } -06 \text{ sec}$  ( $\text{frac}=0.1$ ).

The difference in velocity of the two particle orientations due to differences in damping can be seen in Fig 3.3a. The horizontally oriented particle accelerated more quickly after impact and so reached a higher position on the first bounce. It then decelerated more quickly during impact which means that it rebounded sooner than the vertically oriented particle. Since the dropping height for both orientations was the

same, the impulse (the area under the curves) for both cases was almost the same (apart from the difference between the damping rate).

Fig. 3.4 shows the effect of the time step on maximum contact force during first collision with vertical orientation of particle for a purely elastic particle (damping=0). It has been observed that for a chosen time step, the collision might not necessarily start from the first point of contact between the particle and surface. To ensure that all curves started from the same initial contact, the particle has been positioned so that its edge was touching the surface and was then given an initial contact velocity equivalent to dropping it from an arbitrary drop height ( $v = \sqrt{2gh}$ ). It has been observed that a very large time step (Fig. 3.4a,  $frac > 2.5$ ) resulted in excessive stepwise movement which caused excessive contact force. By decreasing the time step to a fraction of critical time step this type of error has been avoided (Fig. 3.4b). However, a very small time step seems to be unnecessary since there was no a significant difference between the curves for  $frac=0.1$  and  $0.01$ .

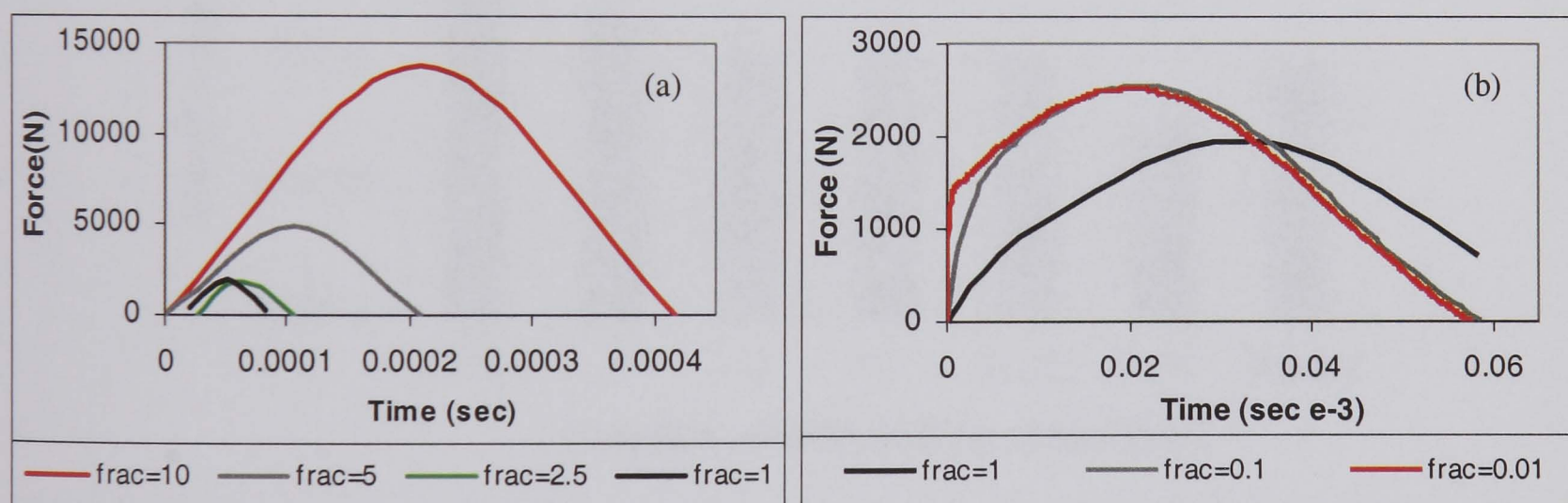


**Figure 3.4** Effect of time step on maximum collision force (damping coefficient=0) for a two element multi-sphere particle dropped on to a flat surface. Initial velocity has been applied to the particle to simulate the collision from an arbitrary height. The particle has been oriented with its major axis normal to the surface.

The accuracy of the simulated collision force has been investigated by comparing the value of impulse calculated from the simulation results and from theory. During particle collision the theoretical impulse is

$$I = m v \quad (3.4)$$

where  $m$  and  $v$  are the mass and velocity of the particle respectively. The area under the Force–Time curve from the simulation has the same dimension as impulse,  $kg\cdot ms^{-1}$ .

For a purely elastic particle, the sum of potential and kinetic energy of the particle remains constant, the collision velocity and the escape velocity will be the same and if the simulation is accurate then

$$I = m v \text{ (from theory)} \cong 0.5 \text{ area under } f\text{-}t \text{ curve (from simulation)} \quad (3.5)$$

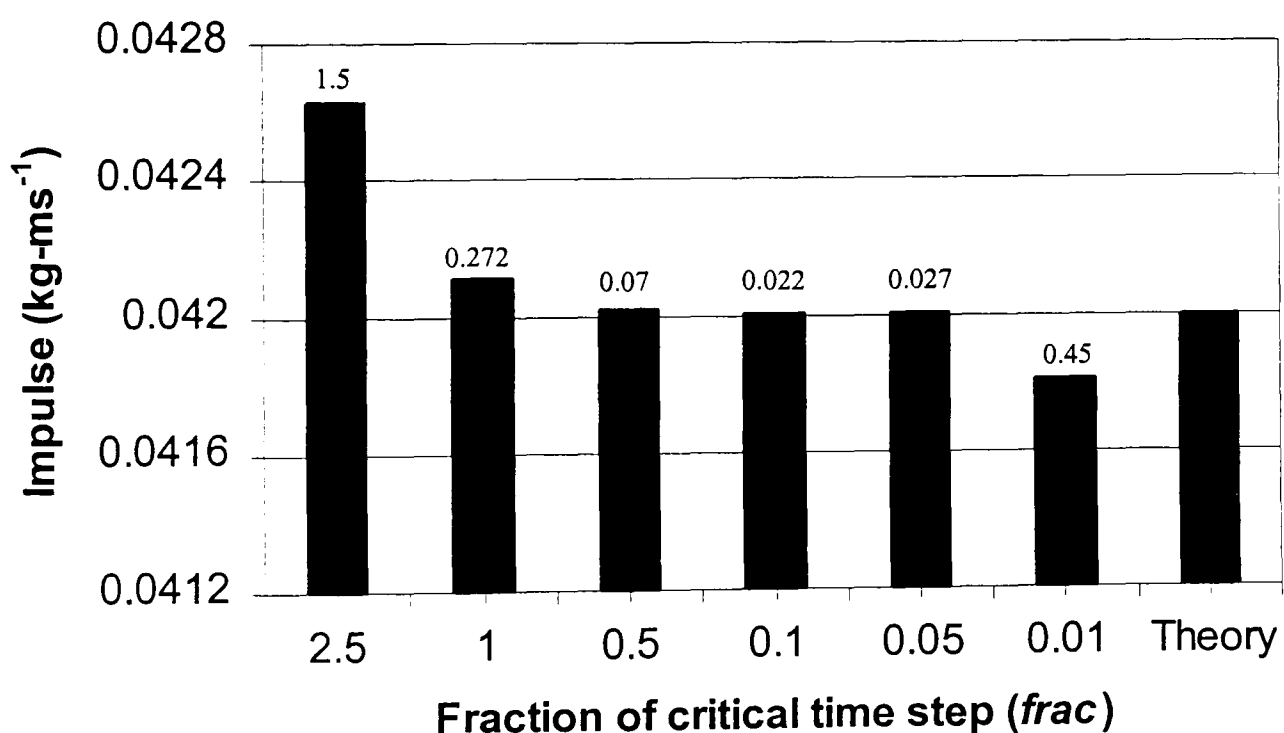


**Figure 3.5** Comparison between theoretical impulse during particle collision and that of simulated with the DE code for different time steps. In each case the percentage of error is shown on the top of the corresponding column.

Theoretical and simulated values are compared in Fig. 3.5. The largest error (1.5 %) was for a time step greater than the critical value ( $frac=2.5$ ). The error at the critical value was 0.28 % which reduced to 0.07 % at  $frac=0.5$ . Further reduction of the time step did not improve the accuracy of the simulation. However, the sharp increase in the error for  $frac$  0.01 is most probably due to the round off error in calculations of

impulse from the product of force and time step in the Force-Time curve. As also observed in the quasi-static tests a very small time step (in this case 0.01 of the critical value) will increase the error. For this case (particle collision) the most accurate results have been obtained with a time step between 0.5 to 0.1 of the critical value which is comparable to that obtained by Raji (1999) based on the rebound height of the particle at each collision.

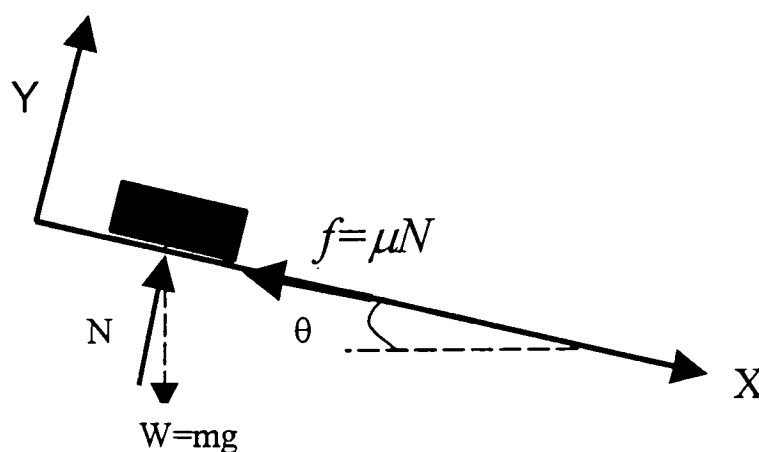
### 3.4 Sliding of a particle on an inclined surface

The equation of motion for a particle placed on a rough inclined surface as shown in Fig. 3.6 is

$$\ddot{x} = [W \sin(\theta) - f] / m \quad (3.6)$$

where  $\ddot{x}$  is particle acceleration in the sliding direction (x axis);  $W$  is the weight of the particle, ( $f = \mu N$ ) is the frictional force between particle and surface and  $\theta$  and  $m$  are the inclination angle and the mass of particle respectively.

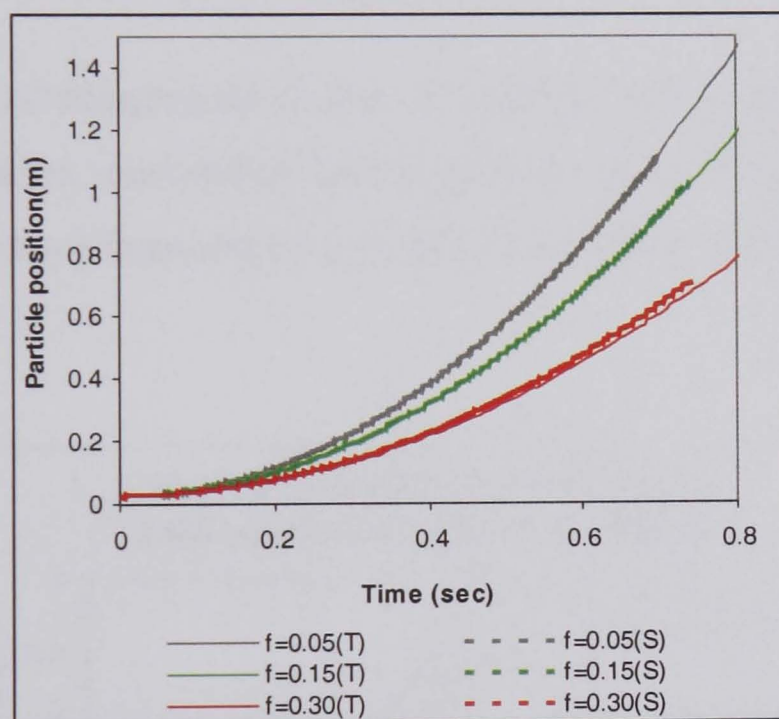
Capsule shaped particles comprised of identical element spheres (varying in number from 5 to 9) have been generated. To prevent particle rolling during sliding the particle has been positioned with its longitudinal axis parallel to the direction of motion. The acceleration, velocity and displacement of the particle during sliding have been calculated using (3.6). The predictions of the DEM code have been compared with theoretical calculations.



**Figure 3.6** Free body diagram of a particle sliding on an inclined surface.

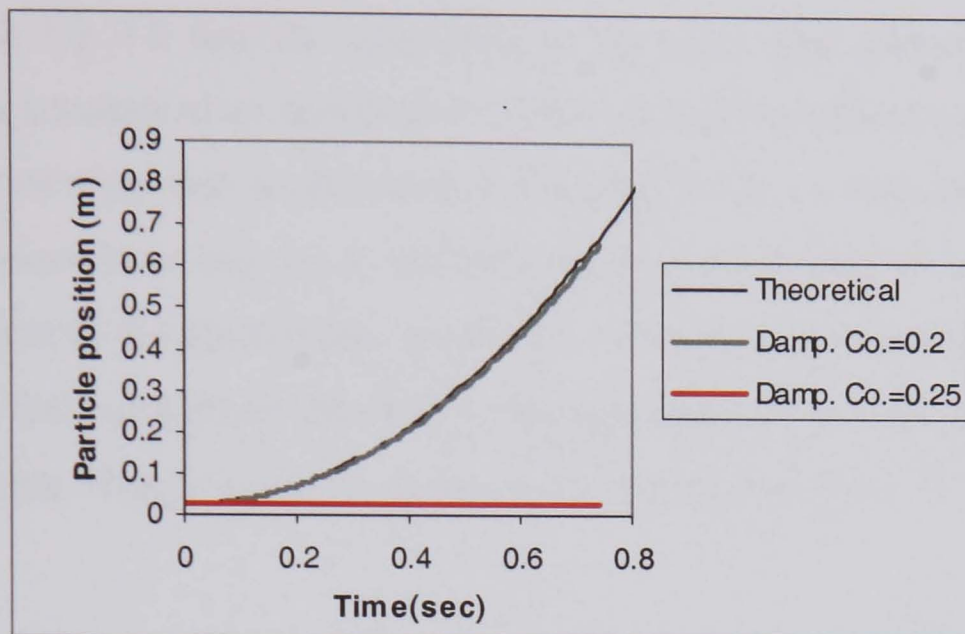
In this series of simulations different coefficients of friction have been chosen and the position of the particle computed. For a physical model, during sliding all kinds of energy dissipation (including tangential damping) is considered, that is  $\mu$  in equation (3.6) is representative of both friction and tangential damping.

Fig. 3.7 shows the comparison between the analytical and simulation results when the tangential damping has been set to zero and only normal damping has been used (1.18). This indicates that the coefficient of friction measured experimentally is sufficient to dissipate energy effectively in the model without the need for tangential damping. In fact, the experimental coefficient of friction includes all types of resistance, including tangential damping. In the other words, the term  $f$  in (3.6) is the representative of all resistance forces against particle motion.



**Figure 3.7** Results of sliding of the particle with different coefficients of friction between the particle and surface in the absence of tangential damping. (T stands for Theory and S for simulation). The inclination angle for these simulations was  $30^\circ$  and the model particle comprised five element spheres.

Fig. 3.8 shows the results of simulation when tangential damping has been applied in addition to friction. It can be seen that when the resultant of tangential damping force and frictional force approached the component of particle weight in the direction of sliding, the particle stuck to the surface (red curve).



**Figure 3.8** Effect of damping on sliding of a particle when applied as an additional dissipation mechanism during sliding on an inclined surface. These results have been obtained for the inclination angle of  $30^\circ$  and  $\mu=0.3$ .

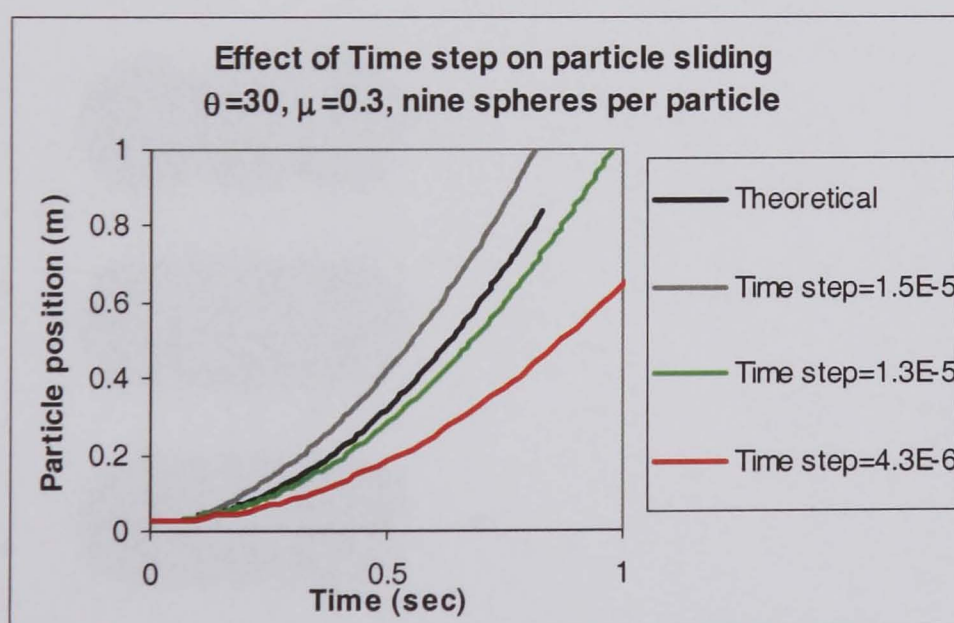


**Figure 3.9** Prediction of the DE model for particle sliding with different time steps for a cylindrical particle comprised of 9-element spheres.

Since in DEM sliding of a particle on a surface is simulated based on the relative velocity of particle and surface, the chosen time step plays an important role in the

simulation results. To show the effect of time step on sliding of the particle, a set of sliding simulations has been carried out over a range of time steps. To eliminate the effect of damping on the results the tangential damping coefficient has been also set to zero.

It can be seen in Fig 3.9 that the magnitude of the time step affected the particle movement which accelerated or decelerated relative to the theoretical value. This was due to the effect of time step on the normal damping force, as discussed previously. Therefore, the chosen time step for a particular application should provide the results as close as possible to the theoretical calculation. Changing the time step altered the normal damping force as a result the particle has been damped at different rates as the time step has been changed which changed the maximum friction force ( $f_s = \mu N$ ) accordingly.

In the multi- sphere method the movement of particles is updated from forces acting on their element spheres so the number of element spheres per particle (which determines the number of contact points) may affect the sliding of the particle. To investigate this effect, three different particles of the same aspect ratio and mass, but with a different number of element spheres have been generated as shown in Fig.3.10.

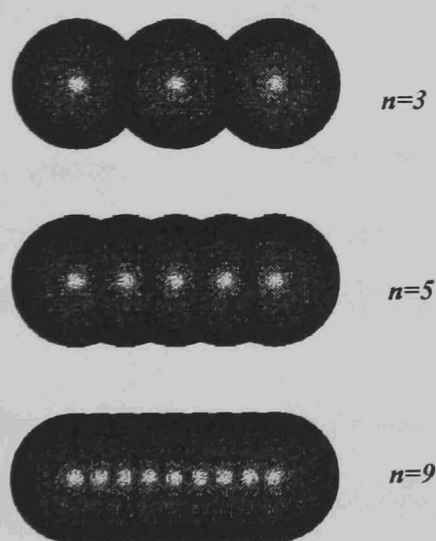


**Figure 3.10** Different model particle configurations for particle sliding simulations on an inclined surface. The particles have the same volume and aspect ratio but different element sphere densities.

The sliding simulations have been carried out for each particle with two different friction coefficients. Since the longitudinal axis of particles was parallel to the sliding direction and all element spheres were the same size, the number of contact points for each particle was equal to the number of their element spheres.

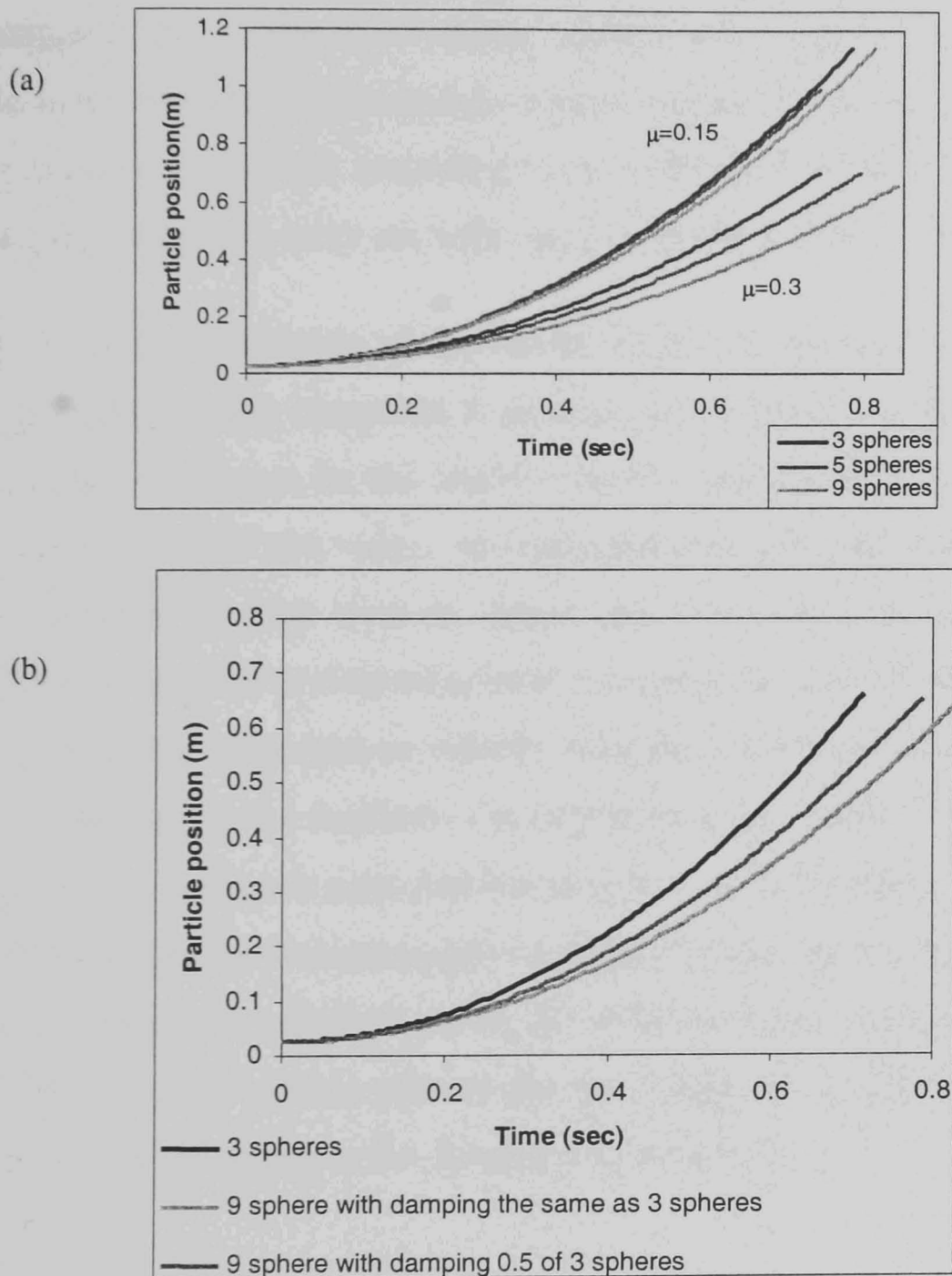


**Figure 3.11** (a) Effect of number of element spheres on particle sliding simulations; numbers show the element spheres per particle. The inclination angle and the damping coefficient were  $30^\circ$  and 0.21 respectively. (b) Relationship between the number of contact points and the damping effect.

As shown in Fig. 3.11 particles with a greater number of contact points per particle decelerated more quickly. The weight of the particle was identical for all simulation, so

that by increasing the number of element spheres in the particle the amount of normal force per contact point decreased but the total normal force for the particle remained almost the same. The differences in rate of particle deceleration were greater for the higher coefficient of friction. This was because each element sphere contributed to the damping effect, resulting in highly damped particle and greater frictional resistance. This suggests that in the multi-sphere method when adjacent element spheres in a particle make contact simultaneously with a surface or another particle the damping force should be normalised according to the number of contact points. This will scale the damping and give a more accurate result as shown in Fig. 3.11b.

In Fig. 3.11b the prediction of the MSM model for sliding of a 3-element spheres model particle has been compared to the sliding of a 9-element spheres model particle. The damping coefficient for the former was 0.21 and for the latter has been set up to equal and one-half of that value. As mentioned, the damping acts individually on the relative velocity of each element sphere and the contacting surface (Eq. 3.3). By increasing the number of element spheres per particles, each element sphere damps the particle according to its relative velocity with the surface, resulting in a more damped particle (sticking on the surface). Consequently more normal force ( $N$ ) between the particle and the surface is provided resulting in a more available friction force ( $f = \mu N$ ) which decelerated the 9-element spheres particle more than 3-element spheres particle. When the damping coefficient for the 9-element spheres particle has been reduced to 0.5 of the 3-element spheres particle the rate of particle deceleration decreased which resulted in a closer sliding to the 3-element spheres particle.

### 3.5 Conveying of a particle

Conveying is a common operation in agricultural processing systems. When a particle is dropped on to a moving surface, it will move at the same speed as the conveyor after an initial instability during which the relative velocity between the particle and surface reduces to zero. However, the physical properties of the particle and surface such as coefficient of restitution (damping) and coefficient of friction can affect the dynamic behaviour of the particle during the unstable period. The following simulation has been carried out to investigate the behaviour of a model particle placed on a moving

conveyor. A capsule shape particle comprised of 5 element spheres has been dropped on to a surface moving horizontally with a constant velocity of 0.01m/sec.

Fig. 3.12 shows the effect of time step, damping and friction on the particle velocity in the direction of particle movement. In general after initial particle instability resulting from particle rebound the model could predict an accurate velocity for the particle (0.01m/sec). The high horizontal velocity of the particle at the beginning was due to the collision force between the particle and the conveyor which corresponds to the initial height of the particle.

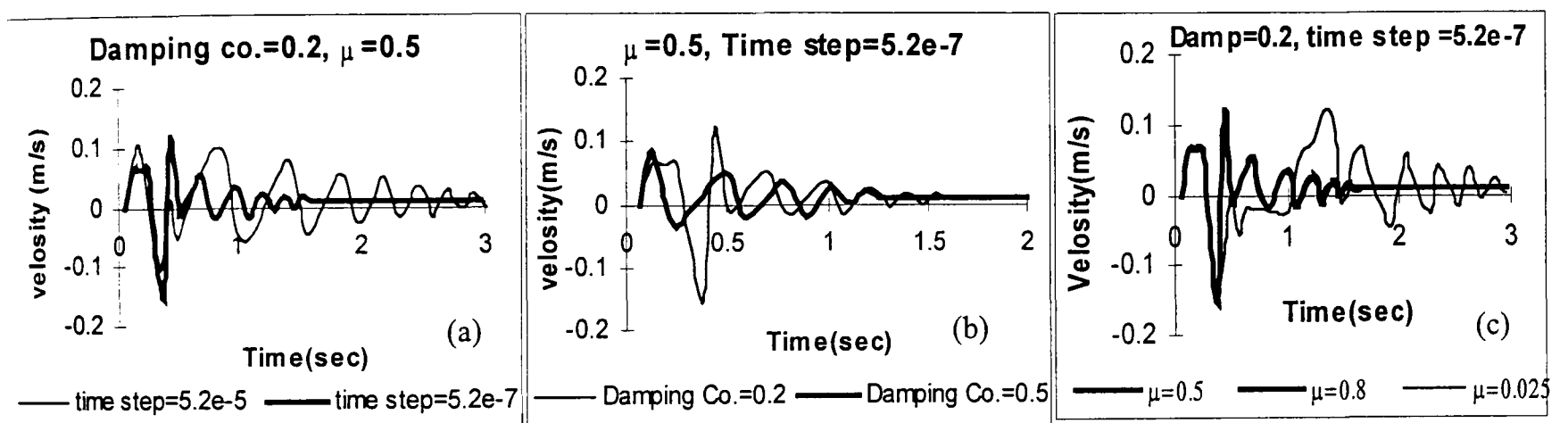


**Figure 3.12** Effect of time step, damping coefficient and coefficient of friction on the prediction of the DE model with Multi-sphere approach for handling simulation of a particle on a horizontal conveyor.

The high normal contact force provided a higher frictional force ( $f=\mu N$ ) between conveyor and the particle, which caused an instantaneous increase in the horizontal velocity of particle. As the time passed the normal force has been damped and reached a constant value which was almost equal to the weight of the particle. However, the unstable period altered when related model parameters have been changed. Fig. 3.12a illustrates the effect of time step on the duration of particle instability. When the time step has been decreased, as has been previously shown (Fig. 3.2), more damping occurred and the particle became stable more quickly. The effect of damping is shown in Fig. 3.12b; as expected by increasing damping, the rate of energy dissipation

increased, resulting in faster approach to stability. In Fig 3.12c it can be seen that for low friction coefficient the duration of particle instability increased.

### 3.6 Rotation and translation of a particle due to a collision force

One of the important features of the DEM with multi-sphere approach is dealing with the updating translation and rotation of particles. This task is carried out by transferring the normal and tangential contact force from contact points on the boundary of the element spheres to the centroid of the particle and calculating the out-of-balance force and moment acting on the particle in each time step. The translational and rotational velocities of the particle are then updated from corresponding accelerations. The following simulation has been designed to verify the accuracy of the proposed algorithm.

A capsule shaped model particle comprised of nine element spheres has been created in free space (i.e. gravitational acceleration set to zero). The particle properties were mass,  $2.43\text{E-}2$  kg, time step;  $8.61\text{E-}6$  sec and mass moment of inertia:  $2.43\text{E-}5$   $\text{kg-m}^2$ .

An instantaneous external force ( $\mathbf{F}$ ) of 1kN has been applied to the particle at a distance 1.5 cm from the particle centroid for the duration of one time step (Fig. 3.13). This set up has been chosen to provide a proper amount of particle rotation during simulation.

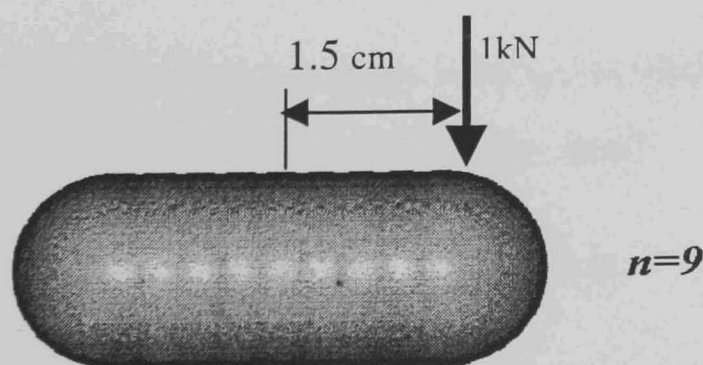


**Figure 3.13** Model particle configuration for rotational and translational simulations of a particle due to an instantaneous collision force.  $n$  is the number of element spheres for the model particle.

According to Newtonian mechanics, the translational and rotational accelerations of the particle for this situation during the period of application of the force are

$$a = F / m = 41152.3 \text{ (m/s}^2\text{)} \quad (3.7)$$

$$\alpha = M / I = 616522.8 \text{ (rad/s}^2\text{)} \quad (3.8)$$

where  $M$  is the moment acting on particle due to the external force.

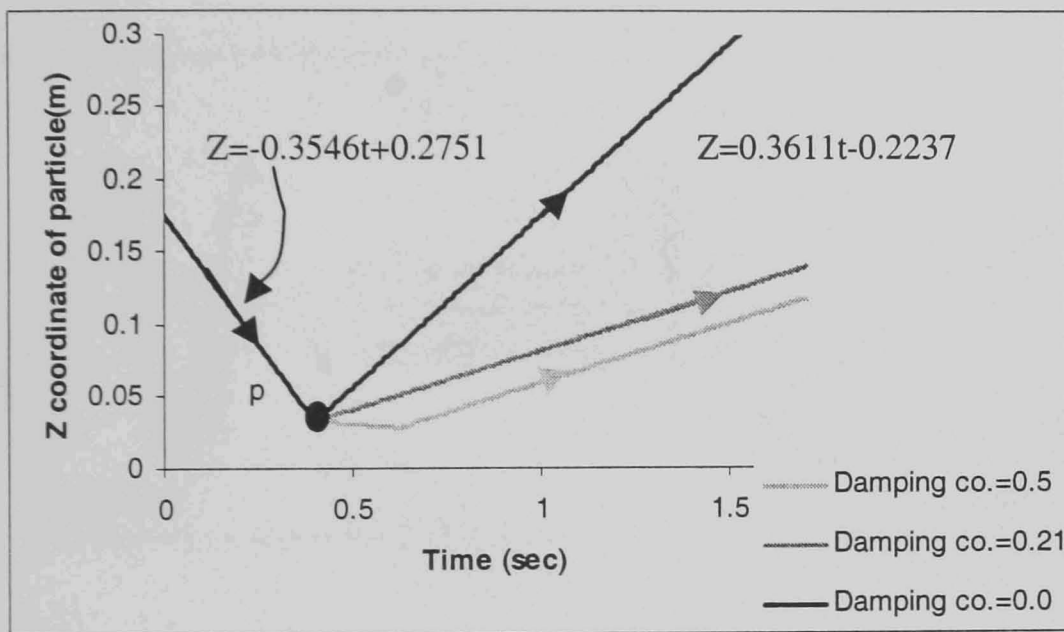


**Figure 3.14** Simulation results for particle translation with and without applying damping. The slope of the lines show the predicted velocity of particle before and after particle collision in the absence of contact and global damping. P is the collision point.

In the next time step the applied force has been removed so that the translational and rotational velocity of the particle remained constant and equal

$$v = a \Delta t = 0.3543 \text{ (m/s)} \quad (3.9)$$

$$\omega = \alpha \Delta t = 5.31 \text{ (rad/s)} \quad (3.10)$$

Fig. 3.14 shows the prediction of the DE model for particle movement before and after collision (point p) with a surface using three different damping coefficients. The slope of the line for translational movement of the particle represents the particle velocity

(0.3546 m/s) in the absence of contact damping which was very close to the theoretical value (0.3543 m/sec). In the presence of contact damping (the lighter curves), when the damping coefficient has been increased the duration of the collision increased (sticking the particle to the surface), which is shown with a horizontal segment, and the amount of energy dissipation during the collision of the particle with the surface increased. Consequently the rebound velocity reduced, this can be seen as a decrease in the slope of the line after collision in Fig. 3.14 for the lighter curves.

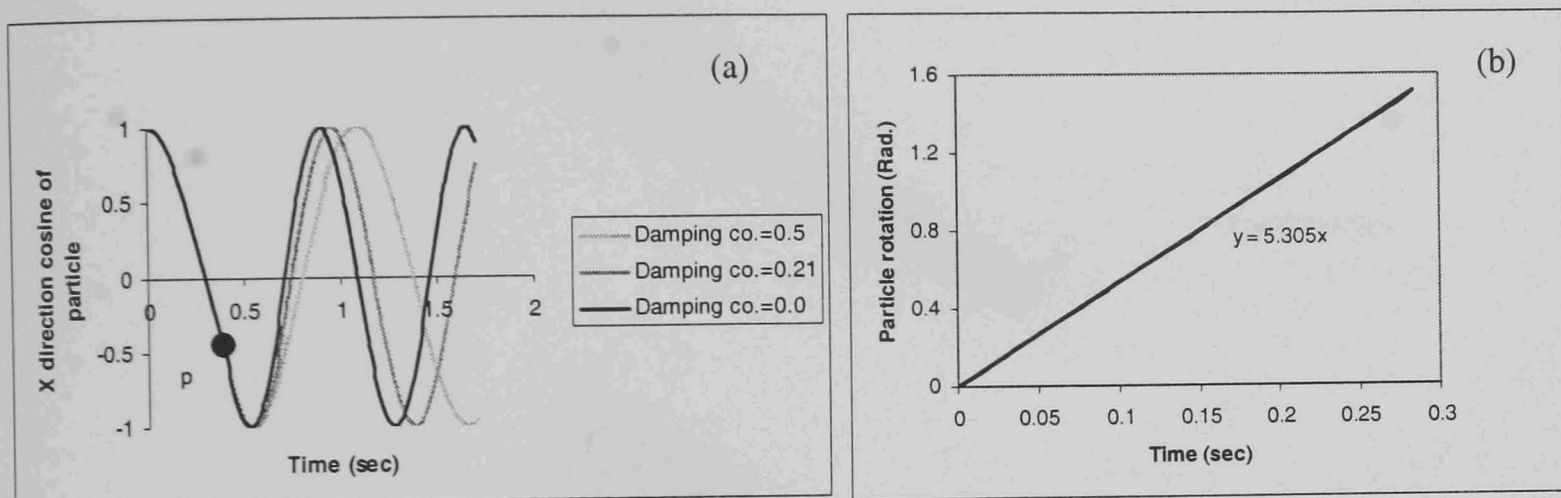


**Figure 3.15** Simulation results for the particle rotation: a) evolution of particle orientation before and after particle collision; b) cumulative particle rotation before particle collision. The slope of this line shows the simulated rotational velocity of the model particle.

Fig. 3.15a shows the change in particle orientation due to particle rotation. Particle rotation before collision with the surface was the same for all damping ratios, but after collision the particle rotation decelerated relative to the magnitude of the damping coefficient. The cumulative rotation of the particle in the absence of contact damping is shown in Fig. 3.15b. The slope of the line represents the predicted particle rotational velocity (5.305 rad/s) which, was very close to the theoretical value (5.31 rad/s). The difference between the theoretical value of  $\omega$  and that predicted by DE model was due to the normalisation of the direction cosines of the unit vector for the major axis of particles (see section 2.3.3).

been set to zero, so that any resistance against particle sliding was due only to pseudo-friction of the model particles.

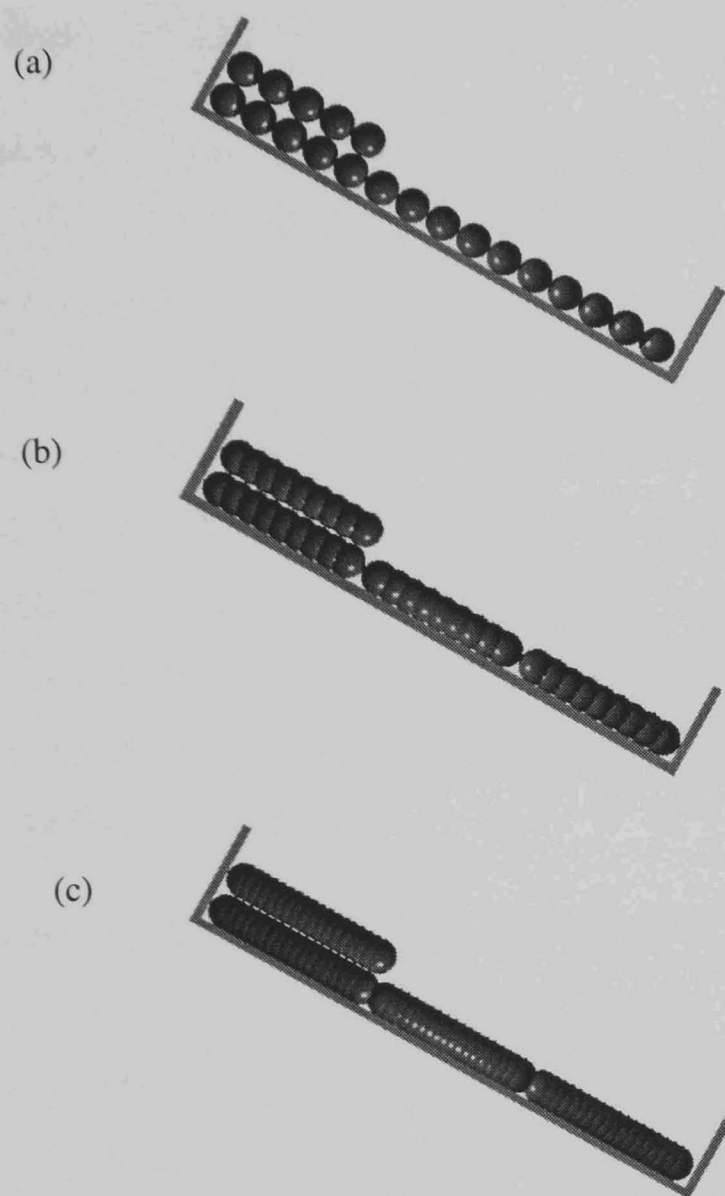


**Figure 3.16** Simulation set up for measuring particle pseudo friction; (a)  $q=1$ , (b)  $q=2$  and (c)  $q=4$ .

### 3.7.1 Simulation results

The theoretical position of a real particle with a given coefficient of friction is

$$X_{(t)} = X_0 + 0.5 g (\sin\theta - \mu \cos\theta) t^2 \quad (3.11)$$

where  $X_0$  is the initial position of the particle,  $g$ ,  $\theta$ ,  $\mu$  and  $t$  are the gravitational acceleration, inclination angle, coefficient of friction and time respectively.

Rearranging (3.11) gives

### 3.7 Pseudo-friction in a multi-sphere model particle

One of the important objectives of the multi-sphere method is to represent real particles with an acceptable degree of approximation to the true shape and surface properties.

As the outer boundary of a multi-sphere model particle consists of spherical segments during contact between two neighbouring model particles, these segments can cause interlocking between the particles. As this attribute of the model particles has the same effect as friction on the movement of particles, this effect can be termed *pseudo-friction*. The pseudo-friction resulting from the element spheres decreases with increase in the number of spheres used to approximate the particle surface. On the other hand, the higher the number of element spheres per particle the higher the relative run time for simulation and the lower the efficiency of the DE model. In the following section the additional roughness (pseudo-friction) resulting from element spheres of a model particle is quantified.

The objective of these simulations was to predict the coefficient of pseudo-friction as a function of element sphere density ( $q$ ) in a model particle. Element sphere density is defined here as the number of sphere per unit length or sphere diameter. The model particles comprised of identical spheres of unit radius. The length of each model particles has been chosen to be five times the diameter of the element spheres (aspect ratio=5). The length of the workspace (simulated box) was three times the particle length. Four particles have been generated in each simulation. Three of them have been placed on the bottom of the box and one has been positioned on top of the first particle. The box has been inclined at an angle of  $30^\circ$ .

Three simulations with model particles of different sphere densities have been carried out. Fig.3.16 a, b and c show the configuration of the model particles with sphere density of 1, 2 and 4 respectively.

Applying the components of gravitational acceleration to the system simulated the sliding of the upper particle. The particles in the first layer covered the bottom of the workspace so they have been trapped and could not move, but the upper particle could slide downward. In all simulations the coefficient of friction between particles has

$$t^2 = \frac{2(X_t - X_0)}{g(\sin \theta - \mu \cos \theta)} \quad (3.12)$$

Plotting  $t^2$  against  $X_t - X_0$  gives  $\mu$  from the slope of the curve

$$S = \frac{2}{g(\sin \theta - \mu \cos \theta)} \quad (3.13)$$

The plots for model particles of different sphere densities are shown in Fig. 3.17.

The corresponding  $\mu$  for each sphere density has been calculated from (3.13) with the result shown in Table 3.4. As shown in this table, the maximum possible pseudo-friction (i.e.  $\theta=1$ , when element spheres are non-overlapping) is equivalent to a coefficient of friction of 0.41. When the sphere density has been increased to four the pseudo-friction reduced to almost zero ( $\mu=0.03$ ). It can be concluded that when sphere density is equal or greater than four the amount of pseudo-friction is negligible and can be ignored.

The pseudo-friction in a model particle is due to the deviation of the direction of the contact force when an element sphere of a neighbouring particle is positioned between two adjacent element spheres of the particle of interest. As the particle density decreases, the maximum deviation in the direction of contact force increases (more interlocking). Consequently, the magnitude of the horizontal component of the contact force, which acts against particle movement, becomes greater as shown in Figures 3.18 to 3.20. They show the simulation results for the direction of contact force and the magnitude of contact force component in the direction of particle sliding for different element sphere densities. When the sphere density was 1 the direction of the contact force for the first contact started from  $120^\circ$  (with reference to sliding direction) which is equivalent to a deviation of  $30^\circ$  from the vertical direction (real situation). The deviation for sphere densities of 2 and 4 are  $14.3^\circ$  and  $7.16^\circ$  respectively (Fig 3.18).

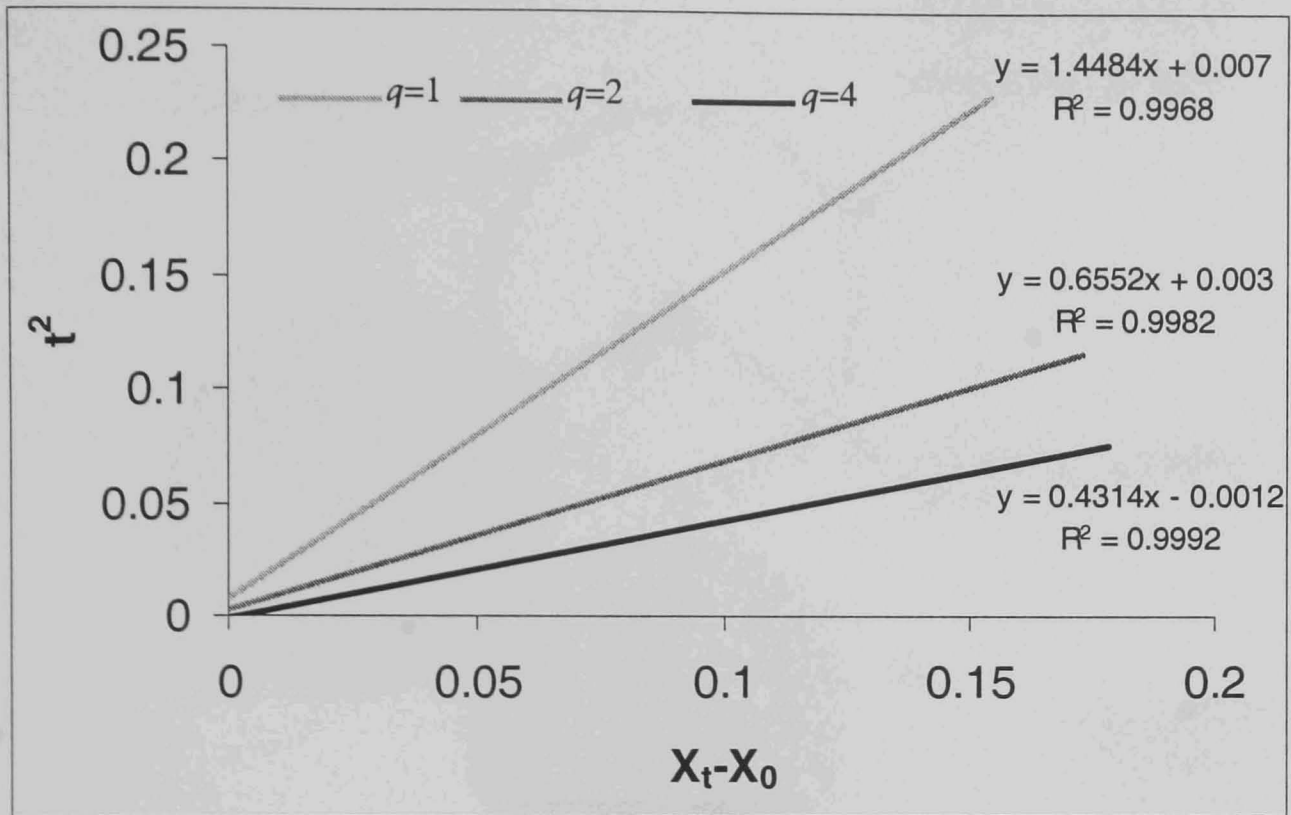


**Figure 3.17** Calculation of pseudo friction in DE multi-sphere model particles with different sphere densities from the plot of  $t^2$  against  $X_t - X_0$ .

**Table 3.4** Pseudo friction coefficient for model particles of different sphere density.

Sphere density ( $q$ )	$\mu$
1	0.41
2	0.22
4	0.03

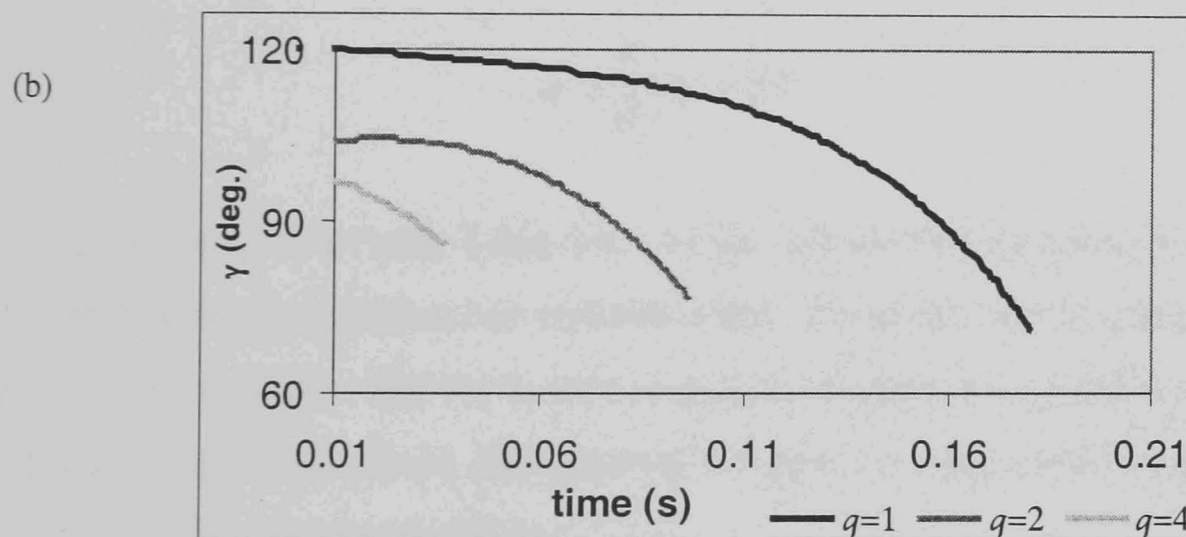
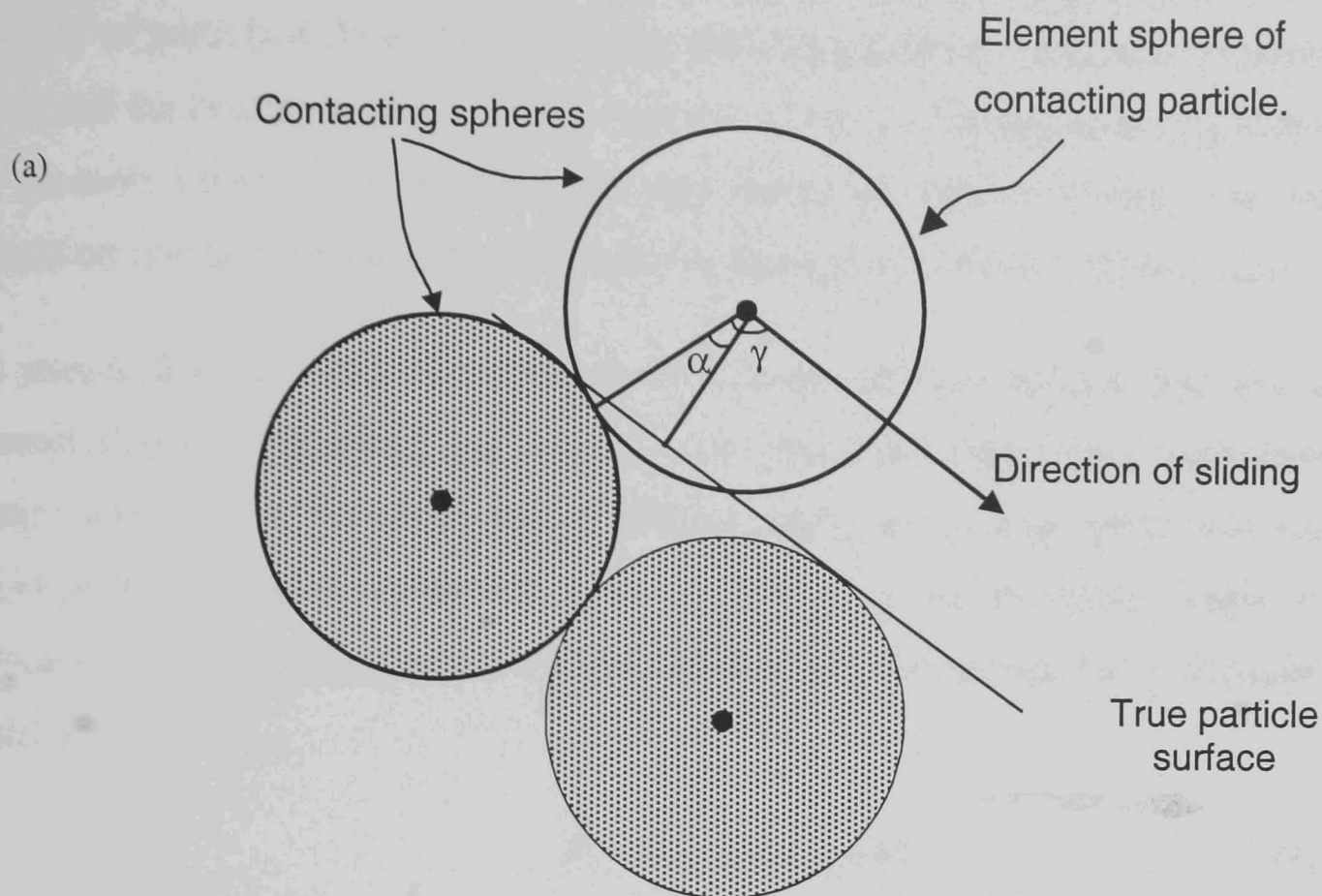


**Figure 3.18** The deviation of contact force from normal direction for the cylindrical model: (a) contact geometry for a model particle of sphere density of 1.  $\gamma$  is the angle between the direction of contact force and the direction of particle sliding and  $\alpha$  is the angle of deviation from normal direction. (b) Evolution of contact force during sliding of one sphere over another.

Figures 3.19 and 3.20 show the magnitude of the component of contact force in the direction of particle sliding and its average trend respectively. The area between the curves and the horizontal axis shows the amount of energy dissipation during sliding of one element sphere over another. By decreasing the sphere density, the energy dissipation (the area between the curves and horizontal axis in Fig 3.20) increases.

The pseudo-friction effect of contact force between element spheres has also been demonstrated by calculating the average tangential force (horizontal component of contact force,  $F_t$ ) at the beginning of sliding (when the sliding speed was small). Knowing the average of tangential force ( $F_t=0.1512N$ ), the inclination angle of the surface ( $\theta=30^\circ$ ), and the particle weight ( $W=0.427N$ ) the normal force between the particles is

$$F_n = W \cos \theta = 0.3698N \quad (3.14)$$

Consequently, the value of  $\mu$  for a sphere density of one ( $\theta=1$ ) can be calculated as

$$\mu = \frac{F_t}{F_n} = 0.409 \quad (3.15)$$

which is in close agreement with Table 3.4. As the particle sliding speed increased, the collision force was much higher but instantaneous. From the results obtained in this section, it can be concluded that the source of pseudo-friction in a model particle is due to the deviation of contact force from normal direction during inter-locking between element spheres of contacting particles.

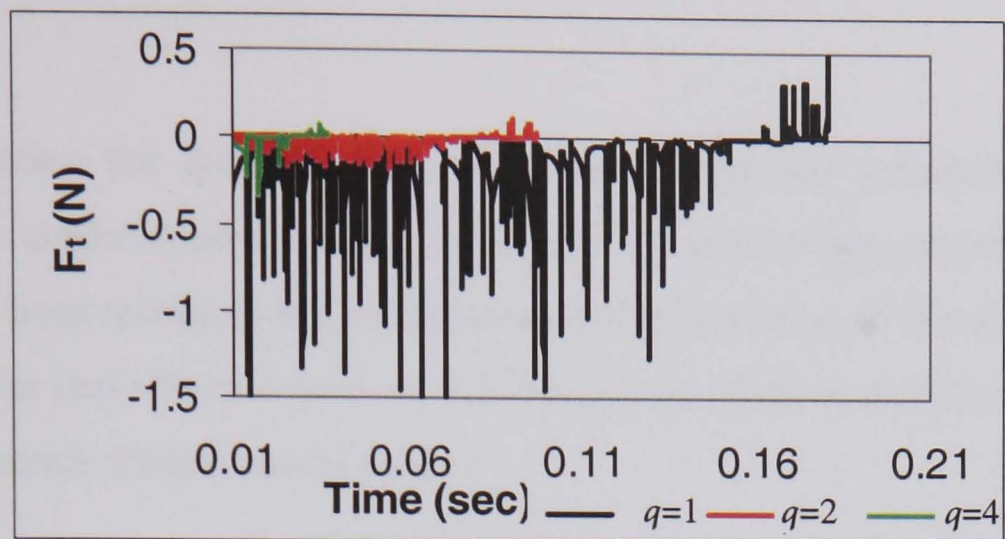


**Figure 3.19** Component of contact force in the direction of particle sliding during sliding of one element sphere over another.

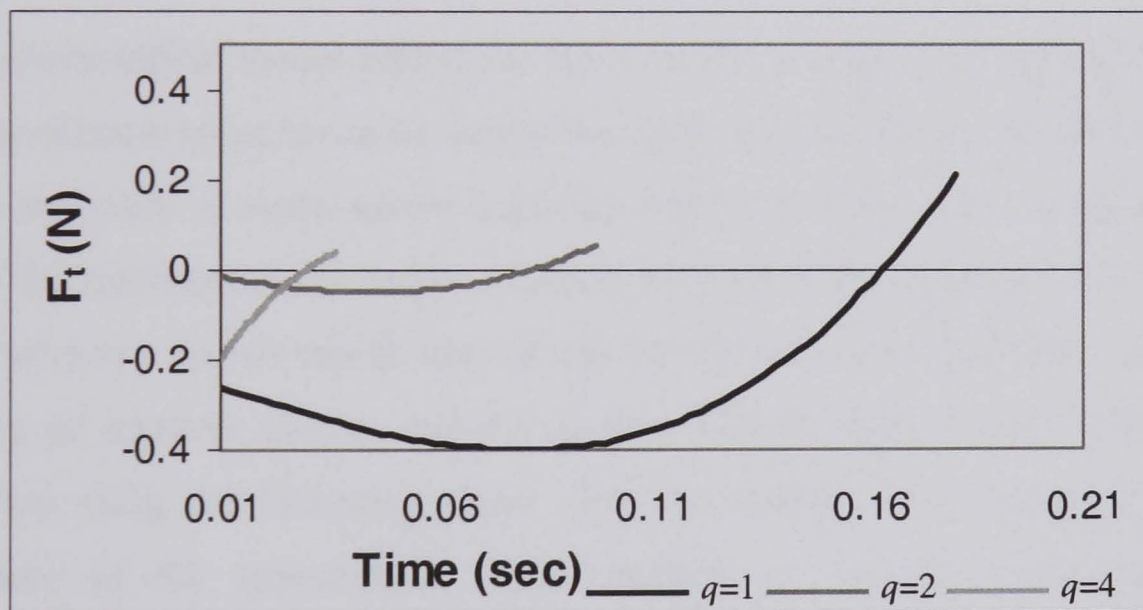


**Figure 3.20** Average trend of the horizontal component of contact force during sliding of one element sphere over another.

### 3.8 Estimation of error in contact force for a multi-sphere particle

In the previous section the quantification of pseudo-friction for cylindrical model particles (identical element spheres) sliding over each other has been presented. The pseudo-friction has been related to the maximum possible deviation of the direction of contact force from the real situation (real particle boundary) when an element sphere of a model particle contacts another model particle.

In the following section a method is presented which quantifies the deviations of the contact force orientation and displacement of the contact point from the true contact point (i.e. between two real particle surfaces) for the more general case of axi-symmetrical model particles comprised of element spheres of varying diameter. This deviation is then related to the amount of pseudo-friction to estimate the additional roughness due to element sphere density.

Once an axi-symmetrical model particle is defined, the number, the diameter and the position of its element spheres can be determined and accordingly the smallest element sphere in an assembly of multi-sphere particles will be known. The maximum error occurs when the smallest sphere makes a contact with another model particle. Having the smallest sphere, a search can be carried out for the maximum deviation of contact force between all adjacent spheres and the smallest sphere from contact with the true particle surface using the following steps. For this analysis it is assumed that the element sphere of the approaching model particle is moving in the direction perpendicular to the boundary of another contacting particle at the contact point (i.e. the direction of contact force is normal to the particle boundary between two adjacent element spheres).

- (i) Assuming that the boundary of the real particle between the two adjacent element spheres is a straight line, the slope of the boundary can be defined as shown in Fig 3.21 where

$$\theta = \sin^{-1}\left(\frac{R_2 - R_1}{L}\right) \quad (3.16)$$

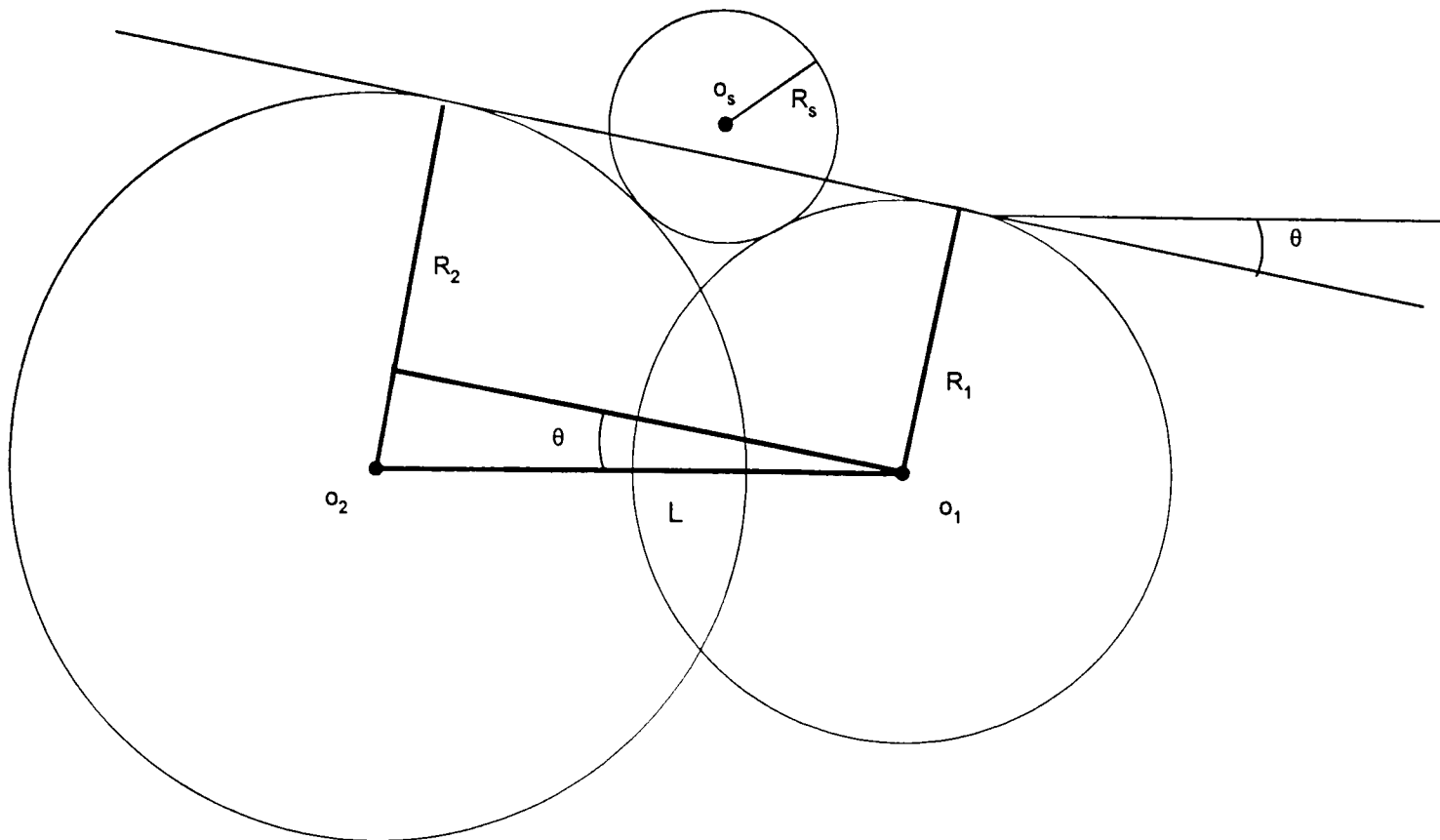


**Figure 3.21** Particle boundary slope determination between two adjacent element spheres.

- (ii) Given the diameter of two neighbouring element spheres and the diameter of the smallest element sphere the distance between their centres can be calculated as

$$\mathbf{a}=\mathbf{R}_2+\mathbf{R}_s, \quad \mathbf{b}=\mathbf{R}_1+\mathbf{R}_s \quad \text{and} \quad \mathbf{c}=\mathbf{L} \quad (3.17)$$

as shown in Fig. 3.22.

- (iii) From Fig. 3.23, using the Cosine Rule, the orientation of normal contact between the spheres ( $\alpha, \beta$  and  $\gamma$ ) can be calculated

$$\begin{aligned} \alpha &= \cos^{-1} [((\mathbf{R}_1+\mathbf{R}_s)^2 + \mathbf{L}^2 - (\mathbf{R}_2+\mathbf{R}_s)^2) / 2\mathbf{L}(\mathbf{R}_1+\mathbf{R}_s)] \\ \beta &= \cos^{-1} [((\mathbf{R}_2+\mathbf{R}_s)^2 + \mathbf{L}^2 - (\mathbf{R}_1+\mathbf{R}_s)^2) / 2\mathbf{L}(\mathbf{R}_2+\mathbf{R}_s)] \\ \gamma &= \cos^{-1} [((\mathbf{R}_2+\mathbf{R}_s)^2 - \mathbf{L}^2 + (\mathbf{R}_1+\mathbf{R}_s)^2) / 2(\mathbf{R}_1+\mathbf{R}_s)(\mathbf{R}_2+\mathbf{R}_s)] \end{aligned} \quad (3.18)$$

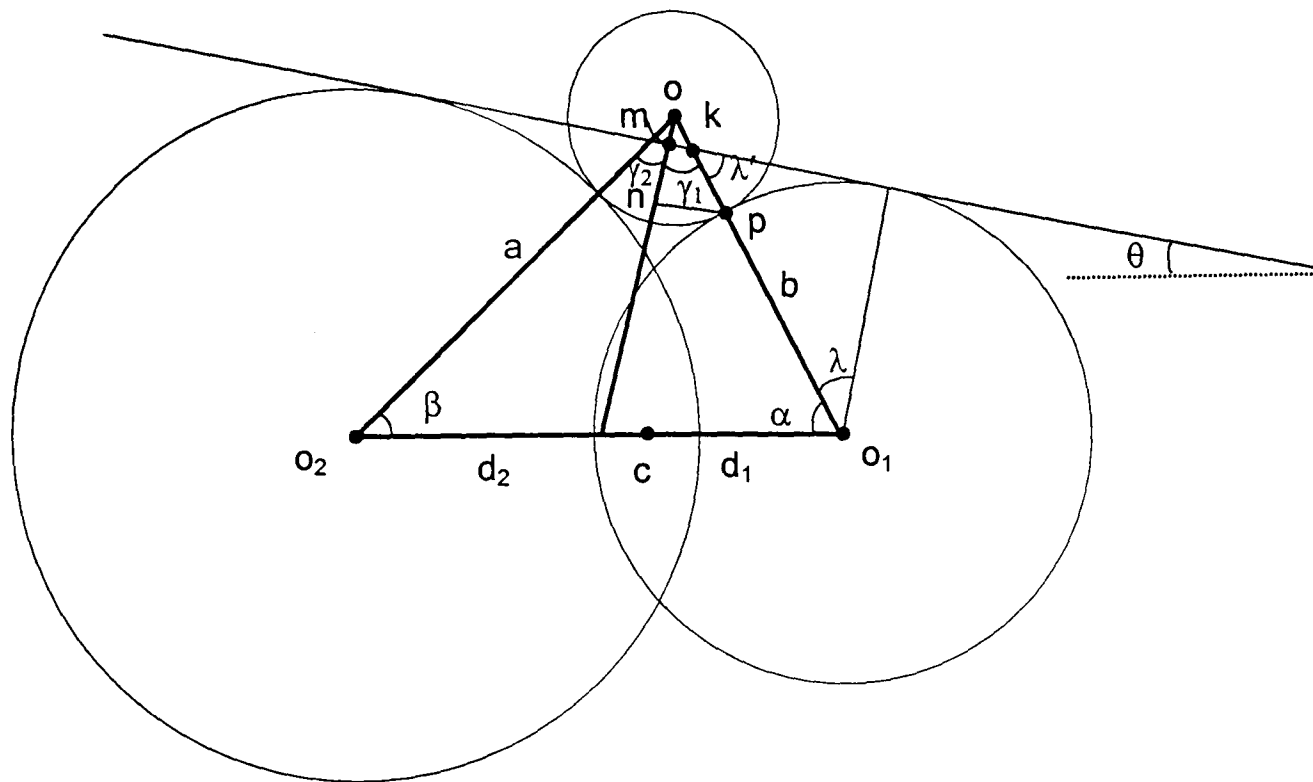


**Figure 3.22** Trigonometric relationship between two adjacent element spheres of a particle when the smallest element sphere belonging to another particle is contacting the particle surface.

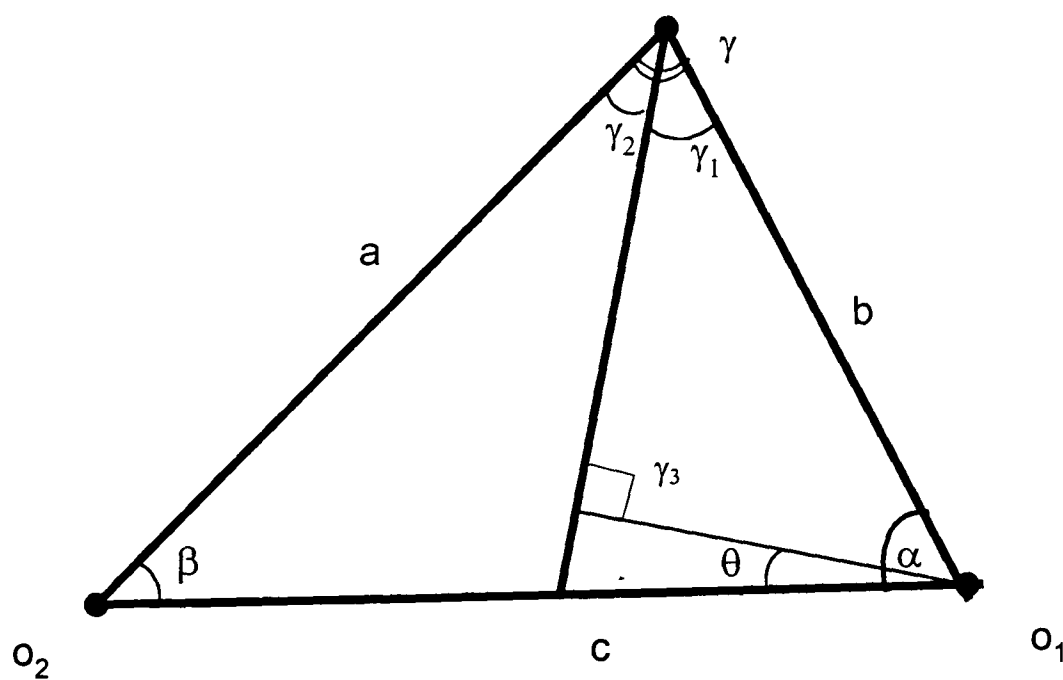


**Figure 3.23** Trigonometric relationship for the deviation of the direction of the contact force between the smallest element sphere and the adjacent element spheres.

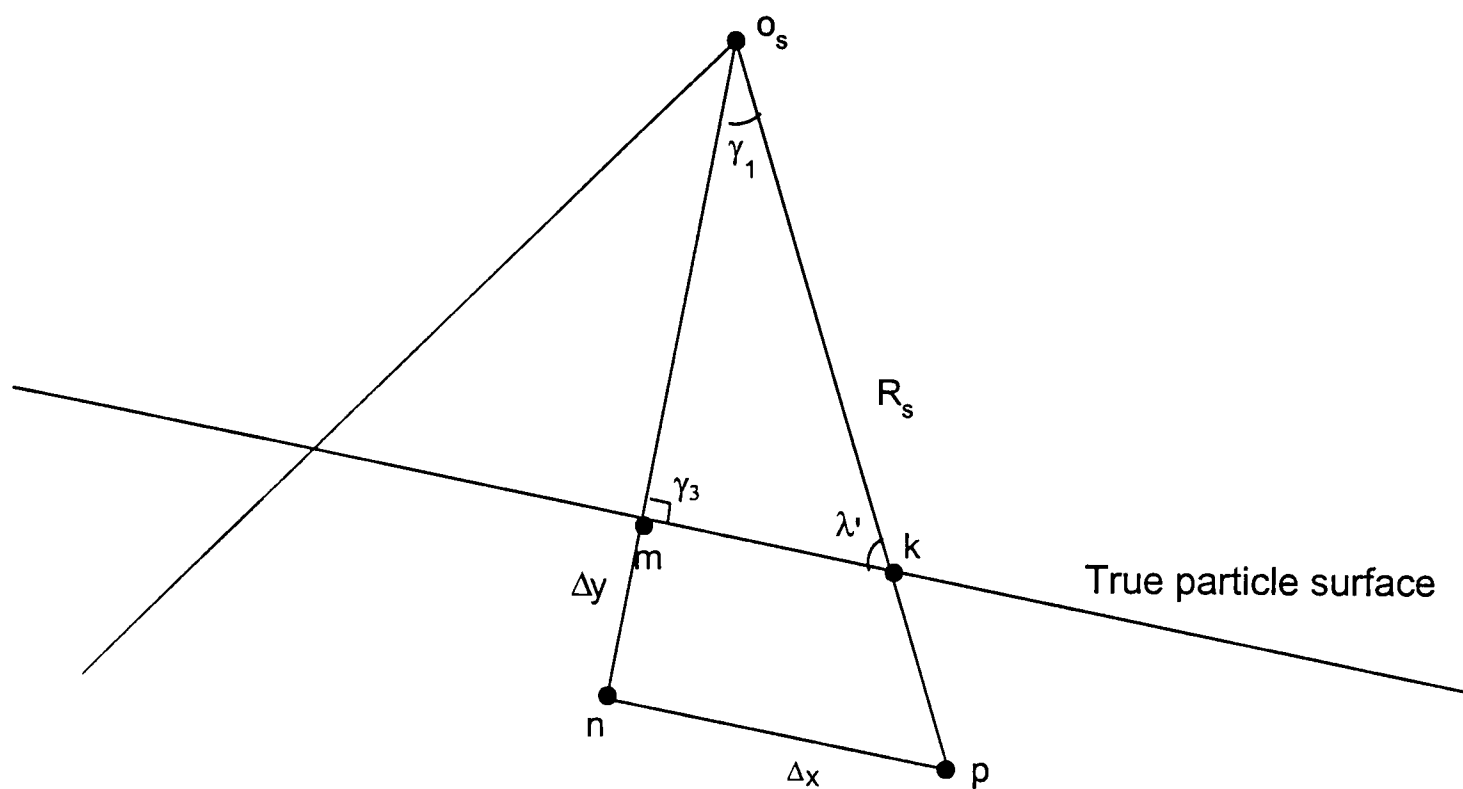


**Figure 3.24** Detail of the trigonometric representation of the displacement of contact point position on element spheres from the “true” particle surface contour.

- (iv) From Fig.3.24 the displacement of the contact point on each of adjacent element spheres can also be determined. Since it is assumed that the normal contact force is perpendicular to the boundary of the real particle boundary such that  $\gamma_3=90^\circ$  then

$$\gamma_1=90+\theta - \alpha \quad (3.19)$$

Also from figures 3.22 and 3.24 it can be shown that

$$o_s k=R_s+R_1(1-1/\cos(\gamma)) \quad \text{and} \quad o_s m= o_s k \cos(\gamma_1) \quad (3.20)$$

The displacement of the contact point in the direction of contact force ( $\Delta y$ ) and normal to its direction ( $\Delta x$ ) for sphere (1) is then

$$\Delta y_1 = (R_s - o_s k)\cos(\gamma_1) \quad \text{and} \quad \Delta x_1 = R_s \sin(\gamma_1) \quad (3.21)$$

For model particles comprised of a number of identical element spheres then

$$\gamma_1 = \gamma_2 = \gamma/2 \quad (3.22)$$

hence, the direction of contact force and the position of contact point would be the same for both adjacent spheres. The maximum error for a model particle comprising equal sized, non-overlapping element spheres is  $\gamma=30^\circ$ ,  $\Delta x=0.25 D$  and  $\Delta y=0.067 D$  where  $D$  is the diameter of the element sphere.

This method therefore, makes it possible to calculate the maximum deviation in the direction of contact force and the position of the contact point selection of a suitable model particle depends on the specific objective of the simulation.

Considering the results obtained in section 3.7 for pseudo-friction, it is seen that when  $q$  is 4 the amount of pseudo-friction is negligible. From above calculations, for a particle comprised of identical element spheres when the sphere density is 4, the deviation in the direction of the contact force is equal to  $7.2^\circ$ . The horizontal and vertical displacement of the contact point are 0.06 and 0.01 element sphere diameters respectively. Therefore, it can be concluded that for a model particle comprised of different element sphere sizes, if the maximum deviation in the direction of contact force for any element sphere is less than  $7^\circ$  the pseudo-friction is negligible and the sphere density is suitable. For any sphere density less than 4 or for non-cylindrical particles, any deviation of contact force greater than  $7^\circ$  the direction and the magnitude of the contact force should be normalised to get better simulation results. Since different contact conditions may occur depending on the dynamic circumstance of approaching particles, the normalising method should consider all different situations. Further investigation is needed to incorporate a suitable normalising method in the DE code to take into account the effect of pseudo-friction for model particles due to additional roughness of model particles resulting from interlocking between sphere segments.

## 3.9 Simulation examples

In this section the objective was to demonstrate the applicability of the MSM for simulation of different industrial and agricultural processing problems. To show the capability of modified DE program some simulation examples are presented. Each simulation involved creating axi-symmetrical particle(s) with a desired shape and a specific workspace geometry. The systems in these simulations are those which are most popular in agricultural processing operations such as filling and discharge of particles from a bin, conveying and particle singulation.

### 3.9.1 Conveying a tapered shape particle in a 2-D simulation

In this simulation a conical shape particle (such as a carrot or a sugar beet) has been generated. The objective was to show that although the modified DE code is a fully 3-D program, it can also be used for generation of a 2-D system. In this way, the  $Y$  direction cosine of the longitudinal axis of the particles during the particle generation has been set to zero. Therefore, the particles have been positioned in the  $X$ - $Z$  plane and the element sphere of the particles could only touch each other through their arc segments, which lay in this plane (this is possible numerically but not in a physical model). Since there was no contact force in the  $Y$  direction, further movement of the particles was restricted in this plane resulting in a 2-D simulation of a 3-D system.

The system comprised an upper conveyor with a constant velocity in the  $X$  axis direction, and a lower moving surface also with a different constant velocity in the opposite  $X$  axis direction and four fixed boundary walls. The upper conveyor has been created by appropriate setting of the middle wall partitions (figure 2.10) through the command line **BOTtom**. The distance between the front and back walls has been set to twice the longitudinal diameter of the model particle.

At the beginning of simulation a model particle comprised of 13 element spheres has been generated at a desired height above the upper conveyor. Gravitational acceleration has been applied to the particle which dropped onto the upper conveyor. The friction between particle and the conveyor caused the particles to move in the direction of travel of the conveyor and dropped onto the lower surface. Figure 3.25

shows 3 sequential snapshots of the particle during simulation. The video clip of this simulation also can be found in Appendix F.

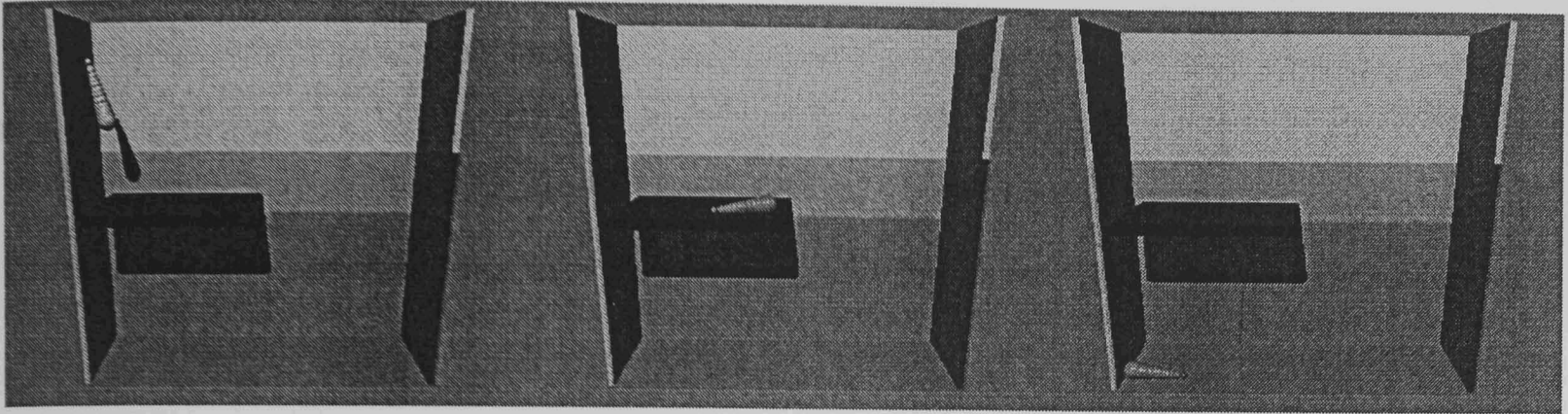


**Figure 3.25** snapshots of particle handling in a 2-D system. Pov Ray has been used to create the pictures.

### 3.9.2 Dropping an irregular shaped particle in a 3-D system

In this simulation an irregular shaped axi-symmetrical particle has been created in the same environment as the simulation presented in 3.9.1. The objective of this example was to demonstrate the ability of the model to create a particle with an arbitrary boundary profile and also to show the ability of the program to model the 3-D rotation of the particle.

A model particle comprised of 15 element spheres with an arbitrary boundary profile has been generated and positioned at a desired height above the upper conveyor with a random orientation. As shown in figure 3.26 the model could simulate the rotation of the particle. This can be seen continuously in the video clip extracted from the simulation results (Appendix F). A similar physical phenomenon is seen frequently during the processing of agricultural materials. It is important for soft materials such as fruits and vegetables since the impact force after particle dropping may cause bruising on the surface of the particle. As shown in Figure 3.27 when a particle is dropped from a higher position depend on the original elevation of particle, the maximum contact force occurs for the first collision and then according to the visco-elastic properties of particle (damping), it will bounce a number of times. This phenomenon is shown in the figure with some peak contact forces after the maximum contact force.

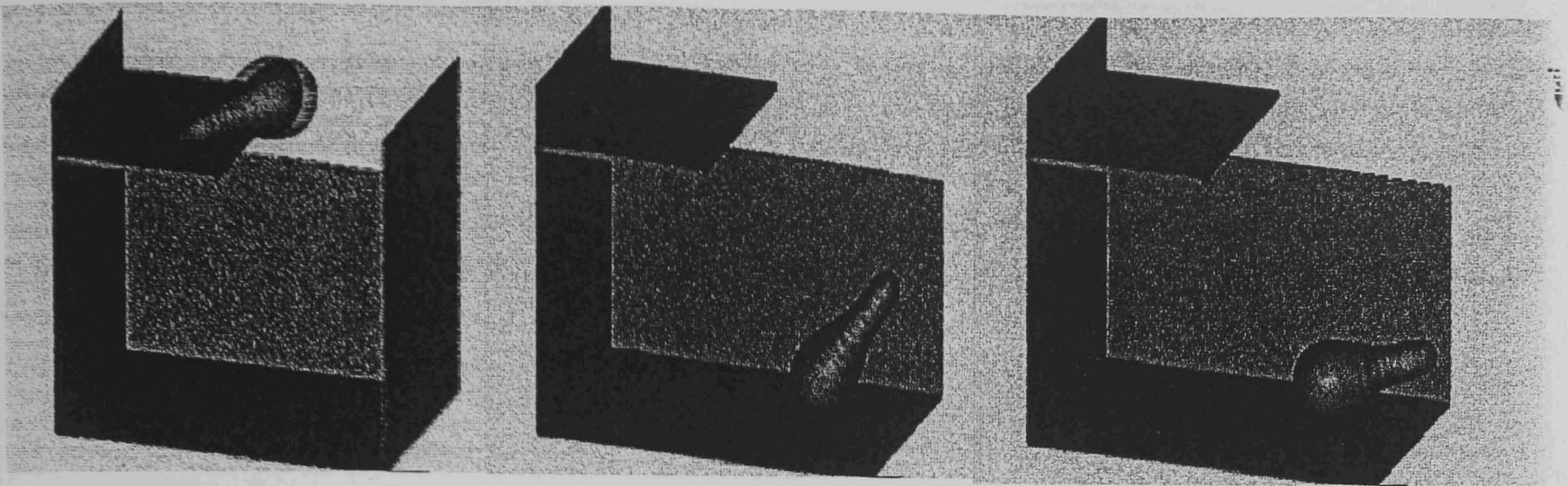


**Figure 3.26** snapshots of particle handling in a 3-D system. Auto cad has been used to create the pictures.

Examples of the type of mechanical information which can be extracted from the MSM model is shown in Figure 3.27. In section (a) of this figure the contact normal force between the model particle and the conveyor has been recorded every 50 time-steps for the whole period (2.5s) of particle conveying and dropping. The discrete recording of the data with data output frequency of every 50 time steps was useful to find the time and place of the critical collisions. However, this kind of recording was not accurate since by stepwise recording some data were missed. For the period of a critical collision (specified by a sharp change in the contact normal force) the frequency of data output increased to every time step (extracting the data in each time-step) (Fig 3.27(b)) to record the evolution of the collision force.

The higher frequency of data output provided the most accurate recording of the collision force, as none of the data was missed. Comparing Fig. 3.27(a) and (b), it is seen that there is a substantial difference between the maximum normal contact force in the two methods (low and high frequency of data output) of extracting the data. The lower maximum normal contact force in Fig. 3.27(a) than (b) indicates that some data were missed by stepwise recording of the data. Fig. 3.27(c) shows the tangential contact forces (abrasive) between the model particle and surface during conveying and dropping. The sharp changes in the magnitude of the tangential contact force indicate the places there was abrasion of the particle by the surface.

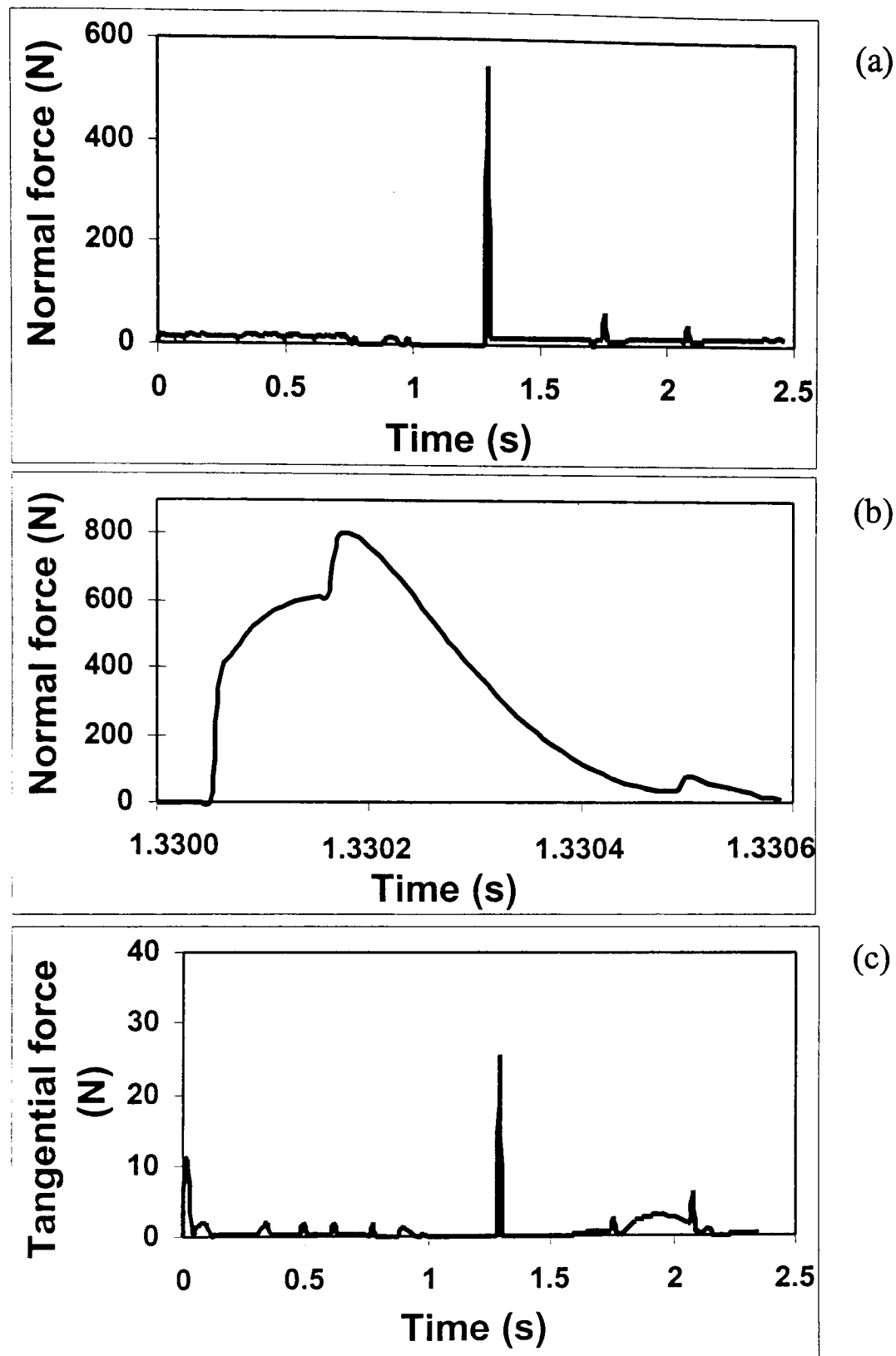


**Figure 3.27** Particle interaction between boundary surfaces and a model particle dropping between two conveyors. a) Normal contact force between model particle and conveyor; b) evolution of collision force between model particle and lower moving surface; c) tangential forces (abrasive) between model particle and conveyors during handling.

Comparison between Fig. 3.27(a) and 3.27(c) shows that this occurred when the normal contact force was high (corresponding to impact). This simulation demonstrates that the model based on the multi-sphere approach is a promising tool for measuring the contact force between non-spherical shaped fruits and vegetable during handling to study bruising for example. More discussion on the collision force and tangential force with details of the effect of time step and damping coefficient on simulation results is presented in Chapter Three.

### 3.9.3 Conveying an assembly of conical particles

This model is the same as discussed in 3.9.1 except that an assembly of particles has been modelled instead of a single particle. Twenty tapered particles each consisting of 13 element spheres have been created in the left hand side of the workspace at the top of a conveyor moving at constant velocity as shown in Fig. 3.28. The particles have been then dropped onto the lower conveyor also moving at constant velocity in the opposite direction. It can be seen that the model was able to simulate the interaction between particles in a 3-D system. Contact data for any particle of interest with other particles or a surface could be recorded (see Fig.3.27 as an example of data output from the MSM code ).

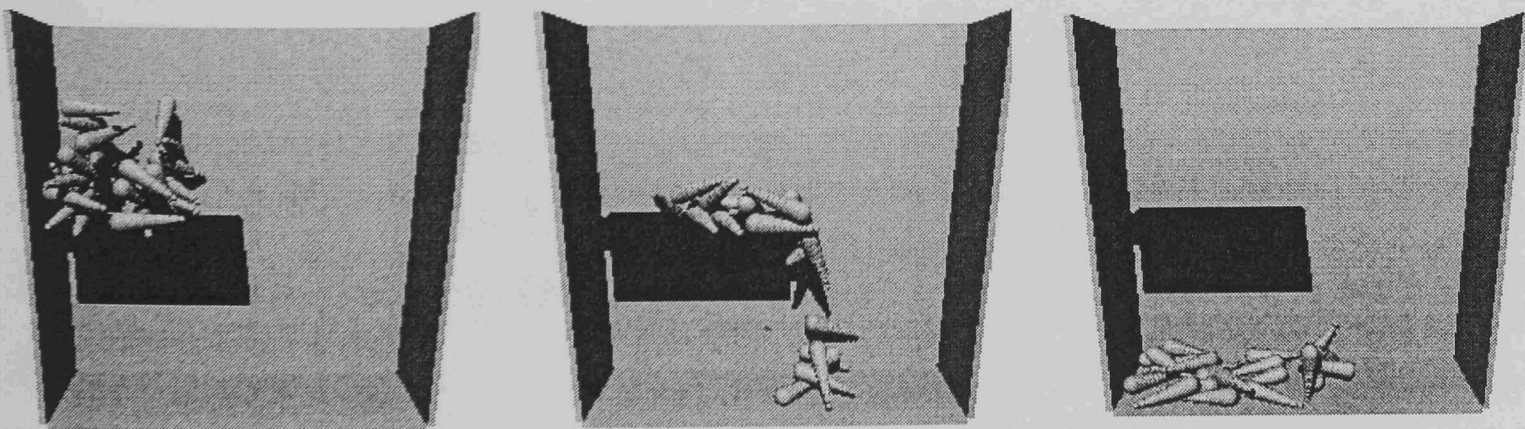


**Figure 3.28** snapshots of particles handling in a 3-D system (Pov Ray pictures).

### 3.9.4 Discharge (flow) of particles from a bin

Flow of particles from a hopper is a common problem in many areas such as grain handling and powder technology. Understanding of the interactions occurring during the flow is needed for better design of silos and hoppers. In this regard a series of simulations have been carried out to show the potential of the DE model to investigate the effect of particle properties such as shape, inter-particle friction and hopper parameters such as orifice size in the flow characteristics of particles.

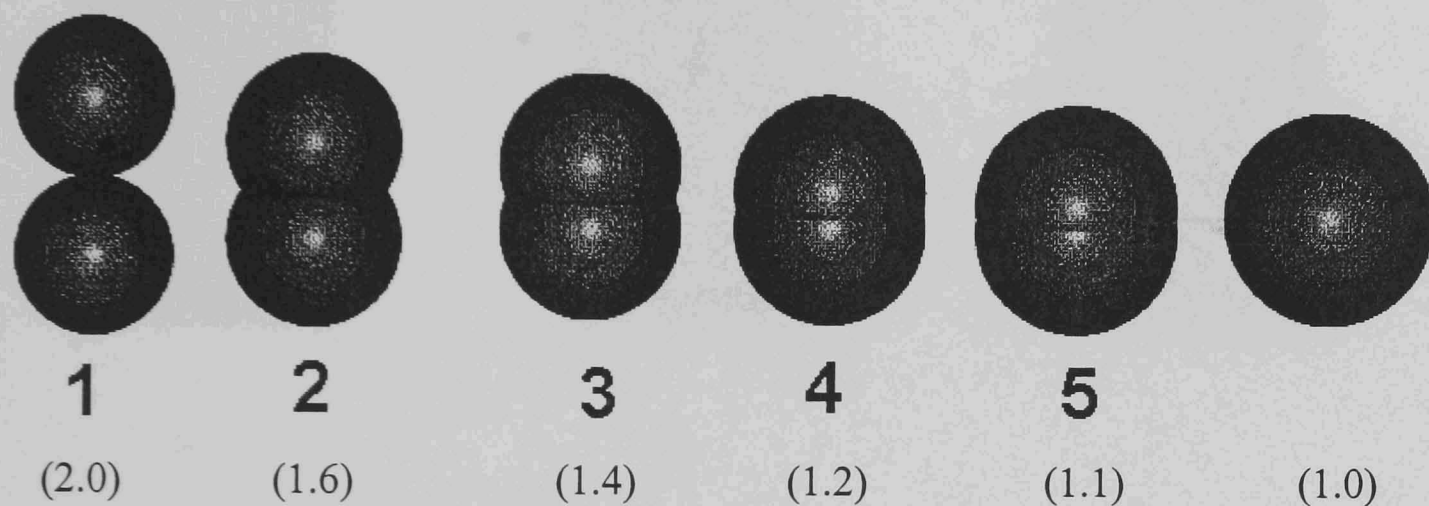


**Figure 3.29** Five different model particles used in the flow simulations. In each case the radius of the element spheres and their overlap are such that the volume of each particle is equal to the volume of a sphere of unit radius. Numbers in bracket show the aspect ratio of the particles.

In these simulations five different model particles each comprised of two element spheres have been generated. In each case the radius and the amount of overlap between the element spheres has been calculated such that the volume of each particle was equal to the volume of a sphere of unit radius but their aspect ratio was different (Fig 3.29).

In each simulation 200 model particles have been randomly generated and then consolidated at the bottom of the upper box by applying gravitational acceleration to the assembly of particles (Fig. 2.13a). The dimensions of the upper box was  $20 \times 10$  cm for all simulations with the enough height to accommodate all the particles. The orifice

has been positioned in the middle of the upper box with 5cm width for all simulations. The flow has been started by the command line **FLOW** in the input file, which repositioned the orifice (wall no. 10) from the centre of the middle wall to the bottom of the workspace. Figure 3.30 shows three snapshots of the flow simulation of 200 model particles each comprised of two element spheres in a 3-D system.

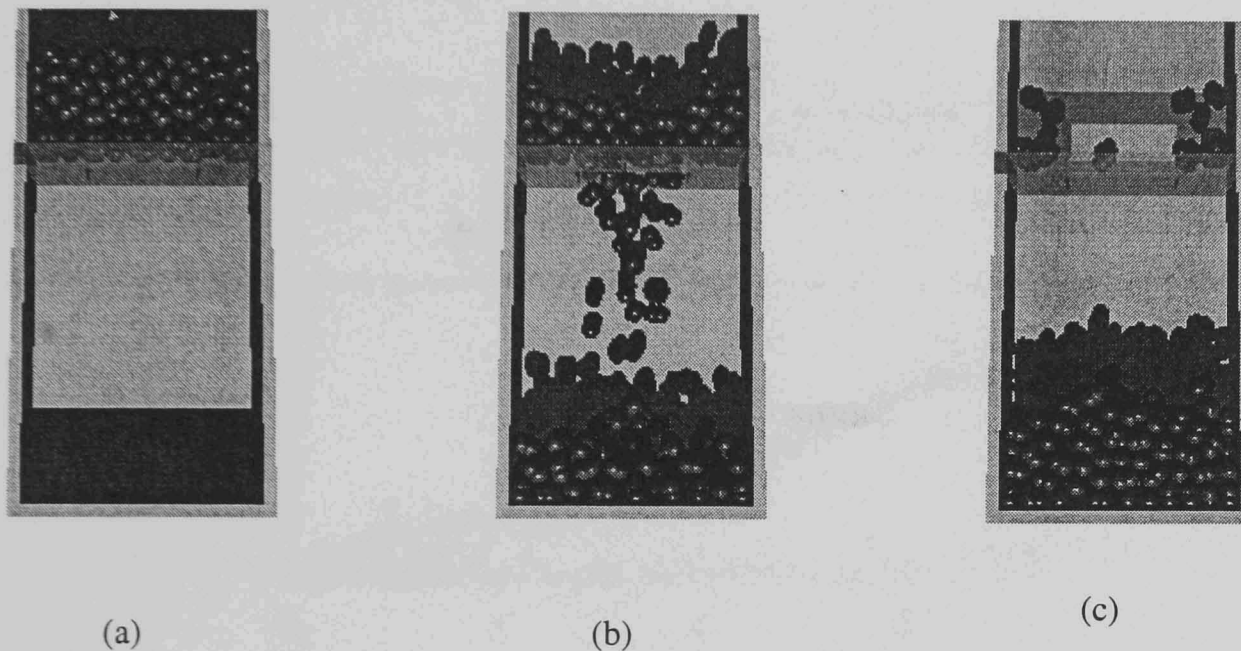


**Figure 3.30** Snapshots of numerical flow experiment for model particles of case 3. (a) At the end of gravitational deposition (consolidation) of particles; (b) during particle flow and (c) at the end of flow (Pov Ray pictures).

During the simulation the cumulative number of particles that passed through the orifice have been recorded and then plotted versus time. Figures 3.31 shows some of these simulation results. In this figure the effect of orifice size and particle shape (particles of different aspect ratio) on the flow of particles and arching phenomenon are shown as an example of the model output. Arching is common during flow of particles from an orifice especially when the orifice is small. It has been predicted that for a particular orifice size, the tendency of arching increases as the aspect ratio of the particles increases.

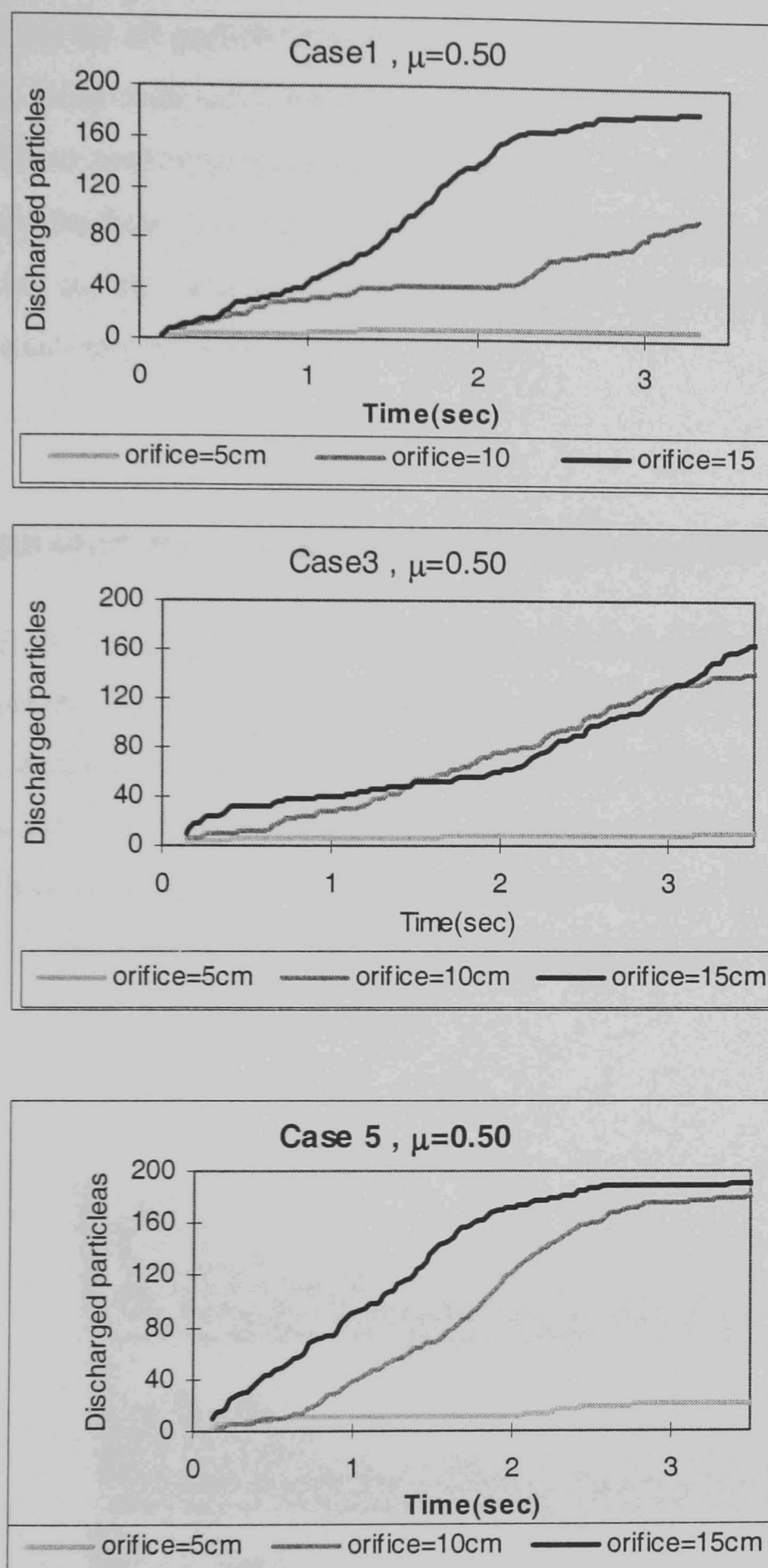


**Figure 3.31** Examples of flow simulation results for model particles of different shapes (aspect ratio) from a flat bottom hopper.

A permanent arch occurred (shown by a horizontal line in the graph) when the orifice was small (5 cm) for all particle shapes. By increasing the orifice size the probability of arching has been reduced however it was still higher for the particles of higher aspect ratio. These preliminary numerical simulations demonstrate that the model can be used to study the flow of a particulate assembly. More numerical experiments on the flow of particles and the details of the effect of particle shape on the different aspects of flow are presented in Chapter Five.

### 3.9.5 Singulation of an assembly of Spheroidal particles

Singulation is the term applied to the process of marshalling fruits from initially disarrayed assembly into a non-contiguous single file (Yong, 1979 and McRae, 1985). It is a common operation during fruits and vegetable inspection and packing. In the following simulation some spheroidal objects have been generated in a random manner and then singulated by means of two conveyors of moving at different speeds in the same direction. The system also consisted of five fixed boundary walls to contain the objects.

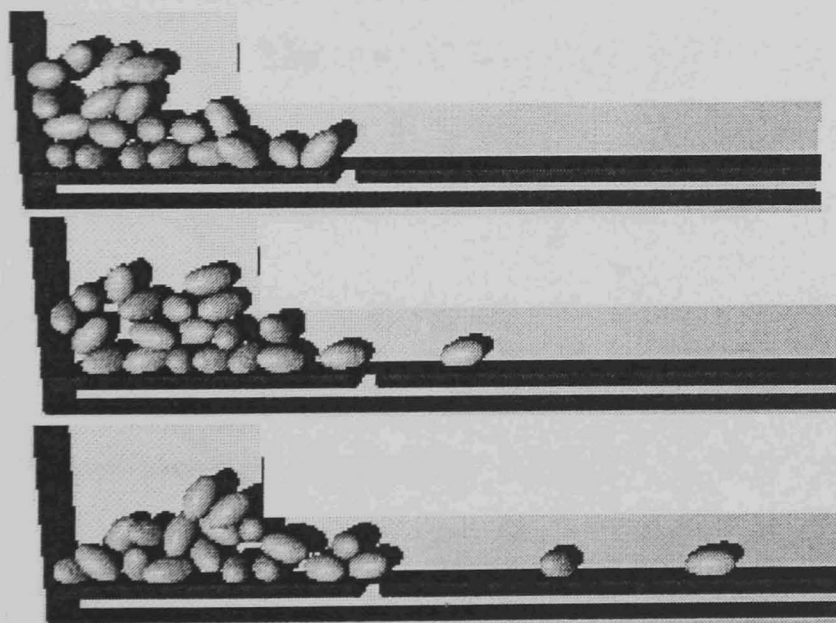


**Figure 3.32** Spheroidal particle singulation simulated by DE model using multi-sphere method.

---

The lengths of conveyors have been selected through command line **BOT**tom to set the partitions of the middle wall (Fig. 2.10). The objects have been selected from an spheroid function of aspect ratio of two and then generated with 15 element spheres of different diameters and overlap. At the beginning of this numerical experiment the particles have been deposited on the top of the left conveyor. The operation has been continued by applying a constant horizontal velocity to this conveyor and the right hand conveyor through a command line started with keyword **MOVE** and followed by two numbers which are the velocity of the left and right conveyor respectively. The relative horizontal velocity between the particles and the conveyors and the friction between them create a horizontal force which moved the particle with the same speed as the conveyors. When particles transferred to the faster conveyor they accelerated which resulted in singulation as shown in Fig. 3.32 (see attached CD in Appendix F for the video clip).

### 3.10 Run time

The major disadvantage of the DEM for modelling many real scale problems is its considerable computational requirement (Horner *et al.*, 1998). Even with the rapid growth in computer power, the problem size usually has to be scaled down in order to achieve reasonable run times. The run time is affected by several factors such as number of particles, relative position of particles (average contact condition), the contact law (linear or non-linear) and the real time for the simulation.

A number of simulations have been carried out in order to evaluate the performance of the program on a serial computer using the multi-sphere approach. In these simulations the effect of number of element spheres per particle run time has been investigated. Two sets of simulations have been performed; in the first set, three assemblies each comprised of 200 multi-sphere particles of aspect ratio two have been created with different numbers of element spheres (2, 3 and 5 element spheres per particle). The radius of the element spheres was unity so that the time step was constant and equal to  $1.0E^{-5}$  sec. Fig 3.33 shows the particle assemblies at the end of consolidation after 300000 time steps (3 seconds real time).

In the second set of simulations three assemblies of single sphere particles have been created with 400, 600 and 1000 particles equal to the total number of spheres in the assemblies of multi-sphere particles with 2, 3 and 5 element spheres per particle respectively. The model was run on a PC workstation with a K6 AMD 380 MHZ processor. The average run time per time step has been measured for each particle per time step and also for each sphere.

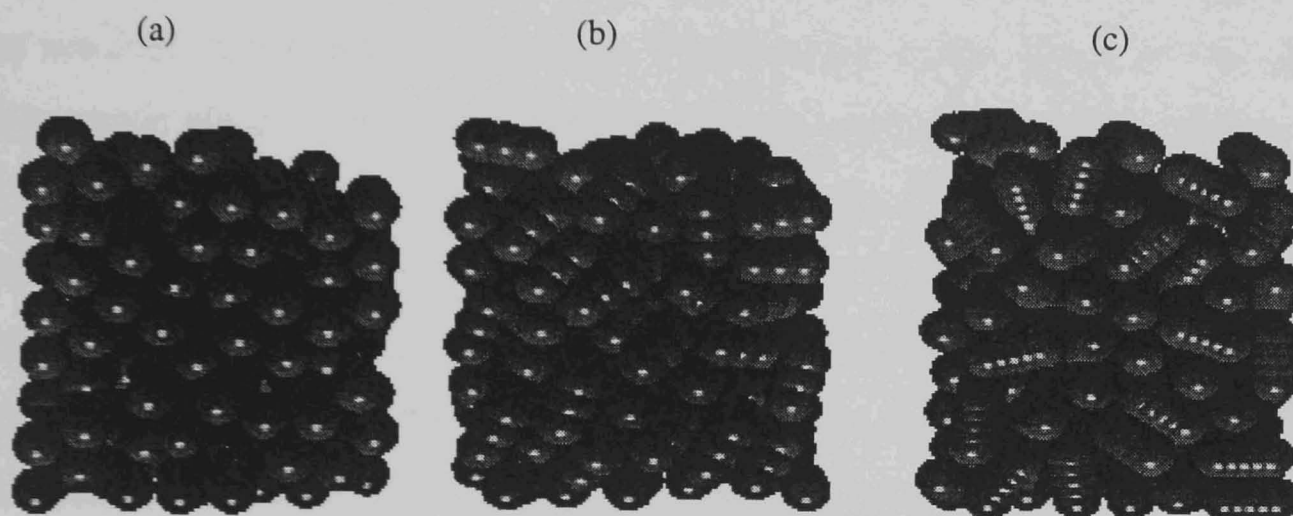


**Figure 3.33** Simulations of gravity deposition of multi-sphere particles: (a) 2-element spheres, (b) 3-element spheres and (c) 5-element spheres particles respectively. The simulation have been performed for the same particle mass, same time step and same time elapsed (same number of time steps).

As expected, in the case of multi-sphere particles, by increasing the number of element spheres per particle the run time per particle increased. Although such a direct relationship was expected, the results (Table 3.5) also show that for multi-sphere particles of high sphere density (number of element spheres per unit length) the run time per sphere was also increased resulted in a non-linear increase in the run time per particle. As the sphere density increased, during the contact search in each sub-box, each sphere should be tested against more spheres requiring more search time. Therefore, for multi-sphere particles, the run time not only increased due to the number of spheres per particles but also increased due to increasing the average run time per element sphere. However it seems that the above justification is not valid when the

---

average run time per sphere for the assembly of particles composed of three element spheres per particle is compared with the result of two-element spheres particles (less run time per sphere in the assembly of three-element spheres per particle). This is likely to be related to the position of the third element sphere in the particle. As shown in Fig. 3.33 (b) for three-element particles, the two other element spheres surrounded the third element sphere as it has been positioned between them. Therefore, the exposed surface of this element sphere has been reduced, consequently during the contact search, this sphere might be tested against smaller number of neighbouring spheres resulted in a smaller search time. Furthermore, as the centre of this element sphere has been placed at the centroid of the particle, the force transformation from the centre of the sphere to the centroid of the particle did not happen, resulted in a less time consumption. However, the run times in tables 3.5 and 3.6 are the sum of the time consumption for contact search and contact force resolution, therefore these tables can not differentiate between the two parts of the run times. This was due to limitations of PC-based code in which there was no command to access CPU time. Because of this the exact reason for the smaller run time for particles of three element sphere can not be determined. Further research require using alternative method which allow obtaining CPU time.

In the case of assemblies of spherical particles (Table 3.6) the average run time per sphere was almost independent of total number of sphere in the model. Comparing spherical particles with multi-sphere particles (in each case with the same number of spheres in the model), it is seen that the run time per sphere for the assemblies of multi-sphere particles is higher than assemblies of spherical particles. Part of this difference is related to the additional calculations for spheres in the multi-sphere particles for transferring the forces and moments from the boundary of the element spheres to the centroid of particles.

**Table 3.5** Average run time per time step of simulations for model particles of different number of element spheres.

Number of spheres per particle	Total no. of spheres in the model	Run time (sec/ $\Delta t$ )	
		Per sphere	Per particle
2	400	$2.5 \times 10^{-4}$	$5.15 \times 10^{-4}$
3	600	$2.1 \times 10^{-4}$	$6.39 \times 10^{-4}$
5	1000	$3.2 \times 10^{-4}$	$15.81 \times 10^{-4}$

**Table 3.6** Average run time per time step for the simulation of the gravity depositions of particulate assemblies of spherical particles.

Total number of sphere in the model	Run time (sec/sphere/ $\Delta t$ )
400	$1.50 \times 10^{-4}$
600	$1.45 \times 10^{-4}$
1000	$1.49 \times 10^{-4}$

### 3.11 Summary

Computer simulation with multi-sphere model (MSM) particles has been applied to a number of common particle-particle and particle-surface contact scenarios. The analytical validation of the model confirmed that this method can be used for operations such as sliding, dropping and conveying of non-spherical particles with high aspect ratio. The effect of parameters such as the time step and damping coefficient will vary depending on the dynamic situation of particles but the following has been determined. Generally, a smaller time step is needed for simulation of particle collision

---

than for a quasi-static system. Also for a quasi-static system a smaller damping coefficient will provide more accurate results.

The multi-sphere method of representing particle shape approximates the surface contour with all or parts of element sphere surfaces. The lobed surface of multi-sphere particles creates a pseudo-friction effect when such particles slide across one another due to the generation of forces opposing the direction of movement. These forces are the component of the contact force between element spheres of separate particles which is parallel to the enveloping or “true” contour. The enveloping contour is the surface to which the element sphere surfaces are tangent. In contact between model particles the contact point will often be inside the true contour. The distance the contact point moves inside and the associated deviation of the direction of the contact force from the normal to the true surface depends on the number and position of the element spheres in a particle. The greater the density of element spheres the lower the deviation in the contact normal direction and subsequently the lower the pseudo-friction effect. The results of the simulations and theoretical calculations showed that pseudo friction is negligible when sphere density is at least four (for cylindrical particles) or the maximum deviation of the normal contact force is less than  $7^\circ$  (for model particles of varying element sphere diameters).

To demonstrate the capability of the modified model some simulation examples have been presented. In these examples different particle shapes have been used in some systems typical of most agricultural system operations. The run time of the MSM model for a simple simulation exercise (consolidation of particulate assemblies) with different sphere densities showed that for particles of high sphere density the average run time per element sphere has been increased resulted in a non-linear increase in the average run time per particle. It has also been observed that for the assembly of multi-sphere particles the average run time per element sphere was higher than the assembly of spherical particles.

## **4. Experimental Validation of the Multi-Sphere Method**

### **4.1. Introduction**

In Chapter three the analytical validation of the MSM along with studies on the effect of time step and damping was presented. While analytical validation provided evidence that the new DE model was properly formulated it could not demonstrate that the MSM could be used to predict the dynamic behaviour of a physical model with specific physical properties.

In the following sections experimental results of the movement of particles in a physical model are compared with the prediction of the MSM DE model. Two different experiments were performed to validate the model at the micro-scale (particle scale) and the macro-scale (bulk scale). In the first experiment the flow of a limited number of particles (10 particles) from a bin were tracked individually and the movement of particles (particle translation and orientation) were compared with model predictions.

In the macro-scale validation the flow of an experimental and simulated assembly comprising a vertical flat bed of 200 elliptical particles through an orifice was compared in terms of bed structure and flow characteristics.

### **4.2. Micro-scale experimental validation**

#### **4.2.1. Materials and methods**

Experiments were conducted on 1:1 scale between the physical model and simulation using approximately identically shaped particles in each. Experiments consisted of vertical displacement of an assembly of two-element particles through a narrow orifice so that particles translated and rotated.

The experimental rig comprised a flat V-shaped hopper with walls made of clear perspex delivering in to a flat column in which moved a motorised piston as shown in Fig. 4.1. The walls were spaced just greater than the diameter of an element sphere which constrained particle movement to two dimensions. Preliminary tests showed that particle rotation about its major axis was minimal during an experiment. Ten particles each comprised of two 45 mm diameter spheres overlapped by 25% of their diameter were used in each experiment. The particles were pool balls made from phenolic resin machined flat at the point of overlap and glued together.

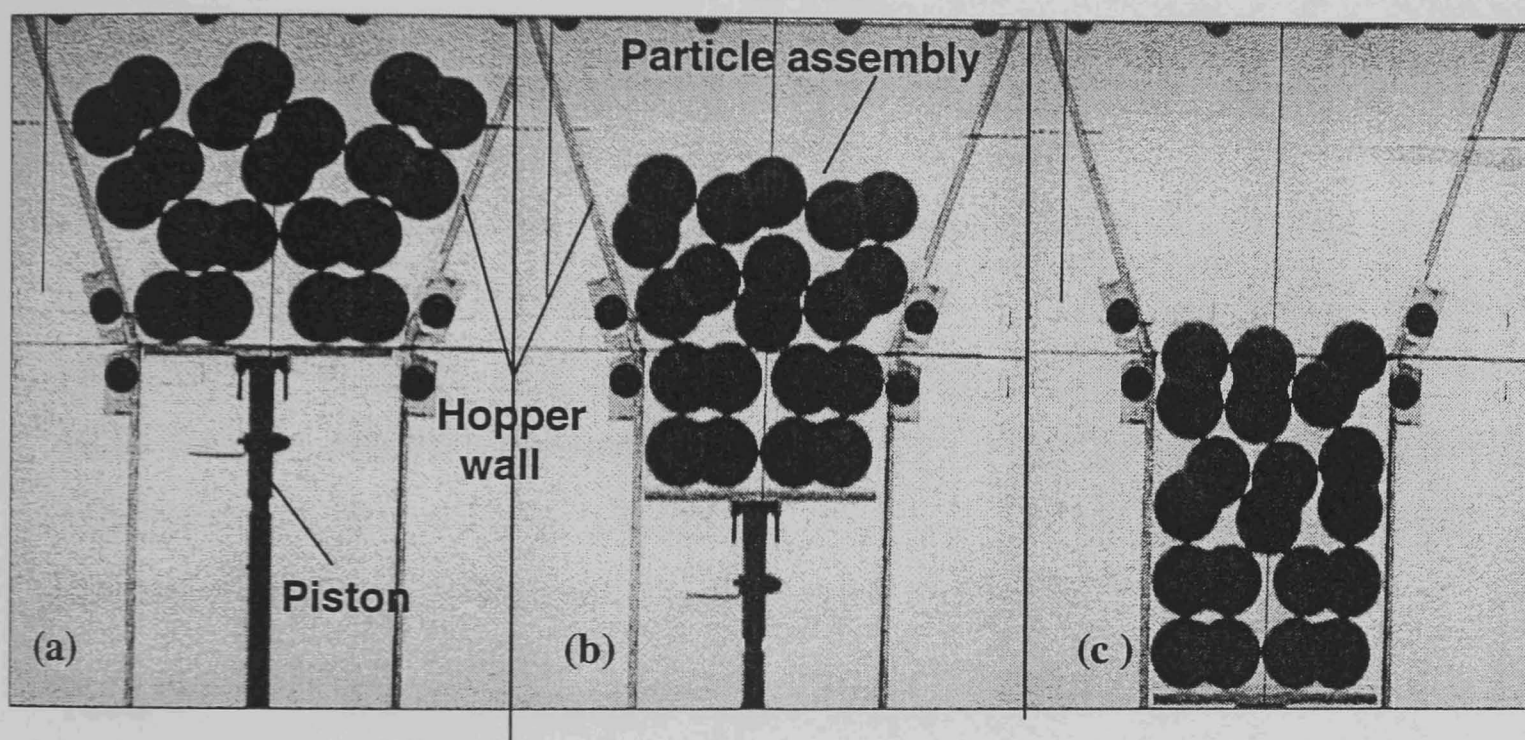


**Figure 4.1** Section of experimental apparatus showing three images from (a) the start, (b) during, and (c) the end of an experimental run.

The physical properties of the spheres are given in Table 4.1. The particle-particle static coefficient of friction was determined by determining the angle at which a block of three rigidly connected particles began to slide over another identical fixed block. The particle-wall coefficient of friction was determined by sliding a block of particles over a sheet of perspex. The coefficient of restitution was determined by dropping a sphere on to a rigidly fixed hemi-sphere and measuring the rebound height. The coefficient of restitution was then calculated from

$$e = (h/H)^{1/2} \quad (4.1)$$

where  $H$  is the drop height and  $h$  is the rebound height. The value shown for  $e$  in Table 4.1 is the mean of 30 replicates. Other data in this table such as Poisson's ratio and Elastic modulus were obtained from the literature (Ritchie, 1965).

In each experiment the particles were placed in the same position and orientation as that of the numerical model. Moving the supporting piston downward, moved the particle assembly at a controlled rate. The velocity of the piston was 4.6 cm/s in all experiments. The piston, drive and drive motor were mounted on a separate frame to that of the hopper to reduce transfer of vibration from the motor to the hopper. A typical arrangement of particles at the start of an experiment is shown in Fig 4.1a. The movement of particles was recorded with a camcorder at a frequency of 50 frames/s. Each frame was extracted from the video file and analysed to determine the particle coordinates and orientation. Each experiment was repeated five times. Two sets of experiments were carried out. In the first set of experiments the same particles were placed in the same positions at the start of each run. The objective was to determine how closely the movement of each particle could be replicated, i.e. how sensitive to initial position was the subsequent behaviour. In the second set of experiments the arrangement of the particles (assembly microstructure) was preserved but different particles were placed in each position in an experiment.

**Table 4.1** Physical properties of experimental particles

Mass	142 g
Element sphere diameter	45 mm
Static coefficient of friction (particle-particle)	0.357
Static coefficient of friction (particle-wall)	0.351
Coefficient of restitution	0.85
Poisson's ratio	0.35
Elastic modulus	6.89 GPa

A numerical simulation was carried out using the measured physical properties and identical hopper and piston geometry. Fig. 4.2 shows the numerical particle set up at the beginning of the run that is identical to the experimental set up (Fig. 4.1a). The velocity of the piston used in the simulation was the same as that in the experiments. Simulations were repeated with the same initial assembly microstructure but using different values for inter-particle friction coefficient to test the influence of this parameter.

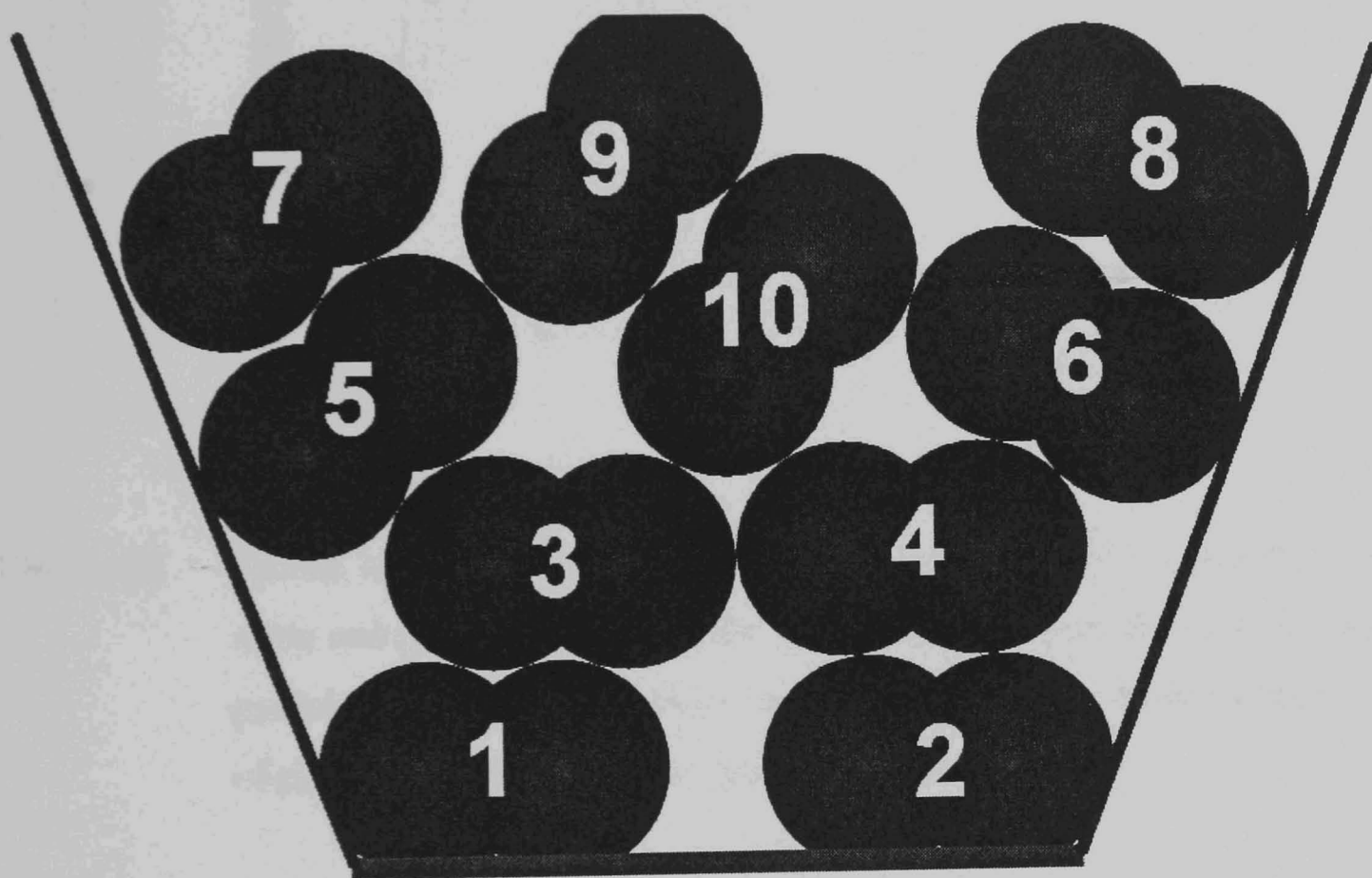


**Figure 4.2** Arrangement of particles in the model assembly to simulate the experimental assembly shown in Fig. 4.1a prior to movement of the piston. Each particle was numbered as shown.

#### 4.2.2. Results and discussion

The tracks of the particle centroids in the two experiments with identical initial assembly structure and particle positions are shown in Fig 4.3. For clarity, the tracks of particles has been separated and shown in two sections. In each section of this figure the track of five particles in both experiments are shown with a pair of curves of the same colour. As it is shown, the tracks for each particle were very similar in both

experiments, which shows that the method of assembly construction resulted in close replication of assembly behaviour.

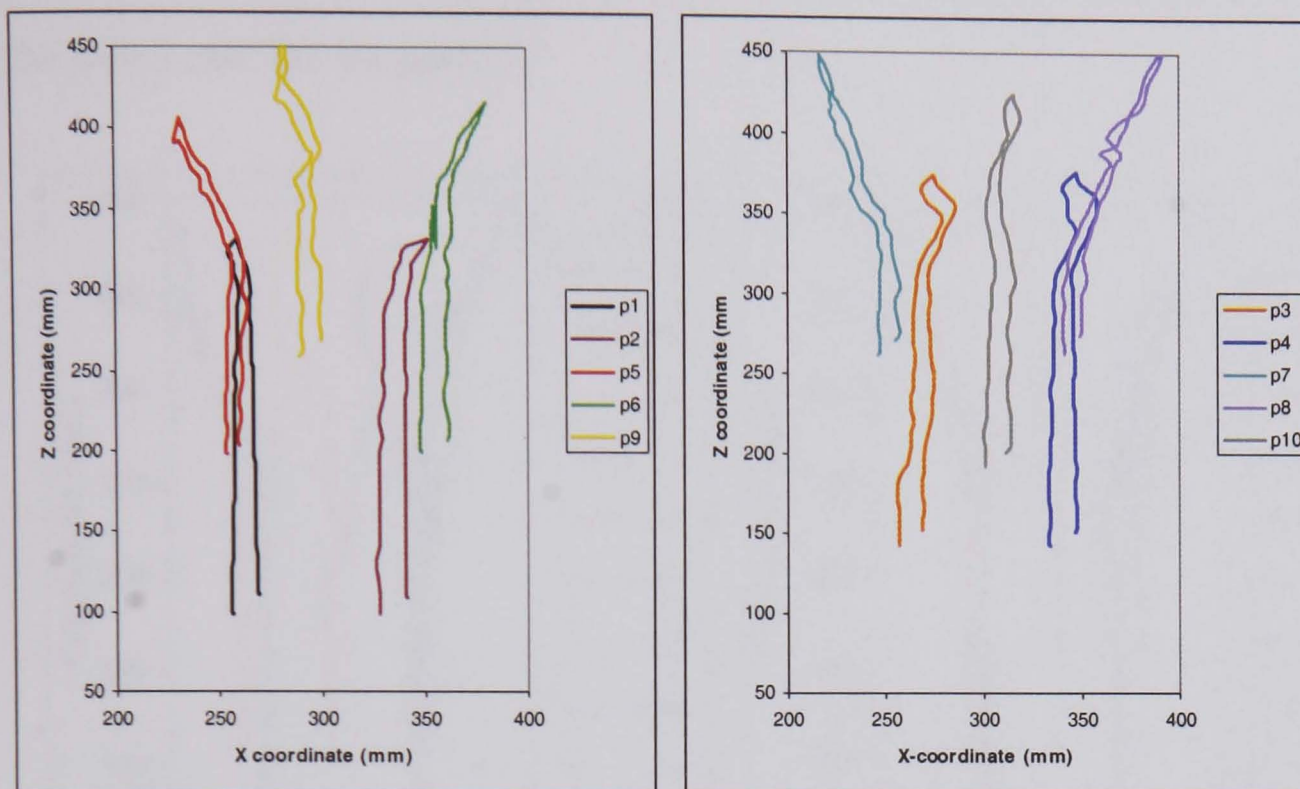


**Figure 4.3** Tracks of the centroids of particles in two experiments (tracks of the same colour), using an identical arrangement of particles (i.e. the same particle with the same position in both replicates), for clarity the tracks of particles has been separated in two sections.

This result also suggested that in order to introduce a variation in the behaviour of the assembly the positions of the particles should be alternated within the same assembly structure. This was because the experimental particles all differed in size and shape by a small amount (due to differences in the amount of overlap and positioning of element spheres) while the simulated particles were all identical. Differences in the size and shape of the real particles were not easily measurable but were implicit in the method of manufacture.

Simulations with particle friction coefficients ( $\mu$ ) of 0.0, 0.1, 0.2, and 0.35 (equal to the static coefficient of friction between particles) resulted in the trajectories shown in Fig 4.4. It can be seen that while the behaviour of some particles was replicated the movement of others (e.g. particle 9) was quite different. The tracks of each particle in the simulation and experiment were compared by calculating the Root Mean Square

(RMS) of the difference in position at identical times. These analysis showed that the best match between experiment and simulation was for simulation using a coefficient of friction of 0.1 (RMS=532mm). The other RMS differences were 1052 for  $\mu=0.0$ , 951 for  $\mu=0.2$  and 731 for  $\mu=0.35$ .

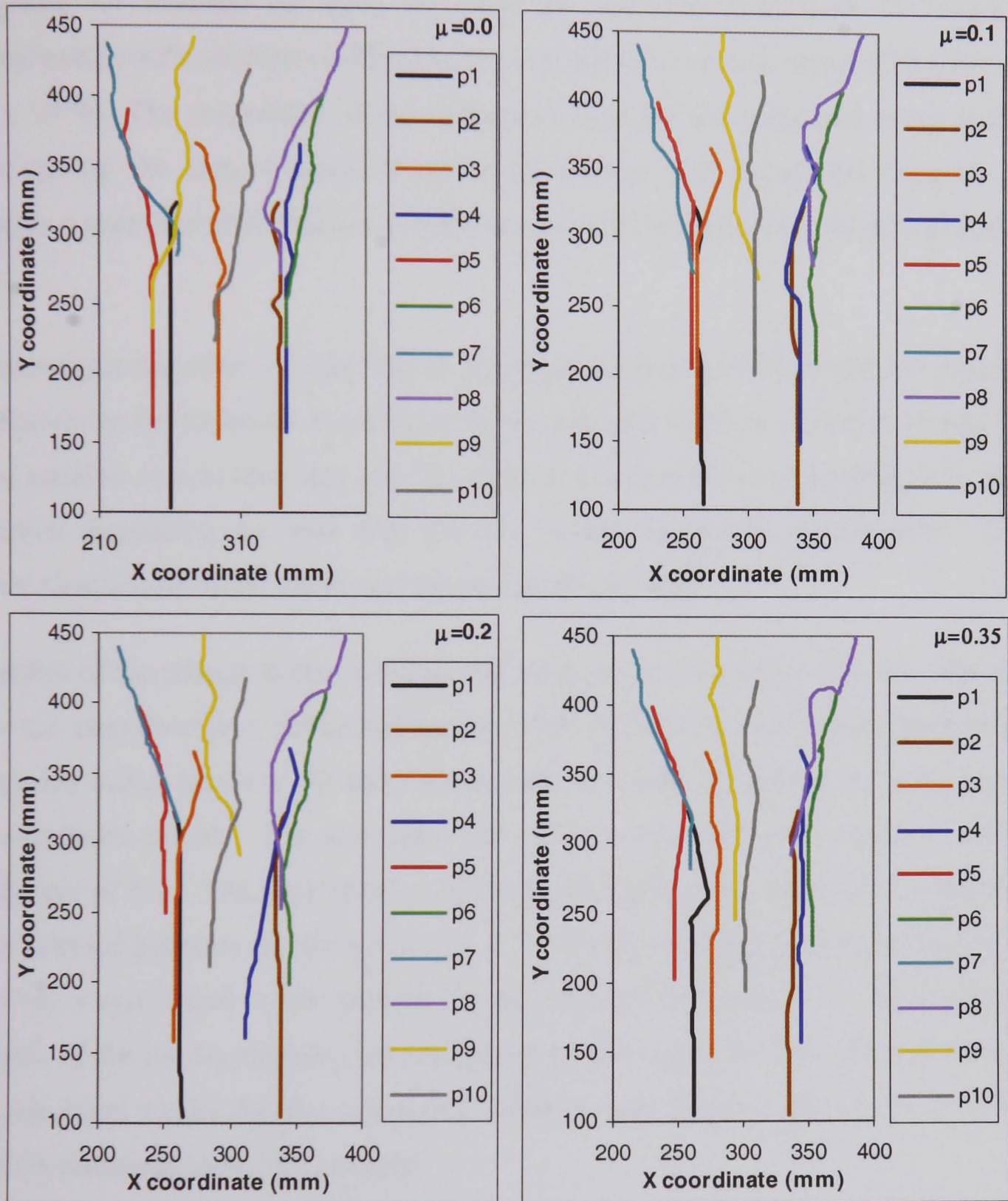


**Figure 4.4** Tracks of particle centroids from simulations using different coefficients of inter-particle friction. The time step for these simulations was equal to the critical time step.

These comparisons showed that the trajectories for a high coefficient of friction ( $\mu = 0.35$ ) and frictionless condition ( $\mu = 0.0$ ) are in poor agreement with the experiment. The closest match was for trajectories using a value of  $\mu$  of 0.1. This is in accord with the commonly observed difference between dynamic and static friction coefficient. The difference between static and dynamic coefficient of friction varies for different materials; for instance for glass on glass the dynamic coefficient of friction is approximately 42% of static coefficient, but for steel on steel it is about 77% (Bloz and Tuve, 1970). The magnitude of the difference between the measured value and the value giving the closest match between experiment and simulation suggests that dynamic rather than static friction coefficients should be used in DE models of particle flow.

To investigate the effect of time step on the predictions of the DE model, the results of simulation for the trajectory of particles were compared with two different chosen time steps, equal to critical time step and 10 times of the standard time step (Fig. 4.5). As it is shown decreasing the time step did not change the results significantly. Thus, further simulations were carried out using critical time step.

Examples of the change in the orientation of particles are shown in Fig. 4.6. The plots show the most divergent curves and the simulated curve for a poor match (particle 6), a reasonable match (particle 10) and a good match (particle 5) between the experimental and simulated curves. The simulated curves were all based on a value of friction coefficient of 0.1. The time series of particle translations (X and Z co-ordinates) of some selected particles are shown in Fig. 4.7, which includes all experimental results. Here the worst match is for particle 1 and the best for particle 10. The statistical analysis of the results showed that the quality of the match between the experimental and simulated tracks for the remaining particles was between these two extremes, which is discussed in the next section.

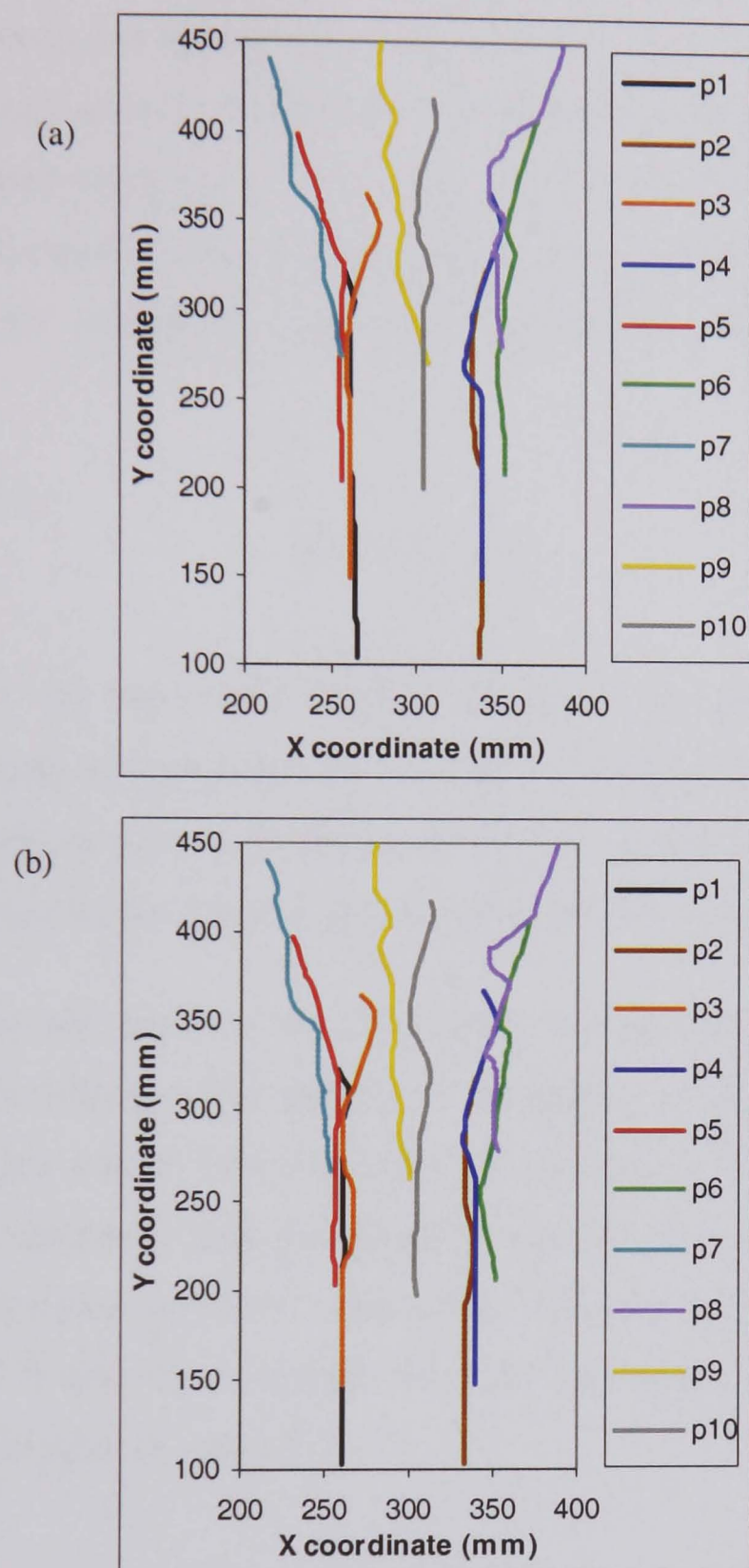


**Figure 4.5** Effect of time step on the prediction of the DE model: a) at critical time step, b) 0.10 of critical time step ( $\text{frac}=0.1$ ). For both replicates the coefficient of inter-particle friction was 0.1.

### 4.2.3. Statistical analysis and discussion

In order to quantify the degree of agreement between the experiments and that of DE model prediction, the following statistical analysis was carried out. Having the track (X and Z co-ordinates) and the orientation of particles for five experimental replicates, the mean and standard deviation of these items for frames were calculated. For each experiment 25 frames were taken with 0.2s time interval (25 frames in total). Based on these calculations the confidence interval for 95 percent confidence level can be calculated as

$$\bar{x} \pm 1.96 \left( \frac{\sigma}{\sqrt{n}} \right) \quad (4.2)$$

where  $\bar{x}$ ,  $\sigma$ , and  $n$  are the mean, standard deviation and number of replications respectively. The result of simulation for the track of particle centroids (X and Z co-ordinates) and orientation then were compared with the confidence interval of each one from experiment to see whether they lay within this interval or not.

The degree of agreement between the experiment and the model prediction in each frame was ranked according to the number of parameters (X and Y co-ordinates and orientation of particle), whose value fell within the confidence interval. The minimum degree of agreement (equal to zero) was given to a particle in a given frame, if none of its position and orientation parameter values fell within the confidence interval. The maximum value of 3 was for a particle for which all three parameter values were within the confidence interval (table 4.2).

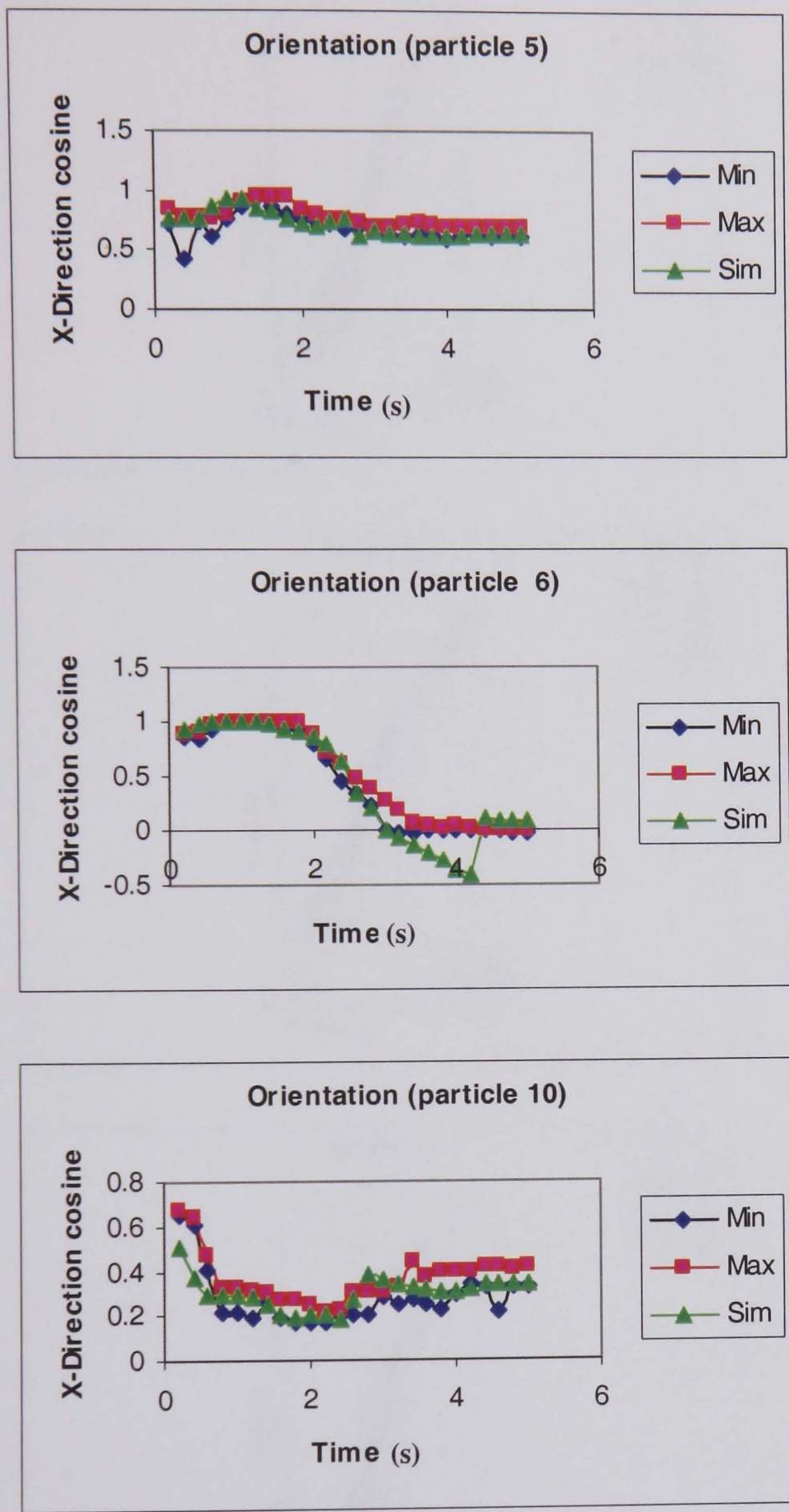


**Figure 4.6** Examples of change in particle orientation in the experiments and simulation. Comparisons were made between the simulation results and the minimum and maximum limits of particle orientation for five experimental replications.

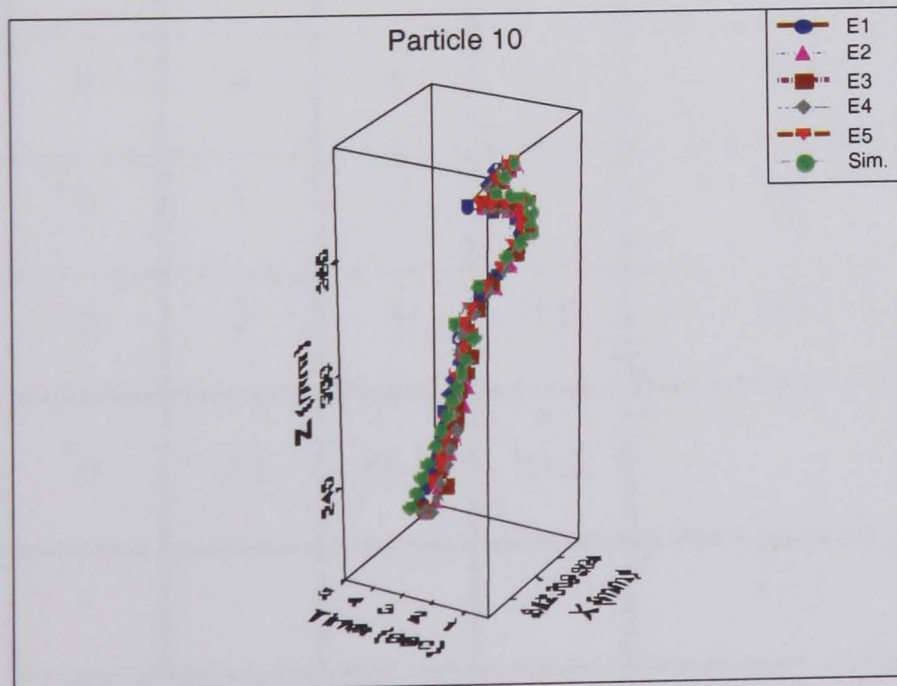
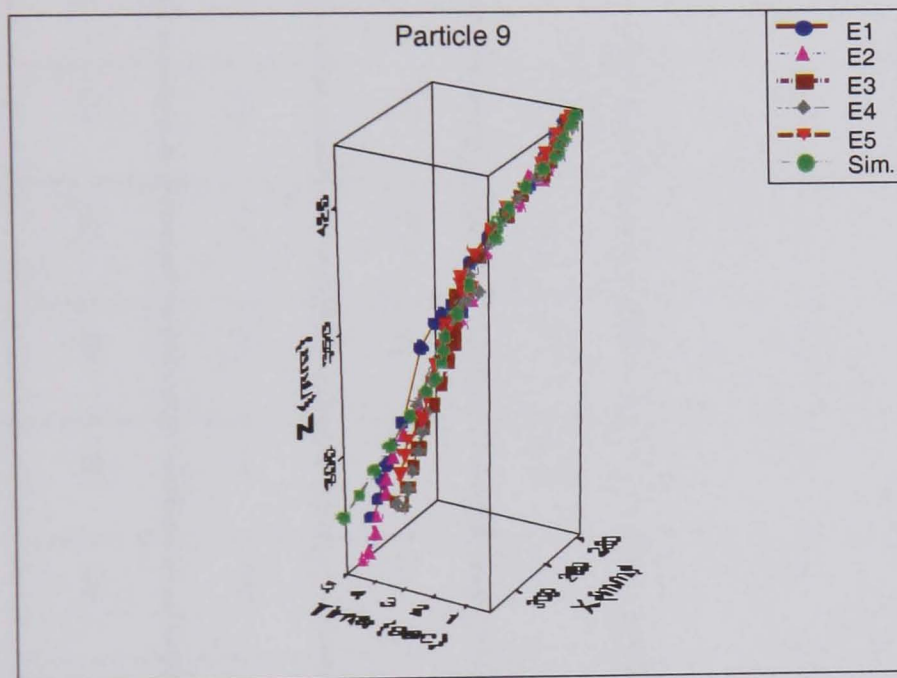
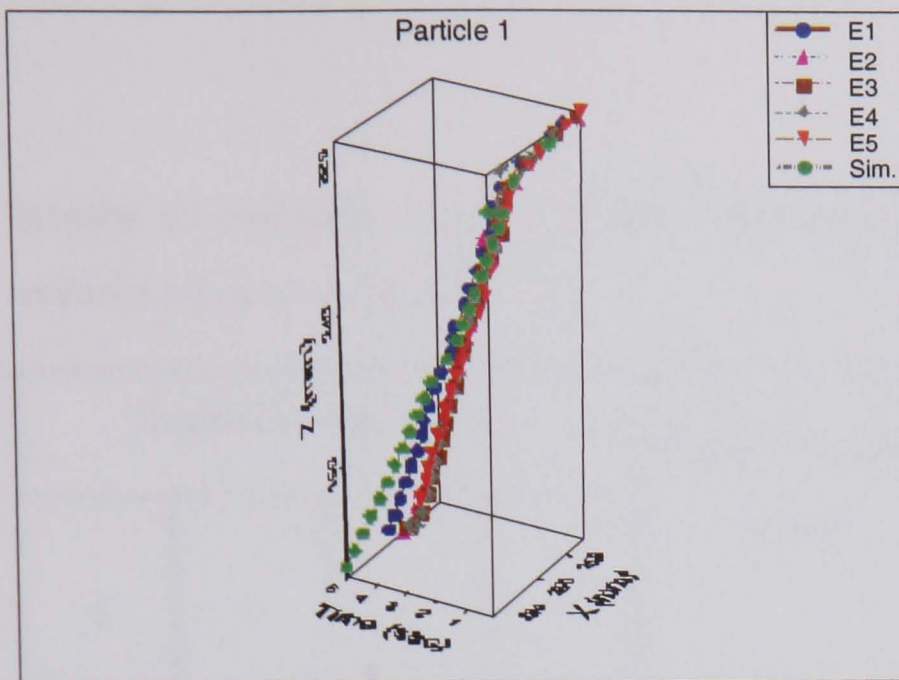


Figure 4.7 Evolution of particle trajectories in experiments and simulation.

**Table 4.2** Results of statistical analysis for quantification of agreement between experiments and simulation.

Particle No.	Degree of agreement				Total weighted points	Maximum agreement %
	0	1	2	3		
1	0	0	17	8	58	77.3
2	0	2	13	10	58	77.3
3	0	2	15	8	56	74.7
4	0	3	2	20	67	89.3
5	0	1	4	20	69	92
6	0	4	7	14	60	80
7	0	3	8	14	61	81.3
8	0	4	8	13	59	78.7
9	0	1	11	13	63	84
10	0	3	4	18	65	86.7
<b>Total %</b>	0	9.2	35.6	55.2	-	-
<b>Average</b>	-	-	-	-	61.6	82.13

Columns 2 to 5 of the table show the degree of agreement for each particle with the above ranking method. Column 6 of this table shows the weighted points which, can be given to a particle according to its rank number as

$$\text{Particle weighted points} = \sum_{i=1}^4 k_i n_i \quad (4.3)$$

where  $k$  is the degree of agreement varies from 0 to 3 and  $n$  is the number of frame with degree of agreement  $k$ . Accordingly, the maximum weighted points 75 (based on 25 frames) was allocated to a particle for which the simulation results in all of its frames were within the confidence interval of experiments (100 % agreement) and the minimum weighted point of zero was for a particle for which the simulation results of no frames were within the confidence level.

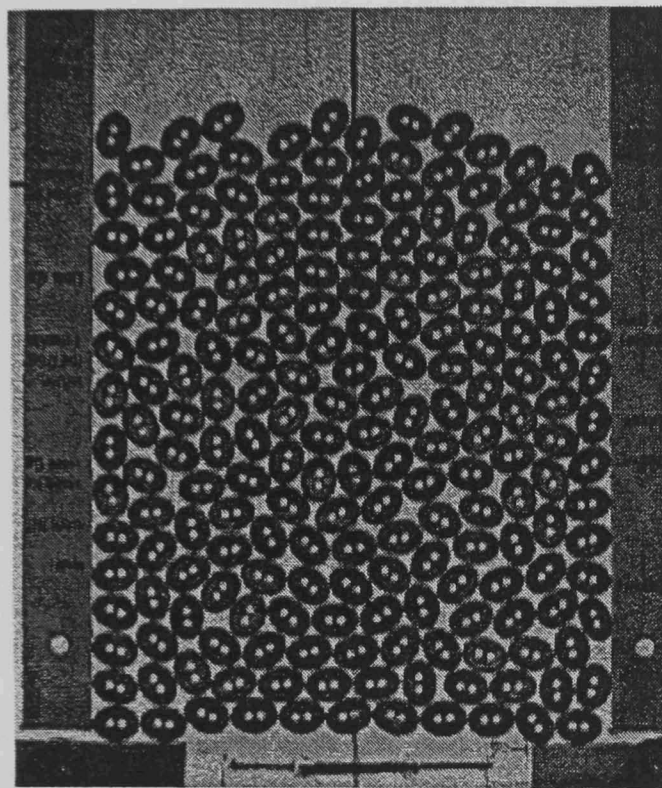
In column 7 the degree of agreement for each particle is shown as percent of full agreement (weighted point equal to 75). It can be seen that the overall agreement between model and experiment was 82.1 %. The best agreement was found for particle number 5 with 92 % agreement and the minimum agreement for particles 1 and 2 with 77.3 % agreement.

Consideration of both the particle translation and change in particle orientation shows that on the whole the match between experiments and simulation was very good given the noise introduced by physical replication of the particle assembly, the variation in physical particle geometry and the hopper structure, the relatively long distance over which each could evolve and the limited exploration of the sensitivity to the magnitude of model parameters.

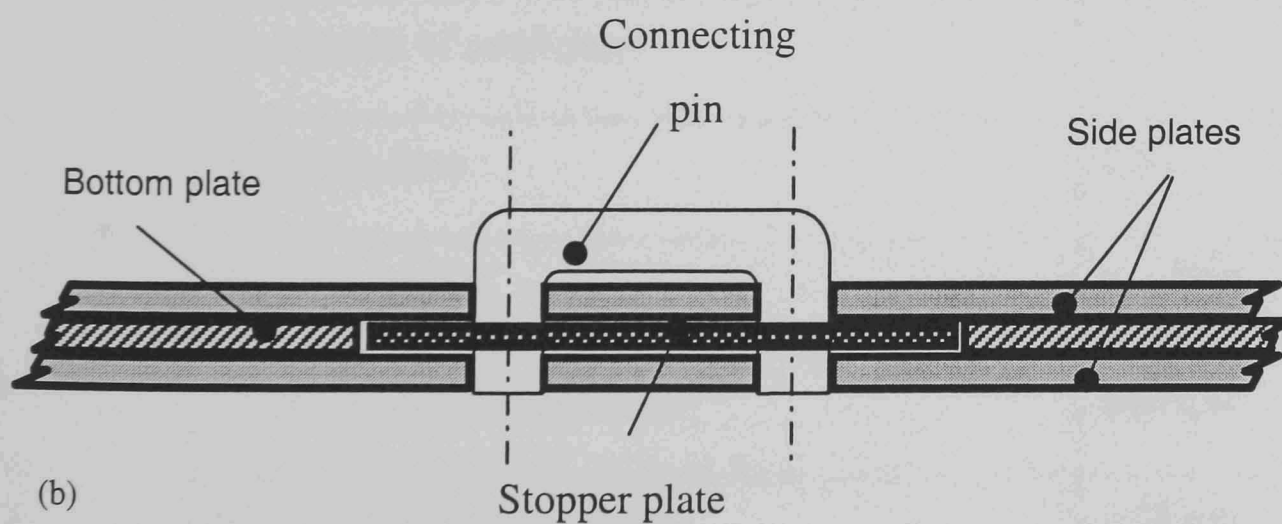
It can therefore be concluded that, at least on a coarse scale, the physical principles and numerical approximations in the DE model are validated by the experimental results. Although the particle shape tested represented the most simple possible multi-sphere shape the principles underlying the MSM should apply to more complex shapes.

### 4.3. Macro-scale experimental validation

Comparisons between experiment and simulation of the flow from a hopper of an assembly of elliptical shaped particles were made at the bulk scale in terms of bed structure such as solid fraction and flow characteristics such as flow rate, velocity profile, the free surface profile and the interface between moving and stagnant regions.



(a)



(b)

**Figure 4.8** Experimental particle assembly for particle flow. (a) The experiment bed consists of 200 elliptical particles, which were machined plastic buttons. The solid fraction of the bed is 0.86. (b) Section through orifice release mechanism.

### 4.3.1. Materials and method

A 2-D, flat-bottomed bin was set up to observe the flow of 200 ellipsoidal shaped buttons with various orifice sizes. The width of the bin was 15 cm for all experiments. The hopper consisted of two parallel sheets of perspex 60 × 60 cm placed a distance apart just greater than the thickness of the buttons which was 0.23 cm (Fig. 4.8).

**Table 4.3** Physical and mechanical properties of experimental particles (buttons). The particle mass and the coefficient of restitution is the average of 10 replications. Poisson's ratio and Elastic modulus were taken from *measurement group* web site.

Mass	0.332 g
Static coefficient of friction (particle-particle)	0.61
Dynamic coefficient of friction (particle-particle)	0.2
Static coefficient of friction (particle-wall)	0.67
Dynamic coefficient of friction (particle-wall)	0.2
Coefficient of restitution	0.72
Poisson's ratio	0.30
Elastic modulus	3.5 GPa
Major diameter of particles	0.69 cm
Minor diameter of particles	0.53 cm

The mechanical and physical properties of particles were either measured experimentally or taken from the *measurement group* web site (<http://www.measurementsgroup.com/Guide/>). As particles were machined buttons it was assumed that the roughness of all surfaces (sides and edge) was approximately the

same. The respective coefficients of friction were therefore assumed to be the same. The particle-particle static coefficient of friction ( $\mu$ ) was calculated by determining the angle at which a button began to slide over a flat surface of another one (parallel placement). To get an average ( $\mu$ ) the upper particle was placed over the lower one in different orientations.

The particle-wall coefficient of friction ( $\mu_w$ ) was determined by sliding a button over a sheet of perspex. The coefficient of restitution was determined by dropping a button from an initial height on to a rigidly fixed button and measuring the rebound height. The fixed button was glued to the ground on its flat surface while the other one dropped on its edge on to the fixed flat surface. The rebound height was recorded using a camcorder and the measurement was repeated ten times. The physical properties of the particles (buttons) are given in Table 4.3.

To determine the particle boundary profile for the purpose of model particle generation, five buttons were taken randomly, scanned and then enlarged. The enlarged pictures were used to measure the long and short diameters of the buttons. The average of the button diameters was used to create a theoretical ellipse. Fig. 4.9 compares the boundary profile of a selected button and the corresponding theoretical ellipse to show that how closely an ellipse function resembles the shape of the buttons. It is seen that an ellipse provides an acceptable fit to the boundary of the experimental particles.

In the simulation the model particles were generated according to the profile of the theoretical ellipse in Fig. 4.9 using seven element spheres per particle as shown in Fig. 4.10. The numerical particle assembly was generated in a single vertical layer in the X-Z plane (i.e. all particles had the same Y co-ordinate). As the model particles were placed in a vertical layer, all contact points took place in a single vertical plane. Therefore, any lateral overlap was prohibited and translation and rotation of particles was restricted to the X-Z plane. The particle flow was therefore quasi-2D although both the experimental and model assemblies were 3D. Experiments with five replications were carried out for the flow of particles from orifices of size 5, 6.5, 7.5, 8.5 and 10 cm (equivalent to 33.3, 43, 50, 57 and 66.7 % of hopper width respectively) and the results were compared with the MSM DE model predictions.

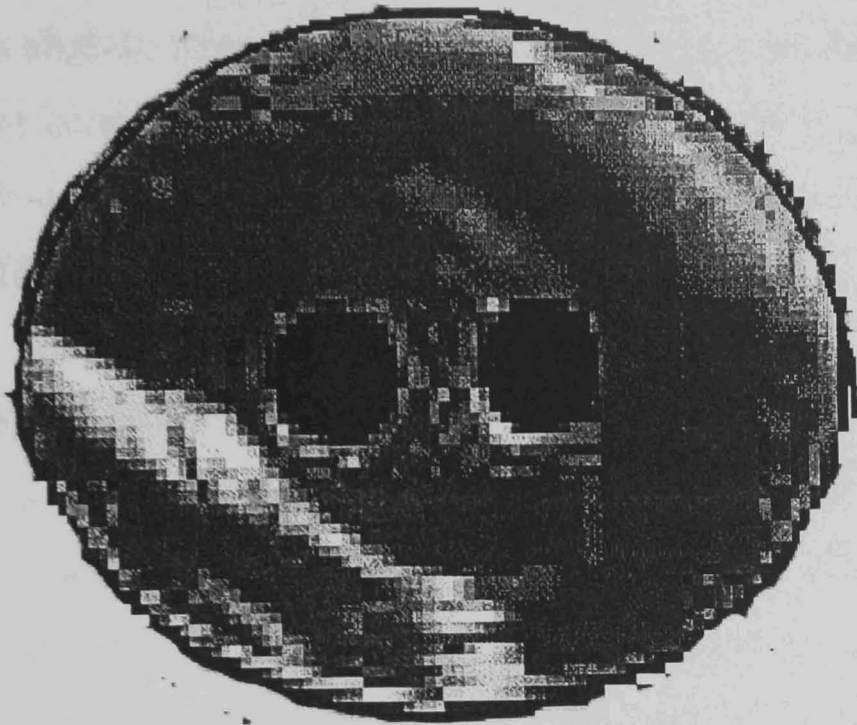


**Figure 4.9** Comparison the profile boundary of the buttons and an equivalent theoretical ellipse of the same size and aspect ratio. The red line is the profile of a theoretical ellipse with the same aspect ratio as the average for the buttons.

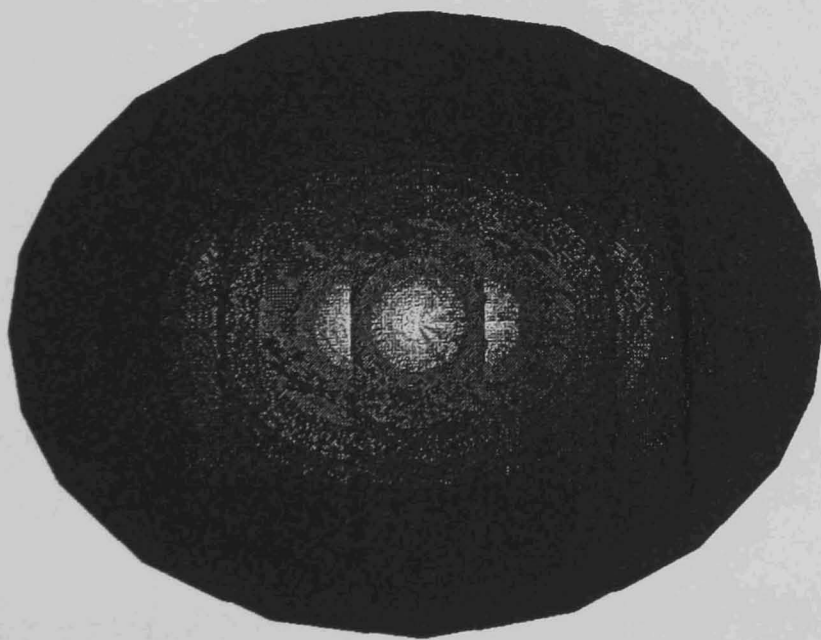


**Figure 4.10** DE model particle with seven element spheres. This particle was created to approximate the boundary of the theoretical ellipse obtained from the real particle boundary.

The orifice in the experimental bin was closed with a stopper made from a rectangular piece of perspex slightly thinner than the thickness of the bin. The stopper was placed by means of two connected pins (as shown in Fig 4.8b) such that releasing the pins could start flow simultaneously along the orifice. The particle beds were discharged through five different orifice sizes (5, 6.5, 7.5, 8.5 and 10 cm). Each experiment was replicated five times. Pictures were taken of the assembly during flow using a camcorder with two shutter speeds (1/50 and 1/4000 sec). In each experiment the shutter speed was chosen according to the purpose of the experiment. The lower speed was used to get a blurred picture of the moving particles for a better indication of the nature of the flow (separating the stagnant and moving region). Sharp images could be obtained using the higher shutter speed (1/4000 sec). The still pictures of flow in simulation and experiment were extracted either from DE model as POV-RAY images or from camcorder as individual frames. The individual frames from experiment were extracted from the video after A/D conversion of the video file at high resolution. The frames were saved as TIF (Tagged Image File) files. These images (POV-RAY pictures from simulation and TIF files from experiment) were analysed to extract the required data for comparisons of the results of experiment and simulation. The following were measured in each image:

- (i) The total number of particles remaining in the bin for calculation of the cumulative particle discharged from the bin during flow.
- (ii) In each image the width of the bin was divided into ten sections. In each section the height of the bed was measured and the bed area was calculated using the average of the bed height in the frame. Having determined the bed area and the total number of particles remaining in the bin, the bulk density and solid fraction could be calculated for each frame.
- (iii) The vertical position of particles whose centroid lay in a band of thickness equal to the mean diameter of the particles at a given height  $h$  was measured. These data were used to calculate vertical velocity of particle. In simulation such data were obtained directly from an output file.

A horizontal band of thickness equal to the mean particle diameter was chosen. This band was located in the convergent flow region of the hopper. The vertical position of

particles whose centroid lay in this band was measured for two successive frames. The position of these particles was then measured in the next frame. The vertical velocity of each selected particle was calculated as the vertical displacement of the particle divided by the time difference between frames. This resulted in two sets of vertical velocity measurement representing particles which passed through the band during the duration of two frames. Having determined the vertical velocity of each particle, the plot of the velocity profile across the bin was carried out by calculating the average of particle position in the horizontal direction between the two frames. In the simulation all particles in the same band and height in the frame of the same number as in the experiment were selected and their vertical velocity were recorded for the period of one frame (8843 time steps) and then the average velocity was calculated for each selected particle.

In each image all measurements including the height of the bed in each section, the position of particles and the total number of particles were obtained manually. To increase the accuracy of the measurement, the images were zoomed to a higher scale during measurement.

### **4.3.2. Results and discussion**

#### **4.3.2.1. Packing structure**

At the first stage of simulations, particles were generated randomly with a minimum distance between particles using a value for the inter-particle coefficient of friction of 0.2. This value was chosen based on the findings from experimental validation at particle scale (section 4.2) that the dynamic coefficient of friction should be set at least half the magnitude of the static coefficient of friction. The reasons for this choice were: i) the dynamic friction coefficient is more appropriate to particle flow and ii) the analytical validation of the model showed that there is a pseudo friction effect between multi-sphere particles which approximates to an equivalent friction coefficient. The maximum value of this friction coefficient is 0.4. This friction can be reduced if the sphere density of model particles is increased (i.e. more spheres are used to represent a particle). The value of 0.2 used in the simulation is a reduction of 0.41 from the value of the measured static friction coefficient of 0.61. The maximum deviation in the

direction of the contact normal force vector between the element spheres of particles was  $2.31^\circ$  using the method described in 3.8. The pseudo friction effect due to this angle equates to a static friction coefficient of approximately 0.02 (Appendix E).

Fig. 4.11a shows the simulated particle assembly after consolidation with (friction between particles). Comparing this figure with Fig. 4.8 (experimental particle bed), it can be seen that the packing structure in the experiment (solid fraction=0.86) is denser than the simulated structure (solid fraction=0.79). There are some big pores in the simulated bed resulting from local arching of particles. This was probably caused by the different method of hopper filling used in experiment and simulation. In the experiment, particles were put in the bin one at a time but in the simulation all particles were generated at the same time and subsequently, by applying gravitational force they consolidated simultaneously. Since in experiment the particles were placed one by one, they had enough time to settle down independently, while in the simulation there was interface between particles. Therefore, the chance of local arching occurring during consolidation was increased which in turn led to a more porous structure for the model particle assembly (Fig. 4.11a).

To obtain a simulated bed structure closer to the experiment, the generation and consolidation processes were changed. As the occurrence of local arching was the main reason for the deviation of simulated bed structure from experiment, in the new method the aim was to reduce the amount of arching during particle deposition. Particles were first generated with more space between them and the inter-particle friction was set to zero. With these preparations although the consolidation period increased slightly, the particles could settle almost independently which was closer to conditions in the experiment. Fig. 4.11b shows the result of consolidation using the second method. It can be seen that using the new method of particle generation and consolidation the simulated bed is in closer agreement with experiment (solid fraction=0.84). In the case of frictionless assembly, prior to starting flow, the inter-particle friction was set to 0.2.

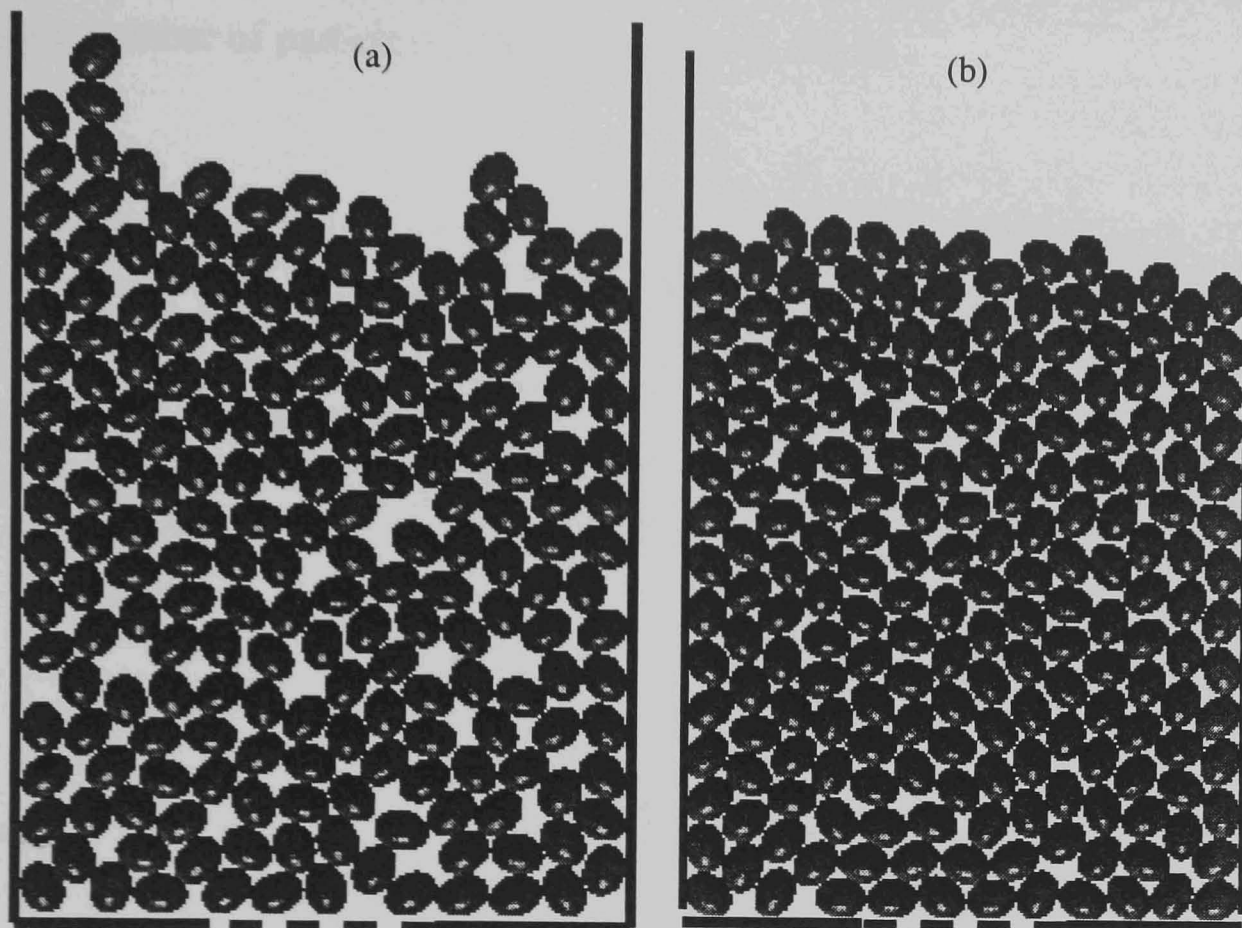


**Figure 4.11** Model particle assembly after generation using a) friction based assembly generation (solidfraction=0.79) and b) frictionless particle generation (solid fraction=0.84).

Fig. 4.12a and b shows the change in the solid fraction during flow and the average during steady state flow respectively in the experiment and simulation (both friction and frictionless based assembly generation) with different orifice sizes. The flow can be defined as steady when the flow rate is approximately constant i.e. the curve of cumulative particles discharged from the bin is linear. The change in solid fraction had the same trend in both simulation and experiment. Once flow started the particle bed became dilated in both experiment and simulation. However, higher solid fractions during flow were obtained for experiment than simulation. Fig. 4.12b shows that, regardless of the method of assembly generation in the model (with friction or frictionless), there was a difference in average solid fraction between experiment and simulations during the steady state flow. Despite the same initial bed structure for experiment and frictionless assembly generation in the model at the beginning, the particle bed dilated more in the simulation than the experimental bed. As the orifice dimension was increased the average solid fraction during steady flow reduced in both

experiment and simulation. This may have been due to bigger gravitational gradient over a larger number of particles when the orifice was wider.

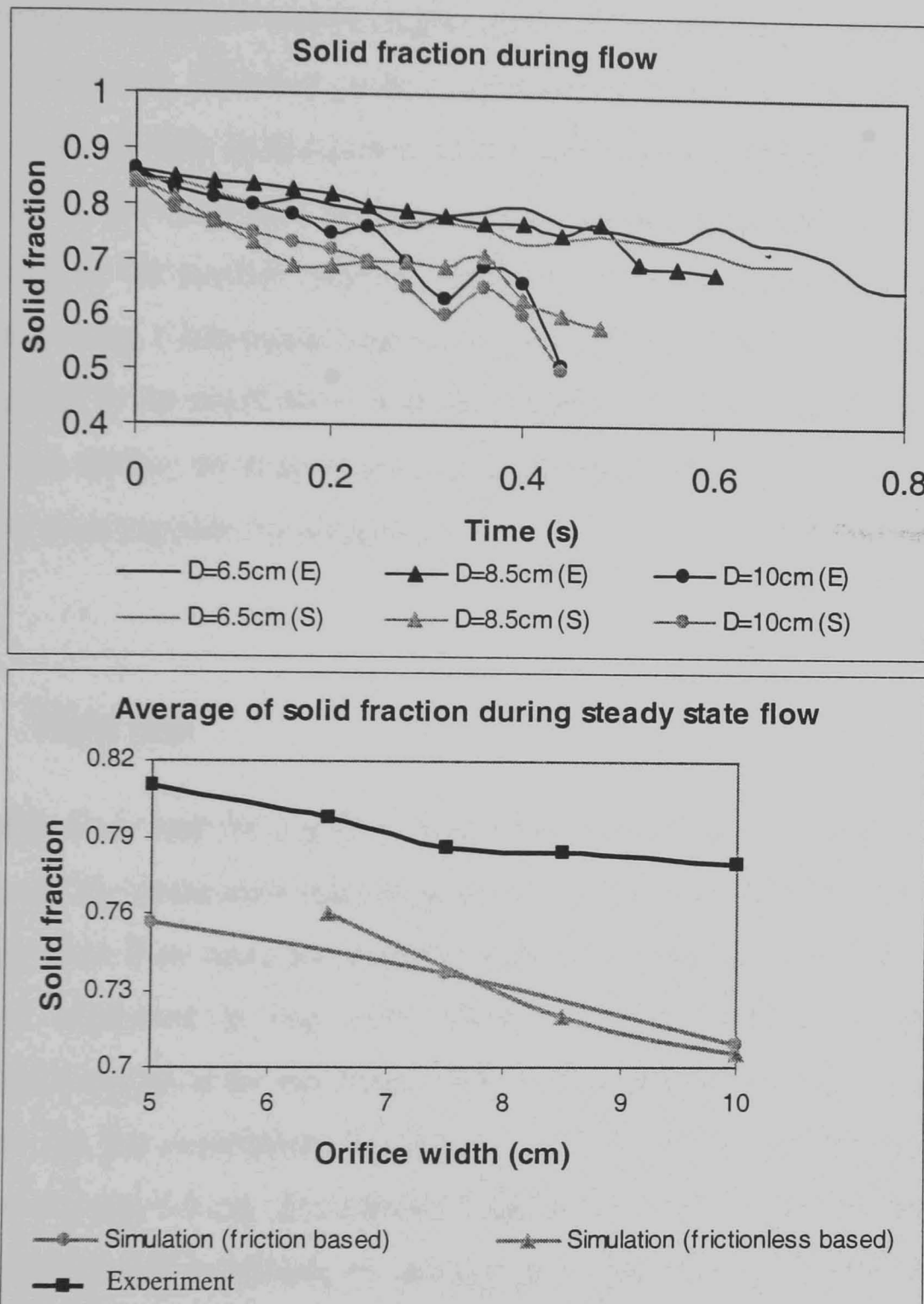


**Figure 4.12** Solid fraction of particle assemblies in the experiment and simulation: a) changing during particle flow in the experiment and simulation (frictionless based assembly generation), the dark curves show the experimental results; b) average during steady flow. The brighter curves show the simulation results for friction and frictionless based assembly generation. The average solid fraction for frictionless-based assembly with 5cm orifice has not been shown due to observation of an arch.

#### 4.3.2.2. Particle flow

Fig. 4.13 shows the cumulative particle mass discharged from the hopper for the experiments and simulation. In each graph, the black solid curve shows the average of five experimental replications and the lighter curve shows the result of simulation for a given orifice dimension. There is general agreement between the curves. As expected, the flow rate reduced with orifice size in both experiment and simulation. As the size of orifice reduced, the roughness of the curves for particle flow increased due to more frequent arching in the smaller orifices. However, for all orifices the occurrences of instantaneous arching ( horizontal segments, indicated by particles of hold up in the flow) were higher in the simulations than the experiments. This may have been due to the nature of the surface contour of the model particles which increased the tendency for particles to stick together momentarily.

#### 4.3.2.3. Flow rate

The steady state flow rate for a given orifice can be calculated from the slope of the linear segment of the cumulative discharge curve as shown in Fig. 4.14. The calculated average steady state flow rates for different orifice dimensions in the experiment and simulation are compared in Fig 4.15. There is a very good agreement between experiment and simulation for the larger orifice dimensions of 10.0, 8.5 and 7.5 cm. The flow rate for the simulation is slightly lower than the experiment for orifice dimensions of 6.5 and 5.0 cm. For smaller orifices the lower value for the simulation were due to the greater incidence of arching as noted in 4.3.2.2. This can also be confirmed from Fig. 4.12 where a higher average solid fraction during flow was observed for smaller orifices, indicating that particles were close together in which case pseudo friction between model particles could be more important. An example of arching in both simulation and experiment is shown in Fig. 4.16.

#### 4.3.2.4. Arching phenomenon during particles flow

The arching phenomenon shown in Figures 4.13 and 4.16 were in agreement with the observations of Walton (1983) who noted that flow is stopped intermittently by the formation of temporary arches for orifices approximately six particles diameters or

less. The orientations and contact force chains between the particles, forming an arch controls the strength and shape of the arch. In both simulation and experiment as the width of the orifice was decreased a stronger and more stable arch was observed resulting in a fluctuating flow. The flow was essentially smooth and continuous for orifices of width greater than ten particle diameters.

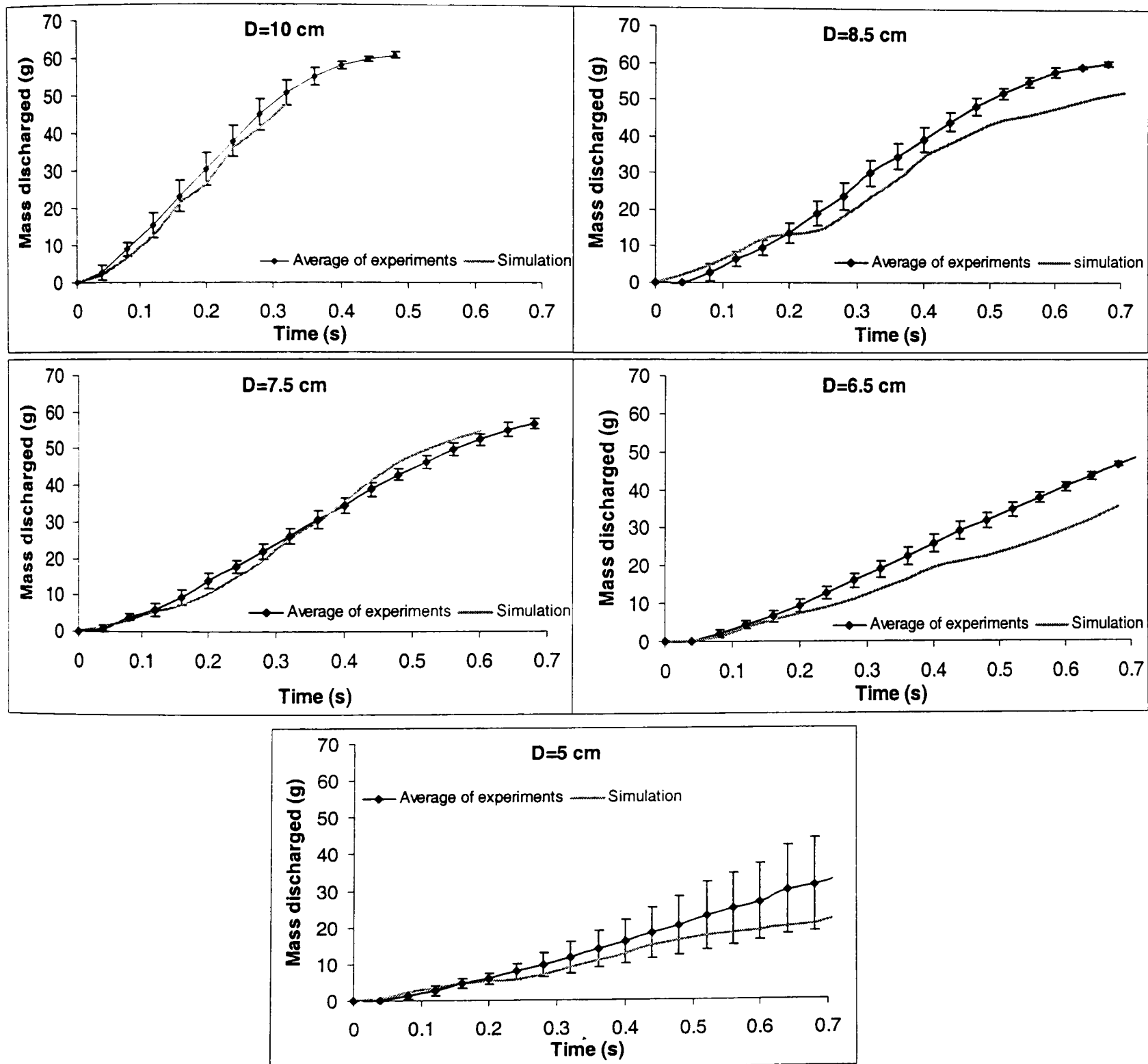


**Figure 4.13** Discharged mass of particles from hopper with different orifice size in the experiments and simulations (error bars show the 95% confidence interval).

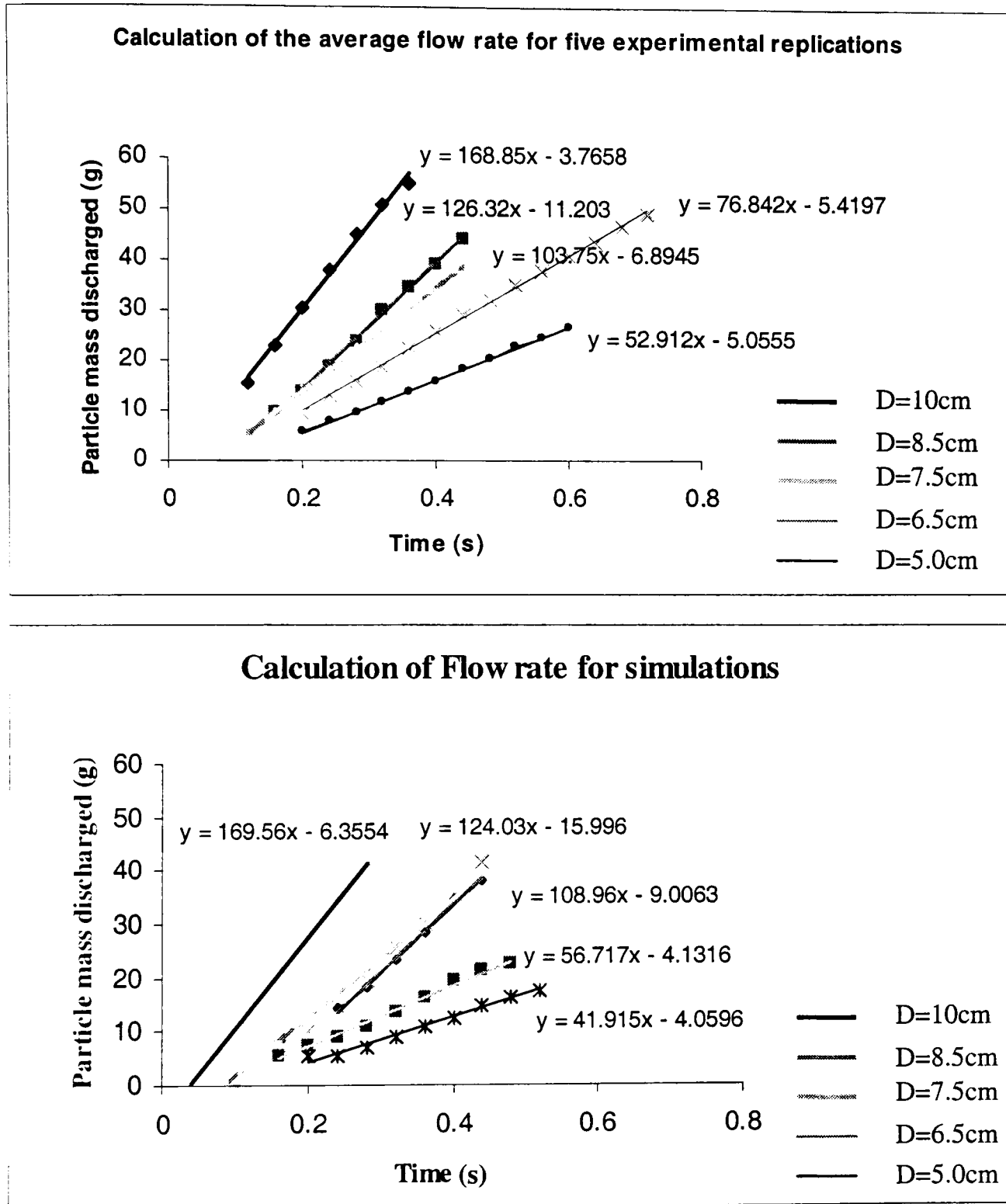


**Figure 4.14** Calculations of flow rate in experiments and simulations for different orifice dimensions. These data were taken from the linear segments of cumulative curves in Fig.4.13.

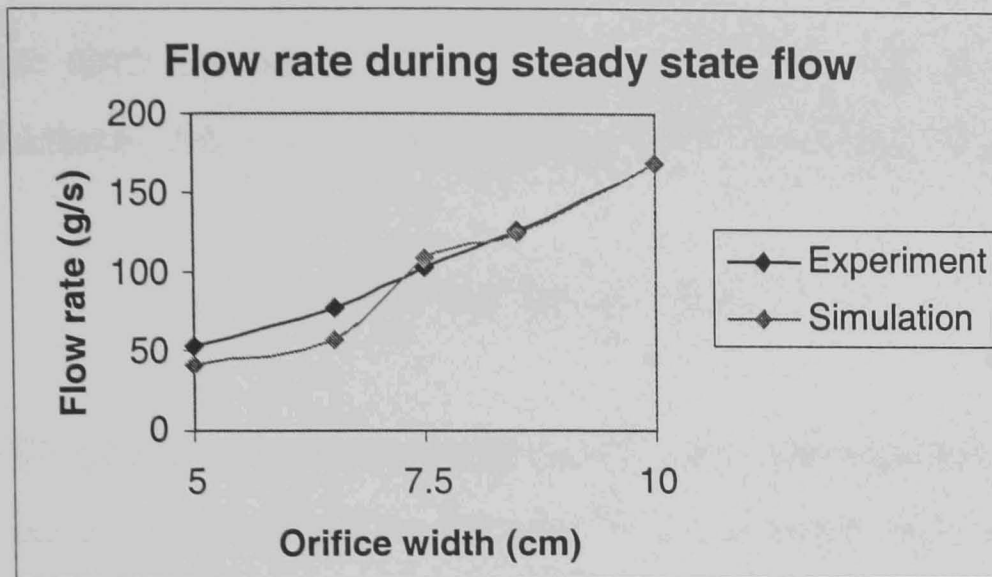


Figure 4.15 Comparison between the flow rate in experiments and that of model predictions for different orifice sizes.

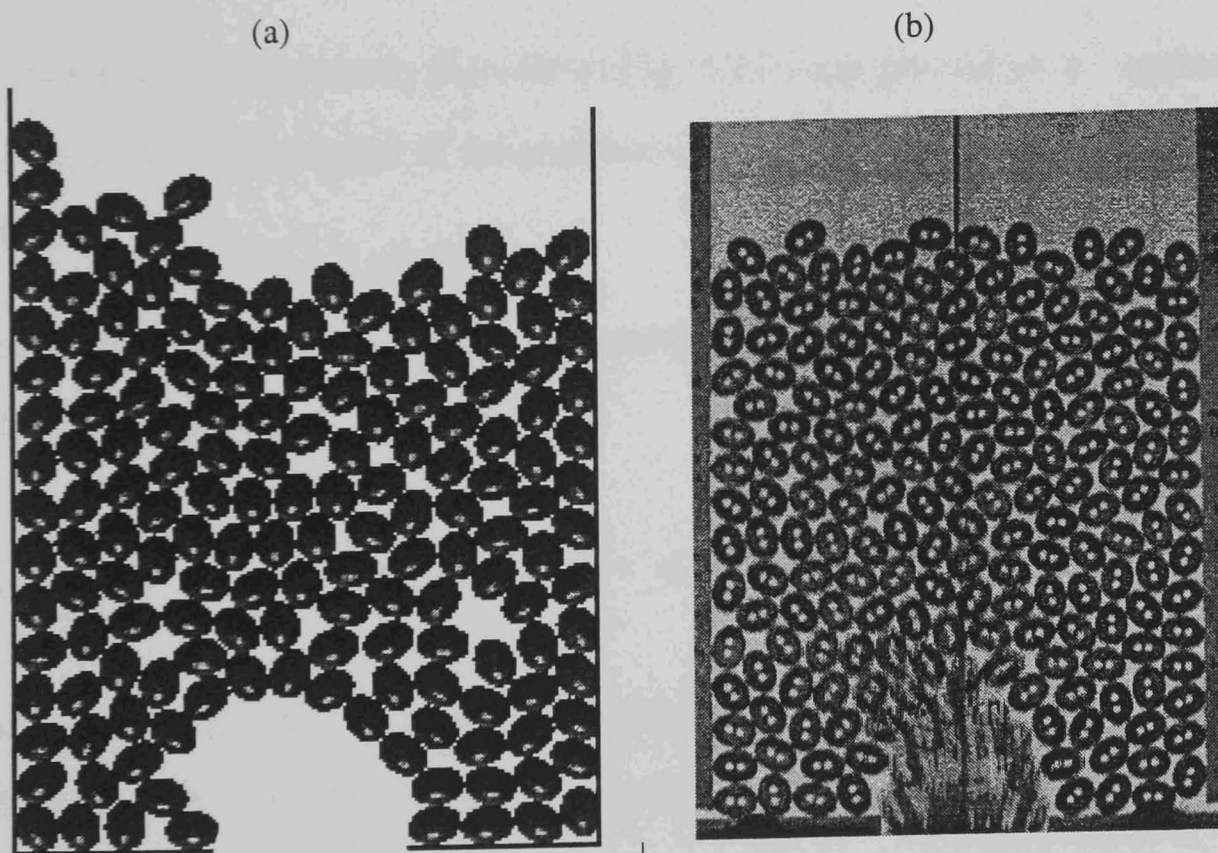


Figure 4.16 The occurrence of temporary arching in: (a) simulation and (b) experiment for an orifice width of 5 cm (equivalent to approximately 5 particle mean diameters).

#### 4.3.2.5. Verification of the Beverloo Equation

The steady state discharge rate  $q$  (g/s) can be predicted from the modified Beverloo equation (Nedderman, 1989; Thornton and Kafui, 1997; Kafui and Thornton, 1997)

$$q = \frac{4\sqrt{2}}{\pi} C g^{0.5} \rho d (D - kd)^{\frac{3}{2}} \quad (4.5)$$

where for a 2-D system  $\rho$  is bulk density (g/cm<sup>3</sup>),  $d$  is mean particle diameter,  $D$  is orifice width and  $g$  is gravitational acceleration.  $C$  is a constant with the value of 0.58 according to Nedderman (1985). The term  $kd$  accounts for the displacement thickness of the shear layer adjacent to the wall or stagnant zone. Beverloo *et al.* (1961) reported that  $k$  is a function of particle shape and roughness with a value of approximately 1.5 for spheres and larger values for angular particles.

When flow rate  $q$  approaches zero in equation 4.5, the term  $(D - kd)$  also approaches zero. The flow rates during steady flow from Fig. 4.14 were plotted as  $q^{\frac{2}{3}}$  against  $D$  as shown in Figure. 4.17. The point of intersection between fitted lines and the horizontal axis equals  $kd$ .

The mean particle diameter for the elliptical particles can be calculated as the diameter of a circle with the same area as the particles

$$\frac{\pi d^2}{4} = \pi ab \quad \rightarrow \quad d = 2\sqrt{ab} \quad (4.6)$$

where  $a$  and  $b$  are the major and minor half diameters of the ellipse. The values of  $a$  and  $b$  for the particles was 0.69 and 0.53 cm respectively which gave a value for  $d$  of 1.2 cm.

From Fig. 4.17 the intersection between the fitted lines and the horizontal axis in experiment and simulation was 0.89 cm and 2.1 cm respectively giving values for  $k$  for experiment and simulation of 0.74 and 1.75 respectively. The higher value of  $k$  obtained from simulations was due to the higher probability of arching in the case of smaller orifices and also possibly because of the surface roughness of multi-sphere elements (pseudo friction) as discussed in the previous section.

Nedderman (1985) stated that for angular particles  $k$  could be higher. This would probably be due to the greater amount of interlocking of angular particles. In the case of experimental and simulated particles, differences in  $k$  are likely to be caused by differences in surface roughness rather than shape given the similarity in the general particle shape. If the comparison between the experiments and simulations is based on data for orifice dimensions of 7.5 cm and greater (where the probability of arching formation is reduced considerably) the prediction of the model is in a better agreement with the experiments ( $k=0.66$ ). Further analysis was carried out based on the value of  $k=0.74$  obtained in the experiments.

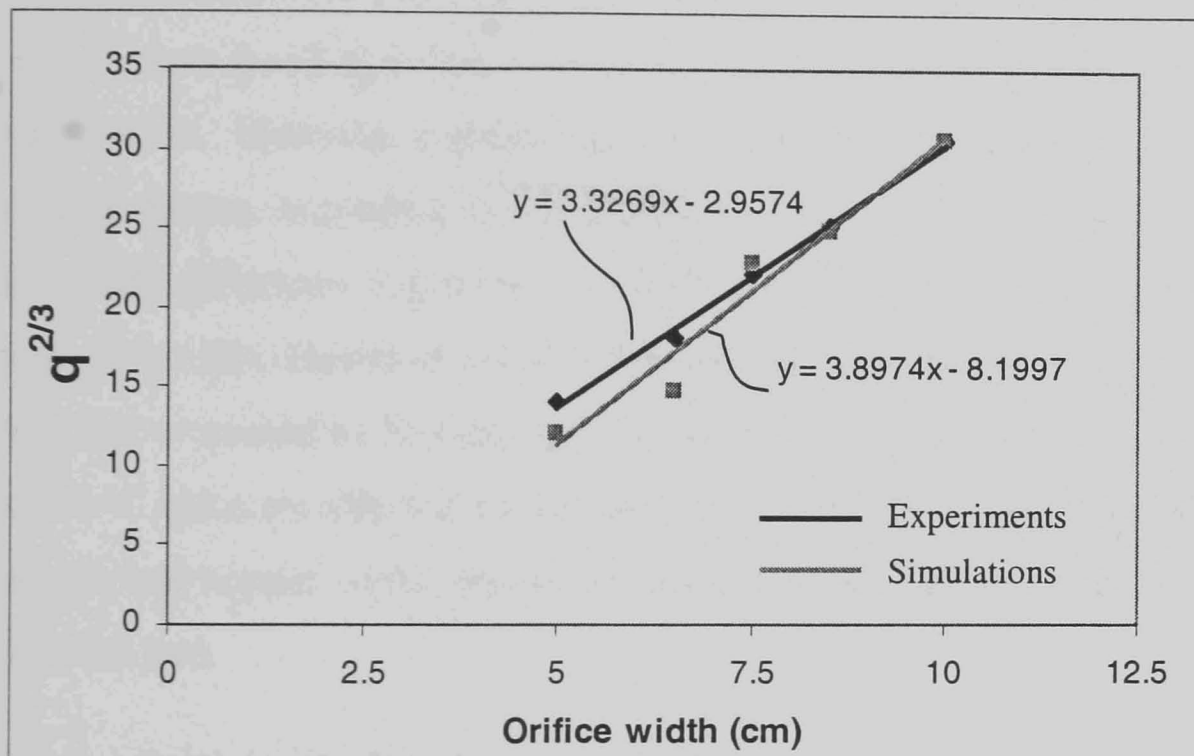


**Figure 4.17** Plot of  $q^{2/3}$  against orifice width ( $D$ ) and fitted lines to calculate the term  $kd$  in the modified Beverloo equation (4.5).

Having determined  $k$ , the factor  $C$  in equation (4.5) could be estimated. In this estimation the bulk density during flow was calculated using the number of particles in the bed, the mass of each particle and the total area of particles bed.

The still pictures of flow in simulations and experiments were extracted from DE model as POV-RAY images or from the video as individual frames. The bulk density during flow in each frame was determined by measuring the profile of the free surface of the particle bed and the total area of the bed as described in section 4.3.1. Having determined the area of the bed ( $A$ ), the total number of particles in the bed ( $N$ ) and the mass of each particle ( $m$ ), the bulk density was calculated as

$$\rho = \frac{Nm}{A} \quad (4.7)$$

The average flow rate  $q$  for each orifice width was calculated from the slope of the linear segment of the cumulative discharge curve (i.e. a constant flow rate assumed for this period) as shown in Fig.4.14. Tables 4.4 and 4.5 show the calculated  $C$  factor in experiments and simulations respectively. As noted above the difference between  $k$  in simulation and experiment was due to the occurrence of arching (Fig. 4.17) in the smaller orifices (5cm and 6.5cm). Thus, further analysis carried out based on  $k$  in the experiment, which also is fitted to simulation for wider orifices without arching. Although slight differences exist between the experiments and simulations for different orifice size, a very good agreement observed between the average  $C$  in experiments and in simulations. However, a greater scatter can be seen in the results of simulations than the experiments. According to the statistical  $t$  test (Table 4.6) it is seen that there is no significant difference statistically between the average  $C$  in the experiments and simulations ( $P=0.90$ ). However the  $C$  value in both experiment and simulation was lower than that of quoted by Nedderman (1985) (0.58). Further simulation is needed to find out how  $C$  and  $k$  are affected by factors such as the ratio of mean particle diameter to orifice size and hopper width, particle roughness, shape and size and also number of particles in the bed.

**Table 4.4** Estimate for  $C$  factor in experiments

D (cm)	q (g/sec)	$\rho$ (g/cm <sup>2</sup> )	C
5.0	52.91	0.237	0.39
6.5	76.84	0.23	0.37
7.5	103.75	0.226	0.4
8.5	126.32	0.226	0.39
10.0	168.85	0.227	0.4
Average	-	-	<b>0.390</b>

**Table 4.5** Estimate for C factor in simulations

D (cm)	q (g/sec)	$\rho$ (g/cm <sup>2</sup> )	C
5.0	41.95	0.217	0.34
6.5	56.72	0.217	0.3
7.5	108.96	0.215	0.44
8.5	124.03	0.208	0.41
10.0	169.56	0.205	0.44
<b>Average</b>	-	-	<b>0.386</b>

**Table 4.6** Statistical *t* test between the average of C in experiment and simulation.

	Average	Standard Dev.	t value	P value
<b>Experiment</b>	0.390	0.0122	<b>0.14</b>	<b>0.90</b>
<b>Simulation</b>	0.386	0.0631		

#### 4.3.2.6. Velocity profile during flow

Nedderman and Tuzun (1979) proposed a kinematic model to describe the velocity profiles across the convergent flow region in a discharging hopper. For steady gravity flow the vertical velocity at a height  $h$  above the orifice is

$$v_z = v_o e^{(-x^2/4Bh)} \quad (4.8)$$

where  $v_o$  is the vertical velocity along the centre line of the hopper,  $x$  is the horizontal distance from this axis and  $B$  is a fitting parameter (kinematic constant).

The velocity profile at a given height  $h$  in the experiment and simulation was calculated by finding all particles which lay in a band equal to the mean diameter of particles as mentioned in 4.3.1. The kinematic model to be tested applies only to the convergent flow region so the height  $h$  must be where particle flow has both horizontal and vertical velocity components. The measured and predicted velocity profiles in experiment and simulation respectively for orifice widths of 7.5 and 10 cm are shown in Fig. 4.18 (a) and (b). These orifices were selected as flow was smooth (with minimum arching) in both experiment and simulation. The fit of the kinematic model to the vertical velocity profile is also shown in these figures. The vertical velocity at the middle of the hopper ( $v_o$ ) for the kinematic model was taken from values in experiment or simulation at a given height. For each profile the factor  $B$  was obtained by iteration using different values of  $B$  until the root mean square of the difference between the model curve and the fitted curve reached a minimum. Values of  $B$  of  $0.82d$  and  $0.56d$  for the 7.5 cm orifice and  $1.02d$  and  $0.62d$  for the 10 cm orifice were obtained.

Using a t-test (Table 4.7) there was no statistically significant difference ( $p=0.92$  and  $p=0.99$  for  $D=7.5$  and  $D=10$  cm respectively) between simulation and experiment. Nedderman and Tuzun (1979) reported the value of  $B$  in the range of  $2d - 3d$  (for glass ballotini) for orifice widths from  $6.3d$  to  $14.6d$  and Kafui and Thornton (1997) found this parameter to be within the range of  $2.8d$  to  $3.5d$  (for 5000 spherical model particles) when the ratio of mean particle diameter to hopper width ( $d/W$ ) equalled 0.02. They also suggested that  $B$  might vary with orifice width, profile height and particle size. Zhang and Ooi (1998) summarised the studies on the effect of particle

size on the kinematic constant  $B$  for different materials including glass ballotini, iron ore, coke, epoxy spheres, sand and polypropylene pellets.

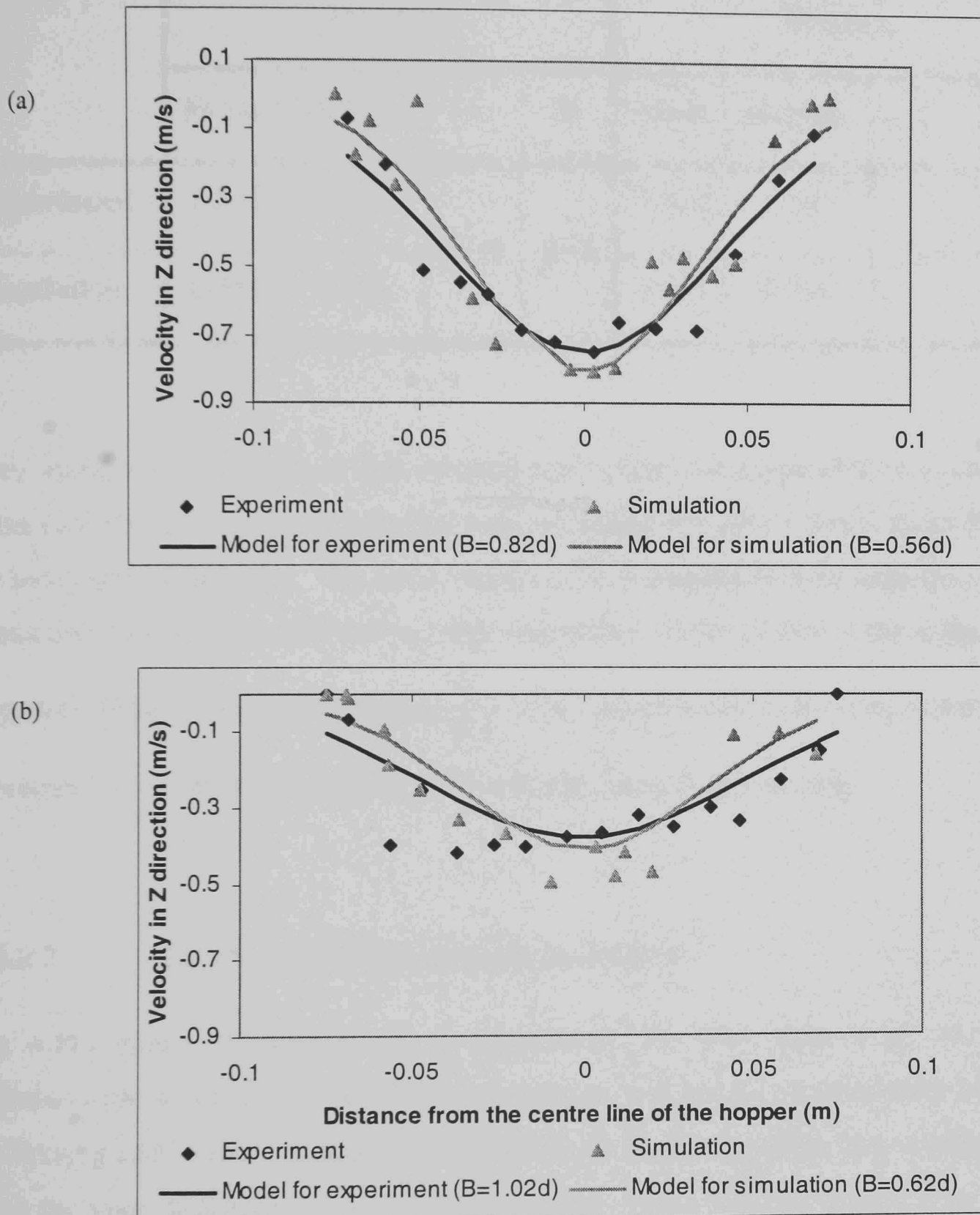


**Figure 4.18** Comparison of velocity profile in experiment and simulation at 9 cm above orifice for: a) 10 cm orifice size; b) 7.5 cm orifice size. The negative values indicate that the velocities are in the opposite direction of the Z-axis. In both cases the curves show the fit of kinematic model with the corresponding  $B$  from experiment and simulation.

**Table 4.7** Statistical  $t$  test between the velocity profiles in experiment and simulation.

	D=7.5cm				D=10cm			
	Mean	St. Dev.	t	P	Mean	St. Dev.	t	P
<b>Experiment</b>	-0.234	0.166	0.10	<b>0.92</b>	-0.409	0.284	-0.02	<b>0.99</b>
<b>Simulation</b>	-0.241	0.183			-0.407	0.315		

They found that the values of this constant were within the range of 2 to 4 times the mean particle size, except for one case (epoxy sphere) for which  $B$  was about 8 times the mean size of particles. The lower values of  $B$  (measured in both experiments and simulations) than those observed by other researchers might be due to the higher ratio of particle diameter to hopper width ( $\frac{d}{W} = 0.08$ ) in this study. Therefore, further work is required to clarify the dependency of the fitting factor  $B$  on this ratio.

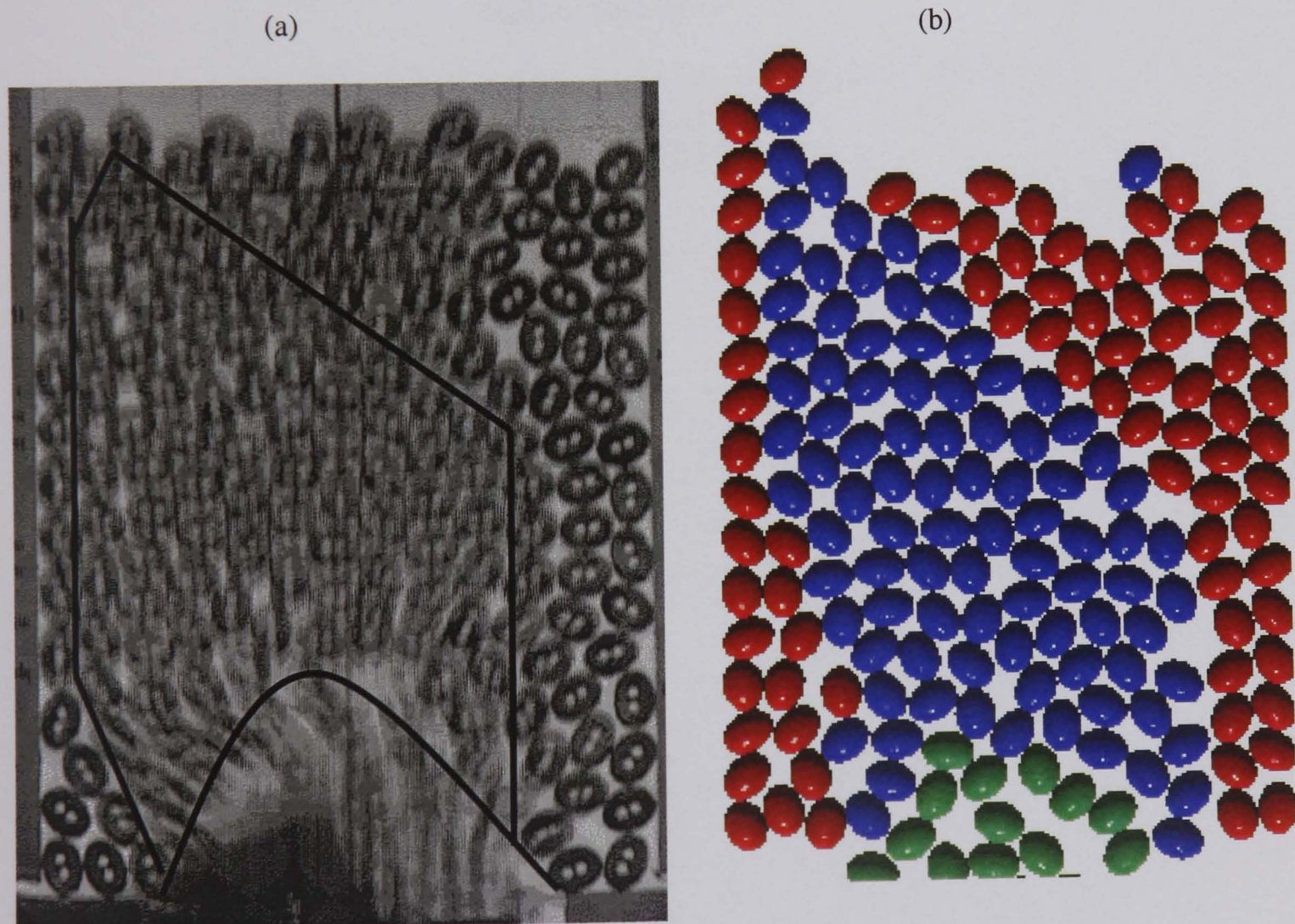
#### 4.3.2.7. Stagnant and flow region boundary

Fig. 4.19a shows the snapshot of an experiment flow for orifice width of 10 cm recorded with slow shutter speed. The figure shows a relatively clear interface between the flowing and stagnant regions. A snapshot at the same time taken from a simulation using the same conditions showed similar structure to the discharging bed (Fig. 4.19). The particles have been coloured according to their velocity to show the separation between the moving and motionless particles. The simulation behaviour showed reasonable correspondence with experiment. Three regions corresponding to different velocity ranges (high, medium and low) with very similar geometry and the formation of shear band can be seen which indicates that the simulation agrees qualitatively with experiment. In both sections (experiment and simulation) an asymmetrical pattern for flow region can be seen, i.e. the stagnant area in the right side of the hopper is bigger than the left side of the hopper. This phenomenon may be related to the shape of

particles and the bed structure before flow. Since the particles were non-spherical (aspect ratio of 1.3), the orientation of particles at the sides of orifice affected the packing structure which is different on each side and may be the source of the asymmetrical flow. More numerical simulations are required to compare the structure of the shear band in the assemblies of spherical and non-spherical particles.

#### 4.3.2.8. Free surface height and shape

The height and general shape of the free surface during flow obtained from simulation agrees approximately with the experiment as shown in Fig. 4.20. However, as the ratio of particle diameter to hopper width is high, even a small change in the position of a particle can change the shape of the free surface significantly. Moreover, as shown in Fig. 4.20 the difference between the method of hopper filling in the experiment and simulation caused a higher free surface in the simulation even before flow which can affect the result of simulation during flow.



**Figure 4.19** Hopper stagnant / flowing regions: a) Photograph of experiment with 10 cm orifice with low shutter speed at 0.08 sec after flow; b) simulation result at the same time, green (high velocity particles), blue (particles with medium velocity), red (particles with very low velocity or stationary).

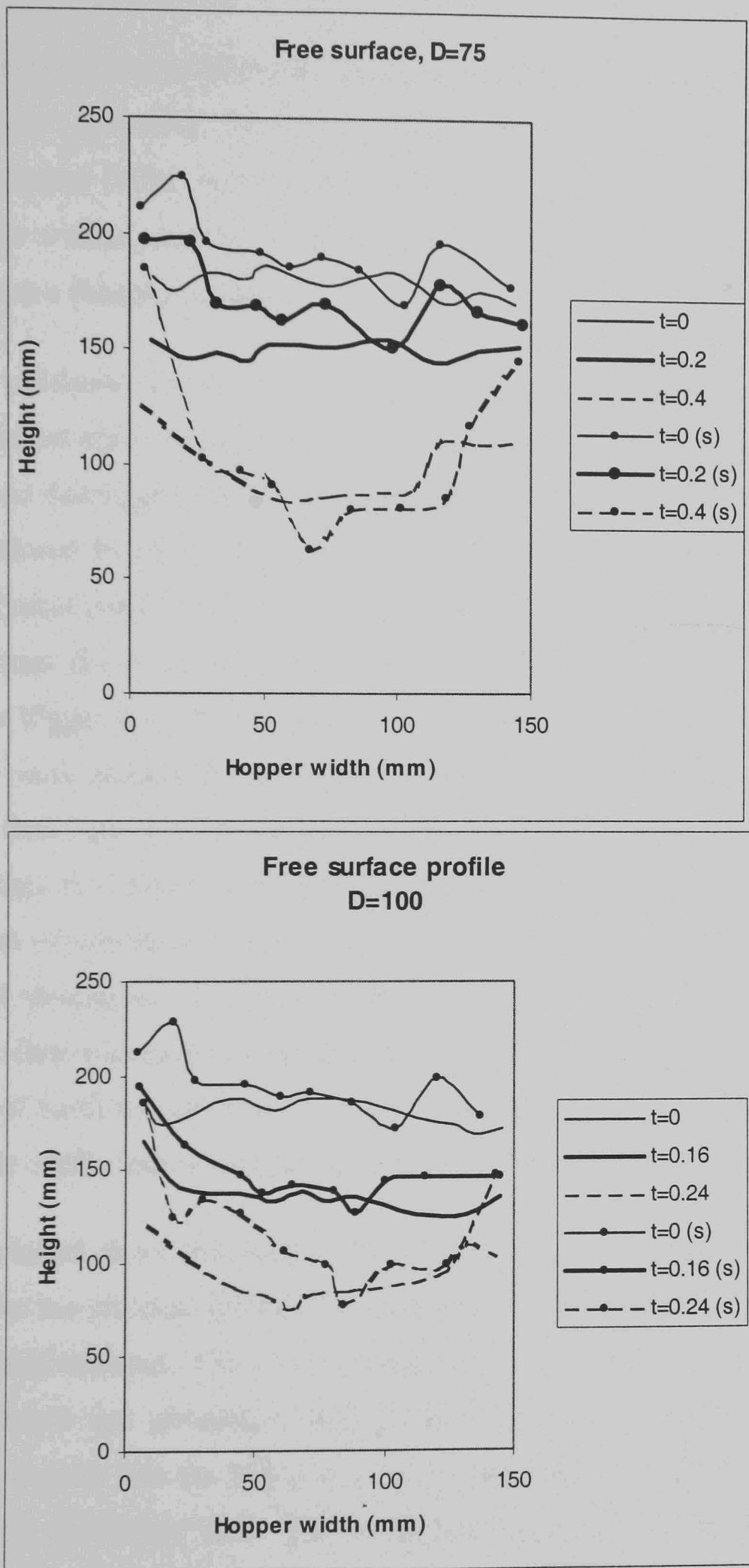


**Figure 4.20** Comparison between the results of simulations and experiments for the formation of free surface during flow in term of height and shape: a) orifice size 7.5 cm and b) 10cm. The (s) means simulation.

#### 4.4. Summary

The method was compared at the micro-scale to experiment by replicating as closely as possible the slow controlled flow of a limited number of particles. There was reasonable agreement (82%) between the predictions of the model and the average of experiments (for a small sample) in terms of correlation between particle co-ordinate and orientation as a function of time.

Experimental validation of the model at a macro-scale revealed good agreement between experiment and simulation in terms of bed structure, flow rate and occurrence of arching. Some discrepancy between experiment and simulation was expected given the noise introduced by physical replication of the particle assembly, and the slight variation in physical particle geometry. The prediction of the model for the flow rate during steady state flow was very close to the average of experiments for the orifice size of equal or bigger than 7.5 cm, but a higher difference was found for the smaller orifices due to more arching for the smaller orifices. Based on the prediction of the model for the flow rate of particles through the orifices of bigger size (7.5 cm and more), the average of C factor in the Beverloo equation obtained from simulation was the same as that of experiments which indicates a very good agreement between the experiment and simulation. Validation of the model in both particle and bulk scales showed that for flow simulation of particles the dynamic coefficient of friction governs the movement of particles rather than the static friction coefficient and it is suggested that the dynamic coefficient of particles is used in the DE model for sliding contacts.

It can be concluded from the results of the micro-scale and macro-scale model validation studies the physical principles underlying the MSM are valid and the model was correctly implemented. The good correlation both quantitative and qualitative between experiment and simulation with simple and more complex multi-sphere particle shapes suggest that the MSM is a useful tool for investigation the effect of particle shape on particulate flow. The validation exercises also showed that it is necessary to take into account the influence of the model bed assembly and particle element sphere density in particular when using the MSM to model particulate flows. In the next chapter the MSM used to investigate the influence of particle shape on the flow characteristics of particles discharging from a flat bottomed hopper.

## **5. An Exploration of the Effect of Particle Shape on Bed Structure and Flow Characteristics of Particles Discharged from a Hopper**

### **5.1. Introduction**

As reviewed in Chapter 1 there were many experimental and numerical investigations of particulate flow. Among these studies, the DEM is now well established as an effective investigation tool. However, most DE studies of the flow of particulate materials have used circular or spherical model particles, which limits its application to non-spherical particulate materials for reasons noted in 1.3.4. It is well established that particle shape affects the flow pattern (see 5.3.2 for detailed discussion). Particle shape will have an influence on particle bed structure and flow characteristics such as packing structure prior to flow (also related to the mode of filling), type of flow, and formation of shear bands.

The DE model (based on the MSM) in this study, has been used to investigate the effect of particle shape on the flow characteristics of particulate assemblies of different shapes.

### **5.2 Hopper configuration and simulation procedure**

A flat bottom hopper of 100cm width (50 times the diameter of a single sphere of unit radius) has been simulated in 2-D i.e. the 3D model particles have been positioned in a single vertical layer. The hopper structure consisted of an upper and lower part. The upper part has been sized to accommodate particles with a very loose structure during the generation stage and to allow consolidation of the assembly before opening the orifice of size 70% of hopper width which has been positioned at the bottom of this section. The height could be changed so that all model particles have been generated in the hopper without any contact (the unconsolidated bed height increased as the particle aspect ratio increased). The orifice has been simulated as a removable wall which has

been positioned at the midpoint of the hopper. The particles discharged from the upper box, collected in a chamber beneath the hopper. A vertical section through the hopper is shown in Fig. 5.1.

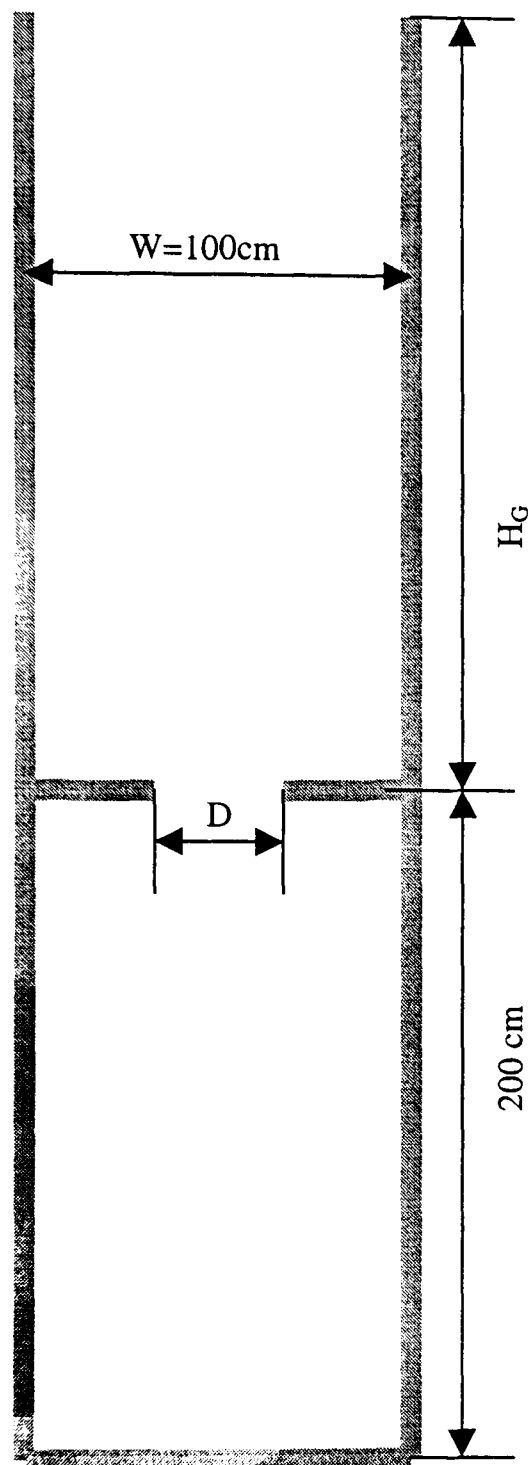


**Figure 5.1** Simulation set up and hopper configuration;  $H_G$  is the height of the upper section which could be changed to accommodate assemblies of different particle shape during particle generation.

Four sets of simulations have been performed with particles of the same volume (each particle comprised of a linear array of mono-sized spheres) with aspect ratios from one to four. This ensured that the effect of pseudo friction due to interlocking between

multi-sphere model particles (discussed in section 3.7) was the same for all particle shapes. The radius of mono-sized element spheres of a non-overlapping multi-sphere model particle of aspect ratio  $n$  with volume equal to the volume of a sphere of unit radius is

$$R_n = \left(\frac{1}{n}\right)^{\frac{1}{3}} \quad (5.1)$$

where  $n$  is the aspect ratio or the number of non-overlapping element spheres in the model particle.

In each simulation mono-sized (spherical and non-spherical) particles have been placed into the hopper in a vertical layer. In the case of non-spherical particles, a random orientation has been given to each particle in the X-Z plane in order to generate random packing of particles. Particles were then allowed to consolidate under a gravity field until particle movement was negligible.

**Table 5.1** Model parameter values.

Elastic modulus	3.5	GPa
Poisson's ratio	0.3	—
Radius of the equivalent single sphere	1.0	cm
Damping coefficient	0.5	—
Coefficient of friction (particle-particle)	0.2	—
Coefficient of friction (particle-wall)	0.5	—
Particle density	2.65	g/cm <sup>3</sup>
Time step	1.0 E <sup>-5</sup>	sec
Number of particles	5000	—
Number of element spheres	5000, 10000, 15000, 20000	—

To study the effect of particle shape on the bed structure independently of the effect of inter-particle friction, the particle-particle and particle-wall coefficients of friction have been set to zero during the consolidation. This method of particle bed preparation also had the effect of speeding up the consolidation process. At the end of the particle bed generation stage the coefficients of friction have been set to the values shown in Table 5.1. The other particle properties and computational conditions used in the simulations are also shown in this Table.

## 5.3. Results and discussion

### 5.3.1. Packing structure

The effect of particle shape on the packing structure of particle beds (the arrangement of particles) at the end of consolidation has been investigated by comparing the results of simulations in terms of bed height, the distribution of solid fraction through the bed, particle co-ordination number and the force acting at the bottom of the hopper. The initial bed height and the bed structure in a frictionless condition for the assemblies of particles comprising aspect ratio from one to four are shown in Fig 5.2. The original bed height increased as the particle aspect ratio became higher due to greater void space between the particles of higher aspect ratio.

During consolidation, non-spherical particles moved downwards differently from spherical particles, because these particles can create voids of different shapes and sizes if the orientation of the adjacent particles is changed. This resulted in a more randomised and more porous structure which in turn led to a bed of greater height. In contrast, spherical particles could slide over another one to occupy any existing space between them, as they were relatively free to slide against each other. It is seen that while the spherical particles could slide against each other to occupy the space between the particles, for the elongated particles this could not happen and some relatively large voids have been created due to randomised orientation of the particles.

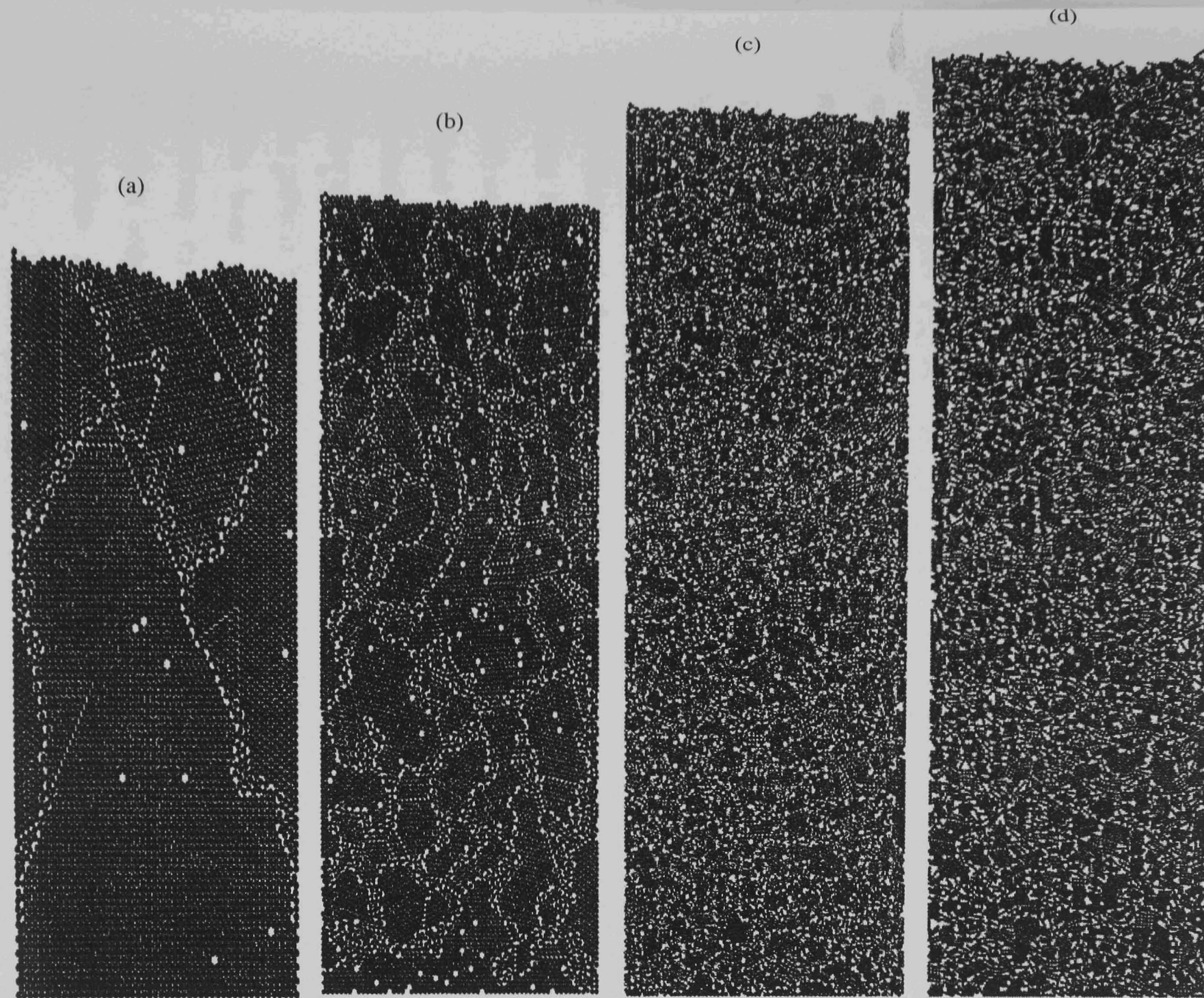


**Figure 5.2** Bed structure at the end of consolidation for particles of aspect ratio: (a) 1, (b) 2, (c) 3 and (d) 4.

The relative position and randomise orientation of particles in the beds resulted in a more porous structure for beds of particles of higher aspect ratio and dissimilar particle bed configuration (general shape of the consolidated bed) for each assembly. Some localised densely packed areas of homogenous particle packing structure have been observed, separated by narrow regions of higher porosity caused by bridging of particles. Dobry and Ng (1992) noted that random arrays of identical spheres tend to crystallise in regular patterns. The size of the homogenous densely packed area was increasingly smaller in beds of particles of higher aspect ratio. There was a greater difference in the size of the area of densely packed particles between beds of particles of aspect ratio one and two (comparing Fig 5.2a and Fig. 5.2b) than between beds of particles of aspect ratio two and three and from three to four (comparing Fig. 5.2c and Fig. 5.2d). This suggests that the change of particle shape from spherical to non-spherical had a greater effect on the packing structure of the particle bed than an increase in the aspect ratio of non-spherical particles.

The packing structure has been quantified by calculation of the solid fraction of the bed. The effect of particle aspect ratio on the packing structure of the particle bed has been investigated by comparing the distribution of the solid fraction and the average solid fraction for the consolidated bed. The distribution of the solid fraction through the bed has been calculated by partitioning the particle bed into a grid of squares (mesh) each  $10 \times 10$  cm, so that in each square a proper number of particles could be occupied (approximately 20 particles). The solid fraction for each square has been calculated from the number of particles which their centroid located inside the square, and the area of the square. Figures 5.3, 5.4 and 5.5 show the solid fraction distribution of the particle bed inside the hopper, the frequency distribution of solid fraction for particle beds of different aspect ratio and the average solid fraction for each respectively. In Fig. 5.3 a lower solid fraction near the free surface has been seen for all particle beds, indicating a looser layer of particles in that region due to the lack of over-burden.

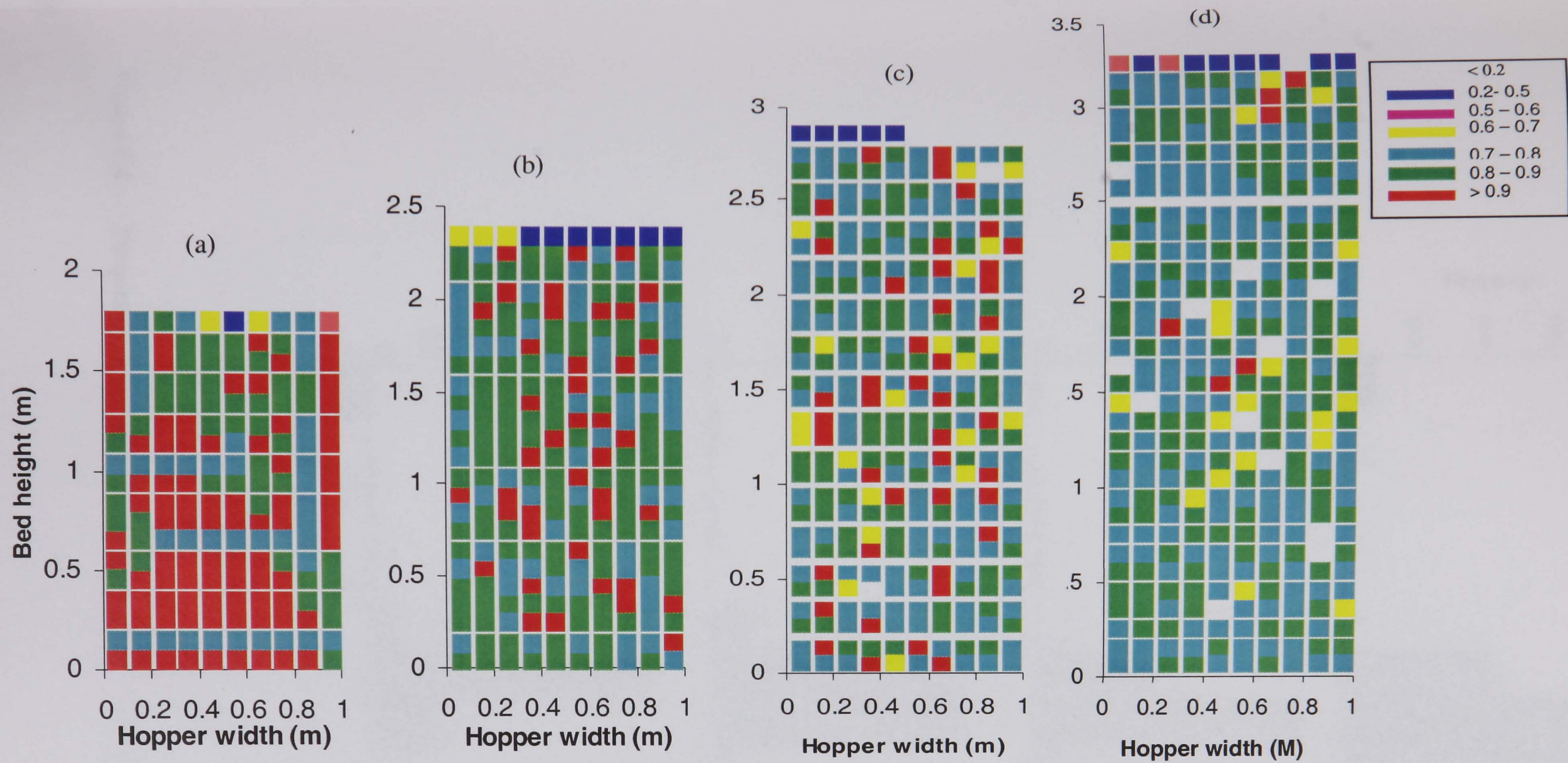


**Figure 5.3** Distribution of solid fraction in the hopper for the consolidated assemblies of aspect ratio (a) one, (b) two, (c) three and (d) four.

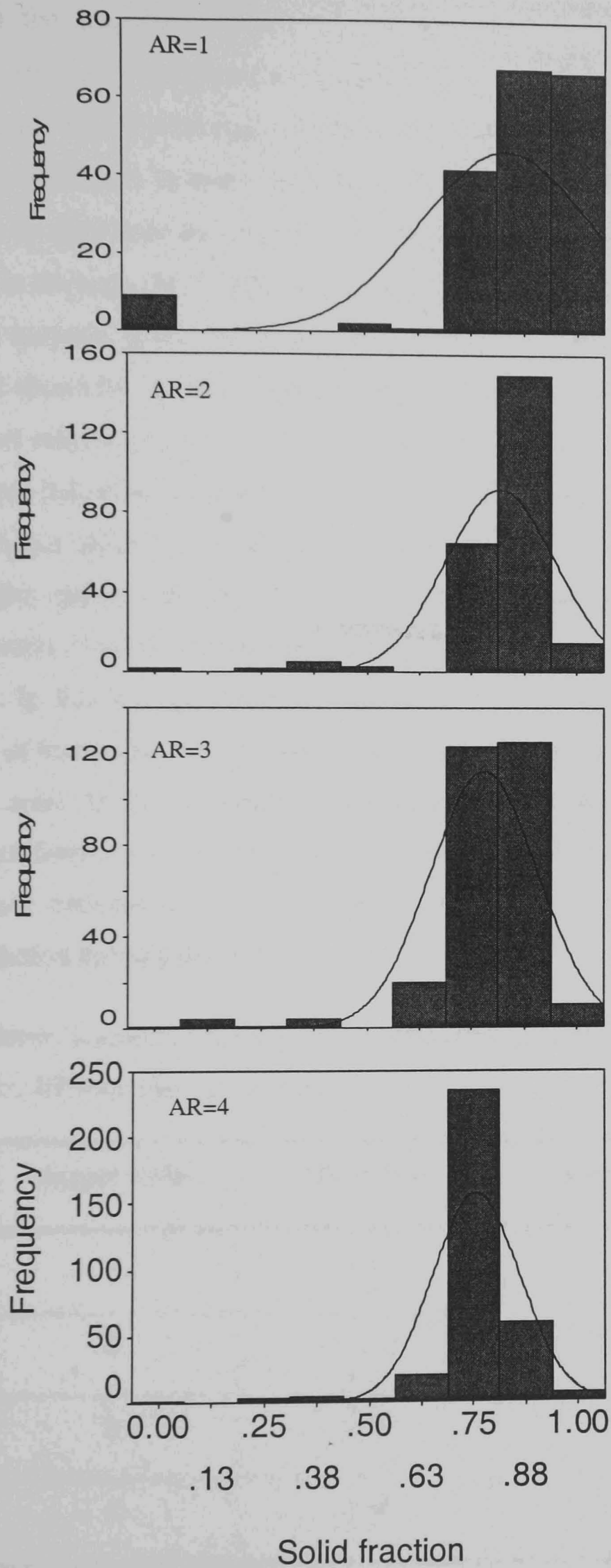


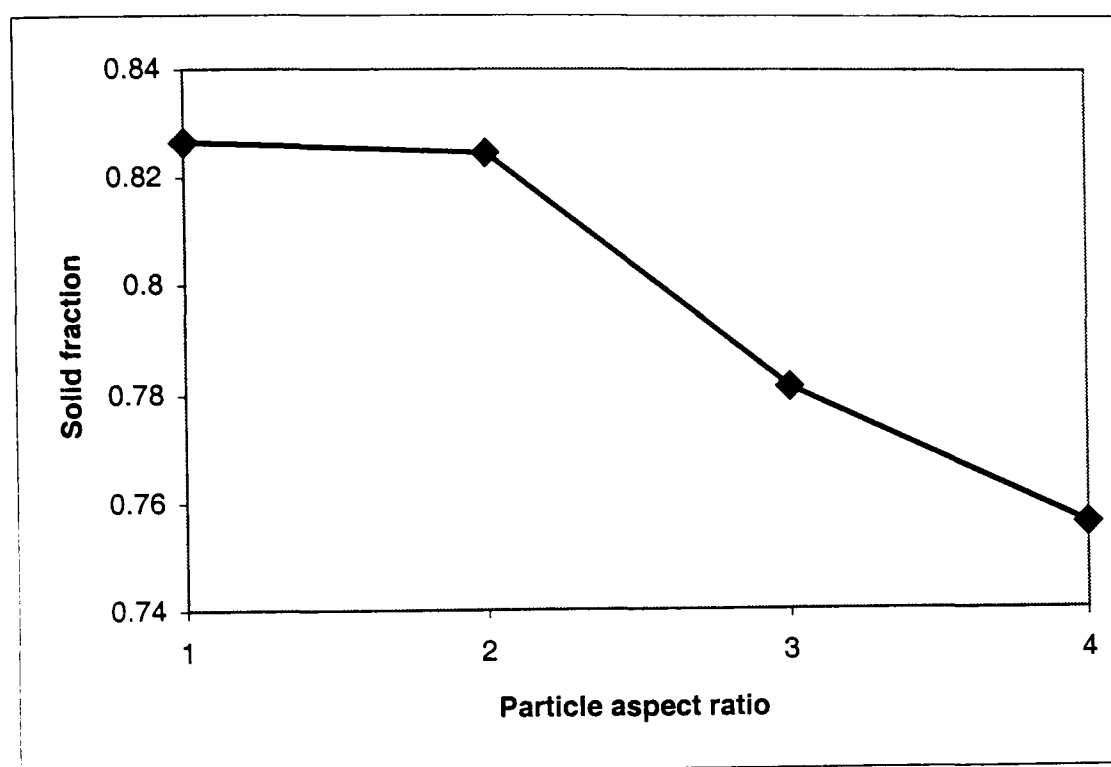
Figure 5.4 Frequency distribution of solid fraction in different particle assemblies.

Fig. 5.4 shows the frequency distribution of solid fraction for different particle assemblies. The frequency distribution of solid fraction is a particular parameter if the assumption is made that in a normal distribution of the solid fraction there is a wide varieties of voids (different in shape and size) in the bed. A normal distribution curve is characterised by skewness and kurtosis. A distribution is negatively skewed when the curve shifts to the right side compare to a normal distribution. A distribution with a higher positive kurtosis means the distribution has more concentration around the mean. Table 5.2 shows the skewness and kurtosis of the curves in Fig. 5.4. It is shown that as the aspect ratio of particles in the bed increased, a lower skewness and higher kurtosis achieved, indicating a closer distribution to a normal distribution for the beds of particles of higher aspect ratio, indicating a wider variety of void shape and size. In contrast, the highly negative skewed for the bed of spherical particles indicates a more uniform distribution of solid fraction for this bed, showing a smaller variation in void size and shape. In this bed the frequency for solid fraction band of 0.5 shows the narrow regions of higher porosity caused by bridging of particles which separated the densely packed areas. In the assemblies of particles of aspect ratio two, and three the solid fraction distributed over a wider range (0.25-.05) which indicates that the regions of higher porosity between the localised area increased which caused to lower the average solid fraction through the bed.

**Table 5.2** Some descriptive statistics of the frequency distribution of solid fraction for different particle assemblies.

Aspect ratio	Skewness	Kurtosis
1	-3.20	9.95
2	-3.09	12.34
3	-2.28	12.59
4	-2.69	13.16

The average solid fraction decreased slightly as the aspect ratio increased from one to two and then decreased sharply as the aspect ratio has been increased further (Fig. 5.5). The overall, reduction in the average solid fraction was about 8 % as bed particle aspect ratio changed from one to four; however most of this reduction occurred between aspect ratio of two and four.



**Figure 5.5** Relationship between the average solid fraction of the particle bed and aspect ratio of particles at the end of consolidation.

### 5.3.1.1. Co-ordination number

Co-ordination number is defined as the average number of contact points per particle in the particulate assembly. This parameter correlates with the degree of dilation of the bed and it can be used as an index for comparison of particle bed structure. For a particulate assembly comprising spherical or elliptical particles, contact between particles can always be considered *point contact*. In assemblies of rod-like particles (e.g. cylindrical particles) in addition to point contact, contact may also occur along a line. In the case of particles with plane faces, contact may also occur over an area. In this research, any number of contacts between the element spheres of two neighbouring particles has been considered as a single contact point, as shown in Fig. 5.6.

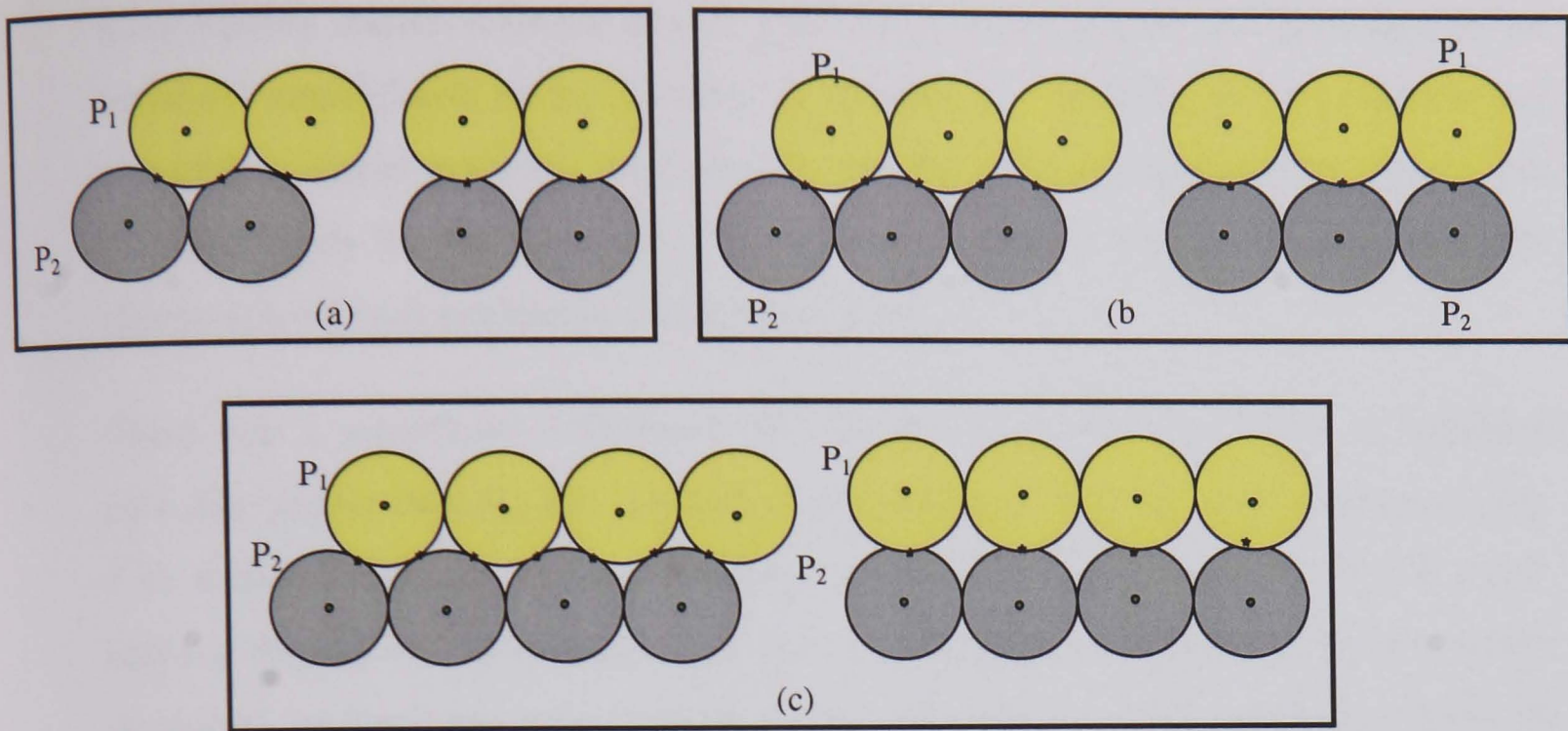


**Figure 5.6** Types of line contact between two multi-sphere particles comprising mono-sized, non-overlapping spheres which have been considered as a single contact for calculation of co-ordination number: (a) particles of aspect ratio two, (b) particles of aspect ratio three and (d) particles of aspect ratio four.

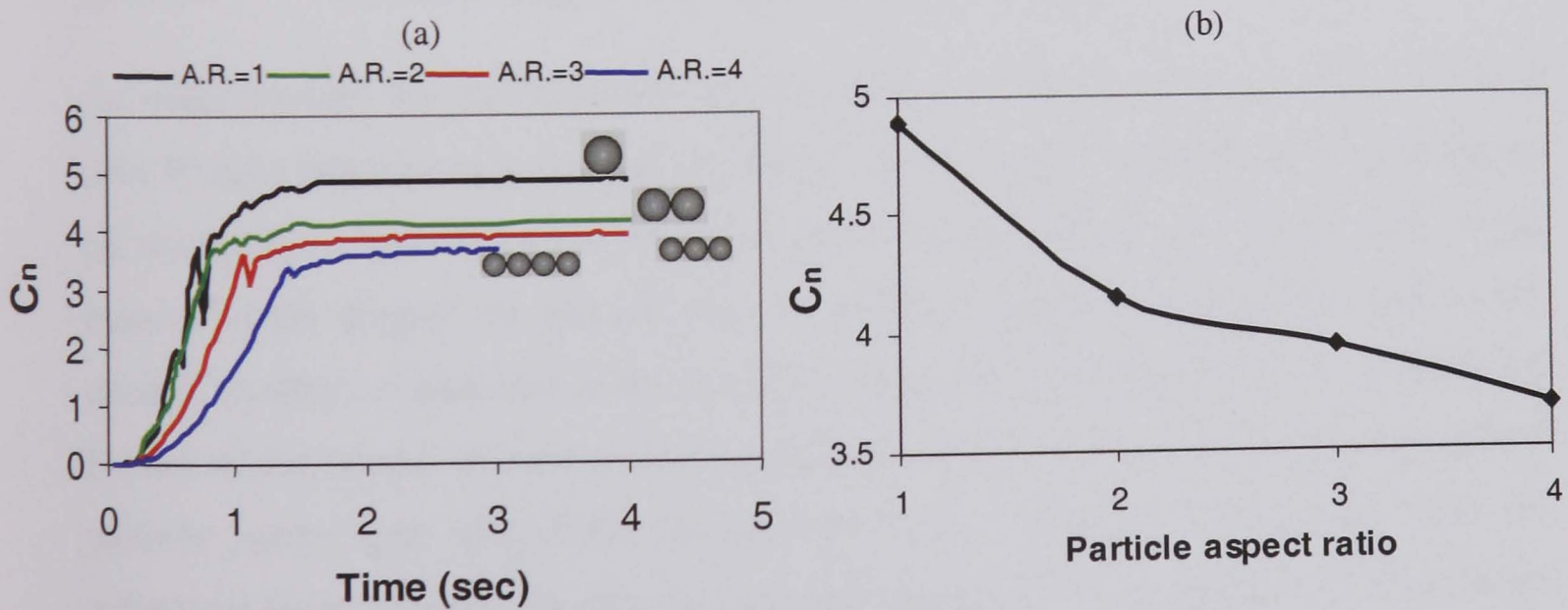


**Figure 5.7** (a) Change in co-ordination number ( $C_n$ ) during consolidation of beds of different aspect ratio, and (b) co-ordination number for the consolidated particle assemblies.

Figure 5.7a shows the prediction of the DE model for the evolution of co-ordination number in particle beds of different aspect ratios during consolidation. The consolidation started with no contact between particles ( $C_n=0$ ) and increased as the particles consolidated in the hopper. A constant  $C_n$  obtained for the particle bed indicated a stable assembly of particles. Despite different original bed height and different trends for the evolution of co-ordination number during consolidation, after almost 1.5s all beds reached in a stable condition.

There was a significant difference between the co-ordination number of spherical particles (aspect ratio=1) and non-spherical particles at the end of consolidation. Fig. 5.7b shows the maximum co-ordination number for particle beds of different aspect ratios at the end of consolidation. The final co-ordination number of the beds generally decreased, as the aspect ratio became higher, indicating a looser packing structure for non-spherical particles. The change in the magnitude of co-ordination number was greater (15.1 %) between beds of particles of aspect ratios of one and two (spherical and non-spherical) than between beds of particles of aspect ratio of two and four (11.3 %).

### 5.3.1.2. Force acting at the bottom of the hopper

As noted earlier, the consolidation step has been simulated for a condition of using zero friction between particles and the weight of the particle assembly was identical for all assemblies. Any difference therefore between the amount of force acting at the bottom of the hopper for particle beds of different aspect ratio might be due to the relative position of particles in the bed (bed structure). The sum of forces acting at the bottom of the hopper at the end of consolidation has been recorded and plotted against particle aspect ratio (Fig 5.8). As shown in this figure, for all particle beds the calculated force between the particle bed and the bottom of the hopper was close to the actual weight of the particles. The difference for the bed of spheres was not considerable (0.02 % of actual weight) and this difference increased to a maximum of 1.25% of actual weight for the particle bed of aspect ratio two, then decreased as the aspect ratio increased. In a frictionless condition the total weight acting at the bottom of the hopper should be the same for all beds. The variation in the total contact force

between particles and hopper bottom for particles of different aspect ratio can be related to the number of contact points with the bottom, the damping forces calculated at each contact point and the fact that in a DE model even in a quasi-static condition the model particles are not at rest (vibrating particles). When the aspect ratio changed from one to two, there were two element-spheres for each particle, but there was not a considerable change in the bed structure (Fig. 5.2a and b) and solid fraction so that more contact points have been found between particles and the bottom (5 more contact points than spherical particles). As discussed in Chapter Three, for a multi-sphere particle the damping acts on the contact points of the element sphere of a particle. Increasing the number of coincident contact points increases the damping. Moreover, as the particles were vibrating in the bed, the relative position and the relative velocity of the contacting spheres have been changed so that the total damping force between the particles and the bottom of the hopper has been changed in an oscillating manner. The record of total damping force between the particles and the bottom of the hopper showed that while the maximum total damping force for bed of spherical particles was 0.4 % of total weight of particles, for the bed of comprising particles of aspect ratio two, the maximum damping force was 1.05 %. Therefore, it is concluded that the higher contact force for particle bed of aspect ratio 2 was due to the higher total damping force between particles and the hopper bottom.

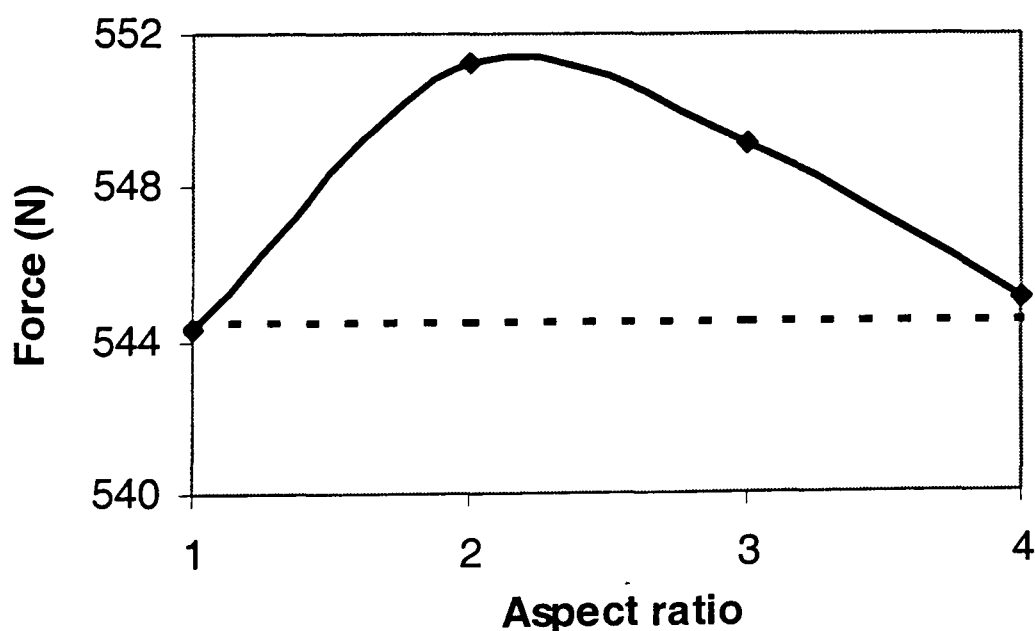


**Figure 5.8** Total force acting on the bottom of the hopper for particle assemblies of different aspect ratio in frictionless contact condition. The dashed line shows the actual weight of assemblies.

In the presence of friction between the particles and walls, the walls will carry part of the weight of the bed. The amount of the bed weight that can be transferred to the wall might be affected by the degree of interlocking between the particles of different aspect ratios. More numerical experiments are needed to investigate the effect of inter-particle friction on the total force acting at the bottom of the hopper in particulate assembly of different aspect ratios and also the average and maximum contact force per contact point at the bottom of the hopper.

### 5.3.2. Effect of particle shape on flow characteristics of particles

The dynamics of the discharge of particulate materials from a hopper is affected by several characteristics of the granular system. Knowledge of the interactions occurring between particles during the discharge can facilitate the improvements to design of a granular system. The complication of the interactions in a particulate system restricts the level of detail that can be obtained from physical experiments. Computer simulation of these systems has provided more detailed information, leading to a better understanding of granular flow, but such investigations have mostly been limited to the flow of spherical (circular) particles (Langston, *et al.*, 1995; Thornton and Kafui, 1997 and Kano, 1998). Cleary (1999) modelled circular and non-circular 2-D particles, where the non-circular particles have been represented using super-quadric functions to create non-circular particles of different aspect ratio and blockiness. By changing the parameters in the super-quadric functions, the particle shapes have been changed from circle to either ellipse or square. It has been observed that although both aspect ratio and blockiness affected the flow rate, the former had a stronger effect on the flow. Changing the shape of particles from circular to elliptical with an aspect ratio of five reduced flow rate by up to 30% and the flow pattern was also quite different i.e. the elongated particles no longer behave as free-flowing independent particles and behave more like deforming, fracturing continua (Cleary, 1999).

In this study, the effect of particle shape on the dynamics of discharged particles has been numerically investigated by simulating the flow of consolidated beds of particles with different aspect ratios. These beds were those as discussed in the previous section. Parameters such as particle track, particle orientation, particle kinetic energy ratio,

particle horizontal velocity, and rotational velocity have been used to study the effect of particle shape.

### 5.3.2.1. Evolution of solid fraction during flow

Figure 5.9 shows the evolution of particle bed solid fraction during particle discharge. A homogenous structure with higher solid fraction (compared with elongated particles) has been seen in the structure of spherical particle assembly during flow, indicating a very free movement for particles, which in turn led to a uniform flow. In contrast, the bed of elongated particles exhibited an uneven distribution of solid fraction through the hopper during flow, resulting in an intermittent flow.

In the bottom row of Fig.5.9 (for elongated particles), after the orifice has been opened, the structure of the bed rearranged itself with a lower solid fraction near the orifice ( $t=1$  sec). By discharging the lower particles near the orifice the upper materials have been stopped by producing a momentary arch. As the flow continued and the created arch remained, the structure of the lower part of the hopper became more porous while the structure of the bed above the arch became denser as the result of slower downward movement of particles in this region ( $t=2$  sec).

The pressure from the particles above the arch pushed the particles adjacent to the sidewalls both downwards and outwards. These particles have been supported by friction with the walls and with some particles below. As the lower particles discharged from the hopper, the lower supports of these particles have been gradually weakened, therefore the existing arch collapsed as the friction force between the particles and sidewalls exceeded the Coulomb limits. The particles above the arch fell abruptly, resulting in a new and more porous structure for whole of the bed ( $t=3$  sec). A fluctuating flow rate has been produced by repeating this behaviour of the bed with elongated particles, especially at the beginning of flow.

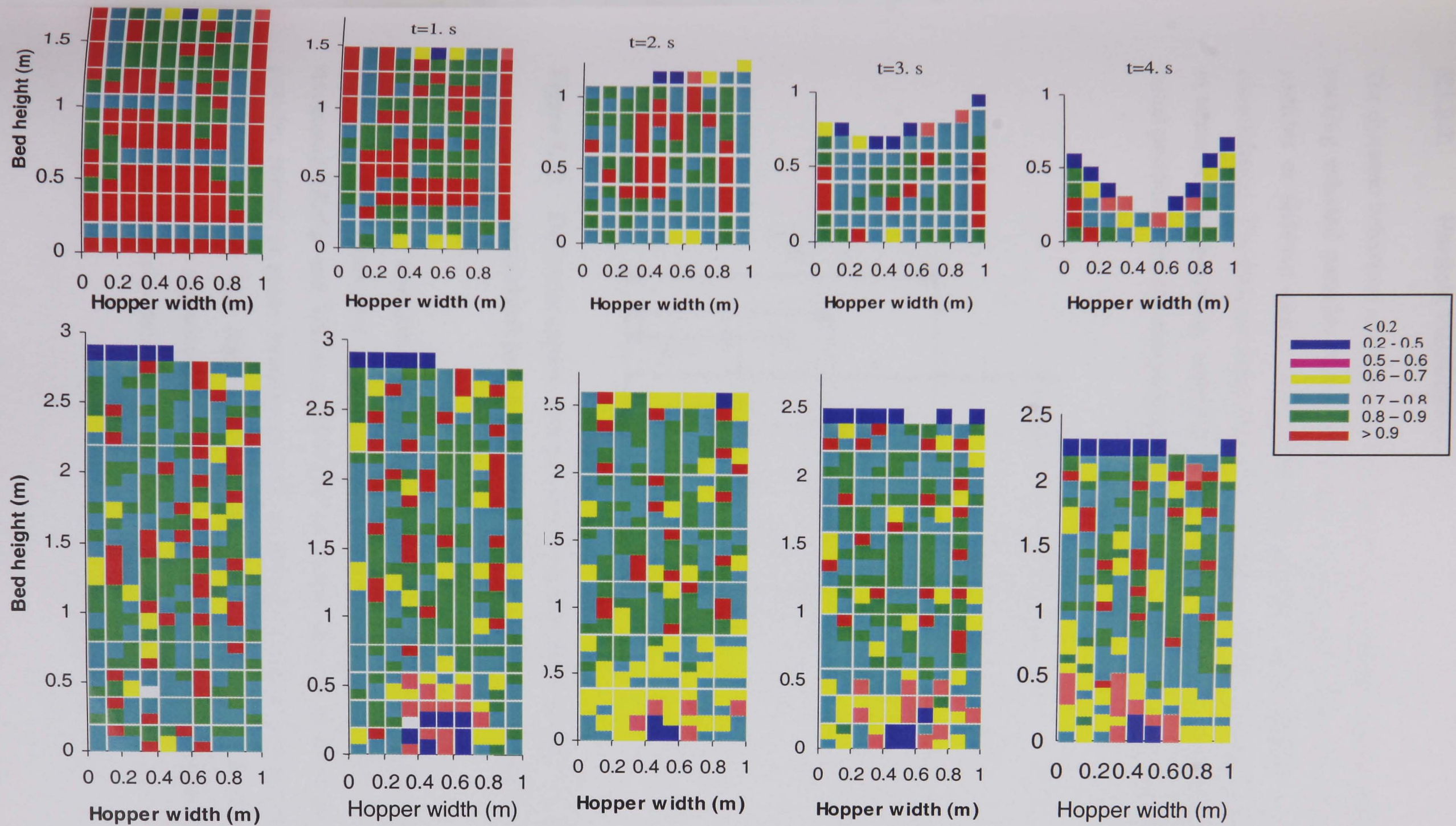


**Figure 5.9** Evolution of solid fraction during flow of spherical particles (top row) and elongated particles with aspect ratio three (bottom).

### 5.3.2.2. Particle trajectories

The dynamic behaviour of the assemblies has been investigated at the particle scale by tracking selected particles through the bed. In each particulate assembly (beds of particles of different aspect ratios) nine particles have been selected at the end of consolidation. The dynamic behaviour of these particles during flow has been recorded in terms of their positions, velocities and rotation. Fig. 5.10 shows the approximate initial position of the selected particles in each consolidated particulate assembly.

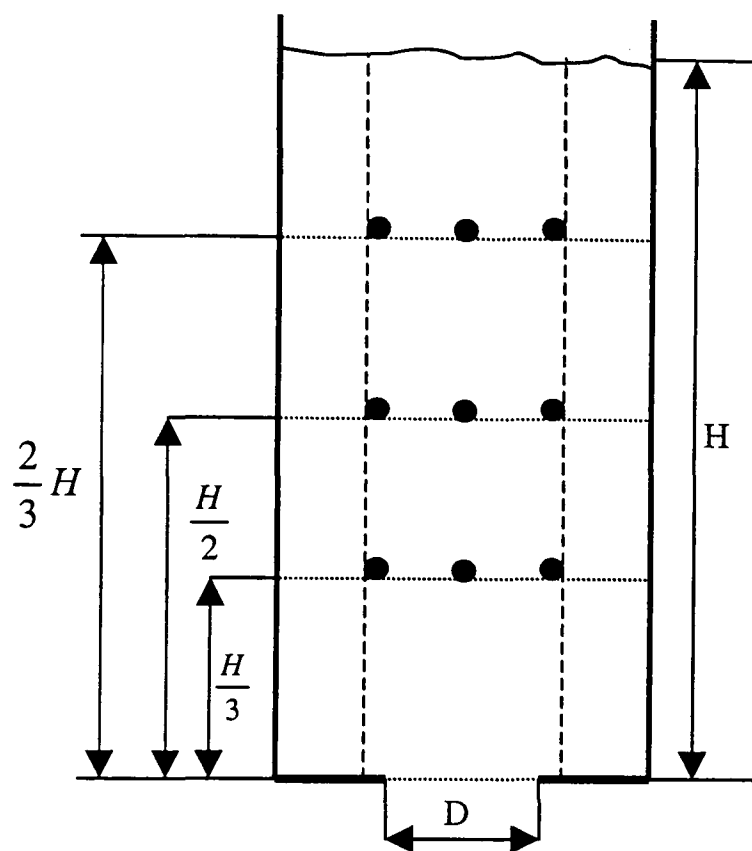


**Figure 5.10** The initial approximate position of the nine selected particles in the consolidated particle assembly.  $H$  is initial bed height and  $D$  is orifice size.

Fig 5.11 shows the trajectories of the selected particles during flow in particle beds of different aspect ratios. For all particle beds convergent or funnel flow zone can be recognised (Kafui and Thornton, 1997) in the lower portion of the hopper, where particles started to move laterally as well as vertically when they approached the orifice. In the plug flow region (upper portion of the hopper) the particles moved downwards without any considerable lateral movement, exhibiting a mass flow with identical behaviour of particles in this region for all particle shapes.

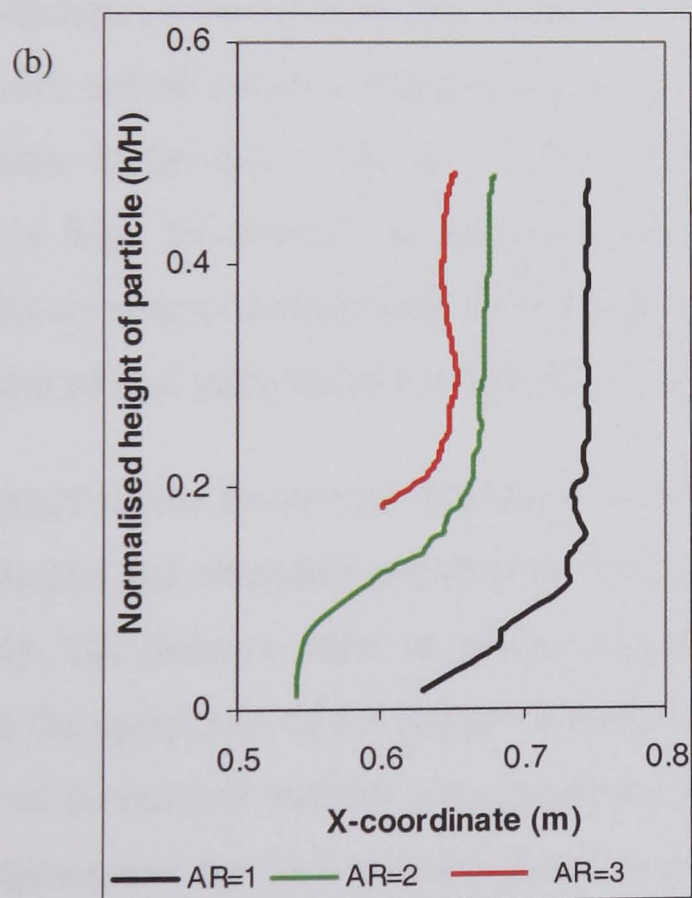
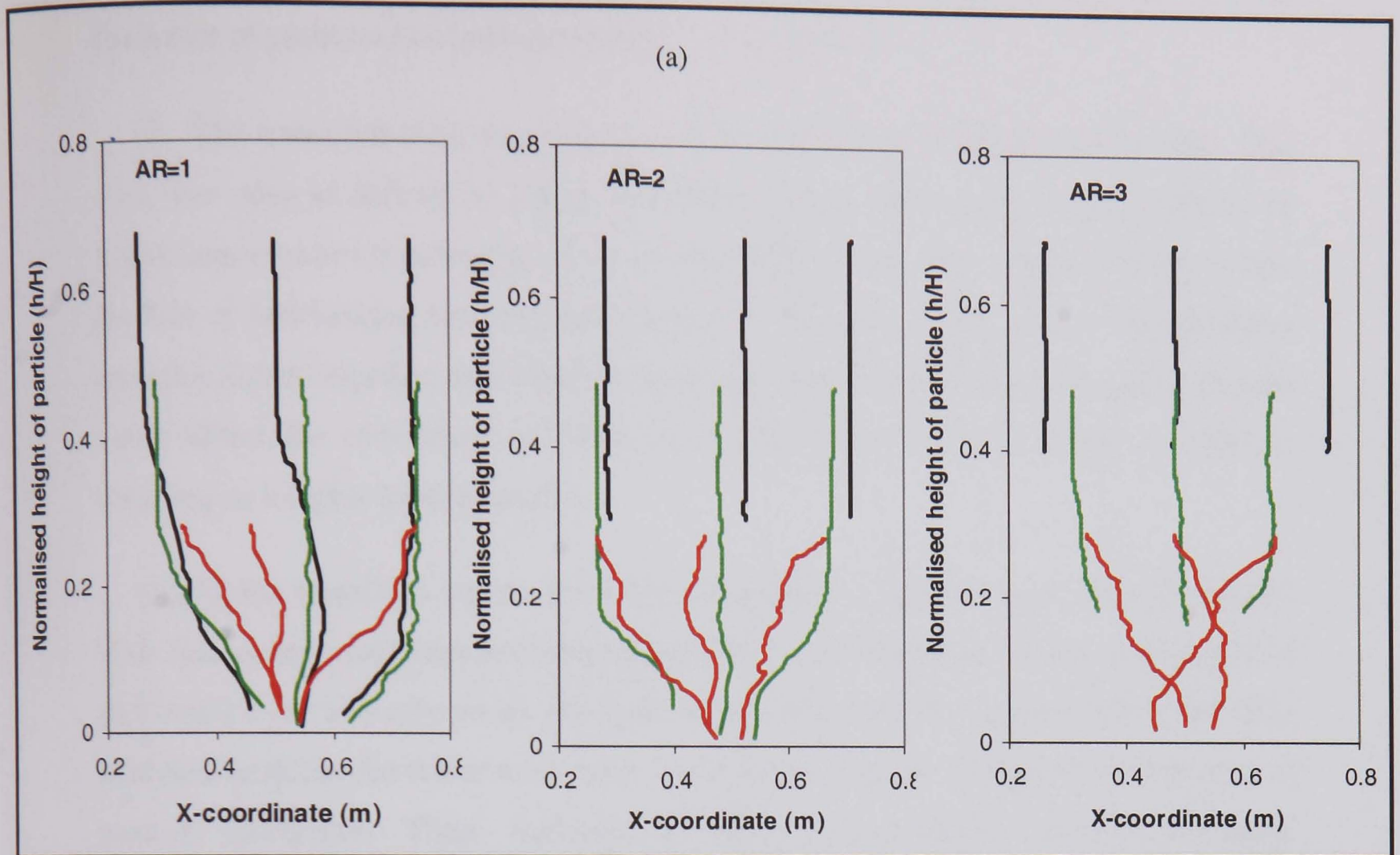


**Figure 5.11** (a) Comparison of the trajectories of nine selected particles in the hopper for different particle aspect ratio, (b) comparison of trajectories of particles in the right side of the hopper for three particle beds of different aspect ratios.

However, in the transition zone, some differences in the height of the zone and the dynamics of particles has been seen (Fig.5.11) as follows:

(i) The transition zone was higher in beds of particles of higher aspect ratio. The *core flow zone* as defined by Zhang and Ooi (1998) became narrower for particles of higher aspect ratios resulting in a concentrated funnel flow. This can be explained from the rate of interlocking between particle beds of different aspect ratios. The elongated particles locked together more tightly, therefore the movement of an elongated particle could affect the movement of others to a greater degree than spherical particles, resulting in a higher transition zone.

(ii) In the transition region for a bed of spherical particles, a smooth (trajectory with less sudden sideways movement) path has been observed for the trajectories of particles i.e. a relatively small fluctuate in the direction of particles, while for non-spherical particles the trajectories were uneven with a sharp change in the direction of particle movement. These indicated a repeated interlocking between elongated particles so that these particles could not move like discrete objects but flowed much more similarly to a fracturing mass of materials (Cleary, 1999). Furthermore, spherical particles started to move laterally with a height closer to the bottom of the hopper even for those particles close to the side walls (Fig 5.11b), indicating a flow which was closer to that of mass flow. In contrast, in non-spherical particle beds, the track of particles show a relatively concentrated funnel flow which would normally be expected for a flat bottom hopper of real particles of non-spherical shape Cleary (1999).

The evolution of orientation and horizontal (lateral) velocities for the selected particles in particle bed of spherical and elongated particles (A.R.=3) are also shown in Fig 5.12 and 5.13 respectively. An inactive state in terms of particle rotation and particle horizontal velocity in the upper part of the hopper indicates a mass flow region. In this region particles moved downward without any significant rotation or lateral velocity, indicating a mass displacement for the bed as the particles discharged from the hopper.

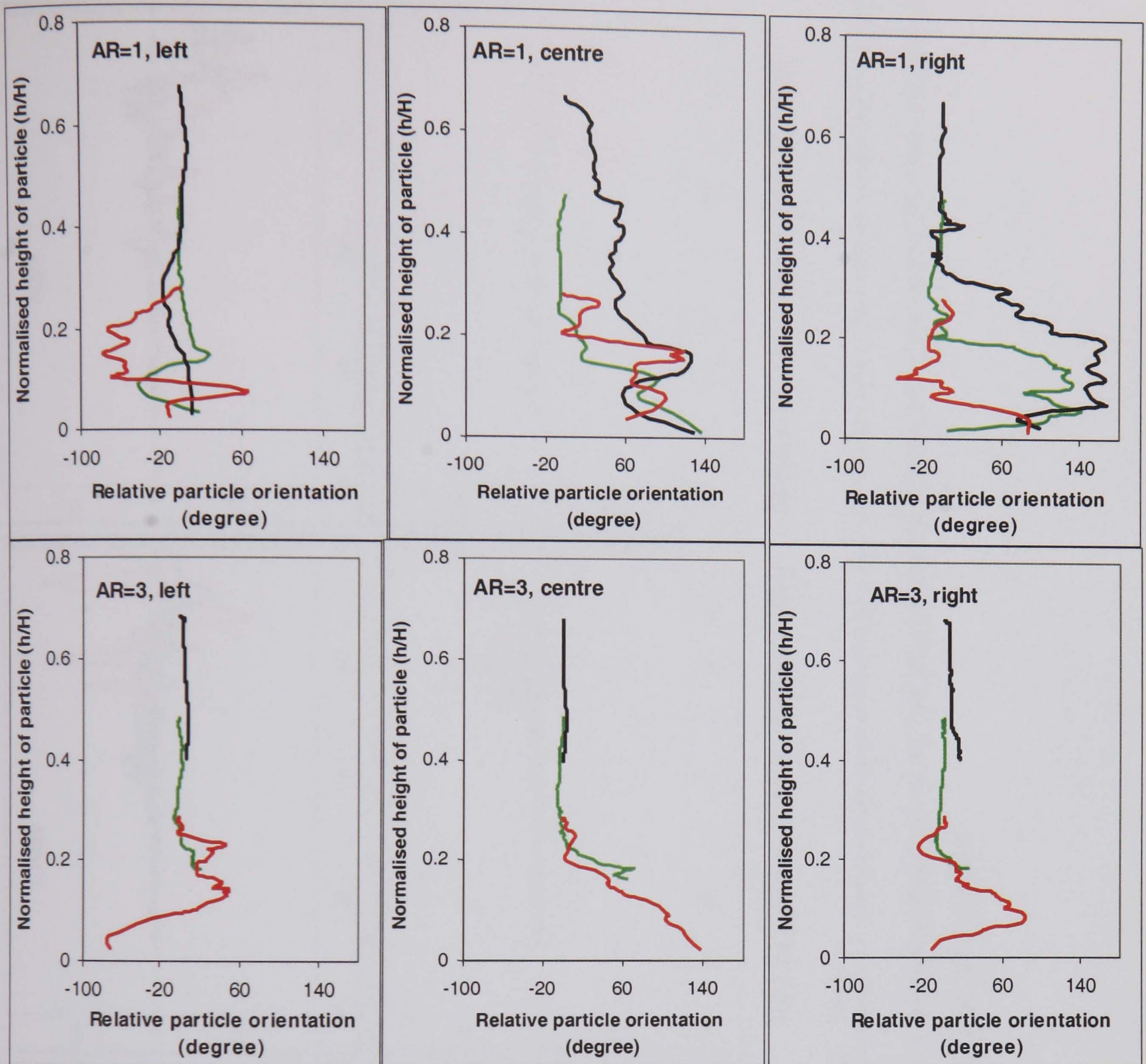


**Figure 5.12** Comparison of the evolution of particle orientation during flow for particle bed of spherical particles (Top) and particle bed of aspect ratio three (Bottom) at left, centre and right side of the hopper. In each graph the black line correspond to the highest particle, the green line to the particle at the middle and the red line to the lower particle.

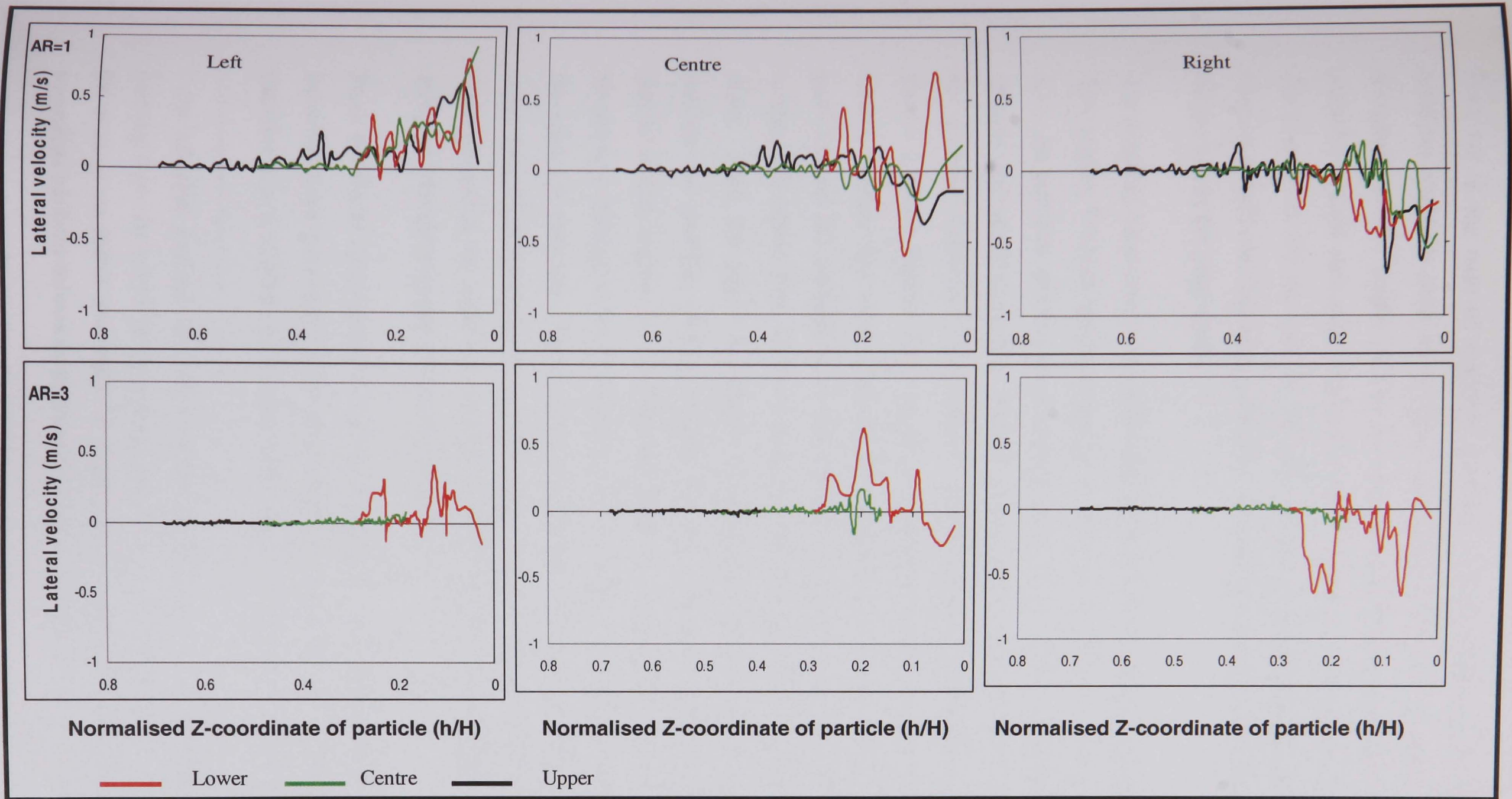


**Figure 5.13** Comparison of the lateral velocities of particles discharge of the bed of particles of aspect ratio three and of the bed of spherical particles at left side, middle and right side of the hopper.

However in the case of spherical particles a slight change in the orientation<sup>1</sup> (i.e. rotation) could be seen in the plug flow region (Fig. 5.12). This characteristic of spherical particle might be due to inter-particle friction and the rolling action of particles against each other whilst moving downwards, representing a more freely and discrete nature for the bed. In the case of non-spherical particles even a very small rotation of particles has been prohibited, indicating a stronger and more rigid structure for the bed in the plug region.

The dynamic behaviour of the beds differed between the transition region and the plug flow region, for both spherical and non-spherical particles as shown in Fig. 5.12 and 5.13. As particles entered the transition zone, they became more active in terms of rotation and lateral velocities. However, some differences could also be recognised in the dynamic behaviour of spherical and non-spherical particles in this region. As shown in these figures for non-spherical particles (A.R.=3), although the particles started to rotate and move laterally, the rotation was not as great as for the spherical particles and the orientation of the particles remained almost unchanged. However, occasionally these particles have been forced to rotate quickly in order to pass each other. Also, the lateral movement of elongated particles was uneven and in some periods the particles almost stopped moving laterally, indicating an uneven flow regime in this region. In contrast, for spherical particles, an active state in terms of rotation (i.e. change in the orientation) has been seen, indicating a greater rolling action for spherical particles. The particles could rotate against each other in order to pass more easily. Furthermore, for the case of spherical particles, a gradual trend has been distinguished in the lateral movement of particles in the left and right side indicating a freely movement of particles towards the orifice.

From the above observations it can be concluded that although the particle beds in the transition zone were much more active than the plug flow region, the flow of spherical particles was smoother, with more independent movement for individual particles. In

---

<sup>1</sup> For spherical particles the initial random orientation has been defined as a unit vector pointing from the centre of the sphere toward its outer boundary. As a particle rotates the direction of its initial unit vector is changed accordingly. For non-spherical particles the orientation has been defined as the direction of the longitudinal axis.

contrast, non-spherical particles have been locked together and did not flow like individual particles even in the transition zone, but moved as a mass of attached material.

The dynamic behaviour of the beds has been also investigated, through the entire bed by recording the energy ratio of particles. The energy ratio has been defined as the ratio of rotational and translational energy of a particle

$$\text{Energy ratio} = \frac{E_r}{E_t} \quad (5.2)$$

where

$$E_r = \frac{1}{2} I \omega^2 \quad (5.3)$$

$$E_t = \frac{1}{2} m v^2 \quad (5.4)$$

and  $m$ ,  $I$ ,  $\omega$ , and  $v$  are mass, mass moment of inertia, rotational and translational velocity of a particle respectively. The energy ratio is a particularly useful parameter if the assumption is made that if the particles in a particulate assembly during discharge from a hopper are rotating a lot relative to their translational velocity then the bed is looser with individual freely movement of particles resulting less shear strength.

The change in the average energy ratio of particles during bed discharge are shown in Fig. 5.14 in the left, centre and right side of the hopper for three particulate assemblies. The following has been observed: (i) Although in all assemblies the rotational energy of particles was lower than their translational energy ( $\text{Log } E_r/E_t < 1.0$ ), the observed rotation was much greater for particle of spherical shape than non-spherical particles in all parts of the hopper (top row of Fig. 5.14). (ii) In all assemblies the particles in the central part of the hopper had the minimum rotation compared to the sides of the hopper and the evolution of the average energy ratio in the sides of the hopper was almost the same (symmetrical) but higher for spherical particles (Fig. 5.14a). Rong *et al.* (1995) observed an intensive rotation for circular particles in the vertical layer next to the sides of the hopper and suggested that the dynamic coefficient of friction between the particles and wall should be used in the calculation of wall loads.

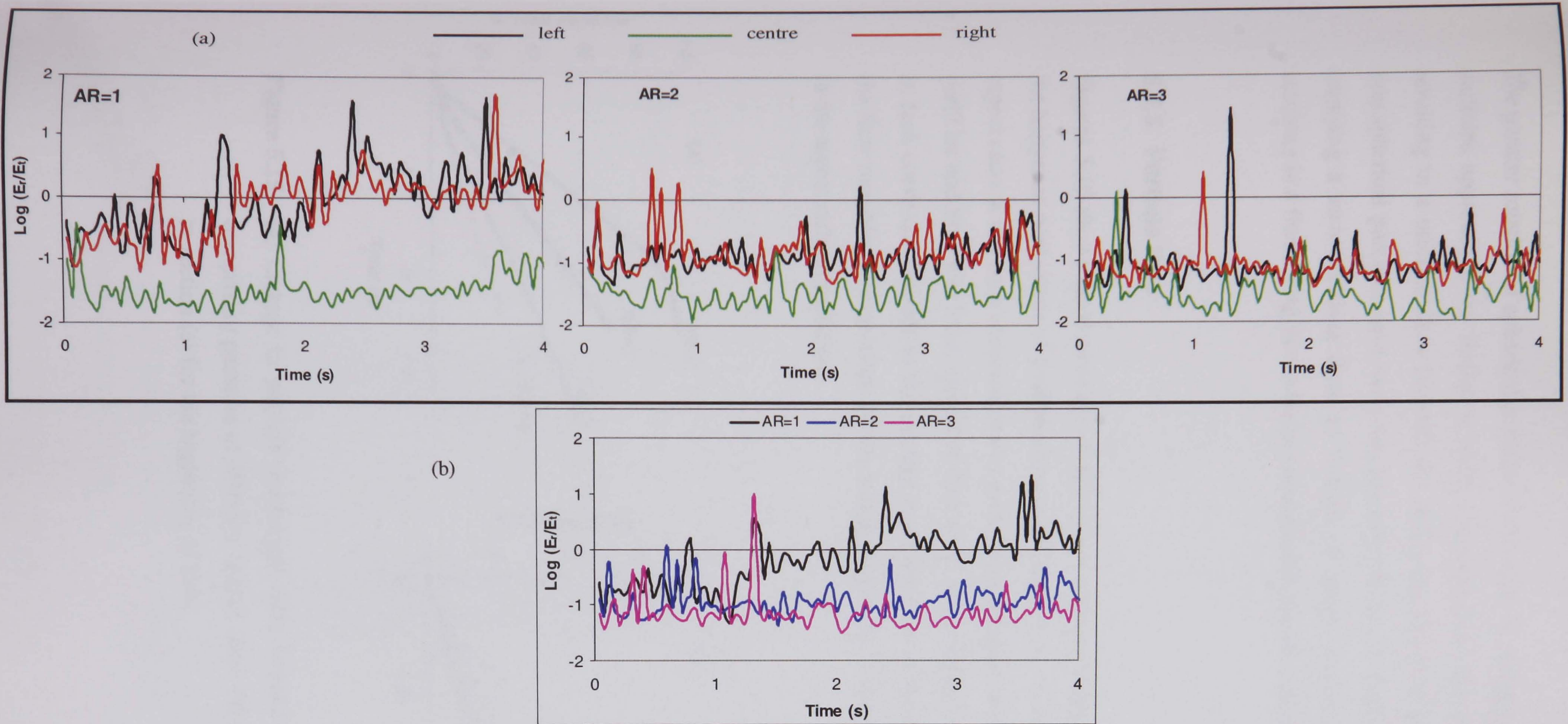


**Figure 5.14** Effect of particle shape on the energy ratio of the particulate assemblies during flow. The top row shows the average energy ratio in the left, centre and right side of the hopper for three particulate assemblies and the bottom shows the average energy ratio in the whole of the hopper for these assemblies.

The greater rotation of spherical particles in the sides of the hopper indicates that these particles approached the orifice in such a manner that they rolled over each other, resulting in a uniform flow towards the orifice as discussed previously. In contrast, non-spherical particles have been displaced in the hopper without noticeable rotation implying a more resisting shear as a result of strong interlocking between particles resulting in a fluctuating flow which is discussed in the next section.

### 5.3.3. Particle flow

Figure 5.15 shows the time series of cumulative number of particles discharged from the hopper as percentage of total particles in the hopper for beds of particle of different aspect ratio. It has been observed that in each curve the relation between the discharged particles and time was linear except at their tails. The gradient of the straight segments in each curve corresponds to the average mass flow rate of the particles. As expected, the flow rate (the average slope of the straight segments) increased with the decrease in the aspect ratio of particles.

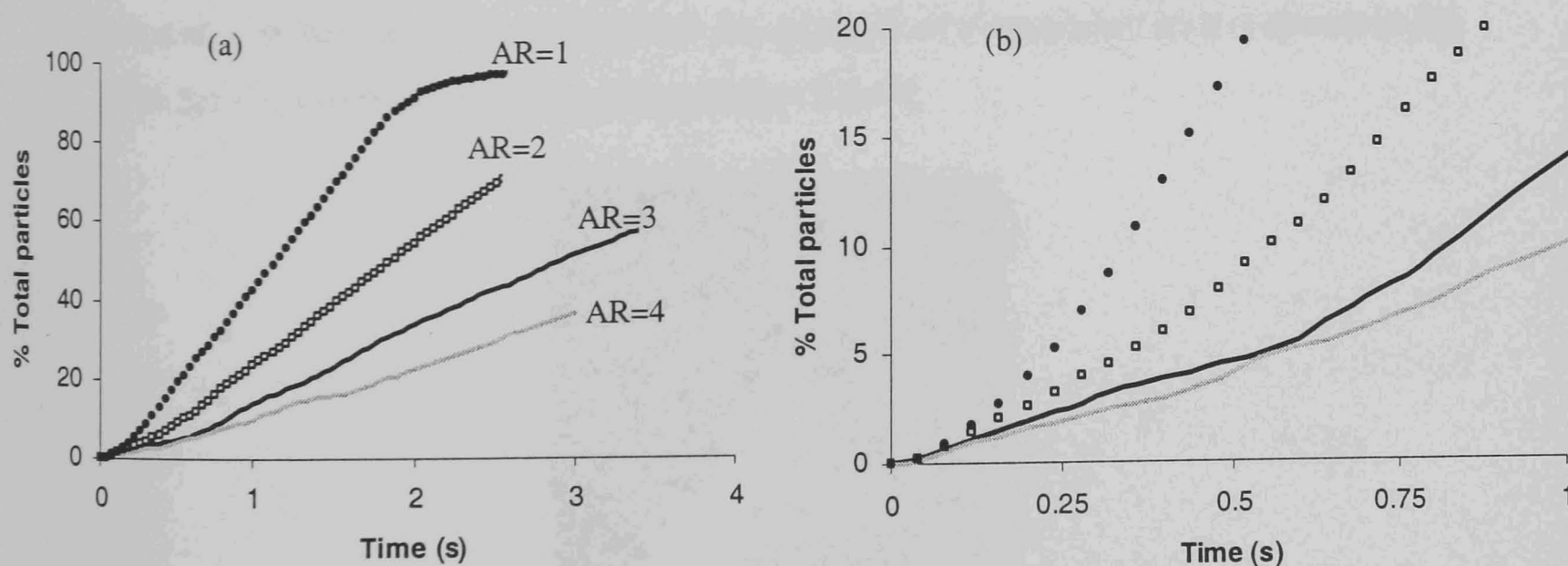


**Figure 5.15** (a) Change in particle discharged from hopper against time for beds comprising particles of different aspect ratio; (b) zoom up of the curves in section (a) for the beginning of flow.

The curves clearly indicate that there was a delay at the beginning of the discharge with a subsequent rapid increase in discharge rate to a constant value. The initial delay period was almost the same for all curves and was approximately 0.08 seconds. However, the period of which the discharge could reach a constant value (non-linear segment of the curves at the beginning) was noticeably dependent on the aspect ratio of particles. The length of this period decreased with the decrease in the aspect ratio of particles (move toward sphericity). This effect of particle shape will be more important in the process of dispensing batches of granular material from a hopper, where an intermittent flow operation occurs. On the other hand, at the end of flow, the constant flow rate started to decrease while the height of material in the hopper fell below a certain minimum. The flow has been terminated while some material remained at both sides of the orifice.

The irregularity of the discharge curves (Fig. 5.15b) also indicated the occurrence of temporary arching phenomena during flow. As shown in the corresponding curves, the roughness of the discharge curves increased as the aspect ratio of particles increased, indicating a fluctuating flow. In other words, while spherical particles displaced freely as individual particles, exhibiting a steady flow, the elongated particles discharged from the hopper as a bunch of joined material formed from arch breakage in the hopper, resulting in a fluctuating flow. An example of a temporary arch is shown in Fig 5.16 for the assembly of elongated particles ( $AR=4$ ).



**Figure 5.16** Example of the occurrence of temporary arching during flow for elongated particles ( $AR=4$ ).

The flow behaviour of the particulate beds also is shown in Figure 5.17 which shows the snapshot of particle positions for the different assemblies. The lower part of this Figure shows the snapshots of hopper filling with a surface friction coefficient of 0.2 for beds of particle of aspect ratio from one to four. As noted in these simulations the height of the lower part was 2m. It is seen that the slope of the heaps (dynamic angle of repose) in these snapshots are significantly different depending on three factors, drop height, particle shape and fill stream rate. Laboratory tests of uniform sized spheres dropping into cylinder also resulted in a range of solid packings depending on both the drop height and filling rate (Macrae and Gray, 1961) due to rearrangements caused by the energy of the impacting particles. By increasing the impact height the kinetic energy and inertia of particles existing near the heap peak cause the heap to flatten. This behaviour has been also observed by Walton and Braun (1993).

The dynamic heap shape for the bed of AR=1 (spherical particles) with lower impact velocity ( $\approx 3$  m/s) and for the bed of AR=2 (non-spherical particles) with higher impact velocity ( $\approx 4.5$  m/s) are shown in Fig.5.17. The slope of the heaps in these two snapshots are significantly different with the non-spherical particles forming a steeper surface than the spheres. It is interesting that despite the higher fill stream rate and lower impact velocity for the bed of AR=1, than the bed of AR=2, which would be expected to result in a steeper mound for the former, the heap was steeper in the latter. This suggests that the particle shape also is an important factor affecting the formation of the heap which dominated the effects of the other two factors. The snapshot of the bed of AR=4 clearly shows the effect of impact velocity and filling rate on the formation of the heap. In this snapshot the impact velocity was approximately 6 m/s and the filling rate was the lowest. It is seen that in this case there was sufficient kinetic energy and inertia near the mound peak to flatten the mound considerably.

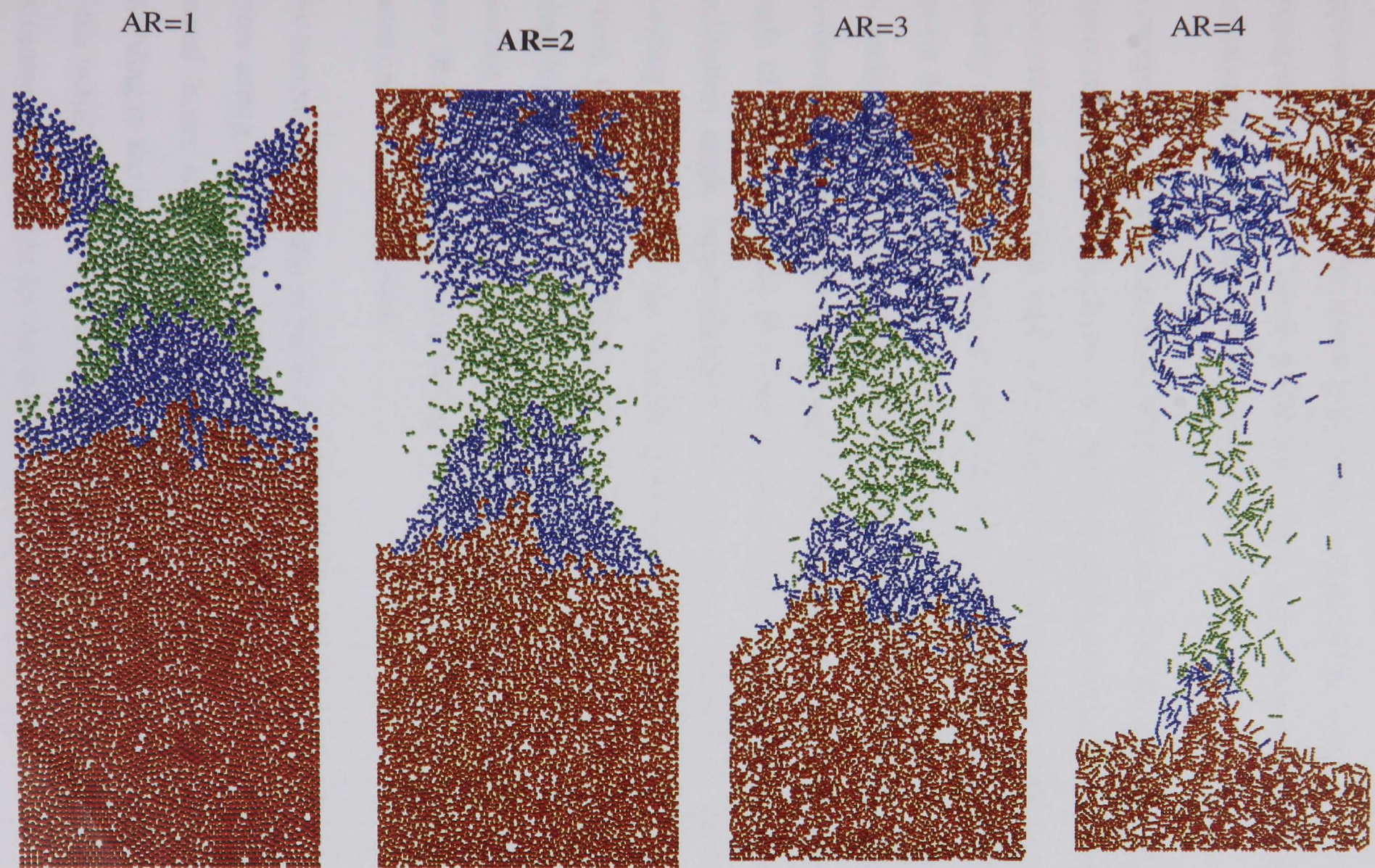


**Figure 5.17** Snapshot of positions at time  $t = 1.4$  s for the assemblies of different aspect ratio.

### 5.3.3.1 Development of shear band

Fig. 5.18 shows the position of particles in the lower portion of the hopper for different assemblies. In each assembly the particles have been coloured according to the velocity of the particle with maximum velocity. The interface of the shear band is seen in these snapshots which is a block of particles with higher velocity sliding relative to the other particles with lower velocity. It has been observed that in all assemblies, shear bands appeared initially in the lower part of the hopper at the early stage of flow and then propagated upwards. These phenomena have also been observed during numerical investigation of circular particles (Rong *et al.*, 1995).

A comparison of the orientation of the initial shear bands for beds of different particle aspect ratio (Fig. 5.18) shows that different angle of shear band orientation has been achieved for spherical and non-spherical particles. This difference appears to be directly related to the shape of particles, since other properties remained identical. It is shown that while for the bed of spherical particles almost a vertical shearing occurred, an inclined shear band has been observed for the beds of non-spherical particles. However, the magnitude of the aspect ratio of particles did not affect the inclination angle of shear band for the beds of non-spherical particles since almost the same inclination angle (approximately  $55^\circ$ ) has been observed in these beds. Vertical shearing occurs due to the relative movement within the materials as it flows to the orifice, thus inducing a dilation, but in horizontal shearing the material cannot easily dilate horizontally due to the constraint imposed by the hopper walls, resulting in an increase in the lateral wall pressure. Theoretical explanations for this phenomenon have been reported by some researchers (Vermeer, 1990; Bardet and Proubet, 1991) based on biaxial test results.

The horizontal shearing in the beds of non-spherical particles caused an increase in the forces acting on the sidewalls which is shown in Fig. 5.19. This figure shows the total normal forces acting on a sidewall of the hopper. The sidewall has been partitioned according to the initial height of the bed, such that the length of each partition was 0.1 of the initial height of the bed ( $H$ ). Each curve shows the total normal force acting on the centre of a partition for the initial stage of the flow.

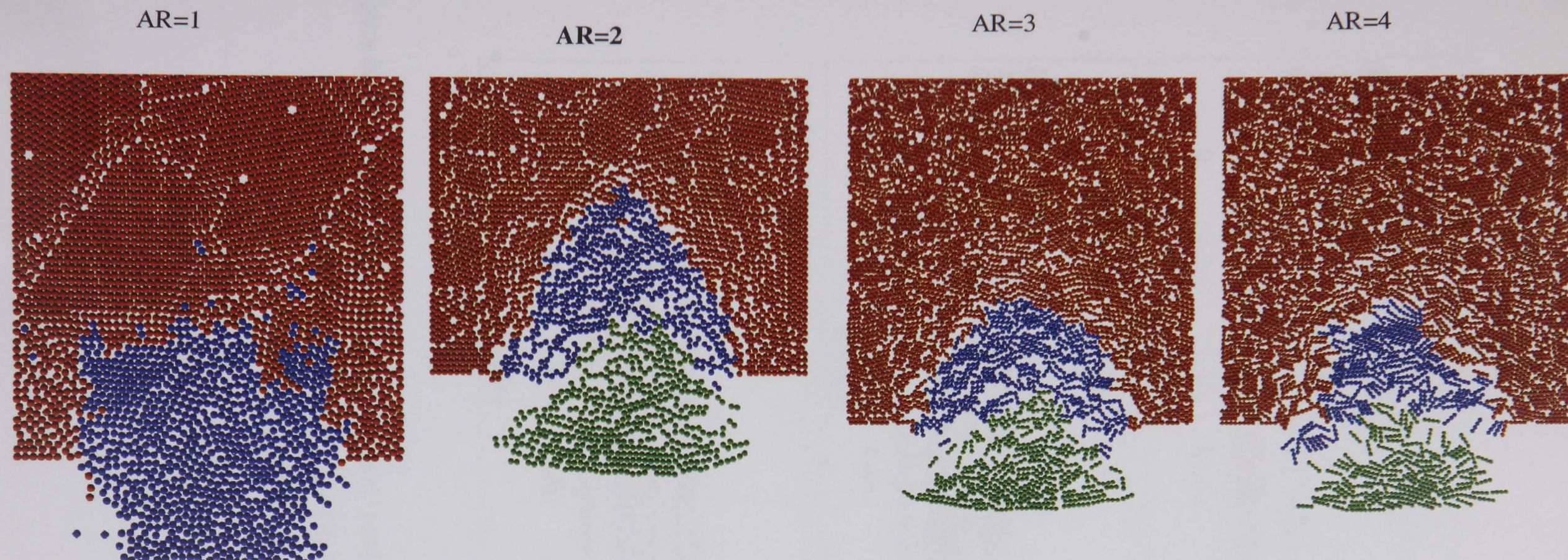


**Figure 5.18** The interface of shear band for the assemblies of particles with different aspect ratio. The particles were coloured according to the velocity of a particle with maximum velocity i.e. green for particles of velocity more than 70 %, Blue for particles of velocity between 30 – 70 % and the red for particles of velocity less than 30 % of the maximum velocity.

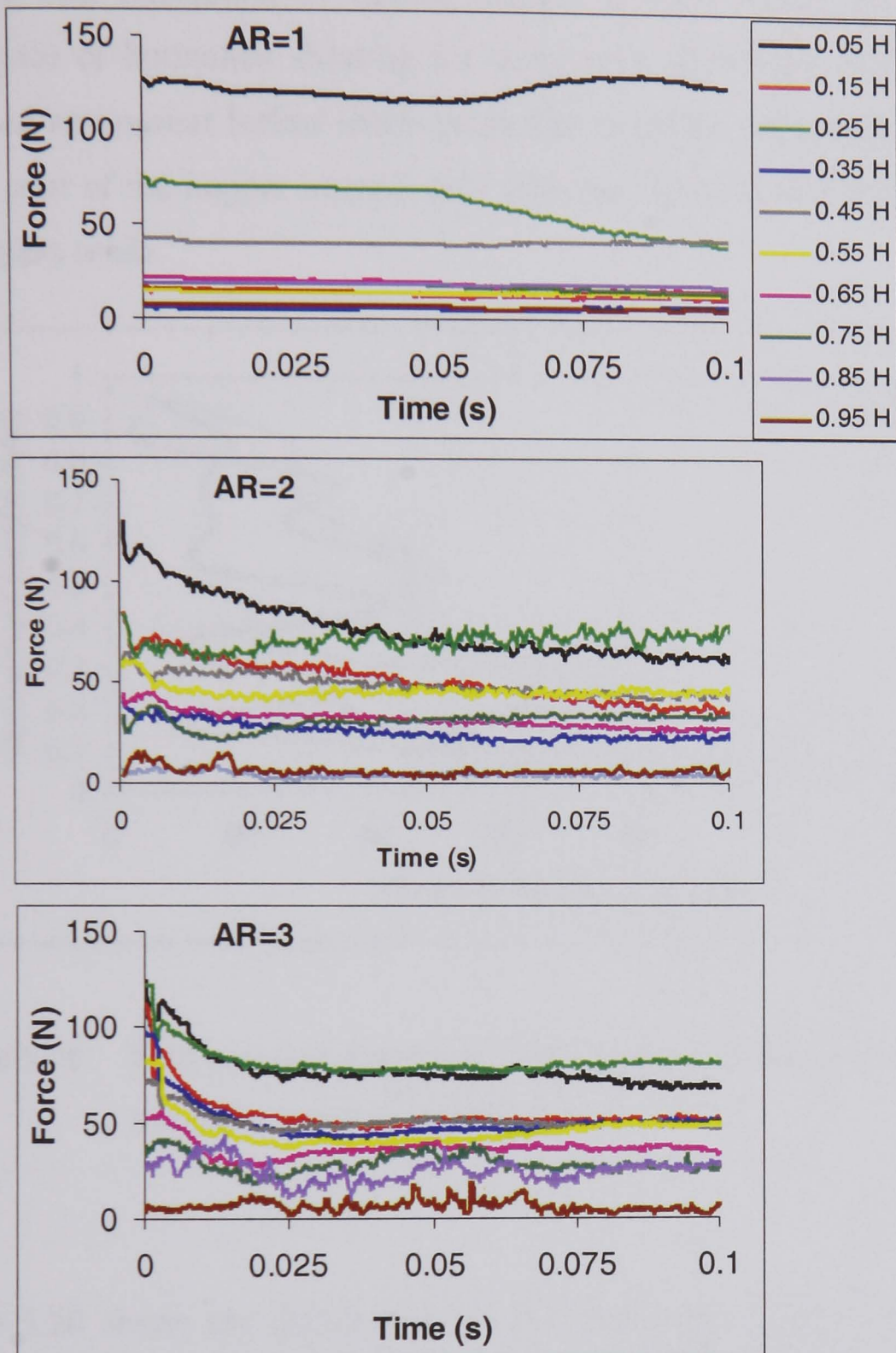


**Figure 5.19** Normal contact force between particles and a sidewall from the beginning of flow in different particle assemblies. The curves show the total normal contact force acting on different parts of the wall. The sidewall has been partitioned into ten vertical sections each equal to 0.1 of the initial height of the bed (H).

This figure shows that while in the bed of spherical particles almost a constant normal forces acted on the partitions of the sidewall, for non-spherical particles a pulse (rapid increase and fluctuation of normal forces) is seen which can be related to the emergence of horizontal shearing for these beds. Behringer and Baxter (1994) also observed an unusual forked shape pulse due to initial orientation of the seeds in the lowest part of the hopper immediately after the opening of a hopper filled with long grain grass seeds.

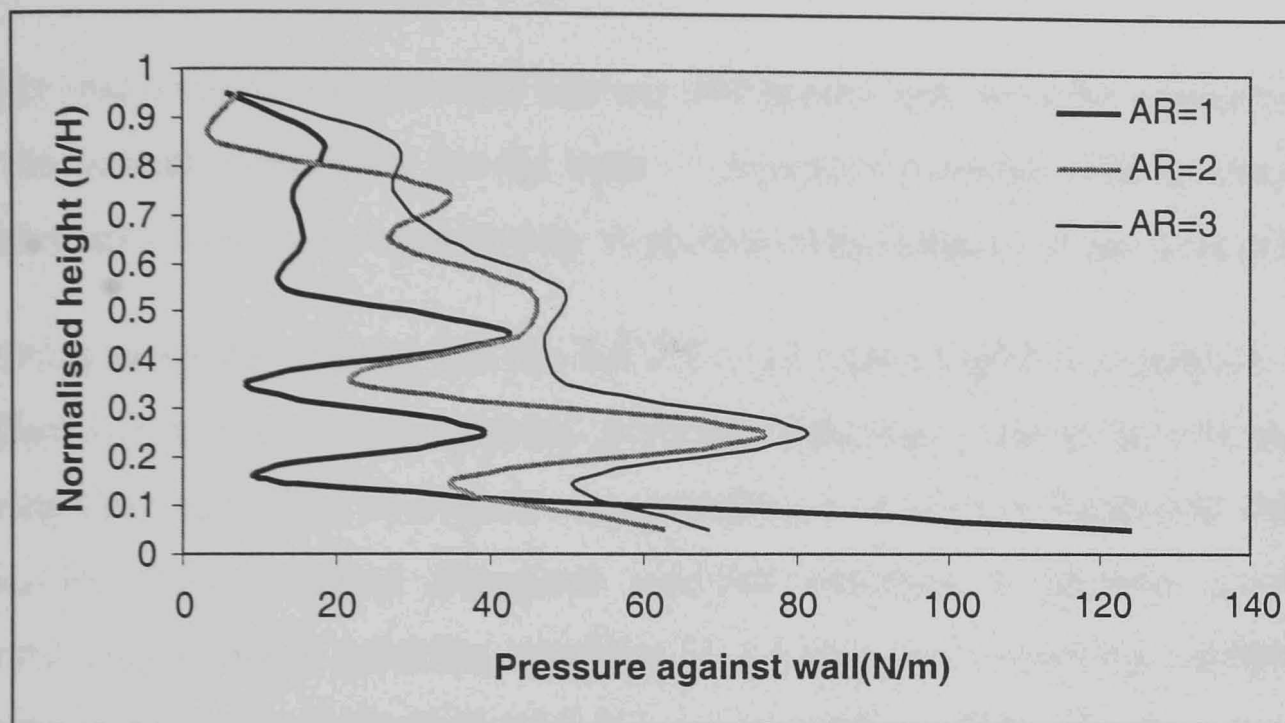


**Figure 5.20** Wall pressure distribution for beds of spherical particles (AR=1) and elongated particles (AR=2 and 3).

Figure 5.20 shows the distribution of wall pressure for beds of spherical and non-spherical particles. While the pressures show the general pattern of a Janssen distribution (Rotter *et al.*, 1998) the change in wall pressure with height is not a continuously increasing curve as presented by Janssen theory. This may be due to the small number of particles making up the wall height. The irregularity of the wall pressure might be less if the ratio of particle size to hopper size was increased (i.e. simulation with a greater number of particles). Comparing the curves, it also can be seen that as the aspect ratio of particles increased, the wall pressure increased with slightly less irregularity in the curves. Rotter *et al.* (1998) observed the same results when the DEM prediction of wall pressure distribution of spherical particles compared with elliptical particles with aspect ratio of 2.

## 5.4. Conclusion

Particle discharge from a flat bottom hopper has been performed employing a DEM model with MSM method. A semi-two dimensional hopper has been prepared by using 3-dimensional particles in a vertical layer. Particulate assemblies comprising particles of different aspect ratios ranging from 1 to 4 has been created using some non-overlapping spheres in order to investigate the effect of particle shape on bed structure and flow characteristics of particles.

There was a distribution of solid fraction within each bed, with the closest distribution to the normal distribution for the beds of elongated particles. The localised densely packed areas have been separated by voids caused by bridging of particles in the beds.

Simulation results showed that the behaviour of beds of spherical particles was quite different from that of non-spherical particles. Spherical particles moved individually during flow and rolled over each other, resulting in a lower resistance to shear with a fluid-like flow, whereas elongated particles exhibited a stronger shear due to interlocking between particles, resulting in a flow, like a breaking continuum. This unique behaviour of spherical particles caused a higher flow rate than non-spherical particles.

The formation of arching has been also simulated by the DE model. A qualitative correlation between the frequency of arching and aspect ratio has been recognised. More arching occurred as the aspect ratio of particles increased. It has been also observed that while the bed of spherical particles sheared vertically, an inclined shearing observed for the beds of non-spherical particles. The horizontal component of shear band has been found to be the cause of pulse in the early stage of the flow in the beds of elongated particles.

The simulation of the filling process and repose tests for frictional spherical and non-spherical particles showed that the shape of heap could be affected by particle shape, as well as drop height and filling stream rate. It has been found that the particle shape dominated the effect of the other two factors i.e. a steeper heap has been found for non-spherical particles than spherical particles even though the drop height was higher for

non-spherical particles. A higher drop height resulted in a flatter heap due to rearrangements caused by the energy of the impacting particles.

It has been observed that variation in bed structure and co-ordination number between beds of spherical ( $A.R=1$ ) and non-spherical particles ( $A.R=2$ ) were much greater than those between elongated particles ( $A.R \geq 2$ ). It can therefore be concluded that the results obtained from the DEM models with spherical particles cannot be generalised to real material comprising non-spherical particles.

## 6. Conclusion and Recommendation for Further Work

### 6.1. Conclusion

The ultimate objective of the research presented in this thesis was to investigate ways of implementing a new numerical model based on DEM for modelling the dynamic behaviour of particulate materials comprised of irregularly shaped particles. To achieve this aim it was necessary to seek a method of particle representation other than simple shapes such as circular and elliptical particles, while ensuring minimum extra computational effort.

A DEM simulation technique incorporating the Multi-Sphere Method with non-linear deformation dependent viscoelastic contact has been successfully used to model the dynamic behaviour of non-spherical axi-symmetrical particles. The preliminary simulations showed that the MSM model is capable of simulating different situations commonly used in agricultural handling and processing operations such as flow and impact problems. In this approach particle geometry is approximated using overlapped spheres of arbitrary diameter which are fixed in position relative to each other. The contact mechanics and contact detection method are the same as those used for spheres except that translation and rotation of element spheres are calculated with respect to the motion of the whole particle.

The MSM approach has been implemented in the existing DEM code 'CONBAL' and the necessary modifications were carried out to generate and update the dynamic situation of irregularly shaped particles rather than spherical particles. The following conclusions can be drawn from the results presented in this work using the modified DE code:

- (i) The DEM with its potential for incorporating characteristic theories and constitutive equations for a range of operations on particulate material, is a useful method for gaining step by step and detailed information on both a micro and macro

scale. However, one of the key factors in the reliability of DE results is the degree of approximation between the shape of model particles and that of real materials.

(ii) The analytical validation of the DEM model with the MSM approach indicated that although the use of an appropriate time step was critical to computational stability, it might also be necessary to alter the time step to get more accurate results. When there was a high relative velocity between contacting bodies a smaller time step was required, while in a quasi-static condition, a higher time step was found to be more appropriate. In the case of elongated particles, the instantaneous velocity of the element spheres at the ends of a particle may increase due to the rotation of the belonging particle which leads to an unstable simulation. Therefore it is necessary to take into account the aspect ratio of the model particles for the calculation of time step.

(iii) The behaviour of visco-elastic materials is better modelled by incorporating damping at contact points. However, in the case of multi-sphere particles, the number of coincident contact points can affect the damping rate between the contacting bodies. Consequently, a normalising method has to be introduced to scale the damping parameter according to the number of coincident contact point between contacting bodies.

(iv) The experimental validation of the DE model with the MSM approach in both particle and bulk scales showed that this model is a promising approach to obtain necessary data for design of some particulate system parts which are in contact with some particles of non-spherical shape. In particle scale validation a satisfactory agreement (82%) was found between the predictions of the model and the average of experiments in terms of correlation between particle co-ordinate and orientation as a function of time. A good agreement also was found between experiment and simulation in terms of bed structure, flow rate and occurrence of arching at macro-scale. However, some discrepancy between experiment and simulation was observed due to the noise introduced by physical replication of the particle assembly, and the slight variation in physical particle geometry.

(v) The results of packing and flow simulations (using the modified code based on MSM) for beds of spherical and non-spherical (elongated) particles showed a considerable deviation in the bed structure and flow characteristics of particles between

spherical and non-spherical particles in terms of solid fraction, co-ordination number, arching and shear band strength. There was a distribution of solid fraction within each bed with the greatest variation observed in the beds of particles with the largest aspect ratio. The uneven solid fraction was due to voids caused by bridging of particles. Spherical particles moved individually during flow and rolled over each other resulting in a lower resistance to shear with a fluid-like flow, whereas elongated particles exhibited a stronger shear due to interlocking between particles resulting in a flow, like a breaking mass of continuum. These results imply that the DE codes with spherical particles will overestimate the dynamic behaviour of real particulate material, even with a small deviation from spherical particles.

## 6.2. Recommendations for further studies

Based on the results and problems encountered in this study and the general requirements for more reliable results the following are suggested for further research:

- Having implemented the MSM approach in a standard DE code, this program can be used for study on different aspects of particulate agricultural operations comprising particles of non-spherical shape such as hopper filling, flow from silos, heap formation and flow from inclined chutes. The method can also be a good alternative to Instrumented Sphere (IS) for studying the relationship between impact and bruising in fruits and vegetables with irregularly shaped particles and different surface properties. These systems have the advantage that can be simulated in full scale, since they usually consist of relatively smaller number of particles.
- In this study the application of *Constructive Solid Geometry* technique (CSG) has been limited to the utilisation of spheres. The study needs to be extended to the combination of spheres with others primitives such as cylinders and cones to generate elongated particle shapes to facilitate the simulation of some agricultural produces such as sausages, crop stalk piece, sugar beet and carrot. Utilisation of cylinders and cones can decrease the total number of primitives (elements) in the model to increase the performance of the model and also remove the pseudo

friction resulting from overlapping spheres in elongated particles. This will provide more realistic results.

- The present study has been restricted to the generation of identical axi-symmetrical particles, however real agricultural materials are assemblies of particles of different shapes and sizes. As there is no theoretical limitation for the generation of any irregularly shaped particle, the method might be extended for the generation of particles with size and shape distribution to improve the accuracy of the prediction of the real bulk behaviour.
- The MSM model has been validated mostly in 2-D system. More investigations may be carried out to evaluate the validity of the model in 3-D.
- In this study the system boundaries (walls) and other system parts were created from some plain surfaces. The *Constructive Solid Geometry* technique (CSG) can also be used for the creation of system parts and the system boundaries with arbitrary geometry by combination of some primitives. Currently this method is being developed using the Muti-Wall Method (MWM). In this method a wall or a system part is created using some triangles (Kremmer, 1999).

**References:**

**Abbaspour-Fard, M. H., Raji, A. O., and Favier, J. F. (1998).** Discrete Element Method of the Modelling of Irregularly Shaped Particulate Agricultural Materials. Paper No. 98-A-057. *In* "International Conference on Agricultural Engineering", Oslo.

**Abbaspour-Fard, M. H., and Favier, J. F. (1999).** Modelling the Dynamic Behaviour of Axi-Symmetrical Fruits Using the Discrete Element Method. *In* "ASAE/CSAE-SCGR Annual International Meeting", Paper No. 996027, July, 19-21, Toronto, Canada.

**Anand, S. and Knott, K. (1991)** An Algorithm for Converting the Boundary Representation of a CAD Model to Its Octree representation. *Computers & Industrial Engineering*. **21** (1-4), 343-347.

**Bardet, J. P. and Proubet, J. (1991)** A Numerical Investigation of the Structure of Persistent Shear Bands in granular media. *Geotechnique* **41**,599-613.

**Barr, A. H. (1981).** Superquadrics and Angle-Preserving Transformations. *IEEE Computer Graphics and Animation* **1**, 11-23.

**Bathurst, R. J., and Rothenburg, L. (1988).** Micro-mechanical Aspects of Isotropic Granular Assemblies with Linear Contact Interactions. *Journal of Applied Mechanics* **55**, 17-23.

**Behringer, R. P., and Baxter, G. W. (1994).** Pattern Formation and Complexity in Granular Flow. *In* "Granular Matter; An interdisciplinary approach" (A. Mehta, ed.), pp. 85-119. Springer-Verlag, New York.

**Beverloo, W. A., Leniger, H. A., and Van de Velde, J. (1961).** The Flow of Granular Solids Through Orifices. *Engineering Science* **15**, 260-269.

**Bjedov, G., and Perry, J. B. (1996).** Parallel Discrete Element Method Simulations. *In* "11th International Conference on Computational Methods in Water Resources.", Vol. 2, pp. 55-61.

- Bolz, R. E., and Tuve, G. L. (1970).** "Handbook of Tables for Applied Engineering Science, 2nd edition," CRC Press.
- Brauer, J. R. (1993).** "Finite Element Analysis," Second Edition/Ed. Marcel Dekker, Inc.
- Brown, G. K., Pason, N. L. S., Timm, E. J., Burton, C. L., and Marshal, D. E. (1990).** Apple Packing line Impact Damage Reduction. *Applied Engineering in Agriculture* **6**, 759-764.
- Bucklin, R. A., Thompson, S. A., and Ross, I. J. (1990).** Bin - Wall Failure Caused by Eccentric Discharge of Free - Flowing Grain. *Journal of Structural Engineering* **116**, 3173-3190.
- Bucklin, R. A., THOMPSON, S. A., and ROSS, I. J. (1991).** Flow Patterns in Model Flat Bottom Grain Bins. *TRANSACTIONS OF THE ASAE* **43**, 577-585.
- Campbell, S.C.(1990).** Rapid Granular Flows. *Journal of Fluid Mechanics, Annual Review.* **22** (57-92).
- Carini, A., and Gioda, G. (1986).** A Boundary Integral Equation Technique for Visco-Elastic Stress Analysis. *International journal for numerical and analytical in Geomechnics* **10**, 586-608.
- Carrillo, A. R., West, J. E., Horner, d. A., and Peters, J. F. (1999).** Interactive Large-Scale Soil Modelling Using Distributed High Performance Computing Environments. *The International Journal of High Performance Computing Applications* **13**, 33-48.
- Chen, P., and Yazdani, R. (1991).** Prediction of Apple Bruising Due to Impact on Different Surfaces. *Trans. of the ASAE* **34**, 956-961.
- Chen, H., and J., B. (1995).** Optimisation of Impact Parameters for Reliable Excitation of Apples During Firmness Monitoring. *Journal of Agricultural Engineering Research.* **61**, 275-282.
- Cleary, P. W. (1998).** Predicting Charge Motion, Power Draw, Segregation and Wear in

Ball Mills Using Discrete Element Methods. *Minerals Engineering* 11, 1061-1080.

**Cleary, P. W. (1999).** The Effect of Particle Shape on Hopper Discharge. In "Second International Conference on CFD in the Minerals and Process Industries", pp. 71-76, CSIRO, Melbourn, Australia.

**Cundall, P. A. (1971).** A Computer Model for Simulating Progressive Large-Scale Movement in Blocky Rock System. In "International Symposium on Rock Fracture", pp. P. II-8, Nancy.

**Cundall, P. A., and Strack, O. D. L. (1979).** A Discrete Numerical Method for Granular Assemblies. *Geotechnique* 29, 47-65.

**Cundall, P. A., and Strack, O. D. L. (1983).** Modelling of Microscopic Mechanisms in Granular Material. In "Mechanics of Granular Materials: New Models and Constitutive Relations." (J. T. Jenkins and M. Satake, eds.), pp. 137-149. Elsevier Science Publishers, Amsterdam.

**Cundall, P. A. (1988a).** Computer Simulations of Dense Sphere Assemblies. In "Micromechanics of Granular Materials" (M. Satake and J. T. Jenkins, eds.), pp. 113-123. Elsevier, Amsterdam.

**Cundall, P. A. (1988b).** Formulation of a Three - Dimensional Distinct Element Model Part I. A Scheme to Detect and Represent Contacts in a System Composed of Many Polyhedral Blocks. *International Journal of Rock Mechanics and Mining Sciences & Geomechanics Abstracts*. 25, 107-116.

**Cundall, P. A., and Hart, R. P. (1992).** Numerical Modelling of Discontinua. *Engineering Computations* 9, 101-113.

**Desai, S. C., and Christian, J. T. (1977).** "Numerical Methods in Geotechnical Engineering.," McGraw Hill Books, New York.

**Diener, R. G., Adams, R. E., Ingle, M., Elliot, k. C., Nesselroad, P. E., and Blizzard, S. H. (1977).** Bruising Energy of Peaches and Apples. In "ASAE Paper for Annual

Meeting". ASAE, St,Joseph.

**Diener, R. G., Singha, S., and Petiti, J. (1983).** Effect of Apple Maturity and Firmness on Bruise Volume. *Journal of Food Process Engineering* 6, 85-99.

**Dobry, R., and Ng, T. T. (1992).** Discrete modelling of Stress -Strain Behaviour of Granular Materials at Small and Large Strain. *Engineering Computations* 9, 129-143.

**Dowding, C., Dmytryshyn, O., and Belytschko, T. B. (1999).** Parallel processing for a discrete element program. *Computers and Geotechnics* 25, 281-285.

**Drake, T. G., and Walton, O. R. (1995).** Comparison of Experimental and Simulated Grain Flows. *Journal of Applied Mechanics, Trans. of The ASME* 62, 131-135.

**Dury, C. M., Knecht, R., and Ristow, G. H. (1998).** Size Segregation of Granular Materials in a 3D Rotating Drum. *Lecture notes in computer science* 1401, 860-862.

**Favier, J. F., Abbaspour-Fard, M. H., Kremmer, M., and Raji, A. O. (1999a).** Shape Representation of Axi-Symmetrical, Non-Spherical Particles in Discrete Simulations Using Multi-Element Model Particles. *Engineering Computations* 16, 467-480.

**Favier, J. F., Abbaspour-fard, M. H., and Kremmer, M. (1999b).** Discrete Element Modelling of the flow of Axi-Symmetrical, Non-Spherical Particles Using Multi-Element Particles. In "The Seventh Annual Conference of the Association for Computational Mechanics in Engineering" (P. Bettess, ed.), pp. 147-150. Penshaw Press, Durham, UK.

**Favier, J., Kremmer, M., and Abbaspour-fard, H. (2000).** Discrete Element Modelling of the Flow of Irregular, Smooth-Surfaced Particles Through an Environment of Arbitrary Geometry. In "Fourteenth Engineering Mechanics Conference" (J. L. Tassoulas, ed.), Austin, Texas, USA.

**Foutz, T. L., and Thompson, S. A. (1993).** Comparison of Loading Response of Packed Grain and Individual Kernel. *Trans. of ASAE* 36, 569-576.

**Ghaboussi, J., and Barbosa, R. (1990).** Three-Dimensional Discrete Element Method for

Antigranulocytes Materials. *International journal for numerical and analytical methods in geomechanics* 14, 451-472.

**Ghadiri, M., and Ning, Z. (1997).** Effect of Shear Strain Rate on Attrition of Particulate Solids in a Shear Cell. In "Powder & Grains 97, 3rd International Congress on Micro-mechanics of Granular Media", Durham, North Carolina, USA.

**Ghanem, R., and Elmcstkamy, M. (1996).** Statistical Model for Sand Compaction Under Cyclic Shear Strain. *Proceedings of Engineering Mechanics*. 2, 722.

**Haff, P. K., (1983).** Grain Flow as a Fluid-mechanical Phenomenon. *Journal of Fluid Mechanics*. 134 (401-430).

**Hart, R., Cundall, P. A., and Lemos, J. (1988).** Formulation of a Three- Dimensional Distinct Element Model Part II. Mechanical Calculations For Motion And Interaction of a System Composed of Many Polyhedral Blocks. *International Journal of Rock Mechanics and Mining Science & Geomechanics Abstracts*. 25, 117-125.

**Hertz (1882).** Ueber Die Berhrunsfester Elastischer Korper. *J.Renie Angew Math*. 92, 156-171.

**Higashitani, K., and Iimura, K. (1998).** Two-dimensional Simulation of the Break-up Process of Aggregates in Shear and Elongational Flows. *Journal of colloid and interface science* 204, 320-327.

**Hocking, G. (1989).** The Discrete Element Method for Analysis of Fragmentation of Discontinua. In "1st Conference on Discrete Element Method", Golden, Colorado, USA.

**Hogue, C. (1998).** Shape Representation and Contact Detection for Discrete Element simulations of Arbitrary Geometries. *Engineering Computations* 15, 374-390.

**Holt, J. E., Schoorl, D., and Lucas, C. (1981).** Predicting of Bruising in Impacted Multi-layered Apple Packs. *Trans. of the ASAE* 24, 242-247.

**Horner, D. A., Carrillo, A. R., Peters, J. F., and West , J. E. (1998).** High Resolution

Soil Vehicle Interaction Modelling. *MECH. STRUCT. & MACH.* **26**, 305-318.

**Huang, H., Detournay, E., and Bellier, B. (1999).** Discrete Element Modelling of Rock Cutting. In "Proceedings of the 37th US Rock Mechanics Symposium - Rock Mechanics for Industry" (B. Amadei and R. L. Kranz, eds.), pp. 123-129, Vail, Colorado (US).

**Hui, K. and Haff, P. K. (1984).** Condition for High Shear Grain Flow. *Journal of Fluid Mechanics.* **145** (223-233).

**Hutter, K., and Schiwiller, T. (1983).** Rapid Plane Flow of Granular Materials Down a Chute. In "Mechanics of Granular Materials: New Models and Constitutive Relations." (J. T. Jenkins and M. Satake, eds.), pp. 283-293. Elsevier Science Publishers, Amsterdam.

**Hwang, K. J., Wu, Y. S., and Lu, W. M. (1996).** Surface Structure of Cake Formed by Uniform- Sized Rigid Spheroids in Cake Filtration. *Powder Technology.* **87**, 161-168.

**Hyde, G. M., Brown, G. K., Timm, E. J., and Zhang, W. (1992).** Instrumented Sphere Evaluation of Potato Packing Line Impacts. *Trans. of ASAE* **35**, 65-69.

**Ikegawa, Y., and Hudson, J. A. (1989).** A Novel Automatic Identification System for Three Dimensional Multi- Block Systems. In "1st Conference on Discrete Element Method", Golden Colorado, USA.

**Jensen, R. P., Bosscher, P., Plesha, M. E., and Edil, T. B. (1999).** DEM Simulation of Granular Media-Structure Interface: Effect of Surface Roughness and Particle Shape. *International journal for numerical and analytical methods in geomechanics* **23**, 531-547.

**Ji, Q. and Marefat M.M. (1997)** Machine Interpretation of CAD Data for Manufacturing Applications. *ACM Computing Surveys.* **29** (3), 264-311.

**Jofriet, J. C., Negi, S. C., and Lu, Z. (1997).** A Numerical Model for Flow of Granular Materials in Silos. Part 3: Parametric Study. *J. Agric. Engng. Res.* **68**, 237-246.

**Johnson, K. L. (1987).** "Contact Mechanics," Second Edition/Ed. Cambridge University Press, Cambridge.

- Kafui, K. D., and Thornton, C. (1997).** Some Observations on Granular Flow in Hopper and Silos. In "3rd International Congress on Micro-mechanics of Granular Media", Durham, North Carolina, USA May.18-22.
- Kafui, K. D., and Thornton, C. (2000).** Numerical Simulations of Impact Breakage of a Spherical Crystalline Agglomerate. *Powder Technology* **109**, 113-132.
- Kano, J., Saito, F., Shimosaka, A., and Hidaka, J. (1998).** Simulation of Mass Flow Rate of Particles Discharged from Hopper by Particle Element Method. *Journal of Chemical Engineering of Japan* **31**, 936-940.
- Kremmer, M. (1999).** "The Reverse Engineering Discrete Element Method for Modelling the Interaction Between Biomaterial and Machinery.", Newcastle University, Newcastle upon Tyne.
- Kremmer, M and J.F. Favier (2000)** Calculating Rotational Motion in Discrete Element Modelling of Arbitrary Shaped Model Objects. *Engineering Computations*. In press.
- Krishnasamy, J., and Jakiela, M. S. (1995).** A Method to Resolve Ambiguities in Corner-Corner Interactions Between Polygons in the Context of Motion Simulation. *Engineering Computations* **12**, 135-145.
- Kuhn, M. R. (1995).** Flexible Boundary for Three - Dimensional DEM Particle Assemblies. *Engineering Computations* **12**, 175-183.
- Kuhn, M. R. (1999).** Structured Deformation in Granular Materials. *Mechanics of Materials* **31**, 407-429.
- Langston, P. A., Tuzun, U., and Heyes, D. M. (1995).** Discrete Element Simulation of Granular Flow in 2D and 3D Hoppers: Dependence of Discharge Rate and Wall Stress on Particle Interactions. *Chemical Engineering Science* **50**, 967-987.
- Langston, P. A., Nikitidis, M. S., Tuzun, U., and Spyrou, N. M. (1997).** Micro-structural Simulation and Imaging of Granular Flows in Two-and Three-dimensional Hoppers. *Powder Technology* **94**, 59-72.

- Li, R.X. (1993)** Generation of Geometric Representations of 3D Objects in CAD-CAM by digital Photogrammetry. *Journal of Photogrammetry and Remote Sensing*. **45 (5)** 2-11.
- Li, C.I., Yu, K.M., and Lan, T.W. (1998)** Implementation and Evaluation of Thin-Shell Rapid Prototype. *Computers in Industry*. **35 (2)**, 185-193.
- Lin, X., and Ng, T. T. (1995)**. Short Communication; Contact Detection Algorithms for Three- Dimensional Ellipsoids In Discrete Element Modelling. *International Journal for Numerical Methods in Geomechanics*. **19**, 653-659.
- Liu, L. F., Zhang, Z. P., and Yu, A. B. (1999)**. Dynamic Simulation of the Centripetal Packing of Mono-sized Spheres. *Physica* **268**, 433-453.
- LoCurto, G. J., Zhang, X., Zakirov, V., Bucklin, R. A., Vu-Quoc, L., Hanes, D. M., and Walton, O. R. (1997)**. Soybean Impacts: Experiments and Dynamic Simulations. *Transactions of the ASAE* **40**, 789-794.
- Lu, Z., Negi, S. C., and Jofriet, J. C. (1997)**. A Numerical Model for Flow of granular Materials in Silos. Part 1: Model Development. *J. Agric. Engng Res.* **68**, 223-229.
- Macrae, J.C. and Gray, W.A. (1961)** Significance of the Properties of Materials in the Packing of Real Spherical Particles. *Br. J. Appl. Phys.* **12**, 164-172.
- Manbeck, H. G., and Nelson, G. L. (1972)**. Method and Instrumentation for Evaluating the Stress - Strain Behaviour of Wheat en-mess. *Trans. of ASAE* **24**, 1338-1341.
- Marshal, D. E., and Burgess, G. J. (1991)**. Apple Bruise Damage Estimation Using an Instrumented Sphere. *Applied Engineering in Agriculture* **7**, 677-682.
- Mazzetti, M. and Ciminiera, L. (1994)** Computing CSG-Tree Boundaries as Algebraic expressions. *Computer Aided Design*. **26 (6)**, 417-425.
- McRae, D. C. (1985)**. A Review of Development in Potato Handling and Grading. *J. Agric. Engng. Res.* **31**, 115-138.
- Meegoda, N. J., and Chang, K. (1993)**. Novel Approach to Develop a Performance

- Based Test for Rutting of Asphalt Concrete. *In* "Airport Pavement Innovations Theory to Practice", pp. 126-140. ASCE, New York, USA.
- Mehta, A. (1994).** "Granular Matter , An Inter-disciplinary Approach.," Springer-Verlag, New York.
- Meriam, J. (1975a).** "Engineering Mechanics "STATICS".," John eiley & Sons, Inc.
- Meriam, J. (1975b).** "Engineering Mechanics "DYNAMICS".," John Wiley & Sons, Inc.
- Mindlin, R. D. (1949).** Compliance of Elastic Bodies in Contact. *Journal of Applied Mechanics* **16**, 259-266.
- Mindlin, R. D., and Deresiewicz, H. (1953).** Elastic Spheres in Contact Under Varying Oblique Forces. *Journal of Applied Mechanics*, 327-344.
- Mishra, B. K., and Rajamani, R. K. (1993).** Simulation of Charge Motion in Ball Mills : Experimental Verifications. *International Journal of Mineral Processing* **40**, 170-186.
- Mohsenin, N. (1970).** "Physical Properties of Plant and Animal Materials.," Gordon and Breach Science publisher.
- Mohsenin, N. (1984).** "Physical Properties of Food and Agricultural Materials.," Gordon and Breach Science Publisher.
- Morrow, C. T., and Mohsenin, N. N. (1968).** Consideration of Selected Agricultural Products as Visco-elastic Materials. *Journal of Food Science* **33**, 686-698.
- Moysay, E. B., and Lambert, E. W. (1987).** Flow Rates of Grains and Oilseeds through Orifices. *In* "Particulate and Multiphase Processes", Vol. 1, pp. 733-742. Hemisphere Publi. Corp., Miami, USA.
- Munjiza, A., Owen, D. R., and Bicani, N. (1995).** A Combined Finite-Discrete Element in Transient Dynamics of Fracturing Solids. *Engineering Computations* **12**, 145-174.
- Nedderman, R. M., and Tuzun, U. (1979).** A Kinematic Model for the Flow of Granular

Materials. *Powder Technology* **22**, 243-253.

**Nedderman, R. M. (1985).** The Flow of Granular Materials Through Orifices. *I.CHEM.E. Symposium Series No. 91, POWTECH 85 Particle Technology*, 281-294.

**Negi, S. C., Lu, Z., and Jofriet, J. C. (1997).** A Numerical Model for Flow of Granular Materials in Silos. Part 2: Model Validation. *J. Agric. Engng. Res.* **68**, 231-236.

**Ng, T. T. (1989).** Numerical Simulation of Granular Soils Under Monotonic and Cyclic Loading : A particulate Mechanics Approaches., Rensselaer Polytechnic Institute.

**Ng, T. T., and Dobry, R. (1990).** CONBAL Simulated Granular Material Using Quartz Spheres With the DEM. .

**Ng, T. T. (1993).** Numerical Simulations for Penetration Process of Concrete Target Using the Discrete Element Method. *AMSE, Applied Mechanics* **171**, 17-24.

**Ng, T. T. (1994).** Numerical Simulations of Granular Soil Using Elliptical Particles. *Computers and Geotechnics* **16**, 153-169.

**Ng, T. T., and Dobry, R. (1994).** Numerical Simulation of Monotonic and Cyclic Loading of Granular Soils. *Journal of Geotechnical Engineering* **120**, 388-403.

**Ng, T. T., and Fang, H. E. (1995).** Cyclic Behaviour of Arrays of Ellipsoids With Different Particles Shape. *ASME, Applied Mechanics* **201**, 59-71.

**Ng, T. T. (1996).** Small- Strain Response of Random Array of Spheres Using Discrete Element Method. *Journal of Engineering Mechanics*, 239-244.

**Ning, Z., and Ghadiri, M. (1995).** Incorporation of Rayleigh Damping into TRUBAL and Determination of the Critical Time Step. . University of Surrey, Original Paper.

**Ning, Z. (1995).** Elasto-Plastic Impact of Fine Particles and Fragmentation of Small Agglomerates, PhD thesis, Aston University.

**Ning, Z., Boerefijn, R., Ghadiri, M., and Thornton, C. (1997a).** Effect of Particle Size

and Bond Strength on Impact of Weak Agglomerates. In "Powder & Grains 97, 3rd International Congress on Micro-mechanics of Granular Media", Durham, North Carolina, USA.

**Ning, Z., Boerefijn, R., Ghadiri, M., and Thornton, C. (1997b).** Distinct Element Simulation of Impact Breakage of Lactose Agglomerates. *Advanced Powder Technology* 8, 15-37.

**Ooi, J. Y., Chen, J. F., Lohnes, R. A., and Rotter, J. M. (1996).** Prediction of static wall pressures in coal silos. *Construction and Building Materials* 10, 109-116.

**Ooi, J. Y., and She, K. M. (1997).** Finite Element Analysis of Wall Pressure in Imperfect Silos. *International Journal of Solid and Structures* 34, 2061-2072.

**Ooi, J. Y., Chen, J. F., and Rotter, J. (1998).** Measurement of solids flow patterns in a gypsum silo. *Powder Technololy* 99, 272-284.

**Ooms, M., and Roberts, A. W. (1985).** Reduction and Control of Flow Pressures in Cracked Grain Silo. *Bulk Solids Handling* 5, 1009-1016.

**Ouadfel, H., and Rothenburg, L. (1999).** An Algorithm for Detecting Inter-Ellipsoid Contacts. *Computers and Geotechnics* 24, 245-263.

**Pang, D. W., Studman, C. J., and Banks, N. H. (1994).** Apple Bruising Thresholds for an Instrumented Sphere. *Trans. of the ASAE* 37, 893-897.

**Paulsen, M. R. (1978).** Fracture Resistance of Soybean to Compressive Loading. *Trans. of ASAE* 21, 1210-1216.

**Peleg, K. (1984).** A Mathematical Model of Produce Damage Mechanism. *Trans. of ASAE* 27, 287-293.

**Peleg, K. (1986).** Simulation of Vibration Damage in Produce Transportation. *Trans. of ASAE* 29, 633-641.

**Pitt, R. E., and Chen, H. L. (1982).** Time Dependence Aspect of the Strength and

Rheology of Vegetative Tissues. *Trans. of ASAE* **26**, 1275-1280.

**Potapov, A. V., and Campbell, C. S. (1998).** A Fast Model for the Simulation of Non-Round particles. *Granular matter* **1**, 9-14.

**Raji, A. O. (1999).** Discrete Element Modelling of the Deformation of Bulk Agricultural Particulates. PhD thesis, Newcastle University, Newcastle upon Tyne.

**Ritchie, P. D. (1965).** "Physics of Plastics," Van Nostrand, Princeton, London.

**Rogers, L. N., and Reeds, J. (1984).** The Adhesion of Particles Undergoing an Elastic-Plastic Impact with a Surface. *Journal of Physics D-Applied Physics* **17**, 677-689.

**Rong, G., Negi, S. C., and Jofriet, J. C. (1993).** DEM Simulation of In-transit Fruit Damage. *ASAE paper NO.93-4018*.

**Rong, G., Negi, S. C., and Jofriet, J. C. (1995a).** Simulation of the Flow Behaviour of Bulk Solids in Bins, Part 1 :Model Development and Validation. *Journal of Agricultural Engineering Research*. **62**, 244-256.

**Rong, G., Negi, S. C., and Jofriet, J. C. (1995b).** Simulation of the Flow Behaviour of Bulk Solids In Bins, Part 2 : Shear Bands, Flow, Corrective Inserts and Velocity Profile. *Journal of Agricultural Engineering Research*. **62**, 257-269.

**Rothenburg, L., and Bathurst, R. J. (1992).** Micro-mechanical Features of Granular Assemblies with Planar Elliptical Particles. *Geotechnique* **42**, 79-95.

**Rotter, J. M., Holst, J. Y., Ooi, J. Y., and Sanad, A. M. (1998).** Silo Pressure Predictions Using Discrete-Element and Finite-Element Analysis. *Philosophical Transactions of the Royal Society of London*. **356**, 2685-2712.

**Sakaguchi, E., Kawakami, S., and Tobita, F. (1994).** Simulation of Flowing Phenomena of Grains by DEM. *International Conference on Agricultural Engineering. Paper No.94-G-Milano*.

**Sanna, A. and Montuschi, P. (1995)** Spatial Bounding of Complex CSG Objects. *IEE*

*Proceedings – Computers and Digital Techniques*. 142 (6), 431-439.

**Sanna, A., Montuschi, P., Fisone, A., and Montrucchio, B. (1997).** A new algorithm for the rendering of CSG scenes. *Computer Journal* 40, 555-564.

**Schembri, M. G., and Harris, H. D. (1996).** Modelling Impact on a Biological Material (Sugar Cane) Using DEM. *International Conference on Agricultural Engineering, Madrid. Paper NO.96F-072.*

**Schmidt, L. C., and Wu, Y. H. (1989).** Prediction of Dynamic Wall Pressure on Silos. *Bulk solids handling* 9, 333-338.

**Selvadurai, A. P. S., and Sepehr, K. (1999).** Two-dimensional discrete element simulations of ice-structure interaction. *International Journal of Solids and Structures* 36, 4919-4940.

**Shukla, A., Sadd, M. H., Singh, R., Tai, Q., and Vishwanathan, S. (1993).** Role of Particle Shape and Contact Profile on the Dynamic Response of Particulate Materials. *Optics and Laser in Engineering* 19, 99-119.

**Sitkei, G. (1986).** "Mechanics of Agricultural Materials.," Elsevier, Amsterdam.

**Spiegel, M. R. (1959).** "Schaum's Outline of Theory and Problem of "VECTOR ANALYSIS" and Introduction to "TENSOR ANALYSIS".," Schaum publishing Company.

**Stuart, J., and Savage, S. B. (1983).** Granular Flows Down Rough Inclines- Review and Extension. *In* "Mechanics of Granular Materials: New Models and Constitutive Relations." (J. J.T. and M. Satake, eds.), pp. 261-280. Elsevier Science Publishers, Amsterdam.

**Taylor, L. M., and Preece, D. S. (1992).** Simulation of Blasting Induced Rock Motion Using Spherical Element Method. *Engineering Computations*. 9, 243-252.

**Thompson, S. A., Usry, J. L., and Legg, J. A. (1985).** Wall Loads as a Function of

Discharge Rate in a Corrugated Model Grain Bin. *European federation of chemical engineering.*, 7-15.

**Thornton, C. (1989).** Application of DEM to Process Engineering Problem. In "1st Conference on DEM", Golden, Colorado ,USA.

**Thornton, C., and Kafui, K. D. (1997).** Numerical Simulations of Granular Flow in Hoppers and Silos. In "The 2nd Israel Conference For Conveying and Handling of Particulate Solids.", Jerusalem, Israel May. 26-28.

**Thornton, C., Ciomocos, M. T., and Adams, M. J. (1999).** Numerical simulations of agglomerate impact breakage. *Powder Technology* **105**, 74-82.

**Thornton, C., Antony, S.J. (2000).** Quasi-static Shear Deformation of a soft particle system. *Powder Technology* **109**, 179-191.

**Ting, J. M., Khwaja, M., Meachum, L. R., and Rowel, J. D. (1993).** An Ellipse Based Discrete Element Model for Granular materials. *Int. Journal for Numerical and Analytical Methods in Geomechanics.* **17**, 603-623.

**Ting, J., Meachum, L. R., and Rowell, J. D. (1995).** Effect of Particle Shape on the Strength and Deformation Mechanism of Ellipse Shape Granular Assemblies. *Engineering Computations* **12**, 99-108.

**Ting, J. M., and Meachum, L. R. (1995).** Effect of Bedding Plane Orientation on the Behaviour of Granular Systems. *ASME, Applied Mechanics* **201**, 43-57.

**Trent, B. C., and Margolin, L. G. (1995).** Numerical Validation of a Constitutive Theory for an Arbitrary Fractured Solid. *Engineering Computations.* **12**, 125-134.

**Tsuji, Y., Tanaka, T., and Ishida, T. (1992).** Lagrangian Numerical Simulation of Plug Flow of Cohesionless Particles in a Horizontal Pipe. *Powder Technology* **71**, 239-250.

**Tsuji, Y., Kawaguchi, T., and Tanaka, T. (1993).** Discrete Particle Simulation of Two - Dimensional Fluidized Bed. *Powder Technology* **77**, 79-87.

- Tuzun, U., and Nedderman, R. M. (1979).** Experimental Evidence Supporting Kinematic Modelling of the Flow of Granular Media in the Absence of Drag. *Power Technology* **24**, 257-266.
- Vemuri, B. C., Chen, L., Vu-Quoc, L., Zhang, X., and Walton, O. R. (1998).** Efficient Collision Detection Algorithms and Accurate Contact Mechanics For Granular Flow Simulation. *Graphical Models and Image Processing*. **60**, 403-422.
- Vibrascrew, I. T. N. (1977).** Improving Material Flow from Bin. *Chemical Engineering Progress* **33**, 82-86.
- Vermeer, P. A. (1990)** The Orientation of Shear Bands in Biaxial Tests. *Geotechnique* **40**, 223-236.
- Vu-Quoc, L, Zhang, X., and Walton, O.R. (2000)** A 3-D Discrete-Element Method for dry granular flows of ellipsoidal particles. *Comput. Methods Appl. Mech. Engrg.* **187**, 483-528.
- Walton, O. R. (1983).** Particle - Dynamics Calculations of Shear Flow. In "Mechanics of Granular Materials: New Models and Constitutive Relations." (J. T. Jenkins and M. Satake, eds.), pp. 327-338. Elsevier Science Publishers, Amsterdam.
- Walton, O. R., and Braun, R. L. (1986).** Viscosity, Granular Temperature, and Stress Calculations for Shearing Assemblies of Inelastic, Fractional Disks. *Journal of Rheology* **30**, 949-980.
- Walton, O. R. (1993).** Numerical Simulation of Inclined Chute Flows of Mono-disperse, Inelastic Frictional Spheres. *Mechanics of Materials* **16**, 239-247.
- Walton, O. R., and Braun, R. L. (1993).** Simulation of rotary-drum and repose tests for frictional spheres and rigid sphere clusters., Lawrence Livermore National Laboratory, Livermore.
- Wanatabeh, R., Hashimoto, H., and Lee, G. G. (1995).** Computer Simulation of Milling Ball Motion in Mechanical Alloying. *Material Transaction, JIm*, **36**, 102-109.

- Wang, C. Y., Wang, C. F., and Sheng, J. P. (1999).** A Packing Generation Scheme for the Granular Assemblies with 3D Ellipsoidal Particles. *International Journal For Numerical and Analytical Methods in Geomechanics* **23**, 815-828.
- Washington, D. W., and Meegoda, J. N. (1996).** Micro-mechanical Simulation of Geotechnical Problems Using Massively Parallel Supercomputers. In "11th Conference on Engineering Mechanics", Vol. 2, pp. 717-721. ASCE, Newark, USA.
- Watanabe, H. (1999).** Critical Rotation Speed for Ball-Milling. *Powder Technology* **104**, 95-99.
- Wilcke, W., Chang, C. S., and Hetzel, G. H. (1992).** Grain Flow through Guarded Horizontal Orifices. *Applied Engineering in Agriculture* **8**, 65-75.
- Williams, J. R., and Pentland, A. P. (1989).** Super-quadratics and Modal Dynamics for Discrete Elements in Concurrent Design. In "1st US Conference on DEM", Golden, Colorado, USA.
- Williams, J. R., and O'Connor, R. (1995).** A linear Complexity Intersection Algorithm for DEM Simulation of Arbitrary Geometries. *Engineering Computations*. **12**, 185-201.
- Xu, B.H. and Yu, A.B. (1997)** Numerical simulation of the gas-solid flow in a fluidized bed by combining discrete particle method with computational fluid dynamics. *CHEM ENG SCI*, **52 (16)**, 2785-2809.
- Xu, S., Shang, O., and Britton, M. G. (1996).** An Endochronic Constitutive Model for Grain en-mess. *Journal of Agricultural Engineering Research*. **63**, 121-128.
- Yokohama, T., Tamura, K., Usui, H., and Jimbo, G. (1996).** Simulation of Ball Behaviour in a Vibration Mill in Relation with Its Grinding Rate: Effects of Fractional Ball Filling and Liquid Viscosity. *International journal of mineral processing* **44-45**, 413-424.
- Yong, Y., and Henderson, J. (1979).** Rotary Singulator. *Trans. of ASAE* **22**, 1229-1231.

- Zacharia, T., and Simunovic, S. (1995).** Massively Parallel Simulation of Welding Process. In "7th Conference on Modelling of Casting, Welding, and Advanced Solidification Processes.", Mineral, Metals & Materials Soc., London.
- Zapp, H. R., Ehlert, S. H., Brown, G. K., Armstrong, P. R., and Sober, S. S. (1990).** Advanced Instrumented Sphere (IS) for Impact Measurements. *Trans. of ASAE* **33**, 955-960.
- Zhang, D., and Whiten, W. J. (1996).** The Calculation of Contact Forces Between Particles Using Spring and Damping Models. *Power Technology* **88**, 59-64.
- Zhang, X., Vu-Quoc, L., Walton, O., Cao, Y., and Vemiuri, B. (1995).** Modelling and Simulation of Dry Soybean Flow. In "SES'95 Society of Engineering Science 32nd Annual Technical Meeting." (S. o. E. Science, ed.), pp. 641-642, New Orleans.
- Zhang, K. F., and Ooi, J. Y. (1998).** A Kinematic Model for Solids Flow in Flat-Bottomed Silos. *Geotechnique* **48**, 545-553.
- Zhang, X., and Vu-Quoc, L. (2000).** Simulation of Chute Flow of Soybeans Using an Improved Tangential Force-Displacement Model. *Mechanics of Materials* **32**, 115-129.
- Zhu, Y., Shukla, A., and Sadd, M. H. (1996).** The Effect of Micro-structural fabric on Dynamic Load Transfer In Two Dimensional Assemblies of Elliptical particles. *Journal of the Mechanics and Physics of solids* **44**, 1283-1303.

## Appendix A

### The explicit and implicit schemes in Finite Difference Approximation Method

The general formula for the FDA is known as Newmark's generalised acceleration method

where for an explicit scheme  $\beta = 1$  and for an implicit scheme  $\beta = 0$  (Raji, 1999).

In the explicit scheme, the approximation solution for  $u$  at time  $t + \Delta t$  is sought in terms of the known values of  $u$  at the previous time level  $t$ . Explicit schemes can be formulated in which some values of  $u$  at time  $t + \Delta t$  are also known. The explicit procedures are fairly straightforward, allow step-by-step estimation of  $u$  directly and do not require solution of simultaneous equations.

In contrast the implicit schemes, require solution of a set of simultaneous equations at time level  $t + \Delta t$ . In these procedures the  $u$  at  $t + \Delta t$  occur as unknowns and the right hand side of the algebraic equations constitute the known values of  $u$  at time level  $t$  (Desai and Christian, 1977).

## Appendix B

### The functions performed by various subroutines in the MSM model

#### **BBTEST**

Test for contacts between sphere-sphere and sphere-wall. The contact between spheres of the same particle and wall-wall contacts are recognised and ignored.

#### **CYCLE**

To cycle through main calculation loop. In each cycle the acceleration, velocity, position of particles updated according to the resultant contact forces and moments.

#### **FORD**

To apply the force-displacement law to each contact point to calculate the contact forces. For each contact point according to the position and velocity of contacting bodies (sphere or walls) the deformation and contact force is calculated.

#### **GETFN**

To create files and interprets the file name parameters in the input file a file name.

#### **HALT**

To terminate the program when there is an error with a proportional error message or at the end of the operation.

#### **INITP**

To calculate initial parameters such as particle mass and time step prior to the calculation cycle.

#### **MATCH**

Matches input string to keyword in table of data in the code which are index to parts of the program where parameters following keyword are required.

**NEXT**

To interpret the command lines for each operation from the input file and locates the position for reading or calculating the necessary parameters from the input line for successive operations.

**PRODUCE**

To generate non-spherical, multi-sphere particles with a random orientation in a workspace of real boundaries (walls).

**REBOX**

To locate the position of spheres and walls and mapping them to the sub-boxes they occupy.

**SAVE**

To save or recall the state of a simulation, data and results at a desirable step during simulation.

**SEARCH**

To search for neighbouring spheres and walls that are potential contact partners and allocate identification address to each contact.

**SET UP**

To start or restart a new simulation. Initialise arrays and variables, specify constants, material properties and parameters required for particle and environment generation are read. The information can be saved and then recalled for a restarting simulation.

**TIDY**

To remove blanks in the input lines and makes the index to location of parameters by recognising the separator between parameters and the terminator at the end of input line.

**UPDATE**

Update the position of spheres during re-boxing.

## Appendix C

### Include files and input files for MSM code

#### (a) MATCOM

```
! MATCOM the Common INCLUDE file for the MSM code
! common block for match package
    LOGICAL::MISS,BAD
    CHARACTER(LEN=1),PARAMETER::ITERM='$'
    CHARACTER(LEN=1)::LINE
    CHARACTER(LEN=15)::FILE
    COMMON/MATCOM/LPNT(40),MISS,BAD,NPBAD,NCHAR
    COMMON/MATCM1/LINE(80)
    COMMON/MATCH2/FILE
```

**(b) A typical BALCOM**

```

!BALCOM, This is the INCLUDE file for MSM code

! In this file the dimension of the arraies are set
!According to the total number of particles and No. spheres per
particles
!IMPLICIT REAL(A-H,O-Z)
INTEGER::BPOINT,BNUM
LOGICAL::RFLAG,DFLAG,LOGFLG,ERROR,GMVFLG,HISFLG,GRVFLG,dflow
!-----If you change the maximum particle number(NBALLM)---
!---You have to change NDIM1=NBALLM AND NDIM=NBALLM*3---
INTEGER,PARAMETER::NDIM1=25
INTEGER,PARAMETER::NDIM=75
!You hav to change NEDIM=NELEMAX*3 accordingly-----
!Also change NTYP=no. of spheres in particl--
INTEGER,PARAMETER::NEDIM=3
INTEGER,PARAMETER::NTYP=15
CHARACTER(4)::HED
COMMON/TABCOM/&
&NERR,ERROR,LUNR,LUNW,LUNH,&
&M1,M1A,M2,M2A,M3,M3A,M4,M5,NVARB,NVARC,NVARW,NTYPM,NTYPS,&
&NKM,NKS,IROUTE,NBOX,MODE,NGROUP,GMVFLG,GRVFLG,HISFLG,BNUM,&
&NBALL,NWALL,NEML,NEMC,NTOT,NPAGE,NLINE,BPOINT,DFLOW,&
&NCONT,RFLAG,DFLAG,LOGFLG,NX(3),ITYPE(NDIM1),NTIME,NOUT,NTOUT,&
&AANORFOR,ANORFOR,ATANFOR,AATANFOR,NCONTW
!--crrr-----
COMMON/BALREL/&
&R(NTYP),AMASS(NTYP),AMOI(NTYP),FIX(NTYP),DENS,GS,POI,&
&AMU,AMUW,TOL,OVLAP,PI,DEGRAD,DEL(3),GRAV(3),VIBRA(3),BOTOM(5),&
&XMAX(3),WINDL(3),WINDU(3),TDEL,FRAC,ALPHA,DAMPCO,SEED,&
&VOLB,EDGRID(3,3),EGRID(3,3),EDUSER(3,3),SLIDE,ATHIRD,&
&SSAMPL(3,3),EDSERV(3,3),GAIN,SERVS0,SERVEM,ACONS1,CONS1&
&,TDISP(NDIM),ADISP(NDIM),VEL(NDIM),FORCES(NDIM),&
&ROT(NDIM),AMOMEN(NDIM),CENTRD(NDIM),RVEL(NDIM),PTDISP(NDIM)
EQUIVALENCE(A(1),DISP(1))
REAL::DISP(NDIM)
COMMON/ELEM/B(NEDIM),TDISPE(NEDIM),DICOS(NDIM),TETAXS(NDIM),&
&NELEM,HDMAX,NADELM(NDIM1),NWALLM,IWALL,AMIO,TMASS,ELVEL(NEDIM),&
&ELFORCES(NEDIM),AMOM(NEDIM),ADISPE(NEDIM),ELROT(NEDIM),&
&ADTETA(NDIM),NELEMAX,MELEM,NTEL,INDEX1,INDEX2,INDEX3
!---crrr
COMMON/BALHIS/A(200000)
COMMON/TRB1/HED(20)

```

## Appendix D

(a) Input file for handling simulation of a single conical particle comprised of 15 element spheres on a horizontal surface (Figure 2.17).

```
START 60.0 7.50 60.0 1728 25 1 15 10
HANDLING A CONICAL PARTICLE ON A HORIZONTAL SURFACE
BOT 30.0 29.0 0.25 7.0 30.0
RAD 1.500 1
RAD 1.431 2
RAD 1.362 3
RAD 1.328 4
RAD 1.259 5
RAD 1.155 6
RAD 1.121 7
RAD 1.051 8
RAD 0.983 9
RAD 0.879 10
RAD 0.810 11
RAD 0.741 12
RAD 0.638 13
RAD 0.569 14
RAD 0.500 15
PRO 2.62 2.0 1.38 1.07 .45 .48 .52 1.41 2.04 2.97 3.59 4.24 5.14 5.37 6.38
DENS 1.8
FRIC 0.5 0.5
FRAC 1.0
DAMP 0.0 0.50
GRA 0.0 0.0 -9.81
MOV 25.0 -25.0
CYC 8000 50 10
STOP
```

**(b) Input file for handling simulation of a single 3-D irregular shaped, axisymmetrical particle comprised of 15 element spheres on a horizontal surface (Figure 2.18).**

```
START 60.0 40.0 48.0 1800 25 1 15 10
HANDLING AN IRREGULAR SHAPED PARTICLE ON A HORIZONTAL SURFACE
BOT 30.0 29.0 0.25 39.50 40.0
RAD 2.100 1
RAD 2.300 2
RAD 2.390 3
RAD 2.530 4
RAD 2.560 5
RAD 2.610 6
RAD 2.670 7
RAD 2.980 8
RAD 3.500 9
RAD 4.280 10
RAD 4.850 11
RAD 5.150 12
RAD 5.400 13
RAD 5.390 14
RAD 5.340 15
PRO 13.5 13. 12.25 11. 10. 8.5 7. 5.5 3.75 1.75 0.0 1. 2.25 2.75 3.25
DENS 1.8
FRIC .5 .5
FRAC 1.0
DAMP 0.0 0.50
GRA 0.0 0.0 -9.81
CYC 100000 1 10
MOV 25. -25.
CYC 1000 50 10
STOP
```

(c) Input file for handling simulation of a bunch of conical particles (20 particles) each comprised of 15 element spheres on a horizontal surface (Figure 2.20).

```
START 60.0 16.0 152.0 2280 310 20 15 10
HANDLING A BUNCH OF CONICAL PARTICLES ON A HORIZONTAL SURFACE
BOT 30.0 29.0 0.25 15.50 30.0
RAD 1.500 1
RAD 1.431 2
RAD 1.362 3
RAD 1.328 4
RAD 1.259 5
RAD 1.155 6
RAD 1.121 7
RAD 1.051 8
RAD 0.983 9
RAD 0.879 10
RAD 0.810 11
RAD 0.741 12
RAD 0.638 13
RAD 0.569 14
RAD 0.500 15
PRO 2.62 2.0 1.38 1.07 .45 .48 .52 1.41 2.04 2.97 3.59 4.24 5.14 5.37 6.38
DENS 1.8
FRIC .5 .5
FRAC 1.0
DAMP 0.0 0.50
GRA 0.0 0.0 -9.81
CYC 50000 1 30
MOV 25.0 -25.0
CYC 6000 50 30
STOP
```

**(d) Input file for simulation of particle singulation of 20 ellipsoid particles  
each comprised of 15 element spheres (Figure 2.24)**

```
START 300.0 15.0 252.0 42000 310 20 15 10
SIMULATION OF PARTICLE SINGULATION
BOT 96.0 4.0 0.25 14.50 1.0
RAD 2.140 1
RAD 2.920 2
RAD 3.460 3
RAD 3.730 4
RAD 4.040 5
RAD 4.370 6
RAD 4.470 7
RAD 4.500 8
RAD 4.470 9
RAD 4.370 10
RAD 4.200 11
RAD 4.040 12
RAD 3.460 13
RAD 2.920 14
RAD 2.140 15
PRO 5.28 4.56 3.84 3.36 2.64 1.44 .72 0.0 .72 1.44 2.16 2.64 3.84 4.56 5.28
DENS 1.8
FRIC 0.5 0.5
FRAC 1.0
DAMP 0.0 0.50
GRA 0.0 0.0 -9.81
CYC 150000 1 10
MOV 20.0 60.0
CYC 5000 100 10
STOP
```

**(e) Input file for simulation of a rotating disk with five spherical particles.**

```
START 140.0 140.0 100.0 15680 25 15 1 10
ROTATING DISK SIMULATION
BOT 20.0 100.0 20.0 100.0 99.0
RAD 2.50 1
PRO 0.0
DENS 1.
FRIC .5 .5
FRAC 1.0
DAMP 0.0 0.50
FAN 10.0
GRA 0.0 0.0 -9.81
CYC 5000 100 20
STOP
```

**(f) Input file for experimental validation of the code with inclined side walls (Figure 4.2)**

```
START 60.0 5.0 120.0 2304 28 10 2 8
EXPERIMENTAL VALIDATION IN PARTICLE SCALE
CON 22.50 31.0 15.0 70.0 4.60
RAD 2.2225 1
RAD 2.2225 2
PRO 1.3915 1.3915
DENS 1.8
FRIC 0.0 0.0
FRAC 1.0
DAMP 0.0 0.50
GRA 0.0 0.0 -9.81
CYC 130000 1 20
FRIC 0.20 0.20
DAMP 0.0 0.05
MOV -4.55
FRAC 0.1
CYC 27980 25 20
STOP
```

## Appendix E

### Estimation of the deviation in contact force direction for a multi-sphere elliptical particle used in the macro-scale validation.

From the model particle configuration, the following data were obtained:

$$R_s=0.433 \text{ cm} \quad R_1=0.433 \quad R_2=0.481$$

The distance between the adjacent element spheres was 0.07 cm ( $L=0.07$  cm)

The slope of the model particle boundary between the adjacent element spheres (equation 3.14) therefor is:

◦

From Equation 3.16 the direction of contact forces between the element spheres (Fig. 3.23) is

$$\alpha = \cos^{-1} \left[ \frac{((R_1 + R_s)^2 + L^2 - (R_2 + R_s)^2)}{2L(R_1 + R_s)} \right] = 131.4^\circ$$

$$\beta = \cos^{-1} \left[ \frac{((R_2 + R_s)^2 + L^2 - (R_1 + R_s)^2)}{2L(R_2 + R_s)} \right] = 44.6^\circ$$

$$\gamma = \cos^{-1} \left[ \frac{((R_2 + R_s)^2 - L^2 + (R_1 + R_s)^2)}{2(R_1 + R_s)(R_2 + R_s)} \right] = 4.1^\circ$$

The deviation of the direction of contact forces then is

$$\gamma_1 = 90 + \theta - \alpha = 1.79^\circ$$

$$\gamma_2 = 4.1 - 1.79 = 2.31^\circ$$

## Appendix F

**Video files for simulation examples presented in Chapter 2.**